

THÈSE DE DOCTORAT  
UNIVERSITÉ PARIS-SACLAY

préparée à  
INSTITUT DE PHYSIQUE THÉORIQUE  
et  
INSTITUTE OF SYSTEMS AND SYNTHETIC BIOLOGY

Ecole doctorale n°564  
Physique de l'Ile-de-France  
Spécialité de doctorat: Physique

**Modèles de l'architecture du chromosome et lien avec la  
régulation de l'expression génétique**

par

**GUILLAUME LE TREUT**

Thèse soutenue le 29 Novembre 2016, à l'Institut de Physique Théorique,  
CEA Saclay, devant le jury de thèse composé de :

RALF BLOSSEY	Dr. examinateur
ENRICO CARLON	Pr. examinateur
RALF EVERAERS	Pr. président et rapporteur
FRANÇOIS KÉPÈS	Dr. directeur de thèse
FRANÇOISE LIVOLANT	Dr. examinatrice
CRISTIAN MICHELETTI	Pr. rapporteur
HENRI ORLAND	Dr. directeur de thèse

NNT : 2016SACLS411



# Remerciements

Je tiens à remercier tous ceux qui m'ont soutenu au cours de ces trois années.

En premier lieu, merci à mes deux directeurs de thèse pour m'avoir accepté comme étudiant. Je remercie François pour avoir cru en mon désir de contribuer à la science malgré mon parcours pour le moins atypique. C'est grâce à son soutien que j'ai pu m'embarquer dans ce projet de recherche. Je lui en suis très reconnaissant. J'espère ne pas l'avoir amené à regretter son choix; en ce qui me concerne je ne le regrette pas. Je remercie également Henri pour m'avoir abreuvé de ses connaissances, en physique bien sûr, mais pas seulement. Je me tiens pour particulièrement chanceux d'avoir pu le côtoyer. Nos discussions étaient sans doute l'occasion pour lui de s'inquiéter de mes lacunes, mais quant à moi je les attendais avec impatience. Je rentrais dans ce bureau comme l'on sauterait dans un puits de savoir, sûr d'y découvrir de nouveaux pans de la physique statistique sur lesquels je plancherais avec enthousiasme ou perplexité sur le chemin du retour. Par ailleurs, beaucoup des résultats présentés dans cette thèse seraient sans doute restés des problèmes sans son aide précieuse. Pour tout cela, je lui suis très reconnaissant.

Le rôle de rapporteur est fastidieux et chronophage. Je tiens donc à remercier tout spécialement Messieurs Everaers et Micheletti d'avoir accepté cette tâche et de s'en être acquittés dans le temps imparti. J'apprécie le regard critique qu'ils ont jeté sur mon travail.

L'Institut de Physique Théorique réunit dans un même endroit une recherche en physique théorique à la pointe, des conditions de travail idéales, et des personnes formidables. En particulier, je tiens à saluer l'équipe administrative qui s'est occupée de toutes mes requêtes avec une diligence et avec une facilité déconcertantes. Je remercie Patrick, Laurent, Loïc, Laure et Anne. Plus particulièrement, je remercie Sylvie pour sa grande gentillesse. Outre son efficacité et son sens de l'anticipation, cela toujours été un plaisir de venir la voir. Je remercie également Michel Bauer de m'avoir concédé une extension de deux mois pour finir ma thèse.

Je remercie Kirone d'avoir accepté d'être mon parrain. En plus d'être un grand chercheur, sa disponibilité, sa sérénité et sa capacité d'écoute m'ont été salutaires lors des quelques phases de doutes que j'ai traversées.

Je remercie les différentes générations de thésards de l'IPhT pour les grandes tablées conviviales du déjeuner, les dîners organisés à l'improviste et nos verres occasionnels. Des anciens: Benoît, Ekaterina, Jérôme, Antoine, Hanna; à ceux de ma génération: Christophe, Xiangyu; puis à ceux arrivés plus récemment: Thibault, Christian, Séverin, Santiago, Romain, Ricardo.

Merci à Frédéric d'être venu doubler les effectifs de notre équipe de recherche pendant une année. Je garde un agréable souvenir de nos discussions aussi bien à l'institut qu'en dehors. Je lui sais gré de m'avoir fait relativiser les difficultés rencontrées et de m'avoir encouragé à persévérer. Je le remercie également de m'avoir incité à adopter une hygiène de vie saine en me faisant découvrir notamment "Dédé la frite".

Je remercie toutes les personnes de l'équipe MEGA à l'iSSB pour avoir entrepris mon instruction en

biologie depuis un niveau que nous conviendrons de ne pas divulguer. Plus particulièrement, un grand merci à Costas, Thibaut, Steff, Julie, François, Brian et Laurent pour la qualité des échanges que j'ai pu avoir avec eux, scientifiques certes, mais surtout pour tous les autres. Je salue également Sylvie, Bernadette et Dominique pour m'avoir assisté dans la complétion des diverses formalités administratives dont j'ai dû m'acquitter.

Je remercie l'IDEX Paris-Saclay d'avoir financé ma thèse.

Je remercie tous mes amis pour les bons moments passés en leur compagnie. Le maintien de mon équilibre mental et de mon intégrité sociale doit beaucoup aux séances dominicales d'Ultimate. Je pense notamment à Antoine, Fady, Hugo, Nizar, Pierre, Simon, Souhad, Charlotte et Juliette; mais aussi aux amitiés qui perdurent depuis l'enfance: Raphaël, Pauline, Carine, Florian, Arnaud et Adrien.

Je remercie ma famille pour avoir toujours fait confiance dans mes choix, et plus fondamentalement pour leur soutien inébranlable et leur présence rassérénante. Je remercie notamment mon père pour m'avoir donné l'envie de réussir et le goût de l'ambition. Et ma mère, inconditionnellement bienveillante, qui envisage toute chose avec une simplicité et un bon sens qui n'a rien de commun, qui sait tout faire et dont l'exemple me rappelle sans cesse que tout est réalisable au prix d'un effort. Je remercie également mes soeurs, Claire qui continue de chasser patiemment toutes mes vilaines habitudes, et Camille sur qui je peux toujours compter pour m'apprendre une chorégraphie.

Enfin, je remercie Maëva pour avoir été présente durant toute cette longue traversée, pour m'avoir fait garder le cap, avoir apporté son regard lucide dans mes moments de désarroi et avoir partagé mes succès. Ses contributions à ce travail et à la personne que je suis devenue sont immenses et je ne lui ferai pas l'affront de vouloir les réduire à quelques mots.

# Preface

The work presented in this thesis manuscript was realized between fall of 2013 and fall of 2016, at the Institut de Physique Théorique, CEA Saclay and the Institute of Systems and Synthetic Biology, Université d'Évry.

The motivation of this work was to provide physical models for the characterization of chromosome folding (or architecture) and understand the role it plays in regulating the genetic expression. The manuscript is organized as follows.

In chapter 1, I give an introduction to chromosome architecture and the current biological conjectures for its role. I also review standard techniques in Physics to model the chromosome. I conclude this introductory chapter by giving an outline of the work presented in the subsequent chapters.

In chapters 2 to 5, I present the results of my research activity during these three years. This resulted in the publication of one research article:

- Phase behavior of DNA in the presence of DNA-binding proteins [1].

Besides, Biology can lead to the usage of a specific vocabulary, or acronyms, whose meaning is sometimes not obvious. Although I have attempted to always define such terms before use, a glossary is available at the end of this manuscript, in order to ease the reading.



# Abstract

Increasing evidence suggests that chromosome folding and genetic expression are intimately connected. For example, the co-expression of a large number of genes can benefit from their spatial co-localization in the cellular space. Furthermore, functional structures can result from the particular folding of the chromosome. These can be rather compact bundle-like aggregates that prevent the access to DNA, or in contrast, open coil configurations with several (presumably) globular clusters like transcription factories. Such phenomena have in common to result from the binding of divalent proteins that can bridge regions sometimes far away on the DNA sequence. The physical system consisting of the chromosome interacting with divalent proteins can be very complex. As such, most of the mechanisms responsible for chromosome folding and for the formation of functional structures have remained elusive.

Using methods from statistical physics, we investigated models of chromosome architecture. A common denominator of our approach has been to represent the chromosome as a polymer with bending rigidity and consider its interaction with a solution of DNA-binding proteins. Structures entailed by the binding of such proteins were then characterized at the thermodynamical equilibrium. Furthermore, we complemented theoretical results with Brownian dynamics simulations, allowing to reproduce more of the biological complexity.

The main contributions of this thesis have been: (i) to provide a model for the existence of transcription factories characterized *in vivo* with fluorescence microscopy; (ii) to propose a physical basis for a conjectured regulatory mechanism of the transcription involving the formation of DNA hairpin loops by the H-NS protein as characterized with atomic-force microscopy experiments; (iii) to propose a physical model of the chromosome that reproduces contacts measured in chromosome conformation capture (CCC) experiments. Consequences on the regulation of transcription are discussed in each of these studies.

To model transcription factories, we implemented a Flory-Huggins polymer theory to characterize the equilibrium of DNA chains interacting with non-specific binding proteins. For sufficiently high DNA-protein binding affinity, this system was shown to exhibit a phase separation with a dilute and a dense phase. We also investigated the structure of the dense phase and showed that for stiff DNA chains, the dense phase may undergo a transition from a globular to a crystalline phase. While globular dense phases can be a model for transcription factories, crystalline dense phases may be a model for bundle-like aggregates in stressed bacteria.

To characterize the formation of DNA hairpin loops by the H-NS protein, we showed the existence of a characteristic length for the H-NS binding region, delimiting two regimes. In one regime, DNA hairpin loops are stable whereas in the other they are not. This result was obtained first from a simplified polymer model with implicit interactions, and then confirmed using Brownian dynamics simulations with explicit proteins.

To model chromosome architecture, we considered a Gaussian chain polymer model of the chromo-

some and added Gaussian effective interactions to model the effect of divalent proteins. The contact probability for any pair of monomers was computed and yielded an analytical closed-form which can be used in an inverse approach to reconstruct an effective polymer model of the chromosome reproducing contact probabilities measured in CCC experiments.

**Keywords:** statistical physics, polymer physics, Gaussian chain, worm-like chain, Flory-Huggins theory, random phase approximation, DNA phases, structure function, transfer matrix, Brownian dynamics, contact probability, DNA-binding protein, chromosome architecture, chromosome folding, chromosome dynamics, gene co-localization, transcription factory, transcription regulation, chromosome conformation capture.

# Résumé

Plusieurs indices suggèrent que le repliement du chromosome et la régulation de l'expression génétique sont étroitement liés. Par exemple, la co-expression d'un grand nombre de gènes est favorisée par leur rapprochement dans l'espace cellulaire. En outre, le repliement du chromosome permet de faire émerger des structures fonctionnelles. Celles-ci peuvent être des amas condensés et fibrillaires, interdisant l'accès à l'ADN, ou au contraire des configurations plus ouvertes comportant quelques amas globulaires, comme c'est le cas avec les usines de transcription. Bien que dissemblables au premier abord, de telles structures sont rendues possibles par l'existence de protéines bivalentes, capable d'apparier des régions parfois très éloignées sur la séquence d'ADN. Le système physique ainsi constitué du chromosome et de protéines bivalentes peut être très complexe. C'est pourquoi les mécanismes régissant le repliement du chromosome sont restés majoritairement incompris.

Nous avons étudié des modèles d'architecture du chromosome en utilisant le formalisme de la physique statistique. Notre point de départ est la représentation du chromosome sous la forme d'un polymère rigide, pouvant interagir avec une solution de protéines liantes. Les structures résultant de ces interactions ont été caractérisées à l'équilibre thermodynamique. De plus, nous avons utilisé des simulations de dynamique Brownienne en complément des méthodes théoriques, car elles permettent de prendre en considération une plus grande complexité dans les phénomènes biologiques étudiés.

Les principaux aboutissements de cette thèse ont été : (i) de fournir un modèle pour l'existence des usines de transcriptions caractérisées *in vivo* à l'aide de la microscopie par fluorescence ; (ii) de proposer une explication physique pour une conjecture portant sur un mécanisme de régulation de la transcription impliquant la formation de boucles d'ADN en tête d'épingle sous l'effet de la protéine H-NS, qui a été émise suite à l'observation de ces boucles au microscope à force atomique ; (iii) de proposer un modèle du chromosome qui reproduise les contacts mesurés à l'aide des techniques Hi-C. Les conséquences de ces mécanismes sur la régulation de la transcription ont été systématiquement discutées.

Afin de modéliser les usines de transcription, nous avons considéré une théorie de Flory-Huggins pour des chaînes d'ADN en interaction avec des protéines liantes. Cela nous a permis de caractériser l'équilibre thermodynamique. En particulier, pour une affinité suffisamment forte avec les protéines, l'ADN se condense, ce qui donne lieu à un système biphasique comportant une phase diluée et une phase dense. Nous avons ensuite montré que pour des chaînes rigides, la phase dense peut passer d'une structure globulaire à une structure cristalline. Une phase globulaire semble être un bon modèle pour les usines de transcriptions, tandis que les amas fibrillaires s'apparentent davantage à une phase cristalline.

Afin de caractériser la formation de boucles d'ADN en têtes d'épingles sous l'effet de la protéine H-NS, nous avons montré qu'il existe une taille caractéristique pour les régions de liaison avec H-NS. Au-dessus, les boucles sont stables tandis qu'en dessous elles sont instables. En utilisant un modèle simplifié de polymère, nous avons obtenu une expression pour cette grandeur, que nous avons ensuite

confirmée à l'aide de simulations de dynamique Brownienne.

Afin de modéliser le repliement du chromosome, nous avons considéré un modèle de polymère Gaussien auquel nous avons ajouté des interactions effectives représentant l'effet de protéines bivalentes. Nous avons alors pu calculer la probabilité de contact entre deux monomères. L'expression obtenue a ensuite été utilisée pour résoudre le problème inverse consistant à trouver le modèle effectif qui reproduit les probabilités de contact mesurés lors d'expériences Hi-C.

**Mots-clefs:** physique statistique, physique des polymères, chaîne gaussienne, chaîne de Kratky-Porod, théorie de Flory-Huggins, random phase approximation, phases de l'ADN, fonction de structure, matrice de transfert, dynamique brownienne, probabilité de contact, protéine se liant à l'ADN, architecture du chromosome, repliement du chromosome, dynamique du chromosome, co-localisation des gènes, usine à transcription, régulation de la transcription, chromosome conformation capture.

# Contents

<b>1</b>	<b>Introduction</b>	<b>1</b>
1.1	Chromosome architecture and genetic expression . . . . .	1
1.1.1	The central dogma of biology . . . . .	1
1.1.2	From a classical to a modern view of transcription . . . . .	2
1.1.3	Multi-scale description of the chromosome . . . . .	5
1.1.4	The role of chromosome architecture . . . . .	5
1.1.5	Experimental data in biology . . . . .	7
1.2	Modelling complexity in biology . . . . .	8
1.3	Polymer model of the chromosome . . . . .	10
1.3.1	Beads-on-string polymer . . . . .	10
1.3.2	Gaussian chain . . . . .	10
1.3.3	Excluded volume and short-range interactions . . . . .	12
1.3.4	Bending rigidity . . . . .	13
1.3.5	Final model of the chromosome . . . . .	18
1.4	Brownian dynamics . . . . .	18
1.4.1	The Langevin equation . . . . .	18
1.4.2	Mapping to real time . . . . .	18
1.4.3	A practical detail: relaxation of polymer systems with excluded volume . . . . .	19
1.5	Organization of the thesis and personal contributions . . . . .	19
	<b>Appendices</b>	<b>21</b>
1.A	Asymmetrical DNA double-helix . . . . .	21
1.B	Continuous worm-like chain . . . . .	21
1.C	Sampling of the Boltzmann equilibrium by the Langevin equation . . . . .	23
<b>2</b>	<b>Modelling of transcription factories</b>	<b>25</b>
2.1	Introduction . . . . .	25
2.1.1	From co-regulation to co-localization . . . . .	25
2.1.2	Co-localization of genes in transcription factories . . . . .	27
2.1.3	Physical origin of transcription factories . . . . .	28
2.2	Model proposed . . . . .	28
2.2.1	Formal nucleus/nucleoid . . . . .	28
2.2.2	First principles model . . . . .	29
2.2.3	Field representation . . . . .	30

2.3	Flory Huggins theory . . . . .	31
2.3.1	Mean-field free energy . . . . .	32
2.3.2	Spinodal condition . . . . .	32
2.3.3	The biphasic regime . . . . .	33
2.3.4	Conclusion . . . . .	36
2.4	Structure of the dense phase . . . . .	38
2.4.1	Random Phase Approximation . . . . .	38
2.4.2	Lattice model of the dense phase . . . . .	42
2.4.3	Phase diagram of the dense phase structure . . . . .	47
2.4.4	Conclusion . . . . .	48
2.5	Discussion . . . . .	50
<b>Appendices</b>		<b>51</b>
2.A	Matrix elements of the Gaussian fluctuations . . . . .	51
2.B	Detection of the coil-globule-crystal transitions . . . . .	54
<b>3</b>	<b>A side-study: computation of the structure function of a worm-like chain</b>	<b>57</b>
3.1	Relevance of the structure function in polymer field theories . . . . .	57
3.2	Expression of the pair correlation function . . . . .	58
3.2.1	Pair correlation and structure function . . . . .	58
3.2.2	Expression in terms of transfer matrices . . . . .	59
3.3	Application to the computation of the structure function . . . . .	60
3.3.1	Transfer matrix method . . . . .	60
3.3.2	Comparison with other methods . . . . .	62
3.4	Discussion . . . . .	63
<b>Appendices</b>		<b>65</b>
3.A	Other methods to compute the pair correlation function of a worm-like chain . . . . .	65
<b>4</b>	<b>Model for the role of nucleoid-associated proteins in regulating transcription</b>	<b>67</b>
4.1	Introduction to nucleoid-associated proteins (NAPs) . . . . .	68
4.1.1	What are NAPs? . . . . .	68
4.1.2	Architectural and regulatory role . . . . .	68
4.1.3	Characterization <i>in vivo</i> . . . . .	69
4.2	The Nucleoid-Associated Proteins of <i>E. coli</i> bacteria . . . . .	69
4.2.1	The Histone-like Nucleoid Structuring protein (H-NS) . . . . .	69
4.2.2	The Factor of Inversion Stimulation (FIS) . . . . .	72
4.2.3	The Heat-Unstable protein (HU) . . . . .	75
4.2.4	The Integration Host Factor (IHF) . . . . .	76
4.2.5	Summary . . . . .	77
4.3	Relevant scale for modeling the effect of NAPs . . . . .	78
4.3.1	Evolutionary selection of random insertions . . . . .	78
4.3.2	Model of NAPs binding sites insertion . . . . .	78
4.3.3	Binding sites spacing analysis from AT content . . . . .	79
4.3.4	Binding sites spacing analysis from ChIP-seq data . . . . .	80
4.3.5	Conclusion . . . . .	85

4.4	Model for the regulatory effect of H-NS . . . . .	87
4.4.1	Experimental evidences of H-NS loops . . . . .	87
4.4.2	Model for the formation of H-NS loops . . . . .	88
4.4.3	Investigation with Brownian Dynamics . . . . .	90
4.4.4	Conclusion . . . . .	95
4.5	Discussion . . . . .	96
<b>5</b>	<b>Reconstruction of chromosome architecture from chromosome conformation capture experiments</b>	<b>99</b>
5.1	Introduction . . . . .	100
5.2	Chromosome Conformation Capture experiments . . . . .	101
5.2.1	Historical context . . . . .	101
5.2.2	Method . . . . .	101
5.2.3	Caveats . . . . .	102
5.2.4	From counts to contact probabilities . . . . .	103
5.3	Previous approaches to predict chromosome folding from Hi-C data . . . . .	105
5.3.1	Models based on an estimate of the distance matrix . . . . .	105
5.3.2	A polymer model reproducing experimental contact frequencies . . . . .	108
5.4	Gaussian Effective Model . . . . .	110
5.4.1	Model . . . . .	110
5.4.2	Naive approach . . . . .	112
5.4.3	One-to-one correspondence between couplings and contact probabilities . . . . .	114
5.4.4	Form factors . . . . .	117
5.4.5	Conclusion . . . . .	118
5.5	Reconstruction from artificial contact probability matrices . . . . .	119
5.5.1	Artificial contact probability matrices . . . . .	119
5.5.2	Direct method for reconstructing a Gaussian effective model . . . . .	120
5.5.3	Stability analysis . . . . .	123
5.5.4	Reconstruction of a stable Gaussian effective model . . . . .	126
5.6	Reconstruction from Hi-C contact probability matrices . . . . .	132
5.7	Discussion . . . . .	132
<b>6</b>	<b>Concluding remarks</b>	<b>139</b>
	<b>Publication</b>	<b>143</b>
	<b>Glossary</b>	<b>157</b>
	<b>Acronyms</b>	<b>161</b>
	<b>Bibliography</b>	<b>163</b>



# Chapter 1

## Introduction

### 1.1 Chromosome architecture and genetic expression

#### 1.1.1 The central dogma of biology

Life depends on the ability of cells to store, retrieve and translate a set of instructions commonly denoted as the genetic code. This information is stored in the genes, which determine the characteristics of each individual.

Since the beginning of the twentieth century, we know that the genetic code is carried by deoxyribonucleic acid (DNA) molecules, with a simple chemical composition. The realization of X-ray diffraction experiments in the 1950s led Watson and Crick (Nobel prize 1962) to propose the correct model for the molecular structure of DNA [2]. Specifically, a DNA molecule consists of two polynucleotide chains (or strands) wound in a double-helix. Each nucleotide is made of a sugar and of one of the four bases: adenine (A), thymine (T), guanine (G) and cytosine (C). The sugars are covalently linked together and form the DNA “backbone”. In addition, the two strands are held together by hydrogen bonds between the bases on the different strands, resulting in a double-helical structure with the base pairs (bp) inside. Actually, bases do not pair at random, but by pair complementarity: A with T and G with C.

The complete sequence of base pairs determines the genetic information of each individual. It is called the genome. The corresponding sequence of letters is enormous. For instance, in the *Escherichia coli* bacterium, it contains  $4.6 \times 10^6$  letters, and more than  $3.3 \times 10^9$  in humans. For comparison, in the latter case it would take more than 1000 books of 1000 pages to write down the full sequence. Besides, specific DNA sequences, the genes, are encountered in the genome. Their number ranges from less than a hundred in simple bacteria to several tens of thousands in higher organisms. For example, approximately 4600 genes are found in *E. coli* and more than 30 000 in humans.

The genes encode macromolecules such as ribonucleic acids (RNA), or polypeptides which are chains of amino-acids more commonly known as proteins. These macromolecules are responsible for most of the biochemical workings of a cell and can be envisioned as molecular “tools”. The central dogma of molecular biology states that DNA sequences from genes are first transcribed into RNA. Furthermore, some RNA transcripts known as messenger RNA (mRNA) are then translated into proteins. The protein synthesis relies on a correspondence between the 4-letter nucleotide alphabet of DNA and the 20-letter amino-acid alphabet of proteins.

In short, the DNA sequences of genes can be seen as a message, handled through two essential and

successive processes which are transcription and translation. Yet in order to adjust the synthesis of proteins to the cell needs the genetic expression can be regulated.

### 1.1.2 From a classical to a modern view of transcription

In a classical work [3], Jacob and Monod (Nobel prize 1965) proposed their vision of the operon system in bacteria, which has been extended to the whole living realm and is still nowadays a pillar of molecular biology. Genetic expression is under the control of particular sequences called promoters, found a few tens of base pairs upstream of the protein encoding sequences. Such regions have typically a size of 300 bp but sometimes can be even longer. The structural unit constituted of one promoter followed by one or several regulated genes is called an operon. The promoter is of critical importance because it is where the protein responsible for the mRNA synthesis, the RNA polymerase (RNAP), is recruited to initiate the transcription of the downstream gene or operon. The affinity of RNAP with the promoter is therefore an indirect measure for the transcription level and represents a handle for its regulation. Transcription factors (TFs), that is to say proteins which can regulate the transcription of a gene, can bind to the promoter thanks to the presence of several transcription factor binding sites (TFBS, fig. 1.1). Importantly the binding of transcription factors to the promoter can alter its affinity with RNAP. When a transcription factors stimulates the transcription it is called an activator (or inducer), and a repressor in the opposite case. At a molecular level, a repressor bound to the promoter area will prevent RNAP binding or obstruct transcription elongation, and an activator bound to the promoter will enhance transcription by recruiting RNAP from the bulk (fig. 1.2).

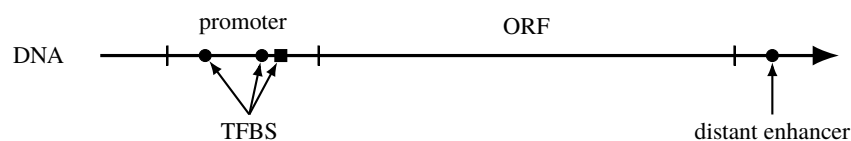


**Figure 1.1** – Organisation of a gene under transcriptional regulation. The open reading frame (ORF) encoding for a protein is preceded by a promoter region where several transcription factor binding sites (TFBS) are found. The promoter region comprises one main binding site and several auxiliary binding sites. In eukaryotes, TFBS participating to the gene expression regulation can sometimes be found very far away on the DNA sequence and are called enhancers.

The transcription factor binding sites can be divided into two sets. The binding site with the highest affinity is called the main binding site and is generally found in the promoter region. Others binding sites entailing a weaker binding are called auxiliary binding sites. These are mainly found in the promoter region, but can also be found outside in some cases. The simultaneous binding of a TF with the main and auxiliary binding sites can also participate to the regulation of the transcription. A famous example is the *lac* repressor system in *Escherichia coli*. In this particular case, efficient repression is achieved only when the *lac* repressor binds simultaneously the main and auxiliary binding sites found 401 bp from each other in the genome. Actually, many other examples of such regulatory systems have been characterized [5, 6]. This type of repression involves the formation of DNA loops from tens to a few hundreds base pairs long. An *in vitro* assay has even constructed a synthetic repressor system involving the interaction between the main binding site of a promoter and an auxiliary binding site separated by 2800 bp on a plasmid [7]. The corresponding DNA loops were observed with electron microscopy imaging and corresponded to the repressed state (fig. 1.3). The existence of distant regulatory elements has now been established for a large number of genes. In eukaryotes specifically, auxiliary binding sites can be found sometimes very far

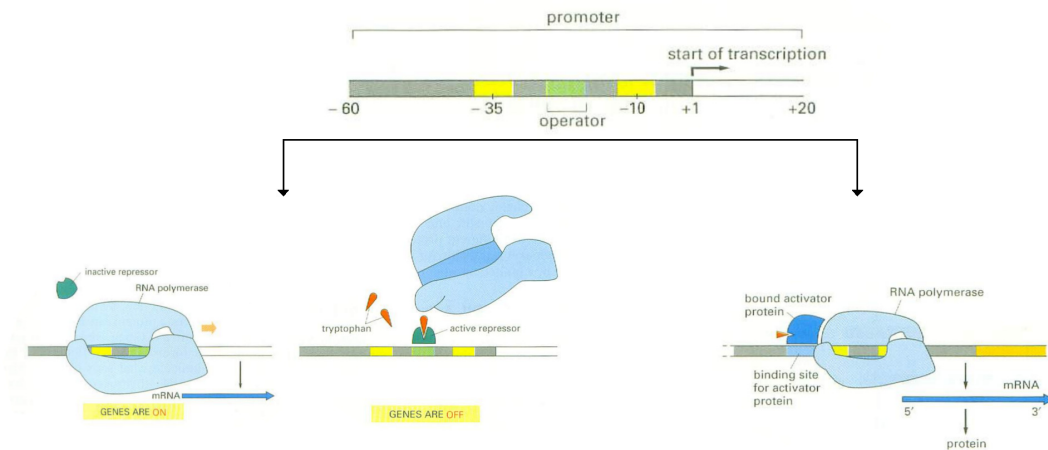


**Figure 1.2** – Classical view of the repressor/activator regulation of the transcription [4].

away from the promoter (tens of thousands base pairs), in which case they are called enhancers. When a TF has a low affinity with its main binding, *i.e.* the promoter is weak, the simultaneous binding with an auxiliary binding site may stabilize the binding of the TF to the promoter. When the main and auxiliary sites are not too far from each other, say less than 200 bp, the formation of a DNA loop may simply prevent RNAP binding by physically forbidding the access to the promoter. More generally, it is conjectured that the interaction with a remote regulatory site (or CIS element) can favor the formation of a complex comprising DNA and proteins which enhances or represses the transcription (fig. 1.4).

Let us now consider the problem of a TF diffusing in the nucleoid (in bacteria) or nucleus (in eukaryotes), whose target is the main binding site found in the promoter region of the regulated gene. The typical square displacement of the protein during the time  $t$  scales like  $\langle x^2 \rangle \sim Dt$ , where  $D$  is the diffusion coefficient. For a protein diffusing in the cytosol, we typically have  $D \approx 10 \mu\text{m}^2 \text{s}^{-1}$  [8]. Hence the average distance traveled by a protein during 10 ms is approximately 300 nm. If we consider that the typical size of the bacterial nucleoid in *E. coli* is 600 nm, then the diffusion time can be quite limiting in regulatory mechanisms of the transcription where proteins have to find their targets on the DNA, scattered within the nucleoid. This is even more critical in eukaryotes, where the size of the nucleus is of several micrometers. The presence of auxiliary binding sites provides an intuitive way to enhance the search process. When a TF is bound to an auxiliary binding sites, it cannot diffuse freely in the cytosol. Instead, it is confined in a sphere whose radius is the contour distance, say  $l$ , between the main and auxiliary binding sites. Hence the TF only explores a reduced volume in comparison to the whole cellular (or nuclear) compartment, of size  $L$ . In other words, the apparent concentration of this TF relatively to the promoter is increased by a factor  $(L/l)^3$ . This is a typical example of local concentration effect.

In summary, it has become clear in the recent decades that the DNA molecule cannot be reduced to a mere “cookbook” with a passive role. Instead, it is directly involved in the genetic expression regulation. Specifically, proteins can use the DNA molecule as a scaffold to build complexes or loops that regulate the transcription [9]. This is possible because most TFs are divalent and have several additional binding sites distributed on the genome.

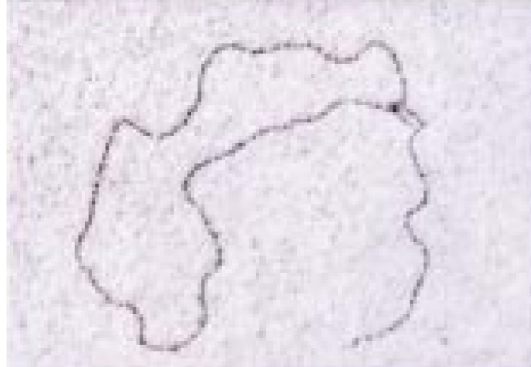


**Figure 1.3** – Electronic microscopy image of a repressor system relying on the formation of a 2850 bp long loop between the main binding site of a promoter and an auxiliary binding site [7].

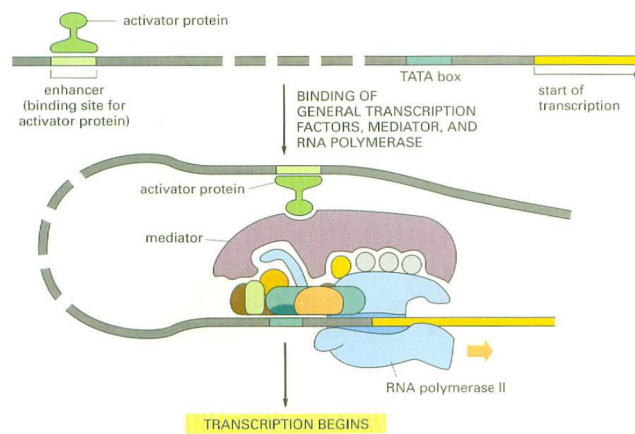


**Figure 1.4** – A distant regulatory sequence can interact with the promoter through a looping mechanism to enhance/repress transcription [4].

### 1.1.3 Multi-scale description of the chromosome

In physiological conditions, scores of proteins are bound to the DNA molecule, which consequently is never found “naked”. The resulting molecule is usually called the chromosome. Although in the classical sense, the chromosome refers to the threadlike structures of condensed DNA observed during mitosis (the process by which a cell becomes two cells), it is nowadays commonly used to designate the double-helical DNA molecule with its structuring proteins. Thus we shall follow this convention from now on. Under the effect of these structuring proteins, the chromosome adopt higher level structures that constitute the chromosome folding, or architecture.

In order to fit inside the bacterial cell or the eukaryotic nucleus, the chromosome is compacted nearly  $10^3$  times, and this is true in all organisms [10]. In *E. coli* for instance, the free chromosome (after lysis of the cell walls) spans a spherical volume with a diameter of approximately  $20 \mu\text{m}$  whereas the length of a bacterium cell is typically of  $1 \mu\text{m}$  (fig. 1.5). Therefore, the chromosome needs to be compacted (or folded) in a multi-scale organisation whose underlying mechanism has remained unclear.

In eukaryotes, there exist four basic levels of folding of the chromosomal chain [11, 12] (fig. 1.6). First, there is the nucleosomal organization enabled by the presence of structuring proteins called histones. Naked DNA wraps around each histone octamer on approximately 147 bp to form a nucleosome. Two consecutive nucleosomes are connected by a linker DNA approximately 80 bp long. Consequently, the chromosome adopts a "beads-on-string" structure, clearly characterized by *in vitro* assays, where the elementary monomer in the chromosomal chain is the nucleosome. A string of nucleosomes gives rise to the 11 nm fiber. Second, the 30 nm fiber is obtained by coiling the 11 nm fiber in a solenoidal structure with about 6 nucleosomes per turn. The chromosomal fiber is then usually designated as chromatin and has a linear packing fraction  $\nu \approx 100 \text{ bp nm}^{-1}$  [13–16]. Note that actively transcribed chromatin tends to be loosely packed and is called euchromatin whereas chromatin containing non-coding or silent genes tends to adopt more compact conformations (often under the effect of structuring proteins) and is usually called heterochromatin. Yet, the 30 nm fiber is apparently only observed in the interphase nucleus. Therefore, a third level of organization exists, in which the chromosomal chain is organized into domains containing from 30 to 100 kbp and resulting in a fiber of diameter 200-300 nm. Finally during mitosis, the ultimate level of compaction consists in an helical folding of the metaphase chromosome, resulting in the well known condensed chromosomes [17, 18]. Presumably, structuring proteins are responsible for transitions from one level of organization to the other.

Bacteria lack histones, therefore the primary level of folding is not achieved and the chromosome can be seen as a fiber of diameter 2.5 nm [13]. However, the bacterial DNA is most often circular and negatively super-coiled. This is known to produce plectonemes. In particular, they have been reported to provide a superior level of organization of the chromosome into domains whose size is estimated to 10 – 20 kbp [19, 20]. Yet, we stress that they are not maintained by scaffolding proteins and for this reason can hardly be compared to chromosome folding in eukaryotes.

### 1.1.4 The role of chromosome architecture

The cooperative binding of hundreds of multivalent TFs producing DNA loops and of structuring proteins on the chromosome can result in sophisticated structures. This kind of global changes can completely re-define the chromosome architecture, and have far reaching consequences on transcription (and presumably other biological processes) that we are just starting to understand.

A modern view of the chromosome is that TFs can form DNA loops resulting in several functional

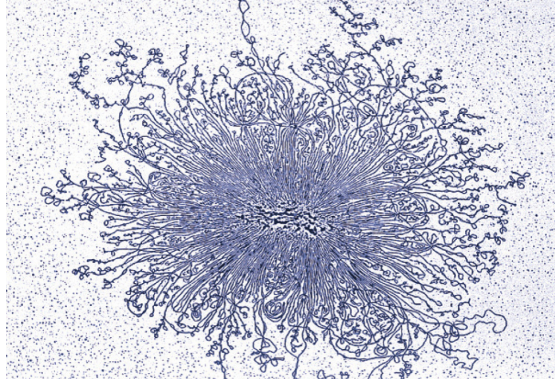


**Figure 1.5** – *E. coli* chromosome after lysis of the cell walls (at the center) [21].

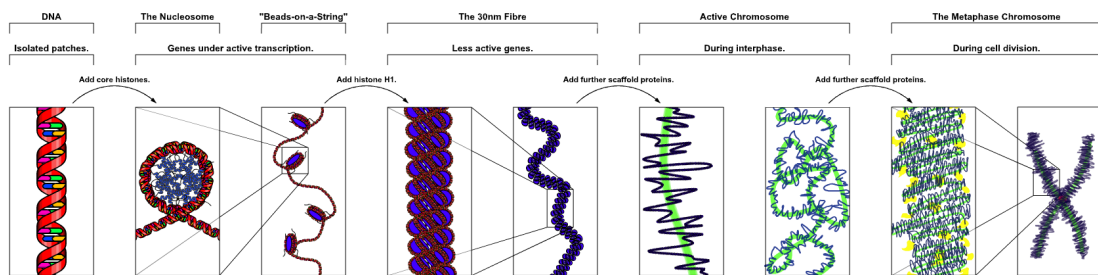


**Figure 1.6** – The four levels of folding of the eukaryotic chromosome [12].

clusters with a “rosette” shape [22,23] or in a solenoidal topology [24,25] (fig. 1.7). It is conjectured that these organizations enable to bring close in space genes whose transcription needs to be synchronized (fig. 1.7). In other words, the spatial distribution of genes inside the nucleus/nucleoid matters. This suggests that the genetic expression of a gene will depend on the genes and proteins encountered in its neighborhood. Hence, the specific folding of the chromosome can result in varying transcription levels along the genome, a phenomenon known as context sensitivity which has remained poorly understood.

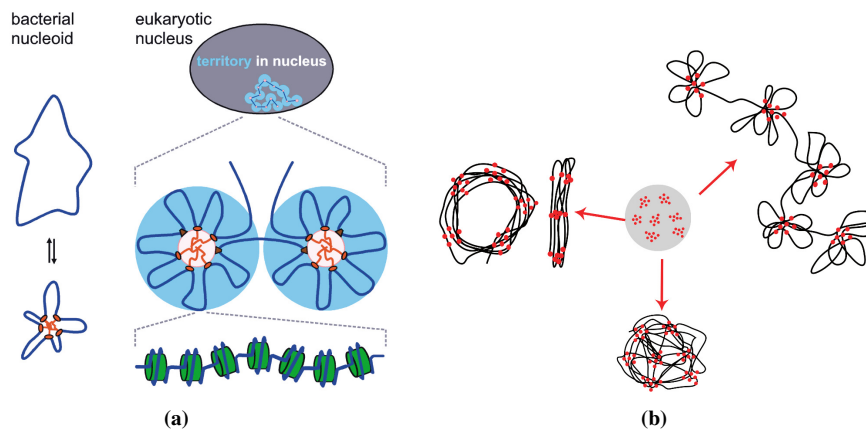


**Figure 1.7** – (a) Organization of the chromosome in “rosettes” by TFs [23].(b) Organization of the chromosome in “solenoid” [25].

Functional structures are also encountered in biological processes radically different from genetic regulation. For instance, in *E. coli* and *Bacillus subtilis* bacteria, following an exposure to assaults inducing double-strand DNA breaks, the chromosome is reorganized into filamentous bundle-like assemblies maintained by the RecA protein. It is assumed that these structures with quasi-crystalline order can at the same time protect DNA from further damages and enhance DNA repair by limiting the dimensionality of the search in the homologous recombination process, hence justifying the name of “repairosome” [26]. Such ordered states, which have been reproduced *in vitro*, are also encountered in other contexts such as viruses, mitochondrial DNA, stressed bacteria, and induce an inactive state for DNA [27].

In summary, recent advances in biology are promoting chromosome architecture as a major determinant of the cell physiology. Back to transcription, while the operon system may be seen as the primitive mechanism for genetic expression, it is has become clear that sophisticated regulatory mechanisms require an interplay between chromosome architecture and transcription. Understanding this link is also relevant to several active areas of research including conditional genetic expression, cell differentiation and epigenetics. Yet many unknowns remains, and we are still far from having resolved this phenomenon.

### 1.1.5 Experimental data in biology

Many important experimental results in biology have been and still continue to be obtained with fluorescence *in situ* hybridization techniques (FISH). In such methods, a fluorescent probe that binds specifically a target DNA (or RNA) sequence by base complementarity is introduced in the cell and monitored with confocal microscopy imaging. This allows the spatio-temporal tracking of a precise location on the chromosome (or locus). For instance, it has been used to investigate spatial organization of transcribed genes [28] or to follow the motion of loci during DNA replication [29]. However, new technologies as

well as new ideas have enabled the steady improvement of experimental techniques in biology. Namely, localization-based super-resolution fluorescence techniques have considerably extended possibilities offered by FISH imaging and enabled to track fluorescent probes at a resolution of a few nanometers, below the diffraction limit. This can be done in two ways. The first is achieved by post-processing images obtained from FISH techniques. Thus the increased resolution does not come from more accurate experimental measurements but from an ingenious data treatment of many consecutive images. The second is achieved in experimental setups implementing stochastic optical reconstruction microscopy or photo-activated localization microscopy (STORM or PALM, Nobel Prize 2014). Alternatively, the tracking of quantum “dots” with two-photon adsorption has enabled imaging in living cells at an unprecedented resolution and with less damages caused to the cell.

Other techniques that have revolutionized experimental biology in the last decade or so are those relying on polymerase chain reactions (PCR) combined with high-throughput DNA sequencing. For instance, ChIP-seq techniques [30–32] allow to measure the probability of binding along the genome for a protein of interest at a resolution of a few tens of base-pairs. Similarly, Hi-C techniques can measure the probability of contact between pairs of DNA sequences on the chromosome and output a contact probability matrix for the whole genome at a resolution of a few kbp [33–35].

The convergence in technologies now makes it possible to apply each of these techniques not on a population of cells but at the single-cell level. Although they still are at their beginning, single-cell techniques can throw light on stochastic fluctuations from a cell to another one in biological processes including chromosome organization and genetic expression.

## 1.2 Modelling complexity in biology

Thanks to modern experimental techniques, the spatial structures of the chromosome that we just discussed have been pretty well characterized. Yet understanding the underlying physics, that would pave the way to an era of quantitative predictions, has remained an important challenge. While it is true that all biological processes result from the superimposition of many individuals abiding by the laws of physics, the resulting system can be of a daunting complexity. In particular, problems in biology are characterized by their high-dimensionality, the non unicity of their solutions and the variety of the microscopical players involved (*i.e.* the presence of disorder).

Proteins are ubiquitous in the cell and their many interactions with DNA form a complex system. On a global scale, the chromosome architecture is constrained and shaped by structuring proteins, namely nucleoid-associated proteins (NAPs) in bacteria and histones in eukaryotes. Yet less abundant but dedicated transcription factors can bind to DNA and locally alter the structure the chromosome (*e.g.* by forming loops). Reconciling these two effects into a single physical model is not an easy task and requires a multi-scale approach. For example, there have been models of statistical physics showing how the cooperative binding of transcription factors can result in abrupt transitions leading to the collapse of the chromosome into loops [36] or to an apparent increased affinity of the TF to the gene promoter [37]. Methods from statistical physics have been very successful in describing a large variety of complex system phenomena in the twentieth century, yet their application to study biological processes has found many caveats. While they are adapted to describe systems with many but identical constituents, and possibly a source of disorder, difficulties arise in biological systems which involve not a few but tens of protein types, hence these models are rarely tractable.

For example, the organization of the chromosomes does not comply with predictions from standard

polymer physics. Indeed, instead of being entangled, chromosomes remain in separated and non overlapping domains known as chromosome territories [38, 39] (fig. 1.8). The configurations adopted by a single chromosome seem best described by the so-called crumpled (or fractal) globule polymer which assumes that strong topological constraints (namely excluded volume) prevents mixing and the equilibrium distribution of the polymer to be reached [40, 41].

It is often hard to know whether a biological process operates at or out of thermal equilibrium. On the one hand the presence of many stationary processes suggests that processes in biology can occur at thermal equilibrium. For example, the transcriptional response to external changes can be achieved within seconds, like the SOS response to stress exposure in *E. coli*. This suggests that for several biological processes, equilibrium, or at least a new stationary state, can be reached quickly. On the other hand, molecular crowding significantly increases the diffusion times, which is also known to result in anomalous diffusion [42, 43]. Furthermore, consistent with the crumpled globule picture, the equilibration time for chromosomes is expected to count in tens of years, suggesting that the chromosomes in the nucleus are never equilibrated [44].

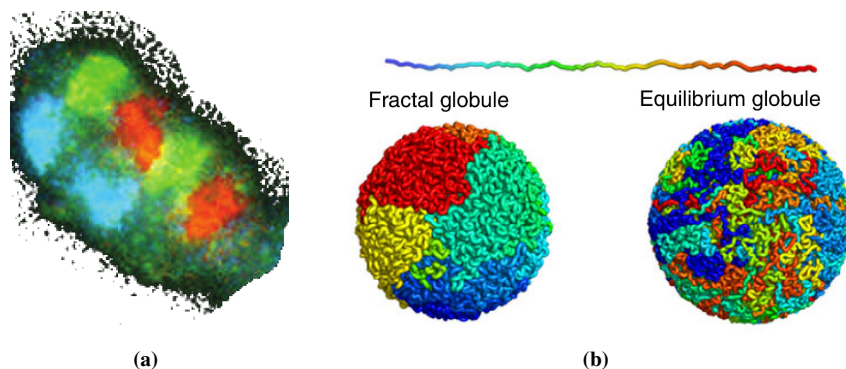


**Figure 1.8** – (a) Fluorescence imaging of the chromosome 12, 14 and 15 in the nucleus of mouse liver cells display an organization into chromosome territories [38]. (b) Crumpled versus equilibrium polymer globules [41].

A strategy to increase our understanding of biology and still retain a reasonable amount of complexity is to resort to molecular dynamics (MD) simulations. Even then, it is not possible in general to perform molecular dynamics simulations at the atomic resolution and produce trajectories corresponding to time scales compatible with biological times (of the order of seconds). Instead, coarse-grained approaches ignoring molecular details such as sequence effects, the double-helical structure of DNA and modeling the solvent implicitly are preferred. This kind of MD, called Brownian Dynamics (BD), has been broadly used in the past to model the dynamics of the chromosome. It has brought valuable insights on several biological processes, including genes co-localization [45], transcription factories [46], or the nucleosomal architecture in eukaryotes [15], and more generally on chromosome architecture [44, 47–49]. Obviously, BD simulations still rely on several simplifying assumptions that reduce the underlying complexity. In particular, a trade-off must be found between the system size, *i.e.* the number of constituents, and the variety of the interactions, *e.g.* the types of proteins or sequence effects. For instance, a common approach is to consider a generic type of protein with average properties, which represent several protein types at the same time [46, 50]. The investigator is then left with several free parameters to fit (or to guess), like binding energies between proteins and DNA, which in general are not known. Because of these limitations, BD simulations cannot be used yet to produce accurate quantitative predictions. However,

when they are in qualitative agreement with experimental observations, they can be of precious help to understand the underlying physics and serve as proof of concept for a physical model.

In the next two sections, we spend some time to review some standard results in statistical physics that will be used at different stages of this manuscript. In particular we introduce standard polymer models of the chromosome and the Brownian dynamics framework.

## 1.3 Polymer model of the chromosome

### 1.3.1 Beads-on-string polymer

Being a long macro-molecule, the chromosome is commonly modeled as a polymer, consisting of the repetition of structural units called monomers [51,52]. The chromosome is then divided into  $N + 1$  “blobs” of size  $b$ , with coordinates  $\mathbf{r}_i$ , with  $i = 0, \dots, N$ . This is the so-called beads-on-string polymer of contour length  $L = bN$  (fig. 1.9). In order to be a consistent model of the reality,  $b$  should be equal to the diameter of the chromosome fiber. For eukaryotes, we will consider the 30 nm fiber, and we obtain  $b \approx 3000$  bp. For bacteria, we will consider the naked DNA with diameter 2.5 nm and we obtain  $b \approx 7.3$  bp (where we have used that one base pair has a size of approximately 0.34 nm). In the sequel, we introduce the standard polymer models that are used to model the chromosome. For an exhaustive review on polymers, we refer the interested reader to the classical literature [53–55].

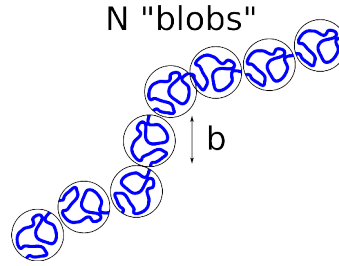


Figure 1.9 – Beads-on-string polymer.

### 1.3.2 Gaussian chain

Assuming that the first monomer is attached to the origin,  $\mathbf{r}_0 = 0$ , the end-to-end vector is defined as:

$$\begin{aligned} \mathbf{R}_e &= \mathbf{r}_N \\ &= \sum_{i=1}^N \mathbf{u}_i, \end{aligned} \quad (1.1)$$

where  $\mathbf{u}_i = \mathbf{r}_i - \mathbf{r}_{i-1}$  is the bond  $i$  vector. The expression in eq. (1.1) may be seen as a discrete stochastic process describing the motion of a particle making random jumps  $\mathbf{u}_i$ . If we assume that all bonds are independently and identically distributed (i.i.d.) random variables with zero mean and variance  $b^2$ , we obtain the mean square end-to-end distance:

$$\langle R_e^2 \rangle = b^2 N, \quad (1.2)$$

where  $b$ , the monomer size, is also called the Kuhn length. Note that for long polymers ( $N \gg 1$ ), we have by the central limit theorem that the probability distribution function (p.d.f.) of  $R_e$  converges to a Gaussian distribution. Another useful quantity is the (square) radius of gyration:

$$R_g^2 = \frac{1}{N+1} \sum_{i=0}^N (\mathbf{r}_i - \mathbf{r}_{cm})^2, \quad (1.3)$$

where  $\mathbf{r}_{cm}$  is the center of mass of the polymer. The radius of gyration gives an account of the spherical volume occupied by the polymer coil, and it has also the advantage of being defined for branched polymers, when the end-to-end vector is not.

If we assume that all bonds  $\mathbf{u}_i$  have Gaussian distributions, then  $\mathbf{R}_e$  has also a Gaussian distribution. This is the so-called Gaussian chain model, which is equivalent to say that monomers are linked one to another by harmonic springs (fig. 1.10). The internal energy of the polymer chain is then simply obtained by summing the contributions of each spring:

$$\beta U_e [\{\mathbf{r}_i\}] = \frac{3}{2b^2} \sum_{i=1}^N (\mathbf{r}_i - \mathbf{r}_{i-1})^2. \quad (1.4)$$

The partition function of the Gaussian chain is then

$$Q_N = \int \prod_{i=1}^N d^3 \mathbf{r}_i \exp(-\beta U_e [\{\mathbf{r}_i\}]), \quad (1.5)$$

and we can compute the characteristic function of the end-to-end distance by Gaussian integral calculus:

$$\begin{aligned} \langle \exp(i\mathbf{k} \cdot \mathbf{R}_e) \rangle &= \frac{1}{Q_N} \int \prod_{i=1}^N d^3 \mathbf{r}_i \exp(-\beta U_e [\{\mathbf{r}_i\}] + i\mathbf{k} \cdot \mathbf{r}_N) \\ &= \exp\left(-\frac{1}{2} b^2 N k^2\right), \end{aligned} \quad (1.6)$$

from which we conclude that  $\mathbf{R}_e$  indeed is normally distributed and with second moment as in eq. (1.2). For completeness, note that eq. (1.4) can be extended in the continuum limit:  $\mathbf{r}_i - \mathbf{r}_{i-1} \leftarrow \dot{\mathbf{r}}(s)$ . The chain is then determined by the space curve  $\mathbf{r}(s)$ , where  $s$  is now a continuous variable between 0 and  $N$ . The energy of the continuous Gaussian chain reads:

$$\beta U_e [\mathbf{r}(s)] = \frac{3}{2b^2} \int_0^N ds \dot{\mathbf{r}}(s)^2. \quad (1.7)$$

In reality, approximating a polymer to a Gaussian chain is only valid for weak perturbations, and in particular when the end-to-end distance is much smaller than the contour distance:  $R_e \ll Nb$ . Otherwise, non-linearities in the bonds elasticity may arise. Besides, Gaussian polymers allow the bond distance to fluctuate quite a lot ( $\langle u_i^2 \rangle = b^2$ ). This will be problematic in BD simulations with excluded volume interactions between the monomers because this would result in possible crossings between different bonds. Therefore, for BD implementations, we will prefer to eq. (1.4), the finitely-extensible non-linear elastic potential (FENE):

$$U_{fene} [\{\mathbf{r}_i\}] = -\frac{3k_e r_0^2}{2b^2} \sum_{i=1}^N \ln\left(1 - \frac{u_i^2}{r_0^2}\right), \quad (1.8)$$

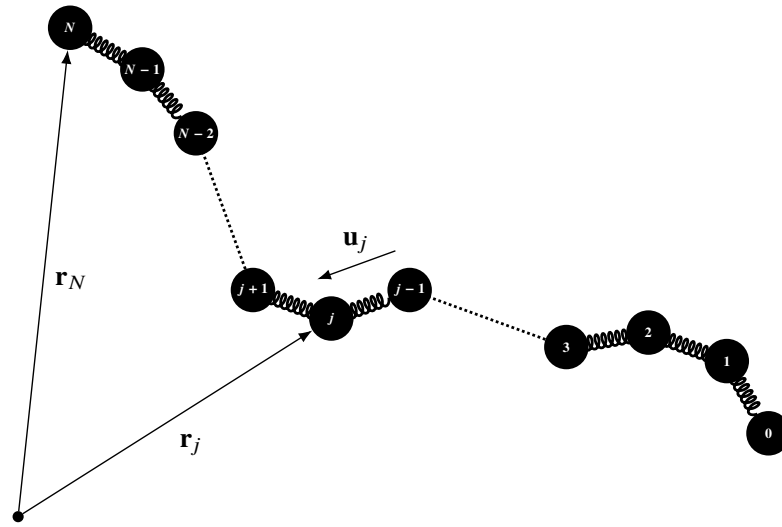


Figure 1.10 – Gaussian chain model.

where  $r_0$  is a distance above which non-linear effects start to appear in the bonds elasticity and  $k_e$  is the rigidity constant of the non-linear spring. Note that for  $u_i \ll r_0$  we recover eq. (1.4), *i.e.* a linear spring (with  $k_e = 1 k_B T$ ). In practical applications, and following the authors who introduced this potential [56], we will generally take  $r_0 = 1.5 b$  and  $k_e = 10 k_B T$ .

### 1.3.3 Excluded volume and short-range interactions

Gaussian chains are also known as phantom chains because monomers can overlap. In real polymers however, monomers cannot inter-penetrate, and it is necessary to introduce excluded volume interactions.

In dilute solutions, the size of real chains depends on the quality of the solvent. In good solvent, the end-to-end distance is still expressed as a power law of  $N$ , as in eq. (1.1), but with another exponent  $\nu$ :

$$R_e \sim bN^\nu \quad (1.9)$$

whose value has been well characterized [53]. Namely, in three dimensions  $\nu \approx 0.588$ . This value is well approximated by the Flory exponent  $\nu_F = 3/5$ . In bad solvent, the chain collapses into a close-packed configuration called globule, in which monomers are in contact. The resulting size of the coil scales like  $R_e \sim bN^{1/3}$ . In the other limit, for very concentrated solutions, chains behave essentially like ideal chains with size  $R_e \sim bN^{1/2}$ .

Let us now consider the nucleoid in *E. coli* with volume  $0.2 \mu\text{m}^3$  and a genome of length  $N_g = 4.6 \times 10^6$  bp. Following the description of chromosome organization given in section 1.3, we may assume that the chromosome is represented by a beads-on-string polymer with  $N = N_g/b$  monomers of size  $b = 7.35 \text{ bp} = 2.5 \text{ nm}$ . It follows that the volume occupied by the polymer is approximately  $N\pi b^2/4$ , from which we obtain that the chromosome volume fraction in physiological conditions is  $\eta \sim 10^{-2}$ . By applying similar arguments to an eukaryotic nucleus of size  $1\text{-}10 \mu\text{m}$  with a genome of length  $N_g = 10^9$  bp, and monomers of size  $b = 3000 \text{ bp}$  corresponding to the 30 nm fiber packaging, we also obtain a chromosome density of the order of  $\eta \sim 10^{-3} - 10^{-2}$ . Thus, we may consider that the chromosome can be modeled as

a polymer in a dilute solution. We will also assume that the cytosol is a good solvent for the chromosome polymer.

Most of DNA-DNA and DNA-protein interactions are in fact Coulombic interactions. Yet ions are present in the cell, giving rise to screened electrostatic interactions. The range of the interactions is given by the Debye-Hückel length scale,  $r_{DH}$ . In physiological conditions, the concentration of salt is  $c_0 \approx 0.1$  M, giving  $r_{DH} \approx 1$  nm [57, 58]. Since interactions decay exponentially for larger distances and since proteins have a size of the order of the nanometer, the range of the interactions will be typically the size of the objects interacting together.

A commonly used two-parameter empirical form for describing non-bonded interactions between two neutral (but possibly polarized) particles is the Lennard-Jones, or “6-12”, potential. For a pair of monomers separated by a distance  $r$ , it reads:

$$V_{LJ}(r) = 4\varepsilon \left( \left( \frac{\sigma}{r} \right)^{12} - \left( \frac{\sigma}{r} \right)^6 \right), \quad (1.10)$$

where  $\varepsilon$  is an energy scale in  $k_B T$  and  $\sigma$  is the hard core distance. Here, the interaction still decays as a power law of the distance  $r$ . A standard method to make this interaction short-range, is to introduce a threshold  $r^{th}$  such that for distances  $r > r^{th}$  the interaction vanishes. Therefore, in practical applications, we will consider the truncated Lennard-Jones potential:

$$U_{ev}(r) = \begin{cases} V_{LJ}(r) - V_{LJ}(r^{th}) & \text{if } r < r^{th}, \\ 0 & \text{otherwise.} \end{cases} \quad (1.11)$$

The form in eq. (1.11) can be used to describe both repulsive and attractive interactions. Indeed, the repulsive or attractive nature of the interaction depends on the sign of the Mayer coefficient:

$$\alpha = \int d^3 \mathbf{r} \left( 1 - e^{-\beta U(r)} \right), \quad (1.12)$$

which is the mean-field potential associated to the generic pair potential  $U(r)$ . When  $\alpha > 0$ , the potential is repulsive, and when  $\alpha < 0$  the potential is attractive despite the presence of a hard core (fig. 1.11). Note that  $\alpha$  has the dimension of a volume, and can be understood as follows. Let us consider an isolated monomer at the center of a spherical volume equal to  $|\alpha|$ , that we call the “volume of influence”. An external monomer penetrating in this volume of influence will tend to be ejected when  $\alpha > 0$  while it will tend to remain inside when  $\alpha < 0$ . In the first case,  $|\alpha|$  is effectively a volume from which the other monomer is excluded, while in the latter case it defines a “basin of attraction”.

In practical implementations, we will take  $\sigma = b$  and  $\varepsilon = 1 k_B T$ . Furthermore, to model a strict repulsive interaction, we will consider  $r^{th} = 2^{1/6} \sigma$ , resulting in  $U_{ev}(r) > 0$  for  $r < r^{th}$ , and consequently  $\alpha > 0$ . This choice also ensures that the repulsive force,  $-\partial U_{ev} / \partial r$ , vanishes precisely for  $r = r^{th}$ .

### 1.3.4 Bending rigidity

In reality, polymer chains are not always flexible and may oppose a resistance to bending. Incidentally, DNA is one of the best characterized examples of polymer with a large bending rigidity. There are different ways to model stiff polymers.

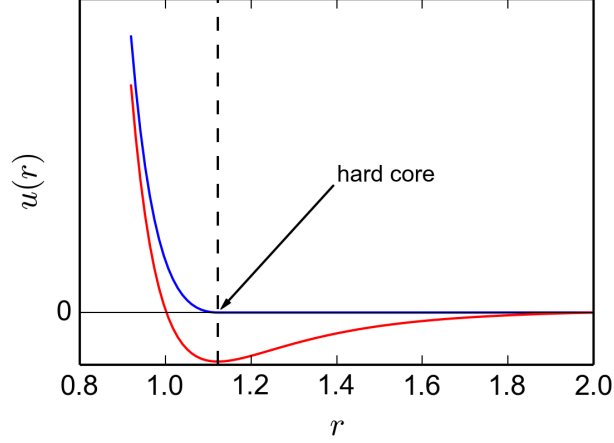


**Figure 1.11** – Potentials of interaction with different shapes. The Mayer coefficient  $\alpha = \int dr (1 - \exp(-u(r)))$  measures the volume excluded for one bead interacting through this potential with a bead attached to the origin. For potentials with an attractive tail (red),  $\alpha$  can be negative. When  $\alpha < 0$  we say that the potential is attractive, otherwise we say that the potential is repulsive.

#### 1.3.4.1 Worm-like chain

##### Model

The discrete worm-like chain, originally introduced by Kratky and Porod [59] to describe polymers with bending rigidity, assumes that the bonds  $\mathbf{u}_i$  are of fixed length,  $b$  (fig. 1.12). For simplicity, we will take  $b = 1$  in the sequel. We therefore introduce the  $N$  spherical coordinates systems  $(\mathbf{w}_i, \mathbf{v}_i, \mathbf{u}_i)$  attached to each bond (the zenith is given by the bond  $i$  direction). The coordinates of bond  $i + 1$  in the frame  $i$  and the corresponding integration measure read:

$$\mathbf{u}_{i+1} = \begin{pmatrix} \sin \alpha_i \cos \zeta_i \\ \sin \alpha_i \sin \zeta_i \\ \cos \alpha_i \end{pmatrix}_{(\mathbf{w}_i, \mathbf{v}_i, \mathbf{u}_i)}, \quad d^2\mathbf{u}_{i+1} = \sin \alpha_i d\alpha_i d\zeta_i, \quad (1.13)$$

where  $\alpha_i$  (resp.  $\zeta_i$ ) is the polar angle (resp. azimuthal angle) associated to frame  $i$ . Hence  $\alpha_i$  is the angle between bond  $i$  and  $i + 1$ . In particular, we have  $\mathbf{u}_{i+1} \cdot \mathbf{u}_i = \cos \alpha_i$ . We will say that the spherical system in eq. (1.13) characterizes the joint  $i$  of the chain.

The Kratky-Porod chain potential is then expressed as:

$$U_b [\{\mathbf{r}_i\}] = \beta^{-1} \kappa \sum_{i=1}^{N-1} (1 - \mathbf{u}_i \cdot \mathbf{u}_{i+1}), \quad (1.14)$$

where  $\kappa$  is a bending rigidity coefficient expressed in  $k_B T$ .

##### Partition function and chain propagator

The partition function may then be written in a compact form:

$$Q_N = \int d^2\mathbf{u}_N d^2\mathbf{u}_1 T^{N-1}(\mathbf{u}_N | \mathbf{u}_1), \quad (1.15)$$

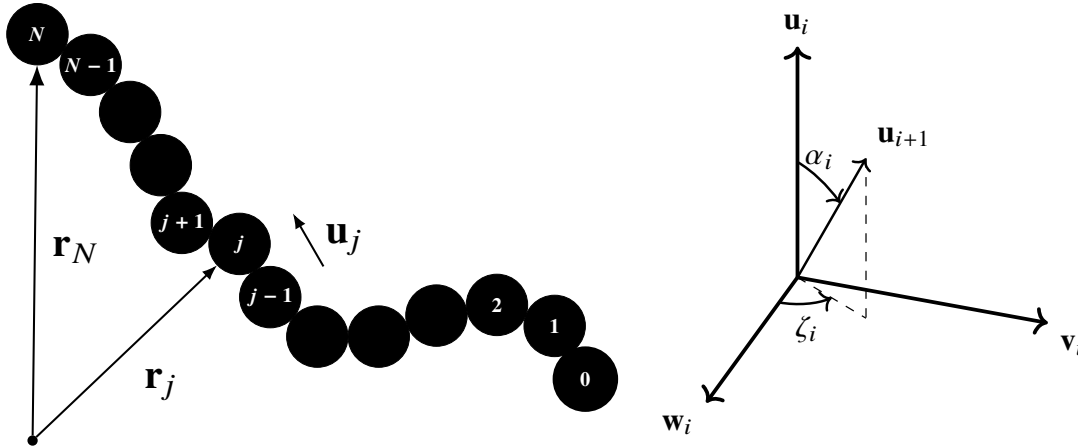


Figure 1.12 – Worm-like chain.

where we introduced the transfer matrix  $T$  with elements:

$$T(\mathbf{u} | \mathbf{u}') = \exp(-\kappa(1 - \mathbf{u} \cdot \mathbf{u}')), \quad (1.16)$$

and can be factorized to give an analytical result. To this end, let us introduce the chain propagator  $q_{N-1}(\mathbf{u})$  and the reduced probability function  $\Psi_N(\mathbf{u})$ :

$$\begin{aligned} q_{N-1}(\mathbf{u}) &= \int d^2\mathbf{u}' T^{N-1}(\mathbf{u} | \mathbf{u}'), \\ \Psi_N(\mathbf{u}) &= \frac{1}{Q_N} q_{N-1}(\mathbf{u}), \end{aligned} \quad (1.17)$$

where we have chosen the underscript  $N - 1$  for the chain propagator to emphasize that it is expressed as the matrix  $T$  to the power  $N - 1$ . Therefore,  $q_n(\mathbf{u})$  is the statistical weight for a polymer with  $n$  joints (*i.e.*  $n + 2$  monomers) to have its last bond (or the first) pointing in the  $\mathbf{u}$  direction. In order to compute  $q_n(\mathbf{u})$ , we make use of the change of variable  $\mathbf{u}_i \cdot \mathbf{u}_{i+1} \leftarrow \cos \alpha_i$ . Using the independence of the joints angles we have:

$$\begin{aligned} q_n(\mathbf{u}) &= \int d^2\mathbf{u}_1 \dots d^2\mathbf{u}_n T(\mathbf{u} | \mathbf{u}_n) \dots T(\mathbf{u}_2 | \mathbf{u}_1) \\ &= \prod_{i=1}^n \left[ \int_0^{2\pi} d\zeta_i \int_0^\pi d\alpha_i \sin \alpha_i \exp(-\kappa(1 - \cos \alpha_i)) \right] \\ &= z^n \quad \text{with} \quad z = 4\pi \frac{\exp(-\kappa)}{\kappa} \sinh \kappa. \end{aligned} \quad (1.18)$$

In particular, we get that the reduced probability  $\Psi_N(\mathbf{u})$  is uniform. In other words, the orientation of the final bond is isotropic. Hence we retrieve the rotational invariance allowed in this model. Due to this factorization of the chain propagator, the partition function is trivially expressed as:

$$Q_N = \int d^2\mathbf{u}_N q_{N-1}(\mathbf{u}_N) = 4\pi z^{N-1}. \quad (1.19)$$

### Oriental correlations

The WLC is also characterized by an exponential decay of the orientational correlations  $\langle \mathbf{u}_{n+1} \cdot \mathbf{u}_1 \rangle$  as a function of the number of joints  $n$ . In order to briefly review this result, let us now introduce the Green function of the discrete WLC:

$$G_n(\mathbf{u}, \mathbf{u}') = \frac{1}{z^n} T^n(\mathbf{u} | \mathbf{u}'), \quad (1.20)$$

where  $n$  is the number of joints between the last bond,  $\mathbf{u}_{n+1} = \mathbf{u}$ , and the first bond,  $\mathbf{u}_1 = \mathbf{u}'$  in a chain with  $n + 2$  monomers. In order to obtain the orientational correlations, we first compute the thermodynamical average  $\langle \cos \alpha_i \rangle$  for any joint  $i$ . A similar computation as in eq. (1.18) yields

$$\langle \cos \alpha_i \rangle = \coth(\kappa) - \frac{1}{\kappa}. \quad (1.21)$$

By expressing  $\mathbf{u}_{n+1}$  in the spherical coordinate system attached to  $\mathbf{u}_n$ :

$$\mathbf{u}_{n+1} = \sin \alpha_n \cos \zeta_n \mathbf{w}_n + \sin \alpha_n \sin \zeta_n \mathbf{v}_n + \cos \alpha_n \mathbf{u}_n, \quad (1.22)$$

we see that

$$\begin{aligned} \langle \mathbf{u}_{n+1} \cdot \mathbf{u}_1 \rangle &= \langle \cos \alpha_n \mathbf{u}_n \cdot \mathbf{u}_1 \rangle + \langle c_1 \cos \zeta_n + c_2 \sin \zeta_n \rangle \\ &= \langle \cos \alpha_n \rangle \langle \mathbf{u}_n \cdot \mathbf{u}_1 \rangle, \end{aligned} \quad (1.23)$$

where we have used the independence of consecutive polar and azimuthal angles, and  $\langle \cos \zeta_n \rangle = \langle \sin \zeta_n \rangle = 0$ . By recurrence, and by substituting eq. (1.21), we obtain the orientational correlations:

$$\langle \mathbf{u}_{n+1} \cdot \mathbf{u}_1 \rangle = \left( \coth \kappa - \frac{1}{\kappa} \right)^n \xrightarrow{\kappa \rightarrow \infty} \exp\left(-\frac{n}{\kappa}\right), \quad (1.24)$$

for  $\kappa \gg 1$ . Therefore,  $\kappa$  characterizes the distance (in unit of monomers) above which the chain loses the memory of its orientation. Following standard notations,  $\kappa$  is usually called the persistence length and noted  $l_p = \kappa$ . For moderate values of  $\kappa$ , we can make use of the two largest eigenvalues ( $\lambda_0 > \lambda_1$ ) of the transfer matrix  $T$ :

$$\begin{aligned} \langle \mathbf{u}_{n+1} \cdot \mathbf{u}_1 \rangle &= \int d\mathbf{u} d\mathbf{u}' \mathbf{u} \cdot \mathbf{u}' G_n(\mathbf{u}, \mathbf{u}') \\ &= \frac{\int d\mathbf{u} d\mathbf{u}' \mathbf{u} \cdot \mathbf{u}' T^n(\mathbf{u} | \mathbf{u}')}{\int d\mathbf{u} d\mathbf{u}' T^n(\mathbf{u} | \mathbf{u}')} \\ &\sim \left( \frac{\lambda_1}{\lambda_0} \right)^n \end{aligned} \quad (1.25)$$

Therefore, the persistence length is more generally defined as  $l_p = -1 / \log(\lambda_1 / \lambda_0)$ . We have computed the persistence length for several values of  $\kappa$  (fig. 1.13). Clearly the persistence length quickly converges to the bending rigidity parameter,  $l_p \rightarrow \kappa$ , and eq. (1.24) can be considered as a good approximation in most cases.

Let us note that similarly to the Gaussian chain, the Kratky-Porod potential in eq. (1.14) can be defined in the continuum limit:  $(1 - \mathbf{u}_i \cdot \mathbf{u}_{i+1}) \leftarrow \dot{\mathbf{u}}^2(s)/2$ . In that case the correlation of the tangents is always:  $\langle \mathbf{u}(0) \cdot \mathbf{u}(s) \rangle = \exp(-s/l_p)$ . The continuous worm-like chain is presented in further details in appendix 1.B.

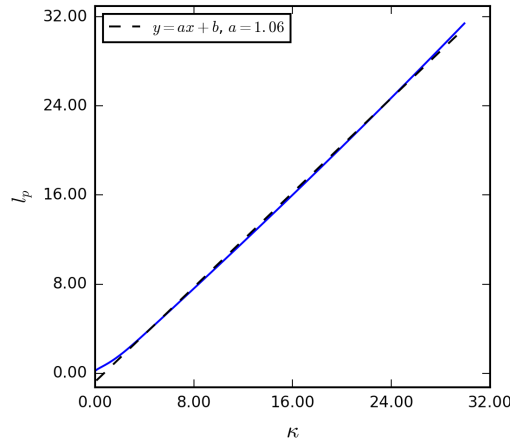


**Figure 1.13** – Persistence length computed from the ratio of the two largest eigenvalues of  $T$  (eq. (1.25)) as  $l_p = -1/\log(\lambda_1/\lambda_0)$  for different values of  $\kappa$ . We have used a discretization of the polar angle  $\alpha$  interval  $[0, \pi]$  in 1000 points (the azimuthal angle is irrelevant and disappear from the integration).

### 1.3.4.2 Gaussian chain with curvature penalty

Although for numerical simulations we will generally consider the WLC model of eq. (1.14), it is not always adapted to analytical calculations because of the constraint on the bond length:  $|\mathbf{u}_n| = 1$ . A simple alternative is to relax this strict constraint and introduce instead a Lagrange multiplier  $\lambda$ . This trick allows us to have an integration measure for the bonds on the full volume instead of the unit sphere. The partition function for this model reads [60–62]:

$$Q_N = \int \prod_{i=1}^N d^3 \mathbf{u}_i \exp\left(-\frac{3}{4}l_p \sum_{i=1}^N (\mathbf{u}_i - \mathbf{u}_{i-1})^2 - \lambda \sum_{i=1}^N u_i^2\right) \quad (1.26)$$

which is a Gaussian integral. Hence it can be computed, and the result in the  $N \rightarrow +\infty$  limit is:

$$Q_N = z^N, \quad z = \left(\frac{4}{3\pi l_p}\right)^{3/2} \exp\left(3 - \sqrt{3\lambda/l_p}\right). \quad (1.27)$$

The Lagrange multiplier can be then determined with a self-consistent argument:

$$-\frac{1}{N} \frac{\partial \ln Q_N}{\partial \lambda} = \langle u_n^2 \rangle = 1 \Leftrightarrow \lambda = \frac{3}{4l_p}. \quad (1.28)$$

Remarkably, this model reproduces the orientational correlations of the WLC, namely

$$\langle \mathbf{u}_1 \cdot \mathbf{u}_{n+1} \rangle = \exp(-n/l_p). \quad (1.29)$$

### 1.3.4.3 Persistence length values for DNA

On the basis of a worm-like chain model, naked DNA has a persistence  $l_p = 50$  nm and the 30 nm fiber has a persistence length  $l_p = 60$ -90 nm [13]. Therefore, in our familiar monomer units, we will typically consider in practical applications  $l_p = 20b$  for the former and  $l_p = 3b$  for the latter.

### 1.3.5 Final model of the chromosome

In summary, by collecting the potentials described in the last paragraphs, the chromosome will be modeled as a beads-on-string polymer with  $N + 1$  monomers, and with a potential energy given by:

$$U = U_{fene} + U_b + U_{ev}. \quad (1.30)$$

## 1.4 Brownian dynamics

Brownian dynamics simulations are molecular dynamics simulations in which many molecular details are coarse-grained. In particular, beads in simulations do not represent an atom nor a base pair, but instead a “blob” which is the basic entity of a mesoscopic description of the chromosome. Furthermore, the solvent (*i.e.* water molecules, plus salt and ions in solution) are not modeled explicitly. Instead, each bead exchanges energy with a thermal bath at temperature  $T$ . The classical framework to describe the Brownian motion of a particle is the Langevin equation.

### 1.4.1 The Langevin equation

Let us consider the motion of a particle with coordinates  $x(t)$ . The Langevin equation is nothing else than the Newton equation of motion for a particle in a viscous medium plus a stochastic term:

$$m\ddot{x}(t) = -\gamma\dot{x} - \frac{\partial U}{\partial x}(x(t)) + \gamma\eta(t), \quad (1.31)$$

in which  $m$  is the mass of the particle,  $\gamma$  is a damping term and  $-\partial U/\partial x$  is the force applied to the particle with  $U$  being the potential energy of the particle. These first three terms are deterministic. In addition there is a stochastic term,  $\eta(t)$  which represents random collisions with the solvent at temperature  $T$ . More accurately,  $\eta$  is an uncorrelated continuous random process with two first moments:

$$\langle \eta(t) \rangle = 0, \quad \langle \eta(t)\eta(t') \rangle = 2D\delta(t - t'), \quad (1.32)$$

where  $D$  is the diffusion coefficient of the particle. It can be shown that in order to sample the Boltzmann equilibrium,  $D$  needs to satisfy the Stokes-Einstein relation (see appendix 1.C):

$$D = k_B T / \gamma, \quad (1.33)$$

where finally from the Stokes' law applied to a bead of diameter  $b$  we get  $\gamma = 3\pi b\mu$ , with  $\mu$  being the fluid viscosity.

In order to produce trajectories of polymer dynamics, the Langevin equation eq. (1.31) is applied to each bead and integrated numerically with the LAMMPS simulation package [63], which uses a standard velocity Verlet integration scheme [64]. Practically, this requires the choice of an integration time step  $dt$ . Unless specified otherwise, we will consider in this thesis  $dt = 10^{-2}$  when there is no excluded volume interaction, and  $dt = 10^{-3}$  otherwise. We also set  $\gamma = 1$  (in simulation dimensionless units).

### 1.4.2 Mapping to real time

BD simulations can be used in order to compute equilibrium quantities and validate theoretical predictions. Furthermore, it is possible to map the simulation time to the real time.

Let us write the diffusion coefficient as  $D = b^2/\tau_B$ . During the time  $\tau_B$ , a particle typically travels through a distance  $b$ , which is its own size. Consequently  $\tau_B$  is the natural unit of time for this diffusive process and is called the Brownian time. In BD simulations we take  $b = 1$  and  $D = 1$  (in dimensionless units), therefore a unit of simulation time correspond to the Brownian time.

The diffusion coefficient in the bacterial nucleoid was found to be  $D = 10 \mu\text{m}^2 \text{s}^{-1}$  [8]. Therefore, for  $b = 2.5 \text{ nm}$  we find  $\tau_B = 600 \text{ ns}$  and for  $b = 30 \text{ nm}$  we find  $\tau_B = 90 \mu\text{s}$ . Consequently, by performing runs of  $10^5$  simulation time units, we can typically produce trajectories corresponding to real times between 10 ms and 10 s.

### 1.4.3 A practical detail: relaxation of polymer systems with excluded volume

In general we will want to start from a random configuration of a self-avoiding polymer. Although we can start from an arbitrary configuration respecting excluded volume constraints, the relaxation to the Boltzmann equilibrium can be very slow. Below is a standard procedure to circumvent this problem and generate quickly an initial configuration for a polymer with excluded volume interactions.

First, perform a relaxation run without excluded volume or short-range attractive interactions. This corresponds to the dynamics of an ideal chain and aims at sampling rapidly a large number of configurations to loose the memory of the initial condition.

Second, perform an intermediate run with few iterations (generally  $10^6$  iterations at  $dt = 10^{-3}$ ) with a soft pair potential:

$$U_{soft}(r) = A \left( 1 + \cos \left( \frac{\pi r}{r^{th}} \right) \right), \quad (1.34)$$

where  $r^{th}$  is the same cutoff as in the truncated Lennard-Jones potential from eq. (1.11). The magnitude  $A$  is progressively increased from 1 to 60 during the run [56], so that we obtain in the end a configuration with no overlaps between the beads.

Finally, the main run with excluded volume and short-range interactions is performed starting from the configuration without overlaps. Several configurations (generally 1000) are extracted from the resulting trajectory, which sample the Boltzmann ensemble. These configurations can be used to compute equilibrium averages according to the ergodic property of the Boltzmann equilibrium.

## 1.5 Organization of the thesis and personal contributions

This thesis aims at proposing physical models for some of the functional chromosome architectures characterized or conjectured in biology. In addition, we have sought to understand at a phenomenological level how these structural features can influence the transcription in living cells. Our strategy has been to start from simple physical models that may capture observed features and use methods from statistical physics to obtain analytical results. However, as mentioned previously, such models are not always amenable to analytical solutions. Therefore, we also have used BD simulations in order to complement our studies and sometimes bring unique insights.

In chapter 2, I present the work published in [1] on the modelling of transcription factories. Transcription factories are clusters of DNA and proteins, characterized *in vivo*, from which most of the transcribed RNAs originate. Despite increasing evidences, very little is known about the structure of these clusters, let alone the underlying physical mechanism. At some point during this investigation, and in the context of a polymer field theory, I needed to compute the structure function of a polymer with semi-flexibility.

Yet no analytical form is known, and this led me to design a method based on complex transfer matrices, that I present in chapter 3.

In chapter 4, I present a model for a regulatory mechanism of the transcription, based on the formation of DNA hairpin loops by the H-NS structuring protein in *E. coli*. The disruption of these structures by external transcription factors may constitute a way to relieve H-NS mediated repression, although this last mechanism has not been investigated in details in this thesis.

In chapter 5, I propose a method to reconstruct the chromosome architecture from contact matrices obtained with Chromosome Conformation Capture experiments. Namely, the resulting polymer model reproduces the experimental contacts. This achievement constitutes a major improvement compared with other methods proposed in the literature.

# Appendix

## 1.A Asymmetrical DNA double-helix

The four fundamental bases can be divided into purines (A and G) and pyrimidines (T and C). A purine contains a single heterocycle in its chemical composition whereas a pyrimidine contains two of them. This introduces an asymmetry in the DNA double-helix. Namely, the DNA molecule has two asymmetric grooves. One groove is smaller than the other. The larger groove, which is called the major groove, occurs when the backbones are far apart, while the smaller one is called the minor groove and occurs when they are close together (fig. 1.14).

The major and minor grooves expose in a different manner the edges of the bases. As might be expected, the major groove provides an easier access to the bases than the minor groove. Hence the specific binding of proteins to DNA is generally achieved by making contacts with bases through the major groove.

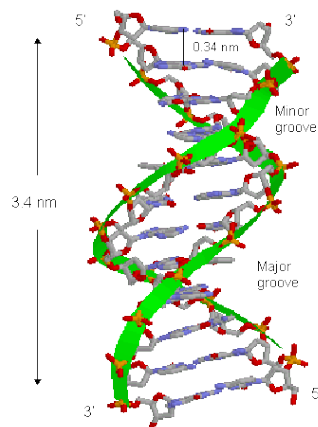


Figure 1.14 – The DNA double-helix is asymmetrical and induced the existence of a major and a minor groove. [65]

## 1.B Continuous worm-like chain

### Model

The Kratky-Porod model [59], also known as Worm-Like Chain (WLC), can be formulated for continuous chains. A polymer of length  $L = bN$  is described by a space curve,  $\mathbf{r}(s)$ , where  $s$  is an arc variable

varying continuously from one end at  $s = 0$ , to the other at  $s = N$ . Here,  $b$  represents a unit length, which is typically the length of the smallest building unit of the polymer. In addition, let us introduce  $\mathbf{u}(s)$ , the unit tangent vector to the curve  $\mathbf{r}(s)$  at coordinate  $s$ . The internal energy of the WLC can be written as

$$\beta U_b [\mathbf{u}(s)] = \frac{\kappa}{2} \int_0^N ds \left( \frac{d\mathbf{u}}{ds} \right)^2 \quad (1.35)$$

where  $\beta = (k_B T)^{-1}$  is the inverse temperature and  $\kappa$  is a bending rigidity parameter. Therefore,  $\beta U_b$  is a functional of  $\mathbf{u}(s)$  which belongs to the unit sphere. Namely, in the spherical coordinate system attached to the  $z$ -axis we have:

$$\mathbf{u} = \begin{pmatrix} \sin \theta \cos \varphi \\ \sin \theta \sin \varphi \\ \cos \theta \end{pmatrix}, \quad d^2 \mathbf{u} = \sin \theta d\theta d\varphi. \quad (1.36)$$

### Partition function and chain propagator

The partition function reads:

$$Q_N = \int D[\mathbf{u}(s)] \exp(-\beta U_b[\mathbf{u}]) \delta(|\mathbf{u}(s)| - 1). \quad (1.37)$$

Because of the constraint on the norm of  $\mathbf{u}(s)$ , computing the integral in eq. (1.37) is rather difficult. We now turn our attention to the Chapman-Kolmogorov (or Schrödinger) equation satisfied by  $\Psi(\mathbf{u}; s)$ , which is the p.d.f. that the last tangent of a chain of length  $s$  is  $\mathbf{u}$ . To this end, we introduce the chain propagator  $q(\mathbf{u}; s)$ , which is the statistical weight that the last (or the first) segment of a chain of length  $s$  is  $\mathbf{u}$ . More formally:

$$\begin{aligned} q(\mathbf{u}; s) &= \int^{\mathbf{u}(s)=\mathbf{u}} D[\mathbf{u}(\sigma)] \exp(-\beta U_b[\mathbf{u}(\sigma)]) \delta(|\mathbf{u}(\sigma)| - 1) \\ \Psi(\mathbf{u}; s) &= \frac{1}{Q_N} q(\mathbf{u}; s) \end{aligned} \quad (1.38)$$

In what follows, we will define the thermodynamical average for any functional  $A[\mathbf{u}(s)]$  of the tangent curve as:

$$\langle A[\mathbf{u}(s)] \rangle = \frac{1}{Q_N} \int D[\mathbf{u}(s)] A[\mathbf{u}(s)] \exp(-\beta U_b[\mathbf{u}]) \delta(|\mathbf{u}(s)| - 1). \quad (1.39)$$

### Chapman-Kolmogorov equation

We can make use of the Markovian structure of the path integral in eq. (1.38) to split the integration over several sub-chains, connected one to the next. In particular, for small variations in the chain length,  $\Delta s$ , and small displacements on the unit sphere,  $\Delta \mathbf{u}$  we can write (see [55]):

$$\begin{aligned} \Psi(\mathbf{u}; s + \Delta s) &= \frac{1}{4\pi} \int d^2(\Delta \mathbf{u}) \Psi(\mathbf{u} - \Delta \mathbf{u}; s) \exp(-\beta \Delta U_b) \\ &= \Psi(\mathbf{u}; s) - \langle \Delta \mathbf{u} \rangle_\mu \frac{\partial \Psi}{\partial \mathbf{u}} + \frac{1}{2} \langle \Delta \mathbf{u}^2 \rangle_\mu \frac{\partial^2 \Psi}{\partial \mathbf{u}^2} + o(\langle \Delta \mathbf{u}^2 \rangle_\mu) \end{aligned} \quad (1.40)$$

where the variation in internal energy is written in terms of the displacement  $\Delta \mathbf{u}$  on the unit sphere:

$$\beta \Delta U_b = \frac{\kappa}{2\Delta s} \Delta \mathbf{u}^2 = \frac{\kappa}{2\Delta s} (\Delta \theta^2 + \sin^2 \theta \Delta \varphi^2), \quad (1.41)$$

and the bracket averages are computed from the Gaussian weight  $\mu$  such as:

$$\begin{aligned}\mu(\Delta\mathbf{u}) &= \frac{1}{4\pi} \exp(-\beta\Delta U_b) \\ \langle\Delta\mathbf{u}\rangle_\mu &= 0, \quad \langle\Delta\mathbf{u}^2\rangle_\mu = \frac{\Delta s}{\kappa}.\end{aligned}\tag{1.42}$$

In the limit  $\Delta s \rightarrow 0$ , we obtain the Chapman-Kolmogorov equation:

$$\frac{\partial\Psi}{\partial s}(\mathbf{u}; s) = \frac{1}{2\kappa} \frac{\partial^2\Psi}{\partial\mathbf{u}^2},\tag{1.43}$$

where the operator  $\partial^2/\partial\mathbf{u}^2$  is the Laplacian on the unit sphere:

$$\frac{\partial^2\Psi}{\partial\mathbf{u}^2} = \frac{1}{\sin\theta} \frac{\partial}{\partial\theta} \left( \sin\theta \frac{\partial\Psi}{\partial\theta} \right) + \frac{1}{\sin^2\theta} \frac{\partial^2\Psi}{\partial\varphi^2}.\tag{1.44}$$

### Oriental correlations

Let us now introduce the Green function,  $G(\mathbf{u}, \mathbf{u}'; s)$ , which is the p.d.f. that a chain of length  $s$  has its last segment oriented according to  $\mathbf{u}$ , and its first segment oriented according to  $\mathbf{u}'$ . Formally, it is defined as

$$G(\mathbf{u}, \mathbf{u}'; s - s') = \langle\delta(\mathbf{u}(s) - \mathbf{u})\delta(\mathbf{u}(s') - \mathbf{u}')\rangle\tag{1.45}$$

In particular, The Green function is related to the reduced probability function:

$$\Psi(\mathbf{u}; s) = \frac{1}{4\pi} \int d^2\mathbf{u}' G(\mathbf{u}, \mathbf{u}'; s - s') \Psi(\mathbf{u}'; s').\tag{1.46}$$

The Green function is particularly useful for analyzing statistical properties. In particular, let us define the orientational correlation function:

$$\langle\mathbf{u}(s) \cdot \mathbf{u}(0)\rangle = \frac{1}{4\pi} \int d\mathbf{u} d\mathbf{u}' G(\mathbf{u}, \mathbf{u}'; s) \mathbf{u} \cdot \mathbf{u}'.\tag{1.47}$$

In order to compute eq. (1.47), we can use the fact that  $G(\mathbf{u}, \mathbf{u}'; s)$  also follows the Chapman-Kolmogorov equation in eq. (1.43), with the initial condition  $G(\mathbf{u}, \mathbf{u}'; 0) = \delta(\mathbf{u} - \mathbf{u}')$ . Then we write:

$$\frac{\partial\langle\mathbf{u}(s) \cdot \mathbf{u}(0)\rangle}{\partial s} = \frac{1}{4\pi} \int d\mathbf{u} d\mathbf{u}' \frac{\partial G(\mathbf{u}, \mathbf{u}'; s)}{\partial s} \mathbf{u} \cdot \mathbf{u}'\tag{1.48}$$

and by using eq. (1.43) and integrating by part (see [54]), we obtain:

$$\langle\mathbf{u}(s) \cdot \mathbf{u}(0)\rangle = \exp\left(-\frac{s}{\kappa}\right).\tag{1.49}$$

In conclusion, the bending rigidity coefficient is usually referred as the persistence length:  $l_p = \kappa$ . It characterizes the contour distance over which orientational correlations decay.

## 1.C Sampling of the Boltzmann equilibrium by the Langevin equation

We recall here why the Langevin dynamics in the stationary regime samples the Boltzmann equilibrium. In the over-damped limit  $\tau_B \ll m/\gamma$  (light particle or viscous solvent), the acceleration term in eq. (1.31)

can be neglected. Hence we obtain the over-damped Langevin equation:

$$\dot{x}(t) = -D\beta \frac{\partial U}{\partial x}(x(t)) + \eta(t), \quad (1.50)$$

where  $\eta(t)$  is an uncorrelated noise with first moments given in eq. (1.32).

Let us now consider a generic observable of the particle position  $f(x)$ . According to the Itô calculation rule, the variations of  $f(x)$  along the particle trajectory reads:

$$df(x(t)) = \frac{\partial f}{\partial x} dx(t) + \frac{1}{2} \frac{\partial^2 f}{\partial x^2} dx(t)^2. \quad (1.51)$$

We will now obtain the continuity equation for  $\rho(x, t)$ , which is the probability that the diffusing particle is at position  $x$  at time  $t$ . On one hand, using eqs. (1.50) and (1.51), we have:

$$\begin{aligned} \left\langle \frac{df(x(t))}{dt} \right\rangle &= \left\langle \frac{\partial f}{\partial x}(x(t)) \frac{dx}{dt}(t) + \frac{1}{2} \frac{\partial^2 f}{\partial x^2}(x(t)) \left( \frac{dx}{dt}(t) \right)^2 \right\rangle \\ &= \left\langle -D\beta \frac{\partial f}{\partial x}(x(t)) \frac{\partial U}{\partial x}(x(t)) + \frac{\partial^2 f}{\partial x^2}(x(t)) D \right\rangle \\ &= \int dx \rho(x, t) \left( -D\beta \frac{\partial f}{\partial x}(x) \frac{\partial U}{\partial x}(x) + \frac{\partial^2 f}{\partial x^2}(x) D \right) \\ &= \int dx f(x) \frac{\partial}{\partial x} \left( D\beta \frac{\partial U}{\partial x}(x) \rho(x, t) + D \frac{\partial \rho}{\partial x}(x, t) \right), \end{aligned} \quad (1.52)$$

where we have used the independence between  $x(t)$  and  $\eta(t)$ , eq. (1.32) and integration by parts to obtain the last line. On the other hand, we have by definition:

$$\frac{d}{dt} \langle f(x(t)) \rangle = \int dx f(x) \frac{\partial \rho}{\partial t}(x, t). \quad (1.53)$$

Therefore, by equating eqs. (1.52) and (1.53), we obtain the heat equation:

$$\begin{aligned} \frac{\partial \rho}{\partial t}(x, t) + \frac{\partial j}{\partial x}(x, t) &= 0, \\ j(x, t) &= -D\beta \frac{\partial U}{\partial x}(x) \rho(x, t) - D \frac{\partial \rho}{\partial x}(x, t), \end{aligned} \quad (1.54)$$

where  $j(x, t)$  is the local density current of particles. The equilibrium is achieved when  $j(x, t) = 0$ , yielding:

$$\rho_{eq}(x, t) \propto \exp(-\beta U(x)), \quad (1.55)$$

which is the Boltzmann distribution.

## Chapter 2

# Modelling of transcription factories

In this chapter, we address the characterization of transcription factories, which are clusters of DNA and proteins where presumably active genes are transcribed. We start by an overview about gene co-regulation, and in particular we introduce recent developments in biology suggesting that the regulation of the expression of genes belonging to a same network entails their co-localization in space. We then introduce transcription factories and discuss what is known about their biological functions.

There are only few physical models for the existence of transcription factories, and still many open questions. Hence, in a first approach, we propose a model grounded in a polymer representation of the chromosome in interaction with a solution of binding proteins, that we call a formal nucleus. In order to characterize the thermodynamical equilibrium of this formal nucleus, a Flory-Huggins free energy model was implemented. We found that depending on the DNA-protein affinity, the DNA chromosome may collapse, resulting in a biphasic regime with a dense and a dilute phase. The dense phase is then a model for transcription factories. Furthermore, we explored the dependence of the collapse on DNA and protein concentrations. In particular, we computed the corresponding phase diagram.

Although the Flory-Huggins theory gives a proof of principle for the existence of clusters of DNA and proteins at equilibrium such as transcription factories, it does not give information on the structure of such a dense phase. By drawing a parallel with an approach based on Hamiltonian paths, used in protein folding, we show with Brownian dynamics simulations that the dense phase has either a molten globule or a crystalline structure, depending on the DNA bending rigidity.

At the end of the Flory-Huggins theory and of the dense phase structure study, we will discuss the biological implications of the results obtained.

## 2.1 Introduction

### 2.1.1 From co-regulation to co-localization

Let us consider a network of co-expressed genes. By co-expressed we mean that the expression of such genes is coordinated in some way. For instance, co-expressed genes might be under the control of the same promoter. More generally, when their expression is directly regulated by the same transcription factor (TF) we say that they are co-regulated. Other cases of co-expression may involve a TF that directly activates the transcription of a gene A, encoding a protein that in turn activates the transcription of a gene B. This example illustrates how transcriptional cascade can occur in network of co-regulated genes. Such

effects may depend on one or just a few TFs, and therefore co-regulated gene networks can entail a broad genetic response to changes coming either from external conditions or from other metabolic pathways. Such transcriptional cascades are not without similarities with cascades occurring in other biological contexts such as for instance kinase pathways in cell signalling.

Whether it is an external TF or a protein encoded by another gene, every protein must diffuse in the nucleoid before reaching its target. In chapter 1 we have estimated the time scale to sample the nucleoid/nucleus to be of the order of seconds, which may be a rate-limiting step in transcription regulation. A natural way to overcome diffusion-limited processes is to place co-regulated genes consecutively and next to each other on the DNA sequence (fig. 2.1a). Consequently, the search for the protein target is biased because it is not far from the place where this protein was initially activated, or even produced (note that this last argument does not apply to eukaryotes because proteins are synthesized in the cytoplasm and then imported in the nucleus). In other words, the search time for a protein transiting from one gene to another can be dramatically reduced if these genes are neighbors in space, *i.e.* co-localized.

Although proximity on the genome sequence is one way to achieve co-localization, it is hardly scalable to networks of tens or hundreds of genes, because this would inevitably lead to large genomic distances for some genes of the network, and hence to large spatial distances. Therefore, other mechanisms must exist in order to bring into spatial proximity genes separated by large genomic distances (fig. 2.1b). An influential view is that some TFs have the ability to bind two (or several) sites on the DNA molecules, resulting in an organization of the chromosome into loops [22–24]. Such TFs are said to be divalent, or more generally multivalent if they can bind more than two DNA sequences simultaneously.

A direct consequence of the binding of divalent TFs is the formation of DNA loops. A case in point is the *lac* operon in *Escherichia coli*, in which repression is achieved when the *lac* repressor binds simultaneously a main site located in the promoter region and an auxiliary sites 401 bp away on the sequence [5,6]. In this context, the strength of the binding maintaining the DNA loop is directly correlated with the efficiency of the repressor system. This looping mechanism can be envisioned as a mechanical regulatory switch which is turned on and off through the binding of TFs. Let us emphasize that *in vitro* and *in vivo* studies have confirmed the existence of DNA loops, sometimes over long genomic distances [7,66], suggesting that specific looping can indeed be a key feature of the transcription regulation even in eukaryotes, where enhancers can be found several kilo base-pairs away from the promoter [67–69].

On the basis of this representation of the chromosome shaped up by divalent TFs, one can think of several physical models. In a stylized view, divalent TFs can be seen as binding spheres able to bind several sites on the DNA sequence (fig. 2.1c). The binding of such a bead at two loci separated by a large genomic distance gives rise to a DNA loop. The superimposition of many such loops not only changes the global chromosome architecture, but has also an impact on transcription, for instance by preventing RNA polymerase (RNAP) to access to the promoter. This has been studied in the so-called strings and binders switch model [36] (fig. 2.1c). Another physical model demonstrated that although it is seemingly more complex than adjusting the affinity of a TF with a given promoter, DNA looping can confer unique and relevant properties to transcription regulation [9,37]. In particular, DNA looping leads to an increased effective binding free energy of a TF to its promoter. In other words, the apparent search volume to find the target is reduced and the local concentration of protein is increased. A consequence of such local concentration effects, which can be envisioned as “molecular traps”, is to stabilize the protein binding versus global fluctuations of the protein concentration in the cell.

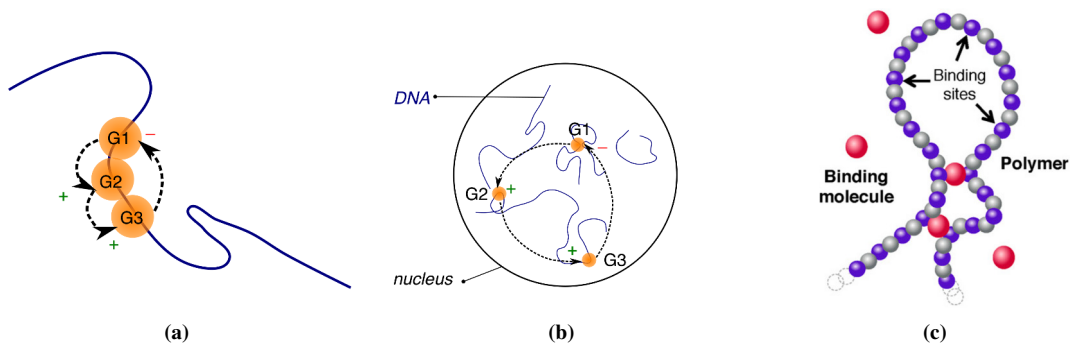


**Figure 2.1** – (a) An in-row layout for co-regulated genes enables an efficient regulation of the genes in the network. For instance when a gene produces a protein which down-regulates the expression of the following, or when high local concentration of RNAP results in an increased transcription of one gene and its neighbours. (b) The in-row layout is hardly scalable to networks of tens or even hundreds of genes. In eukaryotes, but also in bacteria, several regulation networks involve genes which are located at distant coordinates along the genome sequence. (c) Strings and binders switch model [36].

### 2.1.2 Co-localization of genes in transcription factories

Co-localization of co-regulated genes has proven to be more than a surmise. It has been confirmed to occur in prokaryotes [70, 71] and eukaryotes [28, 72] using fluorescence techniques (FISH). In the case of the mouse hemoglobin co-regulated genes (more than 40), a combination of FISH and Chromosome Conformation Capture (3C) techniques demonstrated that these genes tend to co-localize in clusters and exhibited higher contact frequencies than with other non-related genes [28]. These clusters were shown to contain of the order of 8 to 10 genes. Associations between co-regulated genes were also shown to happen between different chromosomes [72].

In a first series of experiments, it was shown that nascent RNA transcripts are synthesized at discrete foci in the nucleus [70, 73]. Later, it was shown that RNAP itself gathers into clusters instead of being uniformly distributed within the nucleus [74]. These clusters with increased concentration of nascent RNA transcripts and RNAP correspond to areas where active transcription occurs. Hence they were called transcription factories. Although the existence of transcription factories were first obtained on mammalian cells, because their large size is a better fit for fluorescence studies, their existence has also been demonstrated in bacteria [75].

In an attempt to connect the co-localization of co-regulated genes with the existence of transcription factories, it was conjectured that by binding to and organizing the chromosome, TFs gather co-regulated genes in transcription factories. In addition to achieve gene co-localization, this may lead to a mutualization of resources, such as the availability of RNAP, TFs or epigenetics marks such as methylations. It would also give a more general account of local concentration effects and their role in regulating the transcription. It is very likely that transcription entails a cellular response that will in turn impact chromosome architecture. Incidentally, the life time of transcription factories was found to be of the order of 5 s [74], suggesting that transcription factories are dynamically re-allocated as a function of the transcriptional state of the cell. In our view, this supports the idea that transcription regulation and chromosome organization are related in some sort of dynamical feedback mechanism which remains to be found.

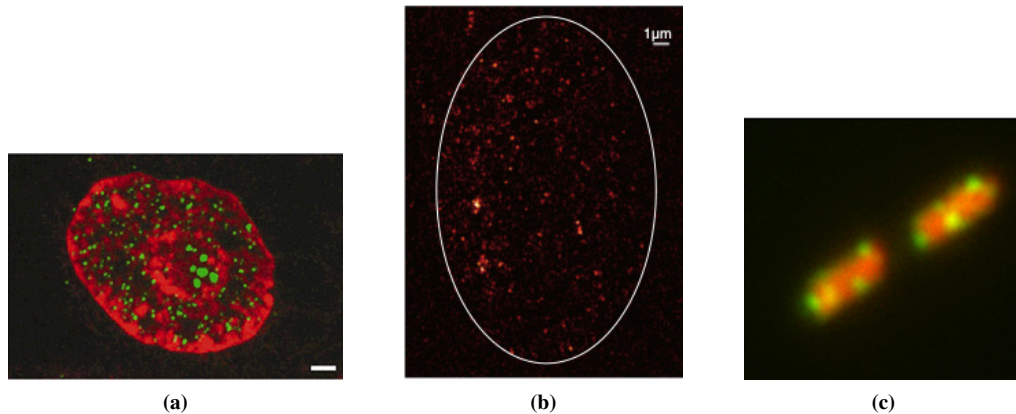


**Figure 2.2** – Transcription factories *in vivo*. (a) FISH imaging of nascent RNA transcripts (green) in human HeLa cells [23]. (b) PALM imaging of RNA polymerase (red) in human osteosarcoma cell [74]. (c) Fluorescence imaging of RNA polymerase in *E. coli* by fusion with green fluorescent proteins [76].

### 2.1.3 Physical origin of transcription factories

The physical origin of transcription factories has remained controversial. Two questions at least may be formulated. First, one can wonder if the formation of transcription factories constitutes a Boltzmann equilibrium. We have mentioned earlier that the typical time for a protein to sample the bacterial nucleoid is 100 ms, which gives the typical time scale for transcription regulation processes. This figure should be compared with the life time of transcription factories which has been measured to be of the order of seconds or tens of seconds [74]. Thus it seems that transcription factories are reminiscent of an equilibrium phenomenon. Second, the structure of the DNA inside such transcription factories has remained elusive. In particular, it is not clear what is the effective diffusion coefficient of TFs or RNAP inside transcription factories. These remarks have motivated the study of the statistical physics of the DNA interacting with TFs.

## 2.2 Model proposed

### 2.2.1 Formal nucleus/nucleoid

We consider a simplified model in which the nucleus (or bacterial nucleoid) is represented by a closed volume  $V$  (fig. 2.3). In the sequel we will indifferently use the words cells and nucleus, since this model is considered to represent either a bacterial cell or the nucleus of a eukaryotic cell. The double-stranded DNA chains are modeled as  $M$  semi-flexible polymer chains of length  $b \times N$ , where  $b$  is the Kuhn length. A DNA monomer is specified by a coordinate  $s$  varying from 0 to  $N$ , and can interact with  $P$  spheres, representing DNA-binding proteins. The typical size of DNA monomer beads and of a protein beads are taken to be equal in this study. In bacteria,  $b \approx 2.5$  nm, is the diameter of the naked DNA fiber, and also corresponds to the size of a typical size of a protein. In eukaryotes,  $b \approx 30$  nm is the diameter of the chromatin fiber, therefore a protein bead rather represents a protein complex. Introducing the subscript  $D$  for DNA and  $P$  for proteins, we shall consider the three pair potentials  $u_{DD}(r)$ ,  $u_{PP}(r)$  and  $u_{DP}(r)$  for the interactions between two beads separated by a distance  $r$ . We will also consider that proteins can bind

to DNA monomers non-specifically. Although this last assumption is strong, it may be considered as a model for transcription factors with a very large number of targets on the DNA, such as nucleoid-associated proteins (H-NS, FIS or HU in bacteria), or even RNAP itself.

In the sequel, we will assume that DNA monomers experience pure excluded volume interactions with other DNA monomers, and similarly proteins-protein interactions are only repulsive. On the contrary, we will assume that proteins can bind to DNA, and therefore the corresponding interaction potential has an attractive tail. Hence we have the Mayer coefficients (see eq. (1.12) on page 13) for each of the three interaction potentials:

$$\begin{aligned}\alpha_D &= \int d\mathbf{r} u_{DD}(r) > 0, \\ \alpha_P &= \int d\mathbf{r} u_{PP}(r) > 0, \\ v &= \int d\mathbf{r} u_{DP}(r) < 0.\end{aligned}\tag{2.1}$$

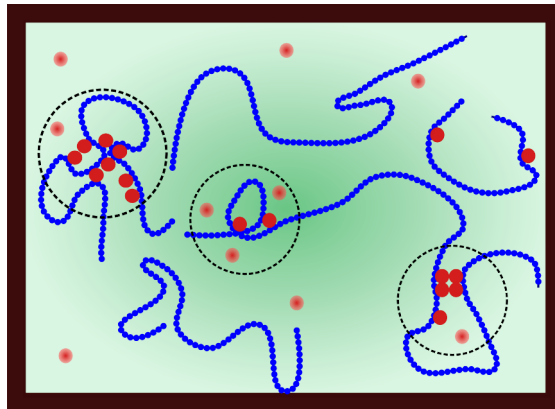


**Figure 2.3** – Stylized view of the bacterial cell or nucleus. It contains DNA chains represented as polymers and binding proteins represented as free spheres. The dashed circles denote transcription factories.

### 2.2.2 First principles model

Starting from the model defined in the last paragraph, we now lay the grounds for a study of the statistical physics of this system. First, we specify the Hamiltonian built from summing over all interactions between microscopical constituents. Let us consider  $M$  polymer chains representing the chromosomes in the nucleus. In this chapter, we will use continuous polymers to model the chromosomes. Thus, every DNA chain  $k$  is represented by a space curve  $\mathbf{r}_k(s)$  for  $k = 1, \dots, M$ , giving the spatial coordinates of monomer  $s$  along the DNA sequence. In addition, we introduce  $P$  proteins with coordinates  $\mathbf{R}_i$  for

$i = 1, \dots, P$ . Using the pair potentials previously introduced, the Hamiltonian for the system reads:

$$\begin{aligned} \beta\mathcal{H} [\{\mathbf{R}_i\}, \{\mathbf{r}_k(s)\}] &= \frac{1}{2} \sum_{i \neq j} u_{PP}(\mathbf{R}_j - \mathbf{R}_i) + \frac{1}{2} \sum_{k \neq l} \int_0^N ds ds' u_{DD}(\mathbf{r}_l(s') - \mathbf{r}_k(s)) \\ &+ \beta \sum_i \sum_k \int_0^N ds u_{DP}(\mathbf{r}_k(s) - \mathbf{R}_i) \\ &+ \frac{1}{3!} w \sum_{I, I', I''} \delta(\mathbf{R}_{I'} - \mathbf{R}_I) \delta(\mathbf{R}_{I''} - \mathbf{R}_{I'}) \end{aligned} \quad (2.2)$$

The Hamiltonian thus consists in a summation over many bodies interactions. Note that because  $u_{DP}(r)$  is a potential with an attractive tail, the system may collapse in a certain range of concentrations of DNA and proteins, if it were not to be compensated by higher order terms. For that reason, we needed to consider an expansion of the Hamiltonian to order three at least, which is a common procedure in polymer physics [77]. In the present study, we have assumed that a Kuhn segment on the DNA and a protein bead have same size  $b$ , and for that reason, the three-body term is a sum over an index  $I$  which can be either a protein or a DNA monomer. The coefficient  $w$  represents a penalty in  $k_B T$  whenever three such beads collapse on the same coordinates. The prefactor of  $1/3!$  is here to ensure a standard form of the associated virial expansion of the osmotic pressure. We will come back to this shortly. We also point out that only the DNA-protein interaction is temperature-dependent, as can be seen from the  $\beta$  prefactor right in front of the potential  $u_{DP}$ .

The partition of our formal nucleus therefore reads

$$Z = \int \frac{1}{P!} \prod_{i=1}^P d\mathbf{R}_i \int \frac{1}{M!} \prod_{k=1}^M D[\mathbf{r}_k(s)] \exp\left(-\beta\mathcal{H} [\{\mathbf{R}_i\}, \{\mathbf{r}_k(s)\}] - \sum_k \beta U_0[\mathbf{r}_k(s)]\right), \quad (2.3)$$

where we introduced the internal energy of the DNA chains  $\beta U_0$ . The functional dependence of the internal energy on the chain configuration depends on the polymer model retained for the chromosome. Specifically, DNA is a rigid biopolymer that can be modeled as a semi-flexible polymer (see section 1.3.4 on page 13).

### 2.2.3 Field representation

We now derive the partition function in field representation. This can be used as a starting point for several standard approximations, including the saddle-approximation and the Gaussian fluctuations analysis also known as Random Phase Approximation in the context of polymer physics. In particular, the mean-field theory, that we will introduce in the next section, can be obtained from a saddle-point approximation.

In order to change the integration in eq. (2.3), which is performed over the individual coordinates of the constituents to an integration over fields, we make a change of variables by introducing the concentration fields:

$$\rho_P(\mathbf{r}) = \sum_i \delta(\mathbf{r} - \mathbf{R}_i), \quad (2.4)$$

$$\rho_D(\mathbf{r}) = \sum_k \int_0^N ds \delta(\mathbf{r} - \mathbf{r}_k(s)). \quad (2.5)$$

We then introduce the following identity in the partition function in eq. (2.3):

$$\begin{aligned}
1 &= \int \mathcal{D}[\rho_D(\mathbf{r})] \delta\left(\rho_D(\mathbf{r}) - \sum_k \int_0^N ds \delta(\mathbf{r} - \mathbf{r}_k(s))\right) \\
&= \int \mathcal{D}[\rho_D(\mathbf{r})] \mathcal{D}[\varphi_D(\mathbf{r})] \exp\left(i \int d\mathbf{r} \rho_D(\mathbf{r}) \varphi_D(\mathbf{r}) - \sum_k \int_0^N ds \varphi_D(\mathbf{r}_k(s))\right),
\end{aligned} \tag{2.6}$$

where in eq. (2.6) we made use of the exponential representation of the delta-functional by introducing an auxiliary field  $\varphi_D(\mathbf{r})$ . A similar identity can be introduced for the protein concentration field. This leads to the following re-writing for the partition function of the system:

$$Z = \int \mathcal{D}[\rho_D] \mathcal{D}[\varphi_D] \mathcal{D}[\rho_P] \mathcal{D}[\varphi_P] \exp(-\beta S[\rho_D, \varphi_D, \rho_P, \varphi_P]), \tag{2.7}$$

with the action

$$\begin{aligned}
\beta S &= -i \int d\mathbf{r} \rho_D(\mathbf{r}) \varphi_D(\mathbf{r}) - i \int d\mathbf{r} \rho_P(\mathbf{r}) \varphi_P(\mathbf{r}) \\
&+ \int d\mathbf{r} d\mathbf{r}' \rho_P(\mathbf{r}') u_{PP}(\mathbf{r}' - \mathbf{r}) \rho_P(\mathbf{r}) + \int d\mathbf{r} d\mathbf{r}' \rho_D(\mathbf{r}') u_{DD}(\mathbf{r}' - \mathbf{r}) \rho_D(\mathbf{r}) \\
&+ \beta \int d\mathbf{r} d\mathbf{r}' \rho_D(\mathbf{r}') u_{DP}(\mathbf{r}' - \mathbf{r}) \rho_P(\mathbf{r}) \\
&+ \frac{1}{3!} w \int d\mathbf{r} (\rho_D(\mathbf{r}) + \rho_P(\mathbf{r}))^3 \\
&- P \ln W[i\varphi_P] - M \ln Q[i\varphi_D] + P \ln \frac{P}{e} + M \ln \frac{M}{e}.
\end{aligned} \tag{2.8}$$

An interesting outcome of this re-writing is the separation of the enthalpic and entropic contributions in the action expressed in eq. (2.8). Namely, the entropy is represented by the last four terms in the action. It depends only on the single-particle partition function of the protein beads, respectively the single-chain partition function of the DNA chains, in the imaginary potential  $i\varphi_P(\mathbf{r})$ , respectively  $i\varphi_D(\mathbf{r})$ , whose expressions are given by

$$W[i\varphi_P] = \int d\mathbf{R} \exp(-i\varphi_P(\mathbf{R})), \tag{2.9}$$

$$Q[i\varphi_D] = \int \mathcal{D}[\mathbf{r}(s)] \exp\left(-\beta U_0[\mathbf{r}(s)] - i \int_0^N ds \varphi_D(\mathbf{r}(s))\right). \tag{2.10}$$

## 2.3 Flory Huggins theory

In this section, we study the Flory-Huggins theory of the bulk of the nucleus. We will show that the existence of a binding energy between proteins and DNA can lead to the formation of a dense phase that one may identify to transcription factories. As pointed out previously, only the DNA-protein interaction is temperature-dependent. In the sequel, we will often refer to the high, respectively low, temperature regime which corresponds to a weak, respectively strong, DNA-protein attraction.

### 2.3.1 Mean-field free energy

Intuitively, one might expect that for high temperatures, the attraction between DNA monomers and binding-proteins vanishes. In this regime, the system contains an homogeneous concentration of DNA monomers and proteins. In other terms, we may perform a mean-field approximation and remove the spatial dependence of the concentration fields:  $\rho_D(\mathbf{r}) \leftarrow c_D = MN/V$  and  $\rho_P(\mathbf{r}) \leftarrow c_P = P/V$ . In the context of polymer physics, this is also called the Flory-Huggins theory [53]. We will frequently refer to these concentrations as the mean-field solutions. Solving the stationary equations for the action in eq. (2.8) can be done (see section 2.4.1). If in addition we assume mean-field solutions, we obtain the free energy function per volume unit:

$$\beta f(c_D, c_P) = \frac{1}{2}\alpha_D c_D^2 + \frac{1}{2}\alpha_P c_P^2 + \beta v c_D c_P + \frac{1}{3!}w(c_D + c_P)^3 + c_P \ln \frac{c_P b^3}{e} + \frac{c_D}{N} \ln \frac{c_D b^3}{Ne}. \quad (2.11)$$

Another way to look at this expression is to consider that an excluded volume penalty  $\alpha$  is applied whenever two beads are in contact. In the case of the DNA-protein interaction, the effective excluded volume  $\beta v$  is negative because the interaction is attractive. The probability to find two beads in contact is proportional to the product of their concentrations. This gives terms of the form  $\alpha \times c^2$  contributing to the free energy function. The two logarithmic terms in the free energy accounts for the configurational entropy of the proteins and DNA chains. Briefly, one can see them as contributions of the form  $(V/b^3)^P/P! \sim \exp(V c_P \ln(c_P b^3/e))$  to the Boltzmann weight, where  $(V/b^3)$  is the number of accessible configurations for one bead of size  $b^3$  distributed uniformly in the volume  $V$ . We may also give an account for the presence the three-body term without resorting to the microscopical Hamiltonian defined in the last section. For this, one needs to consider the Flory-Huggins theory as the limit of a gas on a lattice, where the enthalpic contributions are the first three terms in the right-and side (r.h.s.) of eq. (2.11), and the last two terms are the entropy of the particles. Now, in any gas on a lattice representation, one should take into account the entropy of the vacancies, which in our case should be identified to the solvent. If we assume the system to be incompressible, this entropic contribution has the form  $(c_0 - c_D - c_P) \ln((c_0 - c_D - c_P)/e)$ , where  $c_0$  is the close-packing concentration. An expansion in powers of  $(c_D + c_P)$  truncated at order three yield the three-body term in the free energy.

In the high temperature regime, the DNA-protein interaction term,  $\beta v c_D c_P$ , in eq. (2.11) vanishes. The free energy is therefore a convex function, making the mean-field solution stable.

### 2.3.2 Spinodal condition

When the temperature is progressively decreased, the attractive interaction  $|\beta v|$  increases, until the mean-field solution is no longer stable. This is the so-called spinodal condition, which delimits the region in which the mean-field solution is stable from the region where it is not. This condition corresponds to an inversion of the curvature of the free energy, which in our case reads

$$\begin{vmatrix} \frac{\partial^2 f}{\partial c_D^2} & \frac{\partial^2 f}{\partial c_D \partial c_P} \\ \frac{\partial^2 f}{\partial c_D \partial c_P} & \frac{\partial^2 f}{\partial c_P^2} \end{vmatrix} = 0, \quad (2.12)$$

where the array denotes a determinant. For any given choice of the DNA-protein attraction,  $\beta v$ , the spinodal equation is an implicit equation for a closed curve in the  $(c_D, c_P)$  plane. The range of concentrations enclosed within this curve corresponds to unstable mean-field solutions whereas in the outer

region are stable mean-field solutions. There is a critical temperature  $T^c$  such that for  $T > T^c$  there is no solution to the spinodal condition and the mean-field solution is stable, whereas for  $T < T^c$ , the spinodal condition has solutions. At  $T = T^c$ , the closed curve of solutions reduces to a single point of coordinates  $(c_D^c, c_P^c, T^c)$ .

Let us point out that eq. (2.12) is not tractable by hands, so we solve it numerically. As shown in fig. 2.4, we obtain the following scaling relations for the critical concentrations:

$$\begin{aligned} c_D^c &\sim \frac{1}{\sqrt{N}} \frac{1}{\sqrt{w}}, \\ c_P^c &\sim 1/\sqrt{w}. \end{aligned} \quad (2.13)$$

We observe that for  $T < T^c$ , the spinodal equation consists of an infinite set of doublet pairs  $(c_D^1, c_P^1)$ - $(c_D^2, c_P^2)$  which together are a parametrization for the spinodal line (fig. 2.5a). However, on each spinodal line are found two double solutions, meaning that each doublet pair  $(c_D^1, c_P^1)$  and  $(c_D^2, c_P^2)$  merge into a single critical point  $(c_D^0, c_P^0)$ .

In summary, eq. (2.12) is an implicit equation for a surface in the  $(c_D, c_P, T)$  space, below which the mean-field solutions are unstable. On this surface lies a critical curve where the spinodal condition has a double solution  $(c_D^0, c_P^0)$ , instead of two different solutions (fig. 2.6). At the apex of the critical curve lies the tricritical point  $(c_D^c, c_P^c, T^c)$ , which is the first point where the mean-field solution becomes unstable when the temperature is decreased.

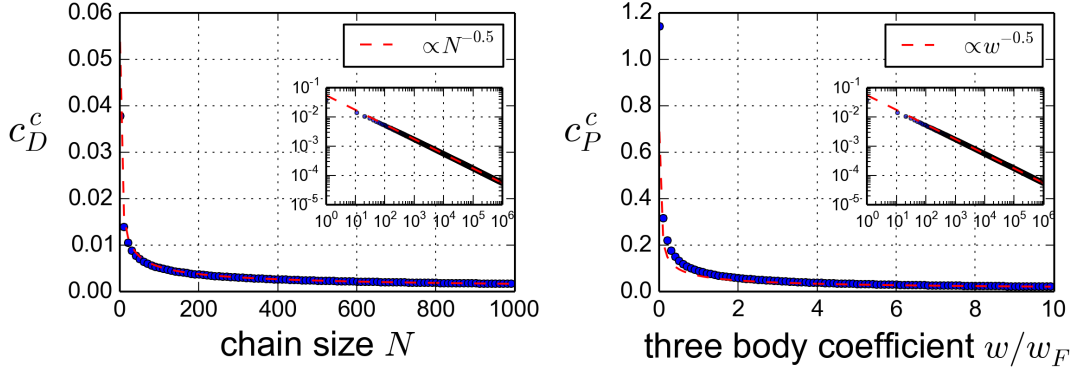


**Figure 2.4** – Scaling of the critical concentrations of DNA and proteins as a function of the parameters of the model.  $w_F = b^6$  is the value of the three-body repulsive core which naturally arises from a Flory-Huggins theory. The insets display the dependence of the critical concentrations on the parameters in log-log scale, over a broad range of values.

### 2.3.3 The biphasic regime

For  $T < T^c$ , the free energy function in eq. (2.11) has an unstable range of concentrations. In this range, the system splits into two phases *I* and *II* which belong to the stable region. The total free energy of the system can be written as the sum of the free energies of the two phases. The equilibrium state is then found by minimizing the total free energy function under the constraints that the total number of particles

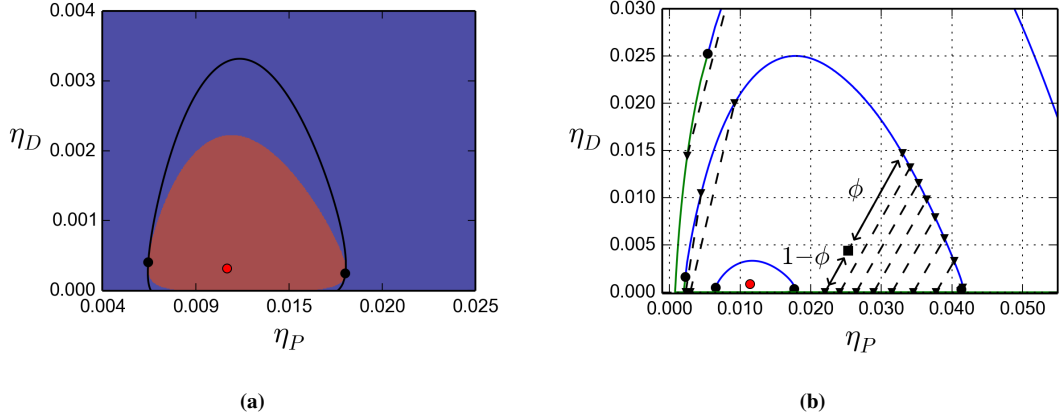


**Figure 2.5** – (a) At  $t = 0.05$ . The binodal, or coexistence, line is the solid black curve. The mean-field solution is unstable in the region colored in red and the system splits into two phases. For concentrations falling into the blue region, the mean-field solution is stable. The black circles are two critical points where the coexistence and the spinodal lines intersect. (b) Binodal, or coexistence, lines at  $t = 0.05, 0.5, 1.0$ . The coexistence line shrinks toward the tricritical point (red dot) when  $t \rightarrow 0$ . For each curve, the dilute phase is shown in green and the concentrated phase is shown in blue. Coexisting states are connected by tie lines (dotted segments). The volume fraction of each phase is determined (black arrows) according to eq. (2.20).

is conserved and the volume constant. This is most easily done by minimizing the Lagrangian:

$$\begin{aligned} \mathcal{L} = & \phi^I f(I) + \phi^{II} f(II) \\ & - \mu_D (\phi^I c_D^I + \phi^{II} c_D^{II}) - \mu_P (\phi^I c_P^I + \phi^{II} c_P^{II}) - \Pi (\phi^I + \phi^{II}), \end{aligned} \quad (2.14)$$

in which  $f(I)$  is a short-hand for  $f(c_D^I, c_P^I)$  and  $\phi^I$  is the volumic fraction of phase  $I$ . The same notations apply for phase  $II$ . The Lagrangian multipliers  $\mu_D$  and  $\mu_P$  have been introduced to conserve the number of DNA monomers and the number of proteins, and are to be identified with chemical potentials. The Lagrangian multiplier  $\Pi$  has been introduced to conserve the volume, and is to be identified to the osmotic pressure. The minimization of  $\mathcal{L}$  relatively to the variables  $c_D^I, c_P^I, c_D^{II}, c_P^{II}, \phi^I, \phi^{II}$  yields the system of equation

$$\begin{cases} \frac{\partial f}{\partial c_D}(c_D^I, c_P^I) & = \frac{\partial f}{\partial c_D}(c_D^{II}, c_P^{II}) & = \mu_D \\ \frac{\partial f}{\partial c_P}(c_D^I, c_P^I) & = \frac{\partial f}{\partial c_P}(c_D^{II}, c_P^{II}) & = \mu_P \\ f(c_D^I, c_P^I) - \mu_D c_D^I - \mu_P c_P^I & = f(c_D^{II}, c_P^{II}) - \mu_D c_D^{II} - \mu_P c_P^{II} & = -\Pi \end{cases}, \quad (2.15)$$

which states that the chemical potentials and the osmotic pressure in the two phases are equal. Note that the writing of the last line can be rewritten more compactly if we introduce the Gibb's free energy, which is the Legendre transform of eq. (2.11):

$$g(c_D, c_P) = f(c_D, c_P) - \mu_D c_D - \mu_P c_P, \quad (2.16)$$

and where the chemical potentials depend implicitly on the concentrations through the equilibrium condition:

$$\begin{cases} \frac{\partial g}{\partial c_D} = 0 \\ \frac{\partial g}{\partial c_P} = 0 \end{cases} \Leftrightarrow \begin{cases} \frac{\partial f}{\partial c_D} = \mu_D \\ \frac{\partial f}{\partial c_P} = \mu_P \end{cases}. \quad (2.17)$$

The system in eq. (2.15) is a system of 3 equations with the four unknown concentration variables, plus the temperature. Hence it is a parametrization for a surface, called the binodal, which completely determines the phase diagram of the system. We solved this system of equations numerically using a quasi-Newton root finding method [64]. The surface obtained is represented in fig. 2.6, where a parameter  $t$  has been introduced as an expansion of the DNA-protein interaction around the tricritical point:

$$\beta v = (\beta v)^c (1 + t). \quad (2.18)$$

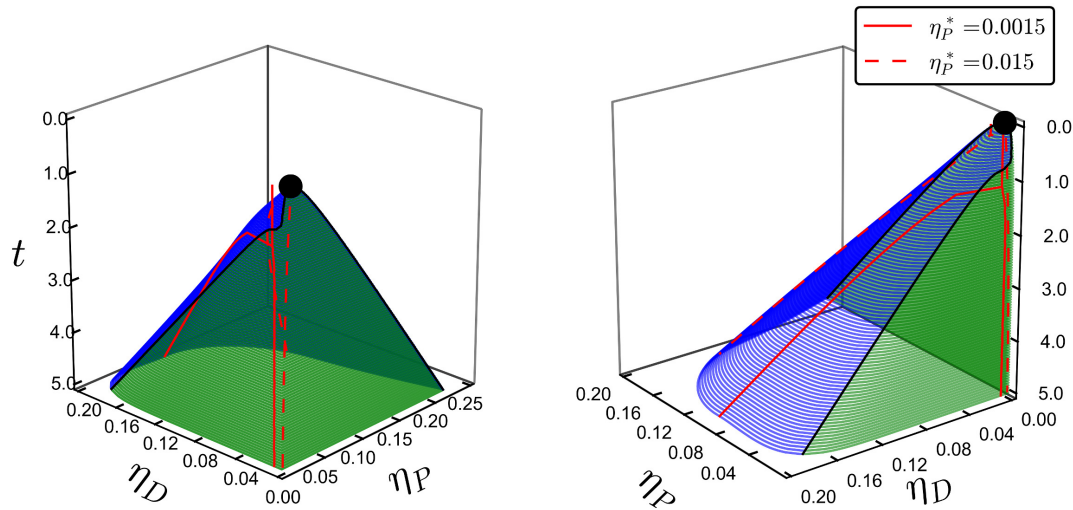


**Figure 2.6** – Phase diagram obtained from the resolution of eq. (2.15). For  $T < T^c$ , any combination of concentrations lying below the binodal curve is an unstable mean-field solution, which results in the system splitting into two phases  $I$  and  $II$  which sits on the binodal surface. The dilute phase  $I$  (green) has lower concentrations than the dense phase  $II$  (blue). The parameter  $t$  from the vertical axis is defined in eq. (2.18). In this diagram, we chose to use the volumic densities instead of the concentrations, which are defined as  $\eta_D = b^3 c_D$  and  $\eta_P = b^3 c_P$ . The black line is the critical curve.

At a given temperature though, there is only one solution for the phase separated system. Indeed, the points on the binodal are uniquely determined by the self-consistent relations:

$$\begin{aligned} \frac{\partial \mathcal{L}}{\partial \mu_D} &= MN/V, \\ \frac{\partial \mathcal{L}}{\partial \mu_P} &= P/V, \\ \frac{\partial \mathcal{L}}{\partial \Pi} &= 1, \end{aligned} \quad (2.19)$$

which yield

$$\phi \begin{pmatrix} c_D^I \\ c_P^I \end{pmatrix} + (1 - \phi) \begin{pmatrix} c_D^{II} \\ c_P^{II} \end{pmatrix} = \begin{pmatrix} c_D = MN/V \\ c_P = P/V \end{pmatrix}, \quad (2.20)$$

and completely determine the dilute and the dense phase from the mean-field concentrations  $c_D$  and  $c_P$ . This relation has a very straightforward graphical interpretation and is a generalization of a Maxwell construct (fig. 2.5b). If we imagine changing the concentration  $c_D$  or  $c_P$ , or more generally going along a path in the  $(c_D, c_P)$  plane, the system will not phase-separate right away when the path crosses the coexistence line. That is because there is a range of metastable mean-field solutions enclosed within the coexistence curve (fig. 2.5a). Continuing along this fictive path, the mean-field solution will become unstable only when the determinant in eq. (2.12) becomes negative. Only then will the system split into two phases. Therefore in general, the transition is first order, except at the two critical points where the coexistence line and the spinodal line intersect.

### 2.3.4 Conclusion

The relevant biological parameter in this approach is the binding interaction between proteins and DNA, which is represented by the mean-field coefficient  $\beta v$ . It is a function of the affinity of the proteins with DNA and depends on the biochemistry of the interaction. What this approach tells us is that for a generic DNA-binding protein, a phase separation is to be expected if the affinity is such that  $\beta v < (\beta v)^c$  and if the concentrations of DNA and proteins fall within the biphasic region. The phase separation gives rise to a dilute phase (*I*) with few DNA and few proteins and a dense phase (*II*) with higher concentrations of DNA and proteins. Because in general  $c_D^I < c_D^c \sim 1/\sqrt{N}$ , the concentration of DNA in the dilute phase is very small. Essentially, the DNA chains are collapsed into molten globules which form the dense phase, with few protruding loops which form the dilute phase. This feature is visible in BD simulations (fig. 2.7). The phase transition characterized is first order almost everywhere, in agreement with a thermodynamical model for the agglomeration of DNA-looping proteins, based on a description with graph ensembles [78].

The globular clusters of the dense phase can be considered as a model for transcription factories observed *in vivo*. Of course in reality there are many different TFs in the cell, which together may contribute to the architecture of the chromosome, including the formation of transcription factories. However, here we considered a generic type of protein. This come to say that the effect of one abundant protein prevails on the others in given physiological conditions. Note that we have adopted a coarse-grained approach in which many details of the chromosome organization such as specific DNA loops or protein complexes are embedded in the bead representation of DNA monomers and proteins. However, DNA clusters are indeed observed in the cell (fig. 2.8). These clusters do not display any internal structure, suggesting that they are globular. This effect can be accounted by the present theory by considering in a general way the effect of all binding proteins on the DNA.

Increasing evidence has suggested that transcription partly proceeds from transcription factories. Although the non-specific hypothesis for the binding of proteins to DNA that we have taken in this model is an over-simplifying assumption of the reality, it is true for instance that RNAP binds widely on the DNA thanks to its  $\sigma$ -unit. The conclusions reached in this Flory-Huggins theory suggest that a biphasic regime can exist, with a dense phase spanning a volume of size  $(1 - \phi)V$  and with local concentrations of DNA and RNAP increased with respect to the mean-field ones. Hence, the equilibrium of complexation reactions such as:



may be shifted towards the formation of complexes and may favour transcription initiation in the transcription factories. This is consistent with some experimental study showing that RNAP clusters are formed during pre-initiation and initiation of transcription [74]. The same authors also proposed that crowding of enzymes, *i.e.* higher local concentrations can aid in rate-limiting steps of gene regulation. From a dynamical standpoint, the confinement of unbound RNAP in a restricted volume can reduce the search time for a promoter. To this extent, it is worth pointing out a study claiming that the promoter search mechanism is indeed dominated by three-dimensional diffusion of RNAP over the monodimensional diffusion (*i.e.* sliding) along DNA [79].

Note that the theory described here is somewhat different from more standard polymer-colloid systems treatments. In the latter case, the system consists of a solution of polymer coils and colloids, and the radius of gyration of one single coil and the diameter of the colloidal particles are comparable. In our case, the proteins can hardly be compared to colloidal particles because their size is comparable not to the radius of gyration of the whole chromosome but instead to the size of one monomer.

The presence of ions in solutions (*e.g.*  $\text{Ca}^{2+}$ ,  $\text{Cl}^-$ ,  $\text{Mg}^{2+}$ ) gives rise to screened electrostatic interactions. For objects of nanometric size like proteins, interactions are short-ranged with a range typically given by the size of the objects in question. Let us also point out that at the mean-field level, the effect of ions in solution only arise through an adjustment of the Mayer coefficients  $\alpha_D$ ,  $\alpha_P$  and  $\beta_V$ . The DNA excluded volume coefficient  $\alpha_D$  will always be positive and accounts for the electrostatic repulsion between negatively charged monomers. The protein excluded volume coefficient  $\alpha_P$  will be positive in general for the same reasons, but for proteins able to dimerize it may take negative values.

The present theory is stated with a general formalism. Hence, we think it may also be adapted to the description of the condensation of DNA by other condensing agents such as multivalent ions. As stated above, within the Flory-Huggins theory, the phase transition induced by condensing agents appears to be first order, except at the tricritical point and on the critical lines. Therefore the transition from the swollen to the condensed state should be discontinuous and present hysteresis effects, which was indeed observed [80, 81]. Interestingly, the Flory-Huggins theory also predicts another effect. For a fixed temperature and for a DNA concentration taken in a prescribed range, if we start with a small concentration of condensing agents that we progressively increase, there will be a value at which the system splits into two phases. Yet, if we keep adding condensing agents, the system will at some point exit the biphasic regime. This phenomenon called re-entrance has been observed in some experimental work using polyethylene glycol (PEG) [82].

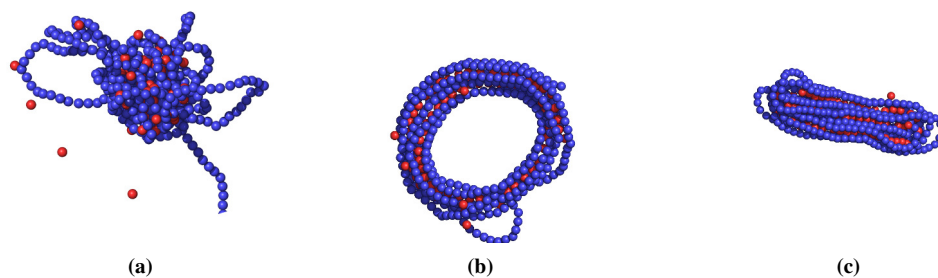


**Figure 2.7** – Snapshots of Brownian dynamics simulations (polymer with  $N + 1 = 400$  monomers). For small persistence lengths (a) the dense phase is a molten globule while it is crystal-like for stiffer chains (b)-(c).

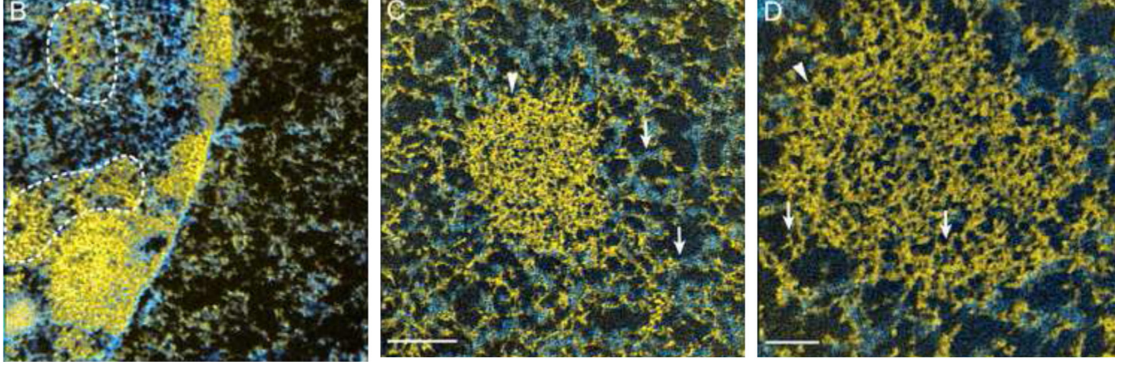


**Figure 2.8** – DNA-protein condensates observed in the nucleus in mouse cells with electron microscopy techniques [83]. The condensates are globular and have DNA (yellow) and proteins (blue), while the rest of the nucleus is filled mostly with proteins.

## 2.4 Structure of the dense phase

In the last section, the Flory-Huggins theory predicted the existence of a phase separation between two homogeneous phases. However, in the Flory-Huggins theory, the chain structure does not come into play, except through the suppression of the translational entropy of the chains. Namely, the dense phase predicted is a globule, that is to say a melt of collapsed DNA with proteins, regardless of the rigidity of the DNA chains. It turns out that DNA is a rigid biopolymer. It is an example of polyelectrolytes, and as such its bending rigidity depends on the screening effect of salt because of the presence of negative charges along its backbone. In physiological condition, the naked DNA has a persistence length  $l_p$  of approximately 150 bp. Several studies have highlighted that the bending rigidity of the polymer has an influence on the micro-structure of the dense phase [46, 84, 85]. The dense phase then adopts stretched configurations which are characterized by the apparition of tube-like or helical structures. This effect is also well characterized through BD simulations (fig. 2.9).

### 2.4.1 Random Phase Approximation

A standard way to characterize the effect of the chain structure is to use the Random Phase Approximation (RPA) [53]. The method consists in expanding the action in eq. (2.7) to second order around the mean-field solution and checking for the stability of the Gaussian fluctuations. The structure function of the DNA chain then naturally arises as a functional parameter for the stability condition of the Gaussian fluctuations. For the sake of simplicity, we will introduce the notation

$$\mathbf{X}(r) = \begin{pmatrix} \rho_D(r) \\ \varphi_D(r) \\ \rho_P(r) \\ \varphi_P(r) \end{pmatrix}, \quad (2.21)$$

and write the partition function in eq. (2.7) as

$$Z = \int \mathcal{D}[\mathbf{X}(r)] \exp(-S[\mathbf{X}]), \quad (2.22)$$

where to alleviate notations, we took  $\beta = 1$ .

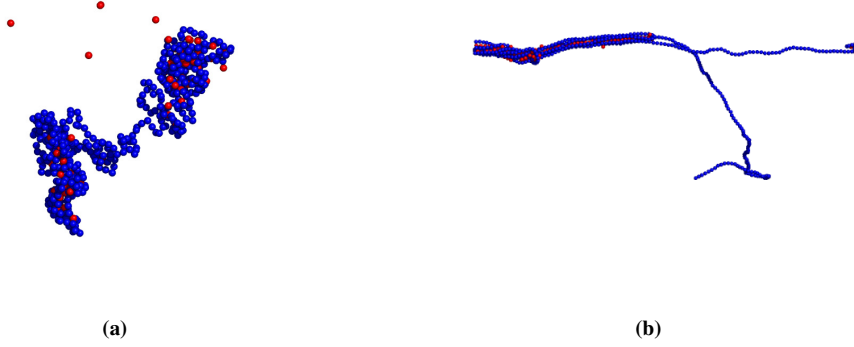


**Figure 2.9** – Two equilibrium configurations of a polymer chain (blue) interacting with binding spheres (red) in the absence of bending rigidity ( $l_p = 0$ ) and with strong bending rigidity ( $l_p = 30$ ), obtained with BD simulations. We used a truncated Lennard-Jones potential with  $\varepsilon = 3.0k_B T$  and  $r^{th} = 2$ . In both cases, the system is phase separated. (a) For  $l_p = 0$ , the dense phase consists of several globular aggregates distributed in a necklace fashion along the chain. (b) For  $l_p = 30$ , the dense phase adopts a tubular structure.

The saddle-point condition,  $\delta S/\delta \mathbf{X}(r) = 0$ , yields the Lagrange equations:

$$i\varphi_D(\mathbf{r}) - \int d\mathbf{r}' u_{DD}(\mathbf{r} - \mathbf{r}') \rho_D(\mathbf{r}') - \int d\mathbf{r}' u_{DP}(\mathbf{r} - \mathbf{r}') \rho_P(\mathbf{r}') - \frac{1}{2} w(\rho_D(\mathbf{r}) + \rho_P(\mathbf{r}))^2 = 0, \quad (2.23)$$

$$i\rho_D(\mathbf{r}) + M \frac{\delta \ln Q}{\delta \varphi_D(\mathbf{r})} [i\varphi_D] = 0, \quad (2.24)$$

$$i\varphi_P(\mathbf{r}) - \int d\mathbf{r}' u_{PP}(\mathbf{r} - \mathbf{r}') \rho_P(\mathbf{r}') - \int d\mathbf{r}' u_{DP}(\mathbf{r} - \mathbf{r}') \rho_D(\mathbf{r}') - \frac{1}{2} w(\rho_D(\mathbf{r}) + \rho_P(\mathbf{r}))^2 = 0, \quad (2.25)$$

$$i\rho_P(\mathbf{r}) + P \frac{\delta \ln W}{\delta \varphi_P(\mathbf{r})} [i\varphi_P] < ++ > = 0. \quad (2.26)$$

Starting from a guess solution (*e.g.* homogeneous fields), the previous system can be solved iteratively or using continuous steepest descent methods. Such procedure is known as numerical self-consistent field methods in the polymer literature [55]. Although the convolutions are easily handled in Fourier space, the difficulty lies in the computation of the functional derivative  $\delta \ln Q/\delta \varphi_D(\mathbf{r})$ . Hence it is a hard computational problem to solve. Based on physical considerations presented in the last section, we may look for the particular homogeneous (mean-field) solution:

$$\mathbf{X}^* = \begin{pmatrix} c_D \\ \phi_D \\ c_P \\ \phi_P \end{pmatrix}. \quad (2.27)$$

The resolution of eq. (2.26) is now straightforward. We obtain the following saddle-point approximation for the partition function:

$$Z \simeq \exp(-S^*) = \exp(-V\beta f(c_D, c_P)), \quad (2.28)$$

where  $\beta f$  is given by eq. (2.11), with  $c_D = MN/V$  and  $c_P = P/V$ . That is to say we recover the Flory-Huggins theory from the last section. The RPA consists in the analysis of the effect of the thermodynamical fluctuations on the mean-field solution. To this end, let us introduce the vector field  $\mathbf{Y} = \mathbf{X} - \mathbf{X}^*$ . An expansion of the action in eq. (2.22) to second order gives

$$Z \simeq \int D[\mathbf{Y}(\mathbf{r})] \exp\left(-S^* - \frac{1}{2} \int d\mathbf{r} d\mathbf{r}' \mathbf{Y}(\mathbf{r}) \frac{\partial^2 S}{\partial \mathbf{X}(\mathbf{r}) \partial \mathbf{X}(\mathbf{r}')} \Big|_{\mathbf{X}=\mathbf{X}^*} \mathbf{Y}(\mathbf{r}')\right), \quad (2.29)$$

or in Fourier space

$$Z \simeq \int \prod_{\mathbf{k}>0} d\mathbf{Y}_{\mathbf{k}} \exp\left(-S^* - \frac{1}{V} \sum_{\mathbf{k}>0} \mathbf{Y}_{\mathbf{k}} \frac{\partial^2 S}{\partial \mathbf{X}_{\mathbf{k}} \partial \mathbf{X}_{-\mathbf{k}}} \Big|_{\mathbf{X}=\mathbf{X}^*} \mathbf{Y}_{-\mathbf{k}}\right), \quad (2.30)$$

where the summation in Fourier space is carried out over the first Brillouin zone. The operator in the quadratic form is a  $4 \times 4$  matrix. Its matrix elements can be computed (see appendix 2.A) and the following expression is obtained in Fourier representation:

$$\frac{\partial^2 S}{\partial \mathbf{X}_{\mathbf{k}} \partial \mathbf{X}_{-\mathbf{k}}} \Big|_{\mathbf{X}=\mathbf{X}^*} = \begin{pmatrix} A_{DD}(\mathbf{k}) & -i & A_{DP}(\mathbf{k}) & 0 \\ -i & c_D S_N(\mathbf{k}) & 0 & 0 \\ A_{DP}(\mathbf{k}) & 0 & A_{PP}(\mathbf{k}) & -i \\ 0 & 0 & -i & c_P \end{pmatrix}, \quad (2.31)$$

with

$$\begin{aligned} A_{DD}(\mathbf{k}) &= u_{DD}(\mathbf{k}) + w(c_D + c_P)^2, \\ A_{PP}(\mathbf{k}) &= u_{PP}(\mathbf{k}) + w(c_D + c_P)^2, \\ A_{DP}(\mathbf{k}) &= u_{DP}(\mathbf{k}) + w(c_D + c_P)^2. \end{aligned} \quad (2.32)$$

Note that the structure of the chain comes into play through the structure factor  $S_N(\mathbf{k})$  which appears in one of the matrix elements. The quadratic fluctuations operator is diagonal in Fourier space. Hence the partition function in eq. (2.30) is a product of Gaussian integrals. It is well-defined as long as for all  $\mathbf{k}$

$$\Gamma(\mathbf{k}) = \det\left(\frac{\partial^2 S}{\partial \mathbf{X}_{\mathbf{k}} \partial \mathbf{X}_{-\mathbf{k}}}\right) > 0. \quad (2.33)$$

The previous equation is a generalization of the spinodal condition for a Fourier mode  $\mathbf{k}$ . When the temperature is lowered, the first mode  $\mathbf{k}^*$  to become unstable sets the temperature when the mean-field solution is no longer stable. If  $k^* = 0$ , then it is simply the spinodal condition of the Flory-Huggins theory, and at the instability, the system splits into two homogeneous phases as described previously. If  $k^* > 0$ , then it is the signature of a micro-phase separation. In that case the homogeneous mean-field solution is no longer a stable solution and instead stable solutions will display spatial modulations of typical length  $2\pi/k^*$ . The determinant in eq. (2.33) can be computed easily and gives

$$\Gamma(\mathbf{k}) = \left(A_{DD}(\mathbf{k}) + \frac{1}{c_D S_N(\mathbf{k})}\right) \left(A_{PP}(\mathbf{k}) + \frac{1}{c_P}\right) - A_{DP}(\mathbf{k})^2. \quad (2.34)$$

The potentials are essentially contact-like because of the screened interactions (we recall that the Debye-Hückel length is  $\sim 1 \text{ nm}$  in the cell), thus the Fourier transforms of the interaction potentials have the expressions:

$$\begin{aligned} u_{DD}(\mathbf{k}) &= \alpha_D, \\ u_{PP}(\mathbf{k}) &= \alpha_P, \\ u_{DP}(\mathbf{k}) &= \beta v. \end{aligned} \tag{2.35}$$

The structure factor for a Gaussian chain with  $N$  Kuhn segments of length  $b$  is given by  $S_N(\mathbf{k}) = ND(k^2 R_g^2)$ , where  $R_g^2 = b^2 N/6$  is as usual the radius of gyration of the chain and  $D(x) = 2/x^2(x - 1 + \exp(-x))$  is the Debye function [53]. There is no analytical expression available for the structure function for a Worm Like Chain (with persistence  $l_p$ ) as it is the case for the Gaussian chain. To date, to the best of our knowledge, it is still an open problem despite several classical and more recent works [86–90]. We first used an approximate expression for the structure factor of a semi-flexible chain found by Thirumalai and co-worker [62], which lead us to propose an alternative method to compute the structure function of a worm-like chain, that we will present in chapter 3.

We have monitored the sign of  $\Gamma(k)$  as a function of the wave number  $k$ . However we do not report it here because we have not found any instability arising for a non-zero Fourier mode, that would characterize a dense phase with micro-structure. On second thought, we suspect that the RPA analysis is not well suited for this system because the phase transition is first order in general (it is only second order when crossing the critical line). In order to illustrate this point, let us consider a generic system with a mean-field order parameter  $\phi$  and a free energy function  $F(\phi)$  displaying a second order phase transition at a critical temperature  $T_c$ . For  $T > T_c$ , the free energy has a single minimum  $\phi^*$  and  $\partial^2 F / \partial \phi^2(\phi^*) > 0$ , *i.e.* the solution is stable. At  $T = T_c$ , the free energy has still one single minimum  $\phi^*$ , yet the curvature at this minimum is null. For  $T < T_c$ , the former solution  $\phi^*$  is unstable, *i.e.*  $\partial^2 F / \partial \phi^2(\phi^*) < 0$ , and the free energy has two minima  $\phi^I$  and  $\phi^{II}$ . Similarly to what has been presented above, one may give an approximation of the partition function of this system by integrating over the Gaussian fluctuations:

$$Z = \int dy \exp\left(-F(\phi^*) - \frac{1}{2} \frac{\partial F}{\partial \phi^2}(\phi^*) y^2\right), \tag{2.36}$$

where  $y = \phi - \phi^*$  is the difference with the high-temperature solution. When  $T < T_c$ ,  $\partial^2 F / \partial \phi^2(\phi^*) < 0$  and this Gaussian integral is no longer defined. The instability is driven by an inversion of the curvature around the high-temperature solution  $\phi^*$  which occurs at  $T = T_c$  (fig. 2.10a). Therefore, for a second order transition the critical temperature  $T_c$  coincides with an instability of the fluctuations around the high-temperature solution. In that case, we say that the phase transition is driven by critical fluctuations. To the contrary, in the case of a first order transition, the high-temperature solution  $\phi^I$  remains stable as we cross the phase transition temperature  $T^*$  (fig. 2.10b). For that reason, the integral over the fluctuations around the high-temperature solution remains a well-defined Gaussian integral and is of no use to identify the phase transition temperature  $T^*$ . In that case, we say that the phase transition is not driven by critical fluctuations. A generalization of this reasoning suggests that RPA will not help in characterizing a micro-phase separation because the transition is not driven by critical fluctuations around the saddle-point solution. Since the RPA did not give any interesting results, we turned to another way to characterize the structure of the dense phase.

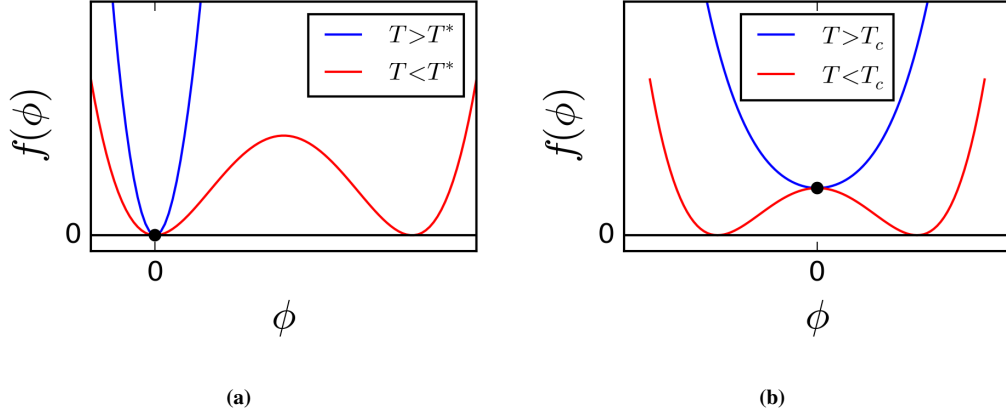


**Figure 2.10** – Comparison between a first order phase transition (a) and a second order phase transition (b). A second order phase transition is therefore driven by critical fluctuations at the high temperature equilibrium, which is not the case for a first order phase transition.

## 2.4.2 Lattice model of the dense phase

### 2.4.2.1 Model

Since the RPA is not appropriate to describe the system in the dense phase, we adopt another approach. Because of their attractive interactions with the DNA, the spheres induce an effective attraction between the DNA monomers. Before coming back to a system in a continuous volume at the end of this section, let us turn our attention to a model of a semi-flexible polymer chain on a lattice that was proposed initially to explain the folding of a protein in compact structures [85, 91, 92] (see fig. 2.11). An attraction energy  $\varepsilon_v$  between non-bonded nearest neighbors is included, which favors compact configurations. A bending energy of the chain is introduced as a corner penalty which favors stretched configurations (or “helices” in the protein folding vocabulary). It penalizes corners by an energy  $\varepsilon_h$  and thus plays the role of a bending rigidity. As we will see, this term induces an ordering transition between a random (molten) globule where corners are mobile in the bulk, and a crystalline phase, where corners are expelled to the surface of the globule.

In order to explore the equilibrium physics of this system, we write the partition function for this system as

$$Z_N = \sum_{SAW} \exp \left( -\beta \varepsilon_h \mathcal{N}_c + \frac{1}{2} \beta \varepsilon_v \sum_{\mathbf{r}, \mathbf{r}'} n_{\mathbf{r}} \Delta_{\mathbf{r}, \mathbf{r}'} n_{\mathbf{r}'} - N \beta \varepsilon_v \right), \quad (2.37)$$

where the sum is carried out on the self-avoiding walks (SAW) of length  $N$ ,  $\mathcal{N}_c$  is the number of corners in the configuration,  $\Delta_{\mathbf{r}, \mathbf{r}'}$  is the nearest neighbor operator on the lattice, and  $n_{\mathbf{r}} = 0, 1$  is the occupancy variable of the lattice sites. The first term in the exponent gives a penalty proportional to the number of corners, whereas the second gives a bonus proportional to the number of neighbors pairs. Note the third term which is introduced to cancel off the interactions between consecutive monomers along the path that were already counted in the second term. Using a mean field theory, Orland and colleagues [85, 91, 92] showed that depending on the attraction energy and the corner penalty, three phases can exist, namely a dilute phase where the polymer is swollen, a condensed phase, which we call a molten globule, where the

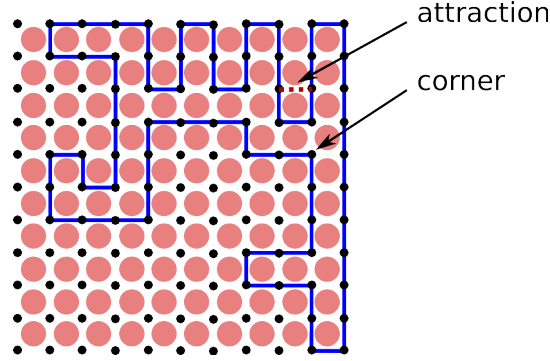


**Figure 2.11** – Lattice model for the collapse of a DNA polymer. The attractive interaction mediated by binding proteins (red spheres) is taken into account implicitly through the introduction of an attractive interaction between neighboring sites.

polymer is collapsed and disordered and finally a second condensed phase where the polymer is collapsed but with a local crystalline ordering. The phase diagram is described simply in the plane  $(\varepsilon_v/T, \varepsilon_h/\varepsilon_v)$ . For fixed small  $\varepsilon_h$ , there is a second-order phase transition at a temperature  $T = T_\theta$  between a dilute and a disordered condensed phase, followed by a first-order freezing transition at  $T_F$  between the disordered condensed phase and a locally ordered condensed phase of the polymer. Upon increasing the chain stiffness  $\varepsilon_h$ , the molten globule region shrinks until it eventually vanishes. Thus, for large stiffness, the polymer goes abruptly from a swollen to a frozen configuration ( $T_F > T_\theta$ ) through a direct first order transition. These theoretical results were readily confirmed and improved by Monte-Carlo simulations [93, 94].

#### 2.4.2.2 Counting Hamiltonian paths

For the sake of completeness we review here in a simple case the methods that were used to obtain the announced results. We consider the extreme case where the polymer has collapsed completely (density  $\eta = 1$ ). That is to say, each of the  $N$  sites of the lattice are occupied by a DNA monomer. When both  $\varepsilon_h = 0$  and  $\varepsilon_v = 0$ , the partition function for this system reduces to

$$Z_N = \sum_{HP} 1, \quad (2.38)$$

where the sum is carried out on the Hamiltonian paths (HP) on the lattice, that is to say paths that visit each of the  $N$  sites of the lattice once and only once. Hence, the partition function is just the number of HP on the lattice. An equivalence to a field theory is obtained by introducing for each lattice site a  $n$ -component field  $\varphi_{\mathbf{r}}$ , and the corresponding partition function

$$Q_n = \int \prod_{\mathbf{r}} d\varphi_{\mathbf{r}} e^{-A_G} \prod_{\mathbf{r}} \left( \frac{1}{2} \varphi_{\mathbf{r}}^2 \right), \quad (2.39)$$

where  $A_G$  is a quadratic action given by

$$A_G = \frac{1}{2} \sum_{\mathbf{r}, \mathbf{r}'} \varphi_{\mathbf{r}} \Delta_{\mathbf{r}, \mathbf{r}'}^{-1} \varphi_{\mathbf{r}'}, \quad (2.40)$$

and  $\Delta_{\mathbf{r}, \mathbf{r}'}$  is as before the nearest neighbor operator on the lattice. The quantity in eq. (2.39) is (up to a normalization), a simple Gaussian average. This average can be computed using Wick's theorem once it

has been pointed out that the elementary contraction reads

$$\langle \varphi_{\mathbf{r}}^u \varphi_{\mathbf{r}'}^v \rangle = \delta^{uv} \Delta_{\mathbf{r}, \mathbf{r}'}. \quad (2.41)$$

Therefore, only products of fields corresponding to sites which are nearest neighbors will give a non zero average. As a result, we obtain that

$$\begin{aligned} \left\langle \prod_{\mathbf{r}} \left( \frac{1}{2} \varphi_{\mathbf{r}} \right)^2 \right\rangle &= \frac{1}{2^N} \sum_{\text{all permutations}} \langle \varphi_{\mathbf{r}_1} \varphi_{\mathbf{r}_2} \rangle \cdots \langle \varphi_{\mathbf{r}_{2N-1}} \varphi_{\mathbf{r}_{2N}} \rangle, \\ &= \sum_{k=1} n^k c_k, \end{aligned}$$

where  $c_k$  is the number of graphs on the lattice containing  $k$  closed paths which together visit all sites of the lattice once and only once. Eventually,  $c_1$  is just the number of Hamiltonian paths on the lattice, and we have the equivalence

$$\sum_{HP} 1 = \lim_{n \rightarrow 0} \frac{1}{n} \frac{\int \prod_{\mathbf{r}} d\varphi_{\mathbf{r}} e^{-AG} \prod_{\mathbf{r}} \left( \frac{1}{2} \varphi_{\mathbf{r}}^2 \right)}{\int \prod_{\mathbf{r}} d\varphi_{\mathbf{r}} e^{-AG} \prod_{\mathbf{r}} 1}. \quad (2.42)$$

This simple equivalence gives an original way to compute the number of Hamiltonian paths on a lattice. Namely, one can perform a saddle-point approximation on the field partition function in eq. (2.39). In that case, an approximation of  $Q_n$  is:

$$Q_n \simeq \int \prod_{\mathbf{r}} d\varphi_{\mathbf{r}}^* \exp \left( -N + d \frac{1}{2} \sum_{\mathbf{r}} \ln \left( \frac{1}{2} \varphi_{\mathbf{r}}^* \right) \right), \quad (2.43)$$

where the \* superscript denotes that the integration is carried out on the saddle-point solutions. One can then go further by making a mean-field approximation, that is to say by considering only saddle-point solutions of norm  $\|\varphi_{\mathbf{r}}^*\| = \varphi$ . It follows from the saddle-point equation that  $\varphi^2 = 2q$  where  $q = 2d$  is the coordination number of the lattice. The integration in the last expression is then performed over the  $n$ -dimensional sphere, whose area is  $2\pi^{n/2}/\Gamma(n/2)$ . Eventually, using the equivalence in eq. (2.42), one obtains the approximation for the number of Hamiltonian paths on the lattice of  $N$  sites:

$$Z_N \simeq \left( \frac{q}{e} \right)^N. \quad (2.44)$$

### 2.4.2.3 The effect of rigidity

Still assuming that the polymer has collapsed completely, we can now slightly modify the previous model by introducing a corner penalty  $\beta\varepsilon_h \neq 0$ . In that case, the partition function for this system reads

$$Z_N = \sum_{HP} e^{-\beta\varepsilon_h N_c}, \quad (2.45)$$

where as before  $N_c$  counts the number of corners in the HP realization. In close analogy to the previous developments, we seek for an equivalence with a field theory. For each site of the lattice, we introduce a

$n$ -component field  $\varphi_\alpha(\mathbf{r})$  for each of the direction  $\alpha = 1, \dots, d$  of the  $d$ -dimensional lattice. This time we introduce the partition function

$$Q_n = \int \prod_{\mathbf{r}} \prod_{\alpha=1}^d d\varphi_\alpha(\mathbf{r}) e^{-A_G} \prod_{\mathbf{r}} \left( \frac{1}{2} \sum_{\alpha=1}^d \varphi_\alpha(\mathbf{r})^2 + e^{-\beta\varepsilon_h} \sum_{\alpha<\gamma} \varphi_\beta(\mathbf{r}) \cdot \varphi_\gamma(\mathbf{r}) \right), \quad (2.46)$$

where  $A_G$  is a quadratic action given by

$$A_G = \frac{1}{2} \sum_{\alpha=1}^d \sum_{\mathbf{r}, \mathbf{r}'} \varphi_\alpha(\mathbf{r}) [\Delta_{\mathbf{r}, \mathbf{r}'}^\alpha]^{-1} \varphi_\alpha(\mathbf{r}'), \quad (2.47)$$

and  $\Delta_{\mathbf{r}, \mathbf{r}'}^\alpha$  is the nearest neighbor operator on the lattice in direction  $\alpha$ . The quantity in eq. (2.46) is again a simple Gaussian average. It can be computed using Wick's theorem with the elementary contraction

$$\langle \varphi_\alpha^u(\mathbf{r}) \varphi_\beta^v(\mathbf{r}') \rangle = \delta^{uv} \delta^{\alpha\beta} \Delta_{\mathbf{r}, \mathbf{r}'}^\alpha, \quad (2.48)$$

and again, only products of fields corresponding to sites which are nearest neighbors will give a non-zero average. Therefore this average selects closed paths on the lattice. However, there is an important difference with the previous case. While making products of the quantity between parenthesis in eq. (2.46), the first term of this quantity will tend to select nearest neighbors only in the direction  $\alpha$ . Yet, given a site  $\mathbf{r}$  and a nearest neighbor  $\mathbf{r}'$ , one can choose for the former a term of the form  $\varphi_\alpha(\mathbf{r})^2/2$ , and for the latter a term  $\varphi_\alpha(\mathbf{r}') \cdot \varphi_\beta(\mathbf{r}')$ , in which case a Boltzmann weight equal to  $\exp(-\beta\varepsilon_h)$  must be applied. Applying Wick's theorem, one is led to consider products of elementary contractions like  $\langle \varphi_\alpha(\mathbf{r}) \cdot \varphi_\alpha(\mathbf{r}') \rangle e^{-\beta\varepsilon_h} \langle \varphi_\beta(\mathbf{r}') \cdot \varphi_\beta(\mathbf{r}'') \rangle$ . In summary, like before, the partition function in eq. (2.46) generates closed paths on the lattice. Yet this time a Boltzmann weight with a penalty equal to the number of turns times  $\beta\varepsilon_h$  is applied to each path. This leads to the following equivalence:

$$\sum_{HP} e^{-\beta\varepsilon_h N_c} = \lim_{n \rightarrow 0} \frac{1}{n} \frac{\int \prod_{\mathbf{r}} \prod_{\alpha=1}^d d\varphi_\alpha(\mathbf{r}) e^{-A_G} \prod_{\mathbf{r}} \left( \frac{1}{2} \sum_{\alpha=1}^d \varphi_\alpha(\mathbf{r})^2 + e^{-\beta\varepsilon_h} \sum_{\alpha<\gamma} \varphi_\beta(\mathbf{r}) \cdot \varphi_\gamma(\mathbf{r}) \right)}{\int \prod_{\mathbf{r}} \prod_{\alpha=1}^d d\varphi_\alpha(\mathbf{r}) e^{-A_G}}. \quad (2.49)$$

In the same spirit as in the previous case, a saddle-point approximation supplemented by a mean-field approximation yields the approximate expression for the partition function in eq. (2.45):

$$Z_N \simeq \left( \frac{q(\beta)}{e} \right)^N, \quad (2.50)$$

where

$$q(\beta) = 2 + 2(d-1)e^{-\beta\varepsilon_h}. \quad (2.51)$$

The expression obtained for the partition function is remarkable because it has the same form as eq. (2.44), but with an effective lattice coordination number  $q(\beta)$ . In the limit  $T \rightarrow \infty$ , one recovers the previous case, with  $q(0) = 2d$ . To the contrary, when  $T \rightarrow 0$ , one has  $q(\infty) = 2$ , which corresponds to straight paths where each monomer only "sees" the previous and the next monomer. The free energy  $f(T) = -T/N \ln Z_N$  has the property to vanish at the temperature  $T_F$ , defined by  $q(\beta_F) = e$ . Starting from the high temperatures,  $f(T)$  is a decreasing function of the temperature until  $T = T^*$ , at which point

the entropy  $S(T^*) = -\partial f/\partial T(T^*) = 0$  and  $f(T^*) > 0$ . When the entropy vanishes, the system freezes in one configuration. Nonetheless this result is obtained within the context of the saddle-point and mean field approximation. A more careful analysis of the partition function in eq. (2.46) based on a Schwartz inequality shows that the free energy is bounded:  $f(T) \leq 0$  [91]. Consequently, the positivity of the free energy in the range of temperature  $T^* < T < T_F$  can only correspond to metastable states. In conclusion, there is a freezing transition at  $T = T_F$  which separates a high temperature regime in which the collapsed polymer is a molten globule from a low temperature regime in which the collapsed polymer is crystal-like and has a (quasi) zero entropy. In the crystalline phase, the configurations look like straight paths with corners expelled to the surface of the lattice (fig. 2.12). These configurations have been studied previously: they are elongated neck structures or toroids [95].

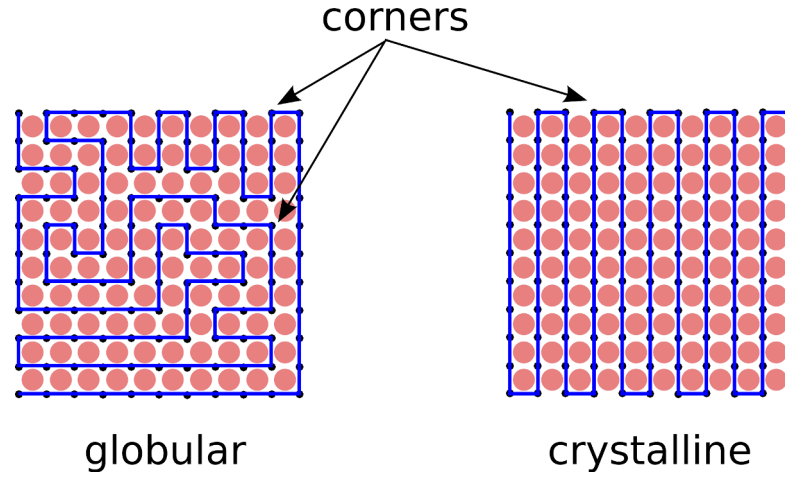


**Figure 2.12** – Two realizations of Hamiltonian paths on a cubic lattice. The globular state contains an extensive number of corners whereas the crystalline state contains a non-extensive number of corners (proportional to the surface).

#### 2.4.2.4 Phase diagram

The methods presented in the two previous paragraphs can be generalized to the case with attractive interactions between nearest neighbors ( $\beta\varepsilon_v < 0$ ) and to a lattice with vacancies ( $\eta < 1$ ). Namely, an equivalence with a field theory in the limit  $n \rightarrow 0$  can be written for the partition function in eq. (2.37). Similarly to the previous cases, a combination of saddle-point and mean-field approximations yields the free energy per monomer:

$$f(\eta, T) = -T \ln \left( \frac{q(\beta)}{e} \right) + T \frac{1-\eta}{\eta} \ln(1-\eta) + \varepsilon_v(1-d\eta), \quad (2.52)$$

where  $q(\beta)$  is defined in eq. (2.51). The full derivation is presented in details in [85]. In the open coil regime  $\eta \simeq 0$  and the free energy reduces to  $f_0(T) = -T \ln q + \varepsilon_v$ . Introducing the reduced temperature  $t = T/\varepsilon_v$ , the equilibrium equation  $\partial f/\partial \eta = 0$  yields non-zero solutions  $\eta^*$  only when

$$t < t_\theta = 2d. \quad (2.53)$$

Therefore, there is a second-order transition between an open-coil state and a globule at  $t_\theta$ . Though, as characterized previously, for  $\beta\varepsilon_h \neq 0$ , there is a freezing transition at a temperature  $t_F$  toward a crystalline

phase. For each  $\varepsilon_h$  the freezing temperature is obtained by equating the free energy in eq. (2.52) with the free energy of a frozen configuration where all the corners, delimiting the non-vacant region, are expelled to the surface:

$$g = -(d - 1)\varepsilon_v. \quad (2.54)$$

In conclusion, the phase diagram announced is obtained in the plane  $(t, \varepsilon_h/\varepsilon_v)$ , in which  $t_\theta$  delimits the coil-globule transition and  $t_F$  the globule-crystalline freezing transition. This phase diagram was later confirmed and refined with the help of Monte-Carlo simulations [93] (see fig. 2.13a).

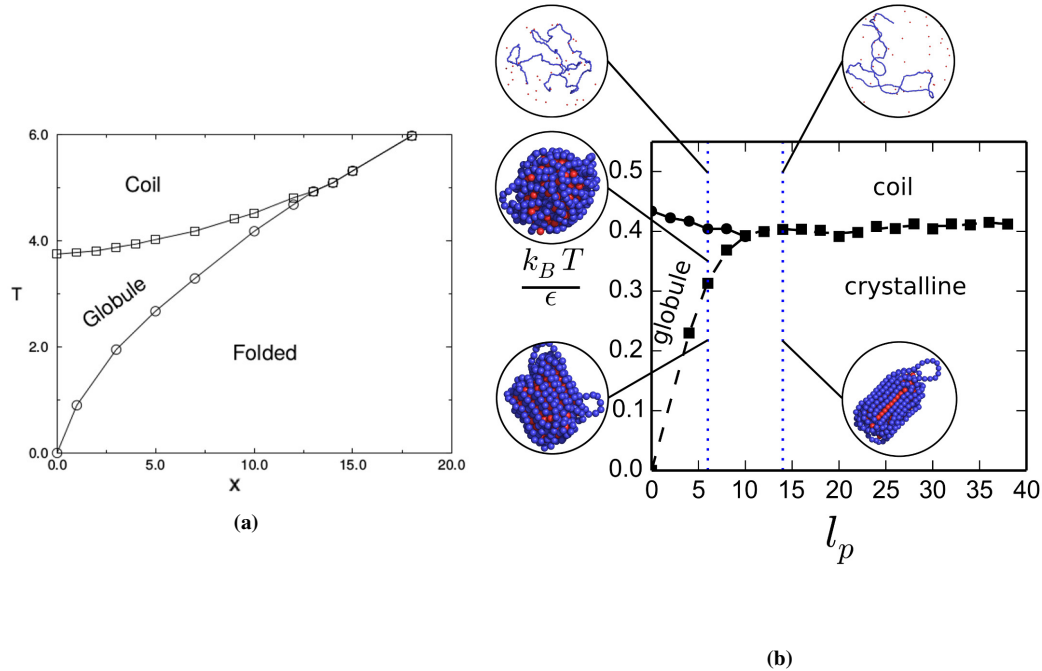


**Figure 2.13** – (a) Phase diagram of the collapse of a polymer on a lattice as defined in eq. (2.37), and computed in [93] from Monte-Carlo simulations.  $x = \varepsilon_h/\varepsilon_v$  (b) Phase diagram of a polymer interacting with spheres in a continuous volume. The phase diagram was computed using BD simulations with  $P = 100$  spheres, a polymer with  $N + 1 = 400$  monomers, as a function of the persistence length  $l_p$  and of the strength of the Lennard-Jones DNA-protein interaction  $\varepsilon$ .

### 2.4.3 Phase diagram of the dense phase structure

The results obtained in this section have enlightened our understanding of the collapse of a rigid polymer. There are however differences with the model of DNA condensation by binding proteins presented in section 2.3. First, the formal nucleus model is not a lattice model. Second, the attractive interactions between DNA monomers are not implicit but mediated by proteins. In that respect, the collapse depends on the concentration of proteins. Third, the bending rigidity of the DNA is not taken into account by discrete corner penalties but is instead modeled using a Kratky-Porod potential with persistence length  $l_p$  (see section 1.3.4 on page 13).

Despite these differences, we have found that the phase diagram of the collapse of a semi-flexible polymer interacting explicitly with spheres in an off-lattice volume is very similar to the phase diagram

obtained for the collapse of a polymer on a lattice presented above (fig. 2.13). Indeed, we performed BD simulations with a polymer chain of  $N + 1 = 400$  beads and  $P = 100$  protein spheres in a cubic volume of size  $L = 100$  with periodic boundary conditions. Polymer beads and protein spheres were interacting through a truncated Lennard-Jones potential with a well depth given by the energy scale  $\varepsilon$  (in  $k_B T$ ). By varying  $l_p$  and  $\varepsilon$  independently, we explored the phase behaviour of this system (appendix 2.B).

There are minor quantitative differences between the lattice/implicit and the off-lattice/explicit cases. Namely the numerical values for the coil-globule and globule-crystal transitions are different. This is due to the difference in the definition of the order parameters, the use of a Lennard-Jones potential for the attractive interaction, the Kratly-Porod model used to take into account the chain bending rigidity, and it is also a consequence of going from a lattice model to a continuous model. Furthermore, the concentration of spheres in solution is smaller than the close packing concentration, making it hardly comparable to an actual solvent. Despite these discrepancies, we can say that the results in both cases are in qualitative agreement.

The main conclusion obtained from the phase diagram of the dense phase is the existence of specific persistence length  $l_p^* \simeq 10$  such that:

- for  $l_p < l_p^*$ , the polymer collapses through a second order coil-globule transition, followed by a first order globule-crystal transition when  $\varepsilon$  increases;
- for  $l_p > l_p^*$ , the coil-globule transition no longer exists and the polymer collapses directly from a coil to a crystalline phase through a first order phase transition.

The coil-globule transition is the same as the phase transition depicted using a Flory-Huggins theory in section 2.3. Yet, when the DNA-protein attraction is strong enough, it appears that the dense phase can be crystalline. Besides, for very rigid chains ( $l_p > l_p^*$ ), the coil-globule transition does not exist because it is precluded by the freezing transition. In this case, the results of the Flory-Huggins theory are no longer valid. Snapshots of the coil, globule, and frozen state computed from MD simulations can be seen in fig. 2.7 and fig. 2.13b.

## 2.4.4 Conclusion

Let us sum up what has been obtained in this section. We have first noticed that the bending rigidity has an influence on the structure of the DNA-protein condensates. We have tried to use the RPA in order to characterize modulations of the DNA and protein concentrations in the dense phase, which is the signature of the existence of a microphase. Yet, the RPA failed because the collapse transition being generally first order, it is not driven by critical fluctuations. We turned to a theory of polymer collapse on a lattice, which is instructive because it predicts the existence of a crystalline phase for large values of the rigidity parameter  $\varepsilon_h$ . Using BD simulations, we effectively recovered this result for our formal nucleus model.

DNA condensation has been well characterized in *in vitro* experimental works [80, 82, 96–99]. Consequently, it is well known that DNA collapses from disperse structures corresponding to swollen coil configurations into ordered, highly condensed states, namely toroids or hexagonal bundles [100, 101]. Namely, such studies have concluded that during its collapse, DNA undergoes transitions through the following three phases: isotropic fluid, cholesteric and crystalline (hexagonal). This is in agreement with our results, demonstrating that our model for the collapse of DNA by proteins is actually more general than what was intended in the first place.

Although it is premature to draw any clear biological conclusion, it is tempting to discuss at least qualitatively potential effects of the crystalline phase on biological functions. In eukaryotes, nucleosomal

organization provides an effective protection against detrimental factors. This organization is absent in prokaryotes, which have a significantly lower ratio of DNA-binding proteins [102]. However, in harsh environmental conditions (radiations, temperature, oxidizing agents and radicals), several bacteria resort to DNA condensation mechanisms to protect their genome. Maybe the most spectacular case is the appearance of macroscopic DNA aggregates with crystal-like order in starved *E. coli* cells. In stressful conditions, the alternative  $\sigma^S$  factor is expressed, in response to low temperature, cell surface stress or oxidative shock. This in turn induces the expression of the DNA-binding protein DPS [103, 104]. In starved cells, DPS is the most abundant DNA-binding protein, with approximately 20 000 DPS proteins per cell. Consequently, DNA is condensed into crystal-like aggregates, which makes it less accessible to damaging factors. Wild-type *E. coli* cells starved for three days remain unaffected by a high dose of oxidizing agents whereas mutants lacking DPS lose viability [103]. This process is reversible. Interestingly, DPS binds non-specifically to DNA. We speculate that when DPS concentration increases, it induces the DNA collapse, and a dense phase appears. For proteins of the size of DPS ( $< 10$  nm), the apparent rigidity of DNA is large ( $\approx 50$  nm). Hence we might be in a case where the coil-globule transition is precluded by the freezing transition. Other examples of DNA compaction by non-specific proteins seem to exist. For instance the protein RecA induces the formation of DNA bio-crystals in *E. coli* which have an essential role in the DNA repair system [26], and the condensation of DNA in crystal-like configurations by spermine and polyamines has also been well characterized [105].

Earlier studies have demonstrated that the frozen phase can present various metastable states [94]. In the large  $N$  limit ( $N$  is the length of one chain), the transition time scale from one to another could be very large, and the system might well never equilibrate within biological time scales. Moreover, the parallel drawn between the Hamiltonian paths theory and the Flory-Huggins theory does not pretend to mathematical rigor. One essential difference is that in our case the attractive interaction between monomers is mediated by spheres. A way to compute more precisely the structure of the dense phase would be to go beyond the homogeneous saddle point approximation leading to the Flory-Huggins theory, for instance by using self-consistent field methods [54, 55], which are quite complex methods in the case of semi-flexible polymers.

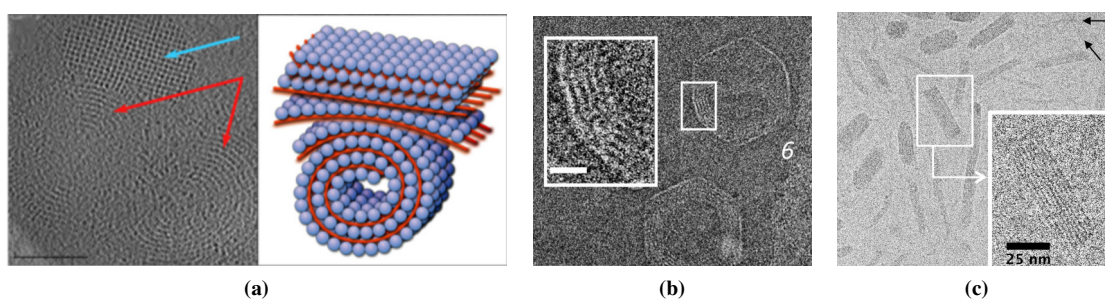


**Figure 2.14** – (a) Electron microscope (EM) images of DNA co-crystals in *E. coli* [26]. (b) CryoEM of DNA condensed inside the T5 bacteriophage in toroidal shapes [100]. (c) DNA-protamines complexes with bundle shapes observed by cryo-imaging with transmission electron microscope [101].

## 2.5 Discussion

We presented here two complementary frameworks to describe the phase diagram of polymeric fluids induced by binding particles, and applied it to a DNA chain interacting with DNA-binding proteins. Starting from a Flory-Huggins free energy, we first computed the mean-field phase diagram and found that at low temperature (*i.e.* high DNA-protein affinity) a biphasic regime exists, consisting of the coexistence of a dilute phase and a concentrated phase. The dilute phase may correspond to swollen configurations of the DNA whereas the concentrated phase is a model for condensed states of DNA. It turns out that the theory may also apply to DNA condensation by multivalent ions. Second, we addressed the characterization of the dense phase structure and showed that the chain bending rigidity can have dramatic effects. Without bending rigidity, the dense phase has no directional order and is a molten globule. However, when the chain bending rigidity is large enough, there is a freezing transition from the globular to a crystalline phase. Eventually for very rigid chains, the coil-globule transition is precluded by the freezing transition and the phase transition predicted in the Flory-Huggins framework does not occur.

In the cell, the existence of a dense phase could be a good approximation for the transcription factories observed experimentally. It is conjectured that this may increase the rate of success in transcription initiation by means of protein crowding and by enhancing the promoter search mechanism. Note that at a scale coarse-grained to a few thousand base-pairs (gene scale), the chromosome is flexible and the dense phase has the structure of a molten globule. Conversely, at a scale of a few base-pairs, the apparent rigidity of DNA is much higher. Thus, the DPS protein, which binds non-specifically to DNA, can induce the collapse of the *E. coli* chromosome into crystal-like aggregates; the dense phase is then frozen. This is not an efficient state for a searching mechanism. But on the contrary, it is very adequate to protect DNA or to halt transcription.

# Appendix

## 2.A Matrix elements of the Gaussian fluctuations

We recall the expression of the action in eq. (2.8):

$$\begin{aligned}
\beta S = & -i \int d\mathbf{r} \rho_D(\mathbf{r}) \varphi_D(\mathbf{r}) - i \int d\mathbf{r} \rho_P(\mathbf{r}) \varphi_P(\mathbf{r}) \\
& + \int d\mathbf{r} d\mathbf{r}' \rho_P(\mathbf{r}') u_{PP}(\mathbf{r}' - \mathbf{r}) \rho_P(\mathbf{r}) + \int d\mathbf{r} d\mathbf{r}' \rho_D(\mathbf{r}') u_{DD}(\mathbf{r}' - \mathbf{r}) \rho_D(\mathbf{r}) \\
& + \beta \int d\mathbf{r} d\mathbf{r}' \rho_D(\mathbf{r}') u_{DP}(\mathbf{r}' - \mathbf{r}) \rho_P(\mathbf{r}) \\
& + \frac{1}{3!} w \int d\mathbf{r} (\rho_D(\mathbf{r}) + \rho_P(\mathbf{r}))^3 \\
& - P \ln W[i\varphi_P] - M \ln Q[i\varphi_D] + P \ln \frac{P}{e} + M \ln \frac{M}{e},
\end{aligned} \tag{2.55}$$

with the single bead and single chain partition functions:

$$\begin{aligned}
W[i\varphi_P] &= \int d\mathbf{R} \exp(-i\varphi_P(\mathbf{R})), \\
Q[i\varphi_D] &= \int D[\mathbf{r}(s)] \exp\left(-\beta U_0[\mathbf{r}(s)] - i \int_0^N ds \varphi_D(\mathbf{r}(s))\right).
\end{aligned} \tag{2.56}$$

We now give the first and second order derivative of the action, which are used to find the saddle-point equations and perform the Gaussian fluctuations analysis. For the sake of clarity, we take  $\beta = 1$  in the

sequel. The first order functional derivatives are:

$$\begin{aligned}
\frac{\delta S}{\delta \rho_D(\mathbf{r})} &= -i\varphi_D(\mathbf{r}) + \int d\mathbf{r}' u_{DD}(\mathbf{r} - \mathbf{r}')\rho_D(\mathbf{r}') + \int d\mathbf{r}' u_{DP}(\mathbf{r} - \mathbf{r}')\rho_P(\mathbf{r}') \\
&\quad + \frac{1}{2}w(\rho_D(\mathbf{r}) + \rho_P(\mathbf{r}))^2, \\
\frac{\delta S}{\delta \varphi_D(\mathbf{r})} &= -i\rho_D(\mathbf{r}) - M \frac{\delta \ln Q}{\delta \varphi_D(\mathbf{r})}, \\
\frac{\delta S}{\delta \rho_P(\mathbf{r})} &= -i\varphi_P(\mathbf{r}) + \int d\mathbf{r}' u_{PP}(\mathbf{r} - \mathbf{r}')\rho_P(\mathbf{r}') + \int d\mathbf{r}' u_{DP}(\mathbf{r} - \mathbf{r}')\rho_D(\mathbf{r}') \\
&\quad + \frac{1}{2}w(\rho_D(\mathbf{r}) + \rho_P(\mathbf{r}))^2, \\
\frac{\delta S}{\delta \varphi_P(\mathbf{r})} &= -i\rho_P(\mathbf{r}) - P \frac{\delta \ln W}{\delta \varphi_P(\mathbf{r})},
\end{aligned} \tag{2.57}$$

and the second order derivatives are:

$$\begin{aligned}
\frac{\delta^2 S}{\delta \rho_D(\mathbf{r})\delta \rho_D(\mathbf{r}')} &= u_{DD}(\mathbf{r} - \mathbf{r}') + w(\rho_D(\mathbf{r}) + \rho_P(\mathbf{r}))^2\delta(\mathbf{r} - \mathbf{r}'), \\
\frac{\delta^2 S}{\delta \rho_P(\mathbf{r})\delta \rho_P(\mathbf{r}')} &= u_{PP}(\mathbf{r} - \mathbf{r}') + w(\rho_D(\mathbf{r}) + \rho_P(\mathbf{r}))^2\delta(\mathbf{r} - \mathbf{r}'), \\
\frac{\delta^2 S}{\delta \rho_D(\mathbf{r})\delta \rho_P(\mathbf{r}')} &= u_{DP}(\mathbf{r} - \mathbf{r}') + w(\rho_D(\mathbf{r}) + \rho_P(\mathbf{r}))^2\delta(\mathbf{r} - \mathbf{r}'), \\
\frac{\delta^2 S}{\delta \rho_D(\mathbf{r})\delta \varphi_D(\mathbf{r}')} &= -i, \\
\frac{\delta^2 S}{\delta \rho_P(\mathbf{r})\delta \varphi_P(\mathbf{r}')} &= -i, \\
\frac{\delta^2 S}{\delta \varphi_D(\mathbf{r})\delta \varphi_D(\mathbf{r}')} &= -M \frac{\delta^2 \ln Q}{\delta \varphi_D(\mathbf{r})\delta \varphi_D(\mathbf{r}')}, \\
\frac{\delta^2 S}{\delta \varphi_P(\mathbf{r})\delta \varphi_P(\mathbf{r}')} &= -P \frac{\delta^2 \ln W}{\delta \varphi_P(\mathbf{r})\delta \varphi_P(\mathbf{r}')}.
\end{aligned} \tag{2.58}$$

In the RPA analysis of section 2.4.1, these derivatives are to be computed at the mean-field solution:

$$\begin{aligned}
\rho_D(\mathbf{r}) &= c_D, \\
\varphi_D(\mathbf{r}) &= \phi_D, \\
\rho_P(\mathbf{r}) &= c_P, \\
\varphi_P(\mathbf{r}) &= \phi_P,
\end{aligned} \tag{2.59}$$

which we denote by the \* subscript in what follows. Evaluating the five first equations in eq. (2.58) at the mean field saddle-point is easily done, whereas it requires further computations for the two last ones. We obtain:

$$\begin{aligned}
\left. \frac{\delta^2 S}{\delta \varphi_P(\mathbf{r})\delta \varphi_P(\mathbf{r}')} \right|_* &= c_P \left( \delta(\mathbf{r} - \mathbf{r}') - \frac{1}{V} \right), \\
\left. \frac{\delta^2 S}{\delta \varphi_D(\mathbf{r})\delta \varphi_D(\mathbf{r}')} \right|_* &= c_D (S_N(\mathbf{r} - \mathbf{r}') - c_D),
\end{aligned} \tag{2.60}$$

where  $S_N(\mathbf{r} - \mathbf{r}')$  is the structure function of the polymer chain. Its expression follows directly from taking the second order derivative in eq. (2.56):

$$\begin{aligned}
c_D S_N(\mathbf{r} - \mathbf{r}') &= \left\langle \int_0^N ds ds' \delta(\mathbf{r} - \mathbf{r}(s)) \delta(\mathbf{r}' - \mathbf{r}(s')) \right\rangle \\
&= \frac{1}{Q_0} \int_0^N ds ds' \int D[\mathbf{r}(t)] \delta(\mathbf{r} - \mathbf{r}(s)) \delta(\mathbf{r}' - \mathbf{r}(s')) \exp(-U_0[\mathbf{r}]) \\
&= \frac{1}{Q_0} \int_0^N ds ds' \int d\mathbf{r}_N d\mathbf{r}_0 \langle \mathbf{r}_N | e^{-(N-s)\hat{U}_0} | \mathbf{r}' \rangle \langle \mathbf{r}' | e^{-(s'-s)\hat{U}_0} | \mathbf{r} \rangle \langle \mathbf{r} | e^{-s\hat{U}_0} | \mathbf{r}_0 \rangle,
\end{aligned} \tag{2.61}$$

where we have introduced the chain propagator:

$$\begin{aligned}
q(\mathbf{r}'s; \mathbf{r}0) &= \int_{\mathbf{r}(0)=\mathbf{r}}^{\mathbf{r}(s)=\mathbf{r}'} D[\mathbf{r}(t)] \exp(-U_0[\mathbf{r}]) \\
&= \langle \mathbf{r}' | e^{-s\hat{U}_0} | \mathbf{r} \rangle \\
&= \langle \mathbf{r}' | \psi(s) \rangle, \quad |\psi(0)\rangle = |\mathbf{r}\rangle.
\end{aligned} \tag{2.62}$$

A proper choice of normalization results in  $|\psi(s)\rangle$  to be the probability distribution function for the last monomer. Consequently, we have

$$\begin{aligned}
\int d\mathbf{r}' q(\mathbf{r}'s; \mathbf{r}0) &= \int d\mathbf{r}' \langle \mathbf{r}' | \psi(s) \rangle = 1, \\
\int d\mathbf{r} d\mathbf{r}' q(\mathbf{r}'s; \mathbf{r}0) &= \int d\mathbf{r} d\mathbf{r}' \langle \mathbf{r}' | \psi(s) \rangle = V.
\end{aligned} \tag{2.63}$$

Eventually, the structure function of the chain has the expression:

$$S_N(\mathbf{r}' - \mathbf{r}) = \frac{1}{N} \int_0^N ds ds' q(\mathbf{r}'s'; \mathbf{r}s). \tag{2.64}$$

Let us emphasize that this result is valid only because  $S_N(\mathbf{r}' - \mathbf{r})$  can be expressed in eq. (2.61) as a matrix product of the three subchain propagators  $q(\mathbf{r}_N N; \mathbf{r}'s')$ ,  $q(\mathbf{r}'s'; \mathbf{r}s)$  and  $q(\mathbf{r}s; \mathbf{r}_0 0)$ . More generally, the chain propagator must obey a Chapman-Kolmogorov equation. For a Gaussian chain it is [53, 55]:

$$\frac{\partial q}{\partial s}(\mathbf{r}s; \mathbf{r}'s') = \frac{a^2}{6} \Delta_{\mathbf{r}} q(\mathbf{r}s; \mathbf{r}'s') - V(\mathbf{r}) q(\mathbf{r}s; \mathbf{r}'s'), \tag{2.65}$$

where  $\Delta_{\mathbf{r}}$  is the Laplacian operator and  $V(\mathbf{r})$  is an external field. It should be noted that the r.h.s. is diagonal in Fourier basis. In the case of the free Gaussian chain,  $V(\mathbf{r}) = 0$ , one obtains for the chain propagator:

$$\begin{aligned}
q(\mathbf{k}, s' - s) &= \langle \mathbf{k} | e^{-\frac{a^2 |s'-s| k^2}{6}} | \mathbf{k} \rangle \\
&= \exp\left(-\frac{a^2 k^2 |s' - s|}{6}\right).
\end{aligned} \tag{2.66}$$

Plugging this result back into eq. (2.64) gives the structure function of the Gaussian chain:

$$S_N(\mathbf{k}) = ND(k^2 R_g^2), \quad (2.67)$$

where  $R_g^2 = a^2 N/6$  is the radius of gyration of the chain and  $D(x) = 2/x^2(x + \exp(-x) - 1)$  is the Debye function.

## 2.B Detection of the coil-globule-crystal transitions

In order to detect the coil-globule transition, we monitored the quantity:

$$q = \frac{\log R_g}{\log N}, \quad (2.68)$$

where  $R_g$  is the radius of gyration of the polymer. For a self-avoiding polymer with scaling law  $R_g \sim bN^\nu$ ,  $q = \nu + cst/\log N$ . In a good solvent, the polymer is swollen with  $\nu = 0.588$  whereas in a bad solvent it collapses with  $\nu = 1/3$ . Thus  $q$  varies like  $\nu$ .

In order to detect the coil-crystalline transition, and following [93], we first defined the quantity

$$n_\alpha = \sum |\mathbf{u}_i \cdot \mathbf{e}_\alpha|, \quad (2.69)$$

in which  $i$  runs over all the bonds of the polymer,  $\mathbf{u}_i$  is the unit vector having the same direction as the bond  $i$  and  $\mathbf{e}_\alpha$  is the unit vector of the corresponding  $\alpha$ -axis ( $\alpha = x, y, z$ ). We chose to monitor the quantity:

$$p = 1 - \frac{n_{min}}{n_{max}}, \quad (2.70)$$

where  $n_{min} = \min_\alpha(n_\alpha)$  and  $n_{max} = \max_\alpha(n_\alpha)$ . It is clear that for an isotropic configuration,  $n_x = n_y = n_z$  resulting in  $p = 0$ . Conversely, for a configuration stretched in one direction, say along the x-axis,  $n_x = 1$  and  $n_y = n_z = 0$ , resulting in  $p = 1$ . Thus  $p$  effectively measures the directional order of the polymer.

We then performed a thermodynamical average over uncorrelated configurations sampled from BD trajectories to obtain  $\langle q \rangle$  and  $\langle p \rangle$ . We carried out this procedure for different values of the DNA-protein interaction, represented by the strength  $\varepsilon$  of the corresponding Lennard-Jones interaction and plotted the values of  $\langle q \rangle$  and  $\langle p \rangle$  as a function of  $\varepsilon$  (fig. 2.15).

In order to identify the transition point, we performed a fit with a sigmoid function:

$$s(x) = \frac{1}{1 + e^{-\lambda x}}. \quad (2.71)$$

The inflexion point,  $x^* = 0$ , was taken to be the transition point. Carrying out this procedure for different values of  $l_p$  gave the phase diagram from fig. 2.13b.

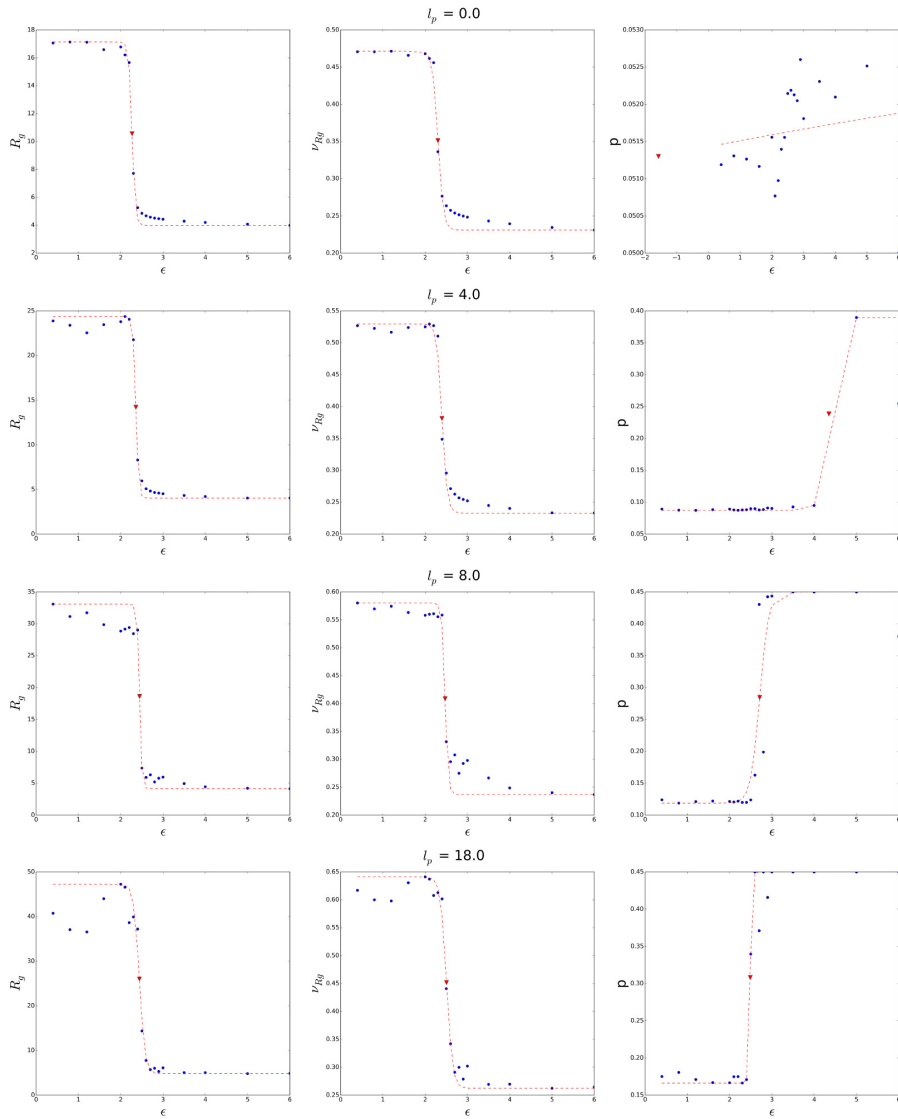


**Figure 2.15** – Collapse of a DNA polymer interacting with binding proteins through a Lennard-Jones potential with strength  $\epsilon$ , for different persistence length  $l_p$ . For each  $\epsilon$  the average values  $\langle R_g \rangle$ ,  $\langle q \rangle \simeq v_{R_g}$  and  $\langle p \rangle$  are computed from BD simulations. A fit with a sigmoid function gives access to the coil-globule transition (for  $R_g$  and  $q$ ) and the globule-crystal or coil-crystal transition (for  $p$ ).



## Chapter 3

# A side-study: computation of the structure function of a worm-like chain

In chapter 2, we have seen that the structure function of a polymer is a quantity that arises in polymer field theories, and in particular in the Random Phase Approximation (RPA). Although this object has an analytical closed-form for a Gaussian chain, it is not the case for a worm-like chain (WLC). However the chromosome is a rigid biopolymer better described by the latter model. Therefore, the RPA analysis in chapter 2 has motivated additional work to compute the structure function of polymer chains with bending rigidity.

In the present chapter, we consider a discrete worm-like chain polymer model. We first introduce the pair correlation function, which is the central quantity required to compute the structure function. We will show that the pair correlation function can be expressed exactly as a power of a transfer matrix with complex entries. We then apply our result to the computation of the structure function for a worm-like chain and compare it to the values obtained with Monte-Carlo simulations, as well as with other existing methods of the literature.

### 3.1 Relevance of the structure function in polymer field theories

In polymer physics, the structure function is a central quantity which characterizes the density fluctuations at thermal equilibrium. More accurately, it is related to the two points correlation function for the polymer density:

$$cS_N(\mathbf{r}) = \langle \rho(\mathbf{r} + \mathbf{r}')\rho(\mathbf{r}') \rangle, \quad (3.1)$$

where  $N$  is the length of the polymer,  $\rho(\mathbf{r})$  is the concentration of polymer and  $c = N/V$  is the mean-field concentration in a cavity with volume  $V$ .

The structure function has key applications in self-consistent field theories of polymer mixtures, including the RPA. Briefly, the RPA looks for Fourier modes  $\mathbf{k}$  driving critical fluctuations (see for instance [53, 55]). The specific shape of the structure function can induce instabilities for non zero wave number  $\mathbf{k}$ , which is in general the signature of a microphase separation.

The analytical expression of the structure function for a Gaussian polymer is known to be the Debye function [53, 54, 77]. Yet, many polymers cannot be considered as such. The example of biopolymers

like DNA, actin and microtubules is a case in point. It is then necessary to take into account a persistence length  $l_p$  which characterizes the distance over which a polymer loses the memory of its orientation. This is the realm of semi-flexible polymers. In a simplified picture, such a polymer can be discretized as a sequence of monomers with inextensible bonds, free to rotate from one to the next. A common way to deal with them is to use the so-called Kratky-Porod model [59], or worm-like chain (WLC), which introduces a penalty proportional to a bending modulus  $\kappa$  when two consecutive bonds are not aligned.

Despite the long interest in computing the structure function for semi-flexible polymers, there is no exact analytical closed-form available. Nonetheless, several solutions have been proposed. Some of them rely on analytical approximates [62, 86, 87, 106], while others provide numerical methods to compute the desired quantity [88–90]. After presenting our method, we will discuss some of them in the sequel.

## 3.2 Expression of the pair correlation function

### 3.2.1 Pair correlation and structure function

Let us start from the discrete WLC presented in section 1.3, with  $N + 1$  monomers. The density of monomers at position  $\mathbf{r}$  is given by:

$$\rho(\mathbf{r}) = \sum_{n=0}^N \delta(\mathbf{r} - \mathbf{r}_n), \quad (3.2)$$

where as usual,  $\mathbf{r}_n$  is the vector of spatial coordinates for monomer  $n$ . If we substitute this expression in eq. (3.1), and integrate the translational degree of freedom, then we obtain:

$$S_N(\mathbf{r}) = \frac{1}{N} \sum_{m \neq n}^N \langle \delta(\mathbf{r} - (\mathbf{r}_n - \mathbf{r}_m)) \rangle, \quad (3.3)$$

in which the terms such that  $n = m$  have been removed when going from a continuous to a discrete chain. Let us now introduce the pair correlation function:

$$g_N(\mathbf{r}) = \langle \delta(\mathbf{r} - (\mathbf{r}_N - \mathbf{r}_0)) \rangle, \quad (3.4)$$

with Fourier transform:

$$\begin{aligned} g_N(\mathbf{k}) &= \langle \exp(i\mathbf{k} \cdot (\mathbf{r}_N - \mathbf{r}_0)) \rangle \\ &= \frac{1}{Q_N} \int \prod_{j=1}^N d^2\mathbf{u}_j \exp \left[ -\kappa \sum_{j=1}^{N-1} (1 - \mathbf{u}_j \cdot \mathbf{u}_{j+1}) + i\mathbf{k} \cdot \sum_{j=1}^N \mathbf{u}_j \right]. \end{aligned} \quad (3.5)$$

From eq. (3.3), we see that the Fourier transform of the structure function,  $S_N(k)$ , can be expressed as:

$$S_N(k) = \frac{1}{N} \sum_{n \neq m}^N g_{|n-m|}(k), \quad (3.6)$$

Note that at  $k = 0$ , we retrieve  $S_N(0) = N + 1$  which is the number of scattering units, *i.e.* monomers of the chain. It is clear that the central quantity to compute is the pair correlation function, but the integral form from eq. (3.5) is out of scope for practical use when  $N$  grows to large values.

### 3.2.2 Expression in terms of transfer matrices

We extend the transfer matrix defined in eq. (1.16) on page 15 to Fourier modes,  $\mathbf{k} \neq 0$ :

$$T(\mathbf{u} | \mathbf{u}') = \exp\left(-\kappa(1 - \mathbf{u} \cdot \mathbf{u}') + i\mathbf{k} \cdot \frac{\mathbf{u} + \mathbf{u}'}{2}\right) \quad (3.7)$$

and rewrite eq. (3.5) as

$$g_N(\mathbf{k}) = \frac{1}{Q_N} \int \left[ \prod_{j=1}^N d^2\mathbf{u}_j T(\mathbf{u}_j | \mathbf{u}_{j-1}) \right] \exp\left(i\mathbf{k} \cdot \frac{\mathbf{u}_1 + \mathbf{u}_N}{2}\right) \quad (3.8)$$

For  $k = 0$ ,  $T$  is real and symmetric, yet for  $k \neq 0$ , the transfer matrix is still symmetric but with complex matrix elements. Note that this kind of transfer matrix had been introduced earlier in the literature, but with  $i\mathbf{k} = f$  real, in order to compute the relative extension of a WLC polymer when a force is applied at both ends [107, 108]. In what follows, we will keep the same notation for  $T$  but it should be kept in mind that it implicitly depends on the wave number  $k$ .

The integration in eq. (3.7) is carried out over the angular variables  $\varphi$  and  $\theta$  in the spherical coordinates system attached to the z-axis (see eq. (1.36) on page 22). However, we can formally integrate out the  $\varphi$  variables. Hence we obtain a reduced transfer matrix  $\hat{T}$ , with matrix elements:

$$\hat{T}(\theta | \theta') = I_0(\kappa \sin \theta \sin \theta') \exp\left(-\kappa(1 - \cos \theta \cos \theta') + ik \frac{\cos \theta + \cos \theta'}{2}\right), \quad (3.9)$$

where

$$I_0(z) = \int \frac{d\varphi}{2\pi} \exp(z \cos \varphi) \quad (3.10)$$

is the modified Bessel function of rank 0. The evaluation of  $I_0(z)$  is performed numerically, for which several routines are available [64]. Besides, one can still use polynomial approximations to save up computational time. Using the reduced transfer matrix, the pair correlation function from eq. (3.8) now reads:

$$g_N(\mathbf{k}) = \frac{1}{Q_N} \int_0^\pi d\theta \sin \theta \Phi(\theta) \hat{T}^{N-1} \Phi(\theta), \quad (3.11)$$

where we defined  $\Phi(\theta) = \exp(ik \cos \theta/2)$ . Note that our notation for matrix-vector product implies that the correct measure,  $d\theta \sin \theta$ , is taken in the integration. In particular, the product of  $\hat{T}$  with the function  $\Phi$  reads:

$$\hat{T}\Phi(\theta) = \int_0^\pi d\theta' \sin \theta' \hat{T}(\theta | \theta') \Phi(\theta'). \quad (3.12)$$

In conclusion, the pair correlation function has been expressed as an integral over one single angular variable  $\theta$ . Besides, it only depends on the norm  $k$  of the Fourier mode considered. As can be expected at that point, a calculation scheme of  $g_N(k)$  will consist in expanding  $\Phi$  on the basis of eigenfunctions of  $\hat{T}$ . However it is worth pointing out that  $\hat{T}$  is not hermitian in general, except when  $k = 0$  for which it is real and symmetric. Therefore in the general case, the eigenfunctions  $Y_n(\theta)$  of  $\hat{T}$  are not orthogonal, *i.e.*  $\int d\theta \sin \theta Y_n(\theta) Y_{n'}(\theta) \neq \delta_{n,n'}$ . We stress that the final form in eq. (3.11) is exact and can be formally rewritten as:

$$g_N(\mathbf{k}) = \frac{\langle \Phi | \hat{T}^{N-1} | \Phi \rangle_k}{\langle \Phi | \hat{T}^{N-1} | \Phi \rangle_{k=0}}. \quad (3.13)$$

### 3.3 Application to the computation of the structure function

In this section, we introduce our method to compute the pair correlation function  $g_N(k)$  and apply it to compute the structure function of a discrete WLC with  $N + 1 = 200$  monomers. Then we compare our results to existing methods.

For computational efficiency, we have used the following expression for the structure function:

$$S_N(k) = \frac{2}{N} \sum_{n=1}^N (N - n + 1) g_n(k), \quad (3.14)$$

which is equivalent to eq. (3.6), but reduces the computational complexity from  $O(N^2)$  to  $O(N)$ .

#### 3.3.1 Transfer matrix method

As announced, we devised a numerical procedure based on eq. (3.13) to compute  $g_N(k)$ . For convenience, we have chosen to make the change of variable  $\Upsilon = -\cos \theta$ , with the uniform integration measure on  $[-1, 1]$ . We also chose a discretization of size  $M$ , through the regular subdivision:

$$\Upsilon_m = -1 + m \frac{2}{M} \text{ with } m = 0, \dots, M. \quad (3.15)$$

Using this discretization, the matrix elements of the reduced transfer matrix  $\hat{T}$  read:

$$t_{mn} = \exp \left( -\kappa (1 - \Upsilon_m \Upsilon_n) - ik \frac{\Upsilon_m + \Upsilon_n}{2} \right) I_0 \left( \kappa \sqrt{1 - \Upsilon_m^2} \sqrt{1 - \Upsilon_n^2} \right), \quad (3.16)$$

where  $I_0(z)$  is the modified Bessel function of rank 0. Similarly, the discrete version of the function  $\Phi$  is a vector with coordinates:

$$\phi_m = \exp \left( -ik \frac{\Upsilon_m}{2} \right). \quad (3.17)$$

For each value of the wave number  $k$ , the discrete matrix  $\hat{T}$  can be diagonalized, namely  $t_{mn} = \sum_j p_{mj} \lambda_j p_{jn}^{-1}$ , where  $\lambda_0 > \lambda_1 > \dots > \lambda_{M-1}$  are the eigenvalues and  $p_{ij}$  is the matrix of coordinates for the diagonal basis. Once again, let us emphasize that both the eigenvalues  $\lambda_i$  and the matrix  $p_{ij}$  depend on the wave number  $k$ . The pair correlation in eq. (3.13) is then finally expressed as the ratio of two sums:

$$g_N(k) = \frac{\left[ \phi_m p_{mj} \lambda_j^{N-1} p_{jn}^{-1} \phi_n \right] (k)}{\left[ \phi_m p_{mj} \lambda_j^{N-1} p_{jn}^{-1} \phi_n \right] (0)}, \quad (3.18)$$

where the summation on indices  $j, m, n$  is implied.

This procedure provides a systematic way to compute the pair correlation function of a discrete worm-like chain for any value of the rigidity parameter  $\kappa$  (fig. 3.1). The pair correlation function obtained correctly interpolates between the Gaussian chain, for which  $g_N(k) = \exp(-k^2 R_g^2)$ , and the rod-like chain, for which  $g_N(k) = \sin(kN)/(kN)$ .

In practice, the numerical complexity lies in the fact that for any wave number  $k$ , we need to diagonalize a  $M \times M$  complex square matrix. As the rigidity of the chain increases (large  $\kappa$ ), a discretization with a larger  $M$  is required, resulting in an increased complexity. For  $\kappa \gg 1$ ,  $T(\theta | \theta')$  is sharply peaked around the straight bond configuration  $\theta = \theta'$ , with a maximum at  $\theta = \theta' = 0$  ( $\pi$ ). As  $T(\theta | \theta')$  becomes localized near  $\theta = \theta'$ , replacing the integral in eq. (3.11) by a Riemann sum with a regular subdivision

such as in eq. (3.15) is not adapted, and  $M$  needs to be increased. Therefore, for very rigid chain, the transfer matrix method is not *ad hoc* since the complexity for diagonalizing a matrix of size  $M$  grows like  $O(M^3)$ . As can be expected, the accuracy reached for the computation of the structure function  $S_N(k)$  will depend on the value of  $M$  (fig. 3.2). In other words, for fixed  $M$ , the quality of our prediction falls off as the rigidity of the chain increases, especially in the small  $k$  regime. On the basis of this analysis, we used a discretization  $M = 1000$  in further applications.

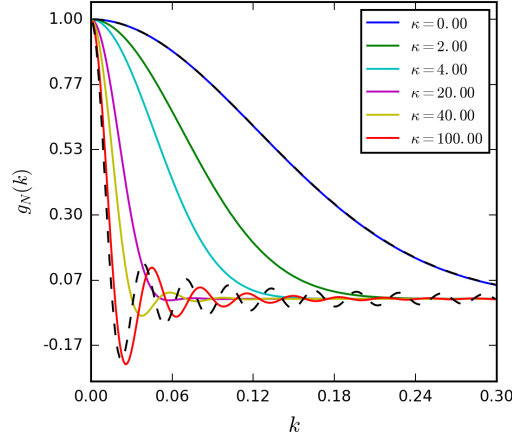


**Figure 3.1** – Computation of the pair correlation function for different values  $\kappa$ . The dotted lines are the Gaussian,  $\exp(-k^2 N/6)$ , and the rod,  $\sin(kN)/kN$  pair correlation functions. We considered a chain of length  $N = 200$  and used a discretization with  $M = 1000$ .

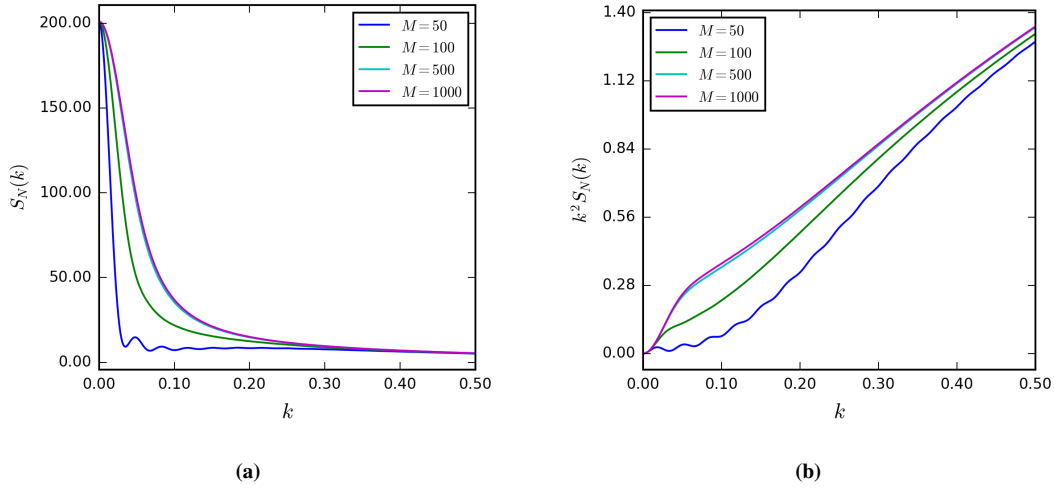


**Figure 3.2** – Transfer matrix computation of the structure function for  $M = 50, 100, 500$  and  $1000$ . We considered a chain of length  $N = 200$  with a bending rigidity  $\kappa = 20$ . (a)  $S_N(k)$  as a function of  $k$ . (b)  $k^2 S_N(k)$  as a function of  $k$  (Kratky plot).

### 3.3.2 Comparison with other methods

As a reference method, we computed the structure function of a WLC using Monte-Carlo simulations. We used a standard Metropolis-Hasting Monte-Carlo algorithm to sample configurations of a discrete WLC in the Boltzmann ensemble. A configuration was defined by the  $N + 1$  coordinates of the monomers  $\{\mathbf{r}_i\}$ . At each iteration, a new configuration  $\{\mathbf{r}'_i\}$  was generated from the previous one using pivot and crankshaft moves. The probability to accept the new configuration was taken as usual to be

$$\Pr(\{\mathbf{r}_i\} \rightarrow \{\mathbf{r}'_i\}) = \min\left(1, \exp\left[-\beta U_b(\{\mathbf{r}'_i\}) - \beta U_b(\{\mathbf{r}_i\})\right]\right) \quad (3.19)$$

where  $\beta U_b$  is defined in eq. (1.14) on page 14. As is well known, the stationary distribution resulting from this Markov process samples the Boltzmann equilibrium. After an initial run intended to reach the Boltzmann equilibrium, we sampled 10 000 configurations every 500 iterations. For  $N + 1 = 200$ , the autocorrelation time appeared to be smaller than the time between two such configurations. Using the ergodicity property of Markov processes, we computed thermal averages by taking an average over the sampled configurations. In particular, the pair correlation function was computed using

$$g_N(k) = \langle \cos(\mathbf{k} \cdot (\mathbf{r}_N - \mathbf{r}_0)) \rangle \quad (3.20)$$

which is equivalent to eq. (3.5) because  $g_N(k)$  is real. As can be seen in fig. 3.3, the structure function obtained with the transfer matrix method and with Monte Carlo simulations are in good agreement.

Other methods to compute the structure function of a WLC can be found in the literature. Two good analytical expressions are available. Khodolenko [87] used an ansatz for the structure factor of a WLC based on a Dirac propagator equation. By design, this model smoothly interpolates between the Gaussian and rod-like chain limits. Although the formula proposed by Kholodenko seems like a good approximate for the pair correlation function, it is not the actual solution for the WLC model. Furthermore, both the physical interpretation of the parameters and the accuracy for intermediate stiffness are not clear. Bhattacharjee and co-workers [62] enforced the constraint on the bond length,  $|\mathbf{u}_i^2 - 1|$ , through a mean-field approximation and relaxed the integration on the unit sphere to the full volume (see section 1.3.4.2 on page 17), and obtained an analytical expression for the pair correlation function. Yet, its accuracy might be called into question for moderate stiffness, due to uncertain contributions of local chain length fluctuations which are not taken into account at the mean-field level. Other methods have been proposed, giving a numerical approximate of the pair correlation function of a WLC. Spakowitz [89] and co-workers computed  $g_N(k)$  as an infinite continued fraction, which must be truncated for numerical evaluation. Although the numerical implementation of the continued fraction seems straightforward, further treatments are required to obtain the structure function, namely an inverse Laplace transform. Zhang and co-workers [90] used the Chapman-Kolmogorov equation satisfied by the Green function  $G(\mathbf{k}, \mathbf{u}; s)$  of a WLC (see appendix 1.B). Physically,  $G(\mathbf{k}, \mathbf{u}; s)$  is the spatial Fourier transform of  $G(\mathbf{r}, \mathbf{u}; s)$ , which is the joint probability distribution that a chain starting at the origin ends up at position  $\mathbf{r}$  with orientation  $\mathbf{u}$ . The associated numerical procedure makes use first of an expansion of  $G(\mathbf{k}, \mathbf{u}; s)$  in terms of the spherical harmonics functions. This method shares similarities with our own approach.

We chose to compare our results (at  $M = 1000$ ) with the analytical forms of Khodolenko and Bhattacharjee (see appendix 3.A), using the Monte-Carlo result as a reference. We observe that the transfer matrix method performs better than the analytical forms of Kholodenko and Bhattacharjee for moderate stiffness (fig. 3.3). Conversely, for strong stiffness, the transfer matrix method would require a higher discretization  $M$ , and therefore it performs less well than the analytical expressions. Note that this could have been expected since both Kholodenko and Bhattacharjee forms are derived from approximations whose validity improves for stiff chains.

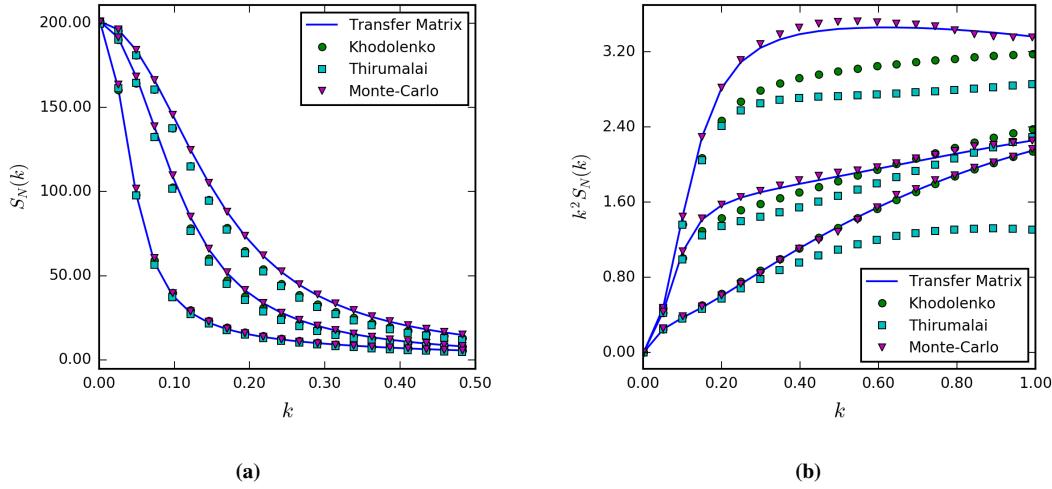


**Figure 3.3** – Comparison of the structure function obtained with different methods, for  $\kappa = 2.00, 4.00, 20.00$ . We considered a chain of length  $N = 200$ . (a)  $S_N(k)$  as a function of  $k$ . (b)  $k^2 S_N(k)$  as a function of  $k$  (Kratky plot).

### 3.4 Discussion

In conclusion, we have presented a method to compute the structure function of a WLC, in Fourier space. The method relies on the eigenvalue decomposition of a transfer matrix with complex entries, which is performed for each value of the wave number  $k$ . Specifically, the pair correlation function, which is expressed as a power of the transfer matrix  $T$ , can be straightforwardly computed with this method.

Our method appeared to be in good agreement with a computation of the structure function obtained from Monte-Carlo simulations of a WLC. In addition, we have compared it with two of the existing analytical approximations that can be found in the literature. We stress that the structure function computed with these methods is not the WLC structure function, because the authors model the polymer bending rigidity using models which are approximation of the WLC model. This might have lead to discrepancies when comparing with our method because the bending rigidity parameter in these models is not exactly the WLC persistence length, although we followed the interpretation given by the authors of these studies. We found that our transfer matrix method performs better for moderate stiffness of the WLC. To the contrary, for large persistence length our method performs less well. This is due to a too sparse discretization of the transfer matrix  $T$ , resulting in a discrepancy between discrete sums and continuous integrals. A practical way to circumvent this issue would be to consider a finer discretization of the transfer matrix  $T$  (larger  $M$ ). This is of course possible, but it should be kept in mind, that the time required to compute the structure function at wave number  $k$ ,  $S_N(k)$ , scales as  $N$  times the time required to diagonalize  $T$ , which is in  $O(M^3)$ .



# Appendix

## 3.A Other methods to compute the pair correlation function of a worm-like chain

### Kholodenko's method

In eq. (11) from [87], the pair correlation function is computed from the expression:

$$g_N(\mathbf{k}) = \begin{cases} \frac{1}{\sqrt{1 - (k/m)^2}} \frac{\sinh(\sqrt{1 - (k/m)^2} mN)}{\sinh(mN)} & \text{if } k < m \\ \frac{1}{\sqrt{(k/m)^2 - 1}} \frac{\sin(\sqrt{(k/m)^2 - 1} mN)}{\sinh(mN)} & \text{if } k > m \end{cases} \quad (3.21)$$

where  $m = 3/(2l_p)$ . This ansatz is obtained from the analogy of the Hamiltonians between Dirac's fermions and semi-flexible polymers.

### Bhattacharjee's method

In eq. (15) from [62], the pair correlation function is computed from the expression:

$$g_N(\mathbf{r}) = \mathcal{N} \left[ 1 - (r/N)^2 \right]^{-9/2} \exp\left( -\frac{3N}{4l_p} \frac{1}{1 - (r/N)^2} \right) \quad (3.22)$$

where  $\mathcal{N}$  is a normalization constant.



## Chapter 4

# Model for the role of nucleoid-associated proteins in regulating transcription

In this chapter, we propose a model providing a direct connection between regulation of the transcription and chromosome architecture.

In bacteria, an example of structuring proteins is the so-called family of nucleoid-associated proteins (NAPs). Hence we will build our analysis on what is known today about these proteins. We first start by a review of the literature on the four main NAPs in *Escherichia coli* bacteria which are: H-NS, FIS, HU and IHF. We will describe the architectural changes induced on the chromosome by these proteins, and what is known of their consequences on genetic expression. In particular, H-NS leads to the formation of DNA filaments and hairpin loops which prevent RNA polymerase binding. Several studies have conjectured that small H-NS/DNA hairpin loops can be unstable or easily disrupted by perturbations, such as the binding of more dedicated transcription factors. Hence this constitutes the basis for a transcriptional switch, which motivates an investigation of the underlying physical mechanism.

Second, we will figure out what is the relevant genomic scale to model the structuring effect of NAPs on the chromosome. To serve this purpose, we will use data from ChIP-seq experiments. We will show that the distribution of H-NS and FIS binding sites on the *E. coli* genome cannot be well modeled by a Poisson stochastic point process where the realization of stochastic events in time corresponds to the insertion of binding sites on the genome. In particular, we will show that deviations from this model occur at short genomic distances, hence giving a likely scale at which evolutionary pressure has been exerted.

Finally, we will explore in more details the formation of DNA hairpin loops under the effect of H-NS. We will show that in order to form stable hairpin loops, binding regions must have a minimum length. This result is first derived using a simple polymer model with implicit interactions, and then confirmed using Brownian dynamics simulations with explicit and divalent proteins. Then we elaborate on possible implications for a regulatory mechanism relying on the disruption of these structures by other proteins such as FIS.

## 4.1 Introduction to nucleoid-associated proteins (NAPs)

### 4.1.1 What are NAPs?

In eukaryotic cells, histones provide a first and significant level of organization of the chromosome. Since bacteria lack histones, the chromosome is not organized into nucleosomes and the relevant description of the chromosome is the naked fiber of diameter 2.5 nm [13]. However, proteins playing a structural role like histones exist. With no surprise, they are called histone-like proteins, or nucleoid-associated proteins (NAPs), and are well known structuring proteins. In *Escherichia coli*, the NAPs family comprises 12 proteins [32], including H-NS, FIS, IHF, HU and StpA (a close analog of H-NS). The stationary phase transcription factor DPS is to be mentioned too, although it is present in significant concentrations only during the stationary phase or in response to stress.

The presence of NAPs is a universal feature among bacteria. In particular, there are found in many *Salmonella* species, like *S. typhimurium* [109]. In other bacteria species, NAPs are not exactly the same as in *Escherichia coli*, but often functional and structural analogs can be found. For instance in *Bacillus subtilis*, FIS is present while H-NS is replaced by the protein Rok, which has a similar structure despite the absence of sequence homology. In *Deinococcus radiodurans*, a radiation-resistant bacteria, H-NS and FIS are not found, but HU and DPS are present in the cell [26]. Unless otherwise stated, we discuss in the sequel the biology of the *E. coli* bacteria.

### 4.1.2 Architectural and regulatory role

Like histones in eukaryotes, NAPs contribute significantly to the compaction of the bacterial DNA. In *E. coli* the 1.5 mm bacterial DNA is folded dramatically to fit into the  $1 \mu\text{m}^3$  volume of the cell. More precisely, DNA is constrained to sit in a small region near the center of the cell [110]. It has been demonstrated that this is mainly due to H-NS, which induces the formation of approximately two clusters per chromosome, which constitute the bacterial nucleoid. It has been shown that Rok has a similar role in *B. subtilis* [111]. Consequently, H-NS is found inside the nucleoid, whereas FIS, IHF and HU are found mostly at its periphery [112, 113].

In general, regions of the chromosome which are trapped inside the nucleoid appear to be transcriptionally silent. Therefore, there is a connection between chromosome architecture and transcription, yet to be resolved. More generally, all NAPs were shown to have an effect on the transcription of a large number of genes. For instance, it is known that the presence of AT-rich regions upstream of gene promoters can dramatically increase transcription [114]. Incidentally, AT-tracks, which are DNA sequences consisting of the repetition of A and T nucleotides, are over-represented in the genome of *E. coli* [19]. Interestingly, H-NS, FIS and IHF bind preferentially to AT-rich regions [115], suggesting that the binding of NAPs to the chromosome is correlated with the role of AT-tracks in regulating the transcription.

NAPs have a strong influence on DNA architecture in the cell and are often called structuring proteins. Yet, it was shown that removing mRNA from *E. coli* bacteria had more impact on the topology and shape of the nucleoid than the removal of H-NS, FIS or IHF, suggesting that the prevalent role of NAPs is not only architectural but also regulatory [115].

In short, the ubiquitousness of NAPs in bacteria points toward a key role maintained throughout evolution. In particular, NAPs are the most abundant transcription factors in *E. coli* [116]. Thus their high concentrations and numerous binding sites scattered across the genome suggest that even today NAPs still play a prevalent regulatory role over other less abundant transcription factors. Presumably,

regulatory functions stem from architectural changes induced on the chromosome. Besides, they are commonly found in bacterial species, suggesting that they are the remnants of a long-lived evolution from a common ancestor. Altogether, these elements represent strong reasons which motivate a more profound understanding of the mechanism by which NAPs regulate gene expression.

### 4.1.3 Characterization *in vivo*

The concentration of NAPs depends on the growth phases of a cell population (fig. 4.1). H-NS concentration remains of the order of 20 000 copies/chromosome [116–118]. For this reason, it is often considered as the NAP of reference. With more than 75 000 copies/chromosome during the exponential growth phase, FIS is the NAP with the highest concentration in the exponential growth phase. Yet its concentration plummets to less than 100 copies/chromosome during the stationary phase [19, 116]. Similarly, the ratio of HU to H-NS is HU:H-NS=2.5 during the exponential growth phase and falls to approximately 1.0 during the stationary phase [110]. IHF concentration is low during exponential growth phase and sharply increases at the onset of the stationary phase [117]. Eventually, NAPs can be ranked according to their concentrations in different growth phases [119, 120]:

- FIS > HU > H-NS > IHF > DPS in the exponential phase;
- DPS > IHF > HU > H-NS > IHF in the stationary phase;

suggesting that bacterial physiology and NAPs concentrations are intimately connected.

Because of their relatively high concentrations and of the small size of bacterial cells, their observation with standard fluorescence microscopy is cumbersome [111]. Indeed, let us consider a bacterial cell with volume  $1 \mu\text{m}^3$ , and a NAP with 20 000 copies resulting in a number density  $c = 2.0 \times 10^4 \mu\text{m}^{-3}$ . The typical distance between two NAPs can be estimated to  $d \approx c^{-1/3} \approx 40 \text{ nm}$ , which is below the visible light wavelength. This issue, also well known as the sub-diffraction limit has been addressed with modern super-resolution techniques [74, 75].

What distinguishes NAPs from other transcription factors is not only their high copy number but also their large number of targets on the chromosome. Thus NAPs bind widely on the bacterial chromosome with a coverage of the order of one binding site for every hundred base pairs (1:100 bp) [111]. Moreover, although less than 10 % of the genome corresponds to non-coding DNA, approximately 50 % of each H-NS, FIS and IHF binding sites fall in the promoter regions, suggesting a strong regulatory role for the NAPs [115].

## 4.2 The Nucleoid-Associated Proteins of *E. coli* bacteria

### 4.2.1 The Histone-like Nucleoid Structuring protein (H-NS)

#### 4.2.1.1 DNA binding

H-NS is a small protein binding widely to DNA (17 % of the chromosome in *E. coli* [32]). Consequently, it was believed for long that H-NS could bind non-specifically to DNA [122, 123]. In fact, state-of-the-art high-throughput ChIP-seq experimental techniques have demonstrated that sites with a slightly increased affinity exist. Specifically, a 6 bp long binding motif has been identified [32] (fig. 4.2). This motif consists in an AT track, with a core of 3 consecutive nucleotides having an information content close to 2 bits of information (for the meaning of bits of information, see [124, 125]). The average number of 3-nucleotide

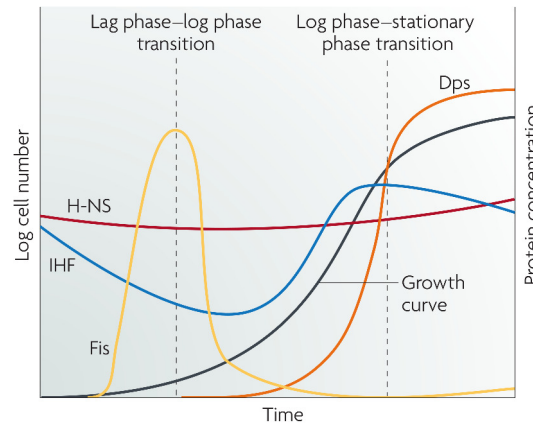


**Figure 4.1** – Evolution of NAPs concentrations across the different growth phases [121].

random draws before returning to an AT 3-nucleotide core is only 8, or equivalently 24 bp. Therefore, despite a bias for AT-rich sequences, it turns out that the binding motif might be quite commonly found throughout the genome, which makes the non-specific binding hypothesis legitimate in a coarse-grained approach.

A H-NS monomer is able to bind DNA with its C-terminal domain. It can also dimerize with another H-NS protein with its N-terminal domain [111]. Such an H-NS dimer is a divalent protein with two DNA-binding domains. Furthermore, H-NS can gain valency by polymerizing with other dimers. Contrary to other NAPs, H-NS does not seem to induce any bending of the DNA upon binding. Thus the old claim that H-NS binds preferentially to curved regions of the DNA might find its origin in the fact that AT-tracks are indeed more flexible. Alternatively, DNA regions presenting a hairpin-like conformation might represent good candidates for subsequent binding by H-NS, since in this case H-NS can bridge the two DNA segments without any enthalpic bending penalty.

Remarkably, H-NS dimers can induce the formation of rigid DNA-H-NS-DNA filaments (or bridges) [122, 123]. Such filaments can nucleate from an initial binding site with higher affinity and elongate in a zipper-like fashion. At moderate H-NS concentrations ( $>1:100$  bp), H-NS-bound DNA molecules display a characteristic structure with many filaments, usually flanked by DNA loops (fig. 4.3a). At larger concentrations, dense structures are observed, presumably due to the existence of complexes containing H-NS oligomers with a high polymerization index.

The mechanisms for the formation of DNA/H-NS bridges has remained elusive however. For instance, it is not clear how DNA binding and polymerization of H-NS dimers result in stable filaments. On one hand, a single molecule experiment demonstrated that two double-stranded DNA molecules previously coated with H-NS fail to make filaments, suggesting that dimerization alone is not sufficient to make filaments. Instead, H-NS dimers, tetramers and other oligomers would bind several DNA sites simultaneously [126]. On the other hand, the packing of DNA into the nucleoid by H-NS has been demonstrated to be highly deficient in mutants where H-NS could no longer polymerize, as evidenced by super-resolution fluorescence microscopy [111]. More accurately, H-NS condenses the bacterial chromosome in approximately two clusters with diameter close to 300 nm in wild-type cells, but these clusters disappear in mutant cells where H-NS cannot dimerize.

#### 4.2.1.2 Thermochemical considerations

As already mentioned, H-NS exists under the form of oligomers with different polymerization indices. *In vivo* studies demonstrated that it is a dimer at low concentration and a tetramer at high concentration [122]. Furthermore, single DNA molecule studies have shown that H-NS has a high off-rate from DNA,  $k^- \approx 1.5 \text{ s}^{-1}$ , suggesting that the DNA/H-NS bridges are fragile [126]. This can ease the dynamical re-organization of the genome architecture. The same authors also measured the binding free energy of a H-NS dimer bound to two DNA sites and found a value close to be  $11 k_B T$ , *i.e.* a binding free energy of  $\Delta^0 f \approx 5.5 k_B T$  per DNA-protein link.

#### 4.2.1.3 Regulatory function

We have seen that H-NS concentration is constant in first approximation, and that it may be considered as the NAP of reference. Structural and/or regulatory changes might result from variations in the concentration ratios of other NAPs relatively to H-NS. For example, the ratio HU:H-NS is 2.5 in the exponential growth phase whereas it is close to 1.0 in the stationary phase. It has been argued that HU counteracts the compaction of DNA induced by H-NS and that the balance between the action of the two NAPs have an important role in regulating the transcription [110].

H-NS over-expression in *E. coli* has radical effects: it stops the cell growth, and makes the cell enter a stationary state, even when induced in the middle of the exponential growth phase. In minimal media, it was even reported to kill the cell [112, 127]. More accurately, H-NS over-expression stops the production of RNA transcripts, and therefore protein synthesis. The resulting nucleoids displayed strong morphological signatures: very dense and compact. Therefore, H-NS is generally considered as a global transcription silencer, through DNA compaction.

In physiological conditions, H-NS represses the transcription of many unrelated and non-essential genes [32, 109, 111, 112, 115, 117, 122, 123]. We stress that H-NS is also involved in the regulation of the *rrn* operon encoding rRNAs, which are extremely abundant constituents of the ribosomes (essential for the cell).

In agreement with the results obtained when H-NS is over-expressed, it was shown that genes repressed by H-NS appear to be bound by H-NS and sequestered in clusters, whereas genes which are not regulated by H-NS do not localize in such clusters [111]. Consistently, a ChIP-seq study has shown that genes bound by H-NS are not bound by RNA polymerase (RNAP) and that their associated RNA transcripts have very low copy numbers in the cell [32]. In contrast, in mutants lacking H-NS, the same genes were significantly expressed and bound by RNAP. The study also confirmed that H-NS preferentially binds to AT-rich regions in agreement with previous claims [109, 118]. The majority of these AT-rich regions are sequences longer than 1000 bp which are significantly enriched in genes acquired by horizontal transfer. Smaller binding regions appeared to correspond essentially to sequences in the promoters of operons or genes. In short, the mechanism of gene repression by H-NS seems to rely on the co-localization of H-NS-bound genes in dense clusters which can not be accessed by RNAP. The global regulation of transcription by H-NS might encompass a transcriptional modulation (by mild repression) of the short promoter-rich binding regions, and complete silencing of large binding regions.

Most AT-rich regions correspond to xenogenic DNA acquired by lateral transfer (from bacterial viruses for example). From an evolutionary perspective, it has been argued that the primary role of H-NS could have been to act as a genome sentinel by silencing the expression of xenogenic DNA [109, 118]. Subsequently, sequences and transcription factors might have evolved independently and occasionally

produced mechanisms able to relieve H-NS-mediated repression. Thus, although H-NS could have acquired its prevalence in the bacterial kingdom because of its xenosilencing role, this system designed for defense might have been diverted from its original function in the course of evolution to serve other purposes, namely transcription regulation. An example is the *rrnB* operon which is repressed by H-NS through the formation of a hairpin loop but activated by FIS (fig. 4.3b).

Incidentally, an interesting candidate for a regulatory mechanism based on H-NS effect is the so-called RNAP-trapping mechanism by the *rrnB* promoter [115]. AFM experiments have demonstrated that upon binding the *rrnB* promoter, RNAP can be trapped in a hairpin loop at the extremity of a DNA/H-NS duplex [122]. This mechanism is thought to enable a fast response to external stimulus because RNAP does not need to be recruited anymore when the H-NS repression is relieved. In the case of the *rrnB* promoter, the stimuli corresponds to the binding of FIS in the promoter region. More generally, other TFs might be able to relieve the H-NS-mediated repression by disrupting the H-NS/DNA complex [109, 118, 123]. On a local scale, H-NS may act in concert with other proteins resulting in specific regulatory functions. The cooperative effect of H-NS hairpin loop repression with a disrupter TF may be envisioned as a transcription “switch”.

H-NS is also a sensor to many environmental changes. For instance, H-NS expression is increased in response to a cold shock. In *Salmonella*, 75 % of the genes having their expression altered by a temperature shift from 25 °C to 37 °C also depend on H-NS concentration [117]. Namely in *S. typhimurium* it was found that an increased temperature results in a diminution of the fraction of H-NS bound to the virulence gene *virF*, hence relieving its repression [109]. This suggests that the heat-shock response is mediated by a change in H-NS expression. Therefore, thermodynamical changes in the environment can alter the relative fraction of H-NS monomers and other oligomers, which induces a physiological response.

As a complementary mechanism, it has been suggested that the H-NS/DNA duplexes might prevent the supercoiling propagation along the chromosome [118], and it was shown that H-NS over-expression correlates with a global decrease of supercoiling.

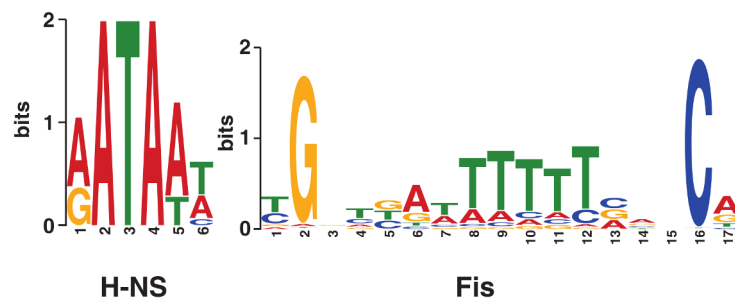


**Figure 4.2** – Position Weight Matrices for H-NS and FIS computed from high-throughput ChIP-seq experiment [32].

## 4.2.2 The Factor of Inversion Stimulation (FIS)

### 4.2.2.1 DNA binding

It was characterized early that FIS is a protein with a degenerate consensus binding sequence which can bind widely on the genome [32, 117, 128–130]. Similarly to H-NS, few sites with higher affinity can be found. In particular, ChIP-seq studies have identified a 15 bp binding motif for FIS [32, 114, 130] (fig. 4.2).

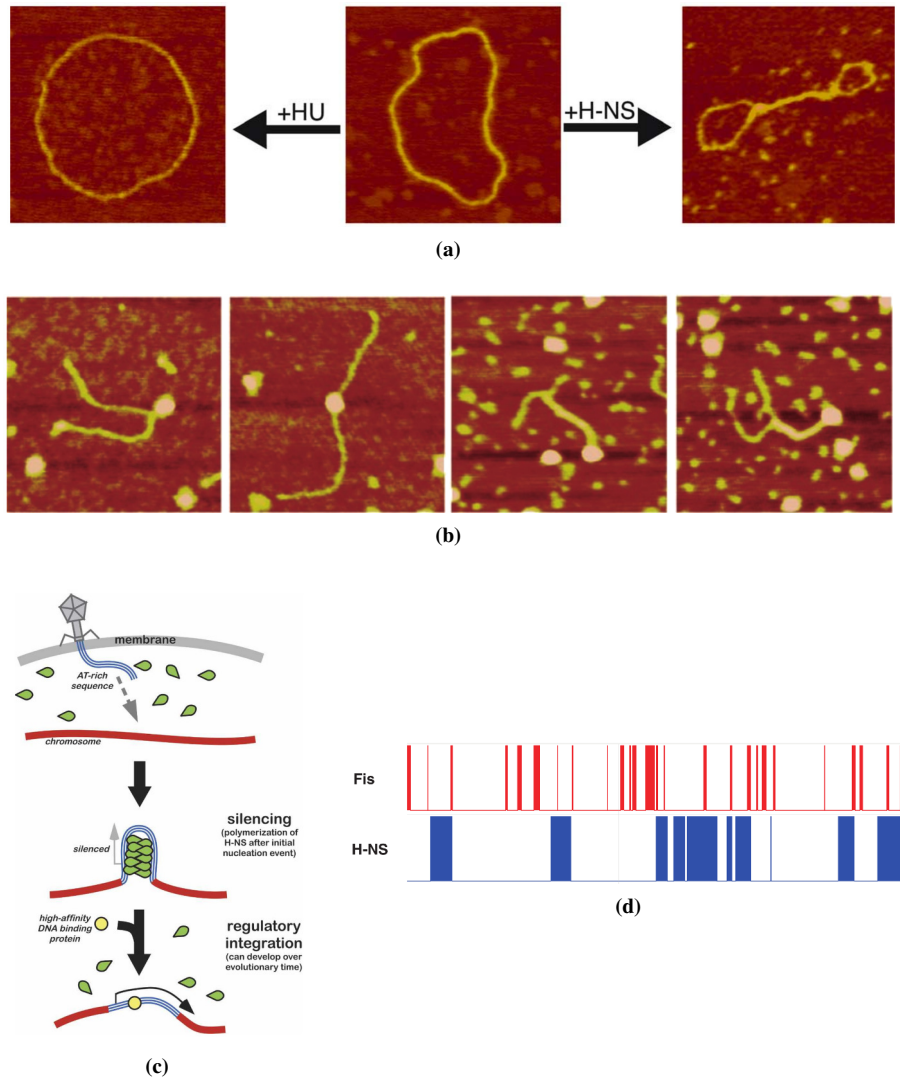


**Figure 4.3** – (a) AFM microscopy image of DNA filaments induced by H-NS [110]. (b) AFM microscopy image of a RNAP bound to a plasmid with the *rrnB* promoter in its center. After addition of H-NS to the solution, RNAP appears to be trapped in a DNA/H-NS hairpin complex (two right images) [122]. (c) Principle of xenogenic silencing by H-NS and regulatory integration [118]. (d) H-NS binding regions are organized into tracks, contrary to other transcription factors and NAPs such as FIS, which are the signature of filaments [32].

Due to the presence of side chains in the protein structure, FIS effectively spans a 21 bp region once bound to DNA [129].

FIS is a homodimer [129, 130], *i.e.* its structure comprises two identical subunits which are assembled together. Each subunit has a helix-turn-helix structure resulting in a protein domain that can bind DNA. Hence FIS is divalent, namely it can bind two DNA sites simultaneously. Upon binding, FIS makes contacts with two consecutive major grooves on the DNA double-helix, separated by approximately 11 bp. However, the length between the binding domains of the two subunits is too short, and consequently DNA is bent by 40-50° [19, 130]. Once bound, FIS can interact with flanking DNA and/or proteins with its side chains. In particular, it has been established that it can bind the  $\alpha$ -CTD domain of RNAP by charge complementarity. This finding supports the view that FIS can recruit RNAP to facilitate the initial binding step of RNAP to the promoter [114, 122].

The DNA structures resulting from the interaction with FIS are different from the structures induced by H-NS. In particular, FIS results in the formation of branched structures in supercoiled circular DNA molecules [119]. This effect is grounded in the formation of DNA loops. *In vitro* assays have shown that DNA branching starts to appear at a protein ratio of 1:160 bp. For higher concentrations, starting with a ratio <1:80 bp (or a concentration > 75 nM), DNA collapses in low mobility complexes [119]. In between, at moderate concentrations, FIS favors the formation of loops. This has also been evidenced with force-extension experiments [129, 130], in which a stretching force is applied at both ends of a linear DNA molecule of 50-100 kbp. For various FIS concentrations, a threshold force was identified, below which the DNA molecule collapses. This appeared to result from the existence of loops induced by thermal fluctuation at low forces. Such loops can be quenched by FIS proteins binding the extremities of the loop. Specifically, upon re-extension of the DNA molecule, discrete steps of DNA molecule size were observed, corresponding to the opening of such quenched loops. Their typical size was estimated to 200 bp. From a regulatory standpoint, formation of loops in promoter regions may potentiate transcription by bringing in proximity remote regulatory sequences. On the contrary, dense aggregates occurring at high FIS concentration are expected to silence transcription in a manner similar to H-NS.

#### 4.2.2.2 Thermodynamical considerations

The concentration of FIS peaks during the exponential growth phase, with approximately 75,000 copies/chromosome ( $\sim 50 \mu\text{M}$ ) [19, 116, 128, 131]. Yet, in the stationary phase, FIS concentration plummets to undetectable levels [32]. Paradoxically, despite being the most abundant NAP in this phase of growth, it remains spatially localized to the periphery of the nucleoid, whereas H-NS for instance is distributed in the whole nucleoid.

It appears that FIS binding to DNA is much stronger than that of H-NS. Indeed, starting from a DNA molecule coated with FIS, it was shown that the introduction of additional DNA molecules providing free competitor binding sites was not enough to drive the dissociation of FIS proteins from the original DNA molecule [130]. Dilution of the solution to increase the entropy of free FIS proteins was also insufficient to drive FIS dissociation. Finally, upon force re-extension of the DNA molecule and breakage of the DNA loops maintained by FIS, it appeared that FIS still remained bound to DNA. From these assays, the apparent dissociation coefficient measured was  $K_d \approx 1 \text{ mM}$ . Besides, ChIP-seq experiments revealed a very strong background signal for FIS binding in the exponential phase, confirming the high affinity of FIS with DNA genome-wide [32].

### 4.2.2.3 Regulatory function of FIS

The role of FIS in regulating the transcription is less clear than with H-NS and has remained rather controversial. It has been argued that FIS is an activator for several genes, including the genes of the macromolecular synthesis (tRNA, rRNA) [131] and the *hns* gene [109, 117]. Early ChIP-chip experiments also demonstrated that 61 % of FIS binding occurs in promoter regions. Besides, 47 % of these binding events were correlated with the binding of RNAP, supporting the role of RNAP recruiter for FIS [19]. Interestingly, it is also claimed that FIS has a role in regulating DNA supercoiling since it was found to be an activator for the expression of topoisomerase I, one of the enzymes responsible for relieving supercoiling [117].

Yet there are also many cases where FIS acts as a repressor. For instance it represses its own expression [115]. Hence there is no general tendency toward activation or repression of the transcription. Even more confusing, some equivalent genes in *Escherichia coli* and *S. typhimurium* appear to be contrary regulated by FIS [131]. Eventually, these results should be taken with caution since the differential expression measured for those genes is sometimes very small. A rather recent ChIP-seq study [32] has even concluded that despite its role as a key activator/repressor for very few genes, such as the *rrnB* operon, in most cases the transcription of genes bound by FIS is not significantly affected by the *fis* gene deletion.

Concerning the *rrnB* operon, it has been shown that FIS binding increases the transcription of the downstream genes by 3 to 7 fold [114]. As detailed previously, this promoter is also under the repressive control of H-NS, which operates through the formation of DNA/H-NS hairpin with RNAP trapped at the apex [122]. FIS has 3 binding sites upstream in the *rrnB* promoter. Such bindings may interfere with H-NS binding, disrupt the DNA/H-NS filament, resulting in the de-repression of the *rrnB* operon. Another evidence of this phenomenon seems to be the observation from ChIP-seq experiments that H-NS and FIS binding are mutually exclusive and anti-correlated [32]. Furthermore, as stated previously, H-NS has a high off-rate, suggesting that the DNA/H-NS filaments can undergo fast dissociation whereas FIS binding to DNA is strong, suggesting that it may prevent H-NS mediated repression for large times.

Several works have sought to relate the action of FIS to supercoiling in bacterial chromosome [115]. In *E. coli* the typical size of a supercoiled domain is of the order of 10 kbp. ChIP-chip studies have shown that there is approximately two FIS proteins bound per supercoiled domain. Therefore the average spacing between consecutively bound FIS *in vivo* is estimated to 5 kbp.

## 4.2.3 The Heat-Unstable protein (HU)

### 4.2.3.1 DNA binding

HU is a dimer whose monomers are coded by the *hupA* and *hupB* genes. Both homodimers and heterodimers are present *in vivo* [132]. HU binds a 9 bp motif on the DNA sequence [110] and bends DNA by approximately 60-70° [133]. The binding motif is quite degenerate and consequently, HU binding is nearly non-specific.

### 4.2.3.2 Regulatory function

A large number of bacteria contain proteins which are close sequence analogs to HU, pointing to an ancient and fundamental role of HU [110, 132]. However, the regulatory function of HU has remained elusive. Some experimental works reported that HU increases transcription initiation. This is maybe because HU

bends DNA and decreases supercoiling when binding to DNA, which may facilitate RNAP binding [117]. HU has also probably an important role in regulating DNA replication and stimulating DNA unwinding at the origin of replication (oriC) of *E. coli* chromosome by regulating the assembly of the pre-replication complex [134].

More specifically, there are strong reasons to believe that HU can relieve the repressive action of H-NS [110,117]. Since H-NS concentration is constant during the cell-cycle, variations in HU concentration may constitute a fundamental mechanism to tune the genetic expression globally. Thus, there is an antagonism between HU and H-NS effects. The main role of HU would be to counteract the compaction of the chromosome by H-NS by opening up the chromosome in order to make it accessible for transcription [110].

#### 4.2.3.3 Thermodynamical considerations

During the exponential growth phase, there are approximately 55,000 HU copies/chromosome, but during the stationary phase, the concentration of HU is reduced to 20,000 copies/chromosome [110,116,117,132]. Furthermore, HU binding to DNA is relatively strong, with a dissociation constant  $K_d \approx 200 - 2500$  nM. As a side remark, similarly to FIS, HU tends to localize at the periphery of the nucleoid, with RNAP and ribosomes.

### 4.2.4 The Integration Host Factor (IHF)

#### 4.2.4.1 DNA binding

IHF binds a 13 bp motif on the genome [135]. Although its binding sequence is shorter than FIS, the binding motif is more constrained, which makes IHF the most specific of the NAPs. IHFs sharply bends DNA upon binding, by about  $160^\circ$ . This implies an important enthalpic cost because DNA is rigid on that scale (it has persistence length  $l_p = 150$  bp), which explains partially why the IHF binding is weaker than with other NAPs.

#### 4.2.4.2 Regulatory function

As with HU, a large number of bacteria contain structural analogs to IHF, pointing to an essential role maintained throughout the evolution. It acts also probably in concert with HU to regulate DNA replication by stimulating DNA unwinding at the oriC [134].

It has also been conjectured that the sharp bending induced on DNA favors the nucleation of H-NS filaments. Hence, IHF might work in concert with H-NS and act as a repressor, in agreement with the finding that IHF binds mostly transcriptionally silent regions [115,132]. Incidentally, IHF concentration increases during the stationary phase, in which many genes are silenced.

#### 4.2.4.3 Thermodynamical considerations

During the stationary phase, there are approximately 20,000 IHF copies/chromosome. This concentration is slightly decreased during the exponential phase but remains close to that value [116]. IHF binding to DNA is also much weaker than that of HU for instance, with a dissociation constant  $K_d \approx 20 - 30$   $\mu$ M. This low affinity might be due to the important enthalpic cost which comes from bending DNA. It seems that the bound protein has no contact with the DNA major groove, suggesting that the binding is mainly entropic, which may be another reason for this low affinity [132].

Protein	H-NS	FIS	HU	IHF
<b>Binding motif</b>	6 bp	15 bp	9 bp	13 bp
<b>Binding specificity</b>	nearly non-specific	nearly non-specific	nearly non-specific	specific
<b>Binding strength</b>	weak	strong	strong	weak
<b>DNA bending</b>	no	40-50°	60-70°	160°
<b>Oligomerization</b>	yes	no	(no)	(no)
<b>Effect on DNA</b>	DNA/H-NS filaments	quenching of thermal loops with average size 200 bp	open/rigidify the double-stranded DNA by decreasing supercoiling	DNA hairpins
<b>Copy number (per genome)</b>	20 000	75 000 in exponential phase and < 100 in stationary phase	55 000 in exponential phase and 20 000 in stationary phase	20 000

**Table 4.1** – Synthetic table for the properties of the four main NAPs in *Escherichia coli*. We used parenthesis for properties in which some doubts remained after careful inspection of the literature.

#### 4.2.5 Summary

NAPs can be quite puzzling at first because they have an effect on the genetic expression of a broad class of genes and on the structure of the chromosome. As such, they illustrate the loose frontier that exists between transcription regulation and chromosome architecture, which with most likelihood implies some sort of feedback mechanism between the two processes.

Their effect on the chromosome architecture entails DNA compaction, DNA bending or the formation of specific structures. H-NS induces the formation of filaments, which makes DNA hardly accessible to other transcription factors, including RNAP. FIS is able to quench DNA loops produced by thermal fluctuations. HU tends to open the DNA double-helix by decreasing supercoiling. IHF can bend DNA in a hairpin configuration. A summary on the properties discussed in this section is given in table 4.1.

We have seen that NAPs are also the transcription factors with the largest concentrations in the cell. This prevalence certainly suggests that their structuring role is coupled with specific functions, probably in regulating the transcription. In this sense, it is remarkable that NAPs, or at least structural analogs, are found in different bacterial species. This fosters the view of a universal role played by NAPs in the bacterial kingdom and acquired early in the course of Evolution by giving a crucial fitness advantage. Subsequently, regulatory mechanisms based on these architectural changes induced on the chromosome may have been selected. In particular, we shall explore a model of regulation based on the formation of DNA hairpin loops (or helices) by H-NS.

### 4.3 Relevant scale for modeling the effect of NAPs

#### 4.3.1 Evolutionary selection of random insertions

Before attempting to model the effect of NAPs on the chromosome architecture and seeking to relate this to biological processes, an important question is: what is the correct scale to investigate this effect? Indeed, performing Brownian Dynamics (BD) simulations at base pair resolution is not realistic because sampling equilibrium configurations would require too much computational power. It is therefore required to coarse-grain some molecular details. For instance, taking a unit length of about one double-helix turn, *i.e.*  $1 \text{ u} \sim 10 \text{ bp} = 3.4 \text{ nm}$  seems at first like a reasonable choice because it is close to the naked DNA diameter of 2.5 nm and therefore allows for a consistent modeling of the bacterial DNA using a beads-on-string polymer. It is also of the order of magnitude of a NAP binding sites (fig. 4.2).

But even at this resolution, modeling the full *E. coli* chromosome would require about  $5 \times 10^5$  beads, let alone the introduction of protein beads to model NAPs which are to interact with DNA. In order to reduce the complexity and focus on the underlying physical process it seems necessary to consider shorter chunks of chromosome. But how to choose their size?

In the case of the *lac* operon, repression occurs through a looping mechanism [5]. It requires the promoter to contact an auxiliary site, 401 bp downstream on the sequence, caused by the binding of the *lac* repressor. Similarly, a repressor system of the coliphage  $\lambda$  was evolved in *E. coli* in which the simultaneous binding of a tetramer with the promoter and an auxiliary binding sites separated by 3600 bp lead to a drastic repression of transcription [7]. In these simple examples, the natural scale for the regulation of transcription is the distance between the promoter and the auxiliary sites.

Such reasoning does not apply to NAPs because the regulatory mechanism has remained less clear, and in particular it cannot be reduced to the formation of one single loop. However, NAPs binding sites may have been acquired and maintained during Evolution by horizontal transfers [118]. Therefore, we will use this assumption to investigate at which scale was exerted evolutionary pressure.

#### 4.3.2 Model of NAPs binding sites insertion

Let us consider the *E. coli* genome of size  $N_G = 4.6 \times 10^6$  bp, with the usual genomic coordinate  $s = 1, \dots, N_G$ . We now introduce the sequence of coordinates:

$$s_0 < s_1 < s_2 < \dots < s_M, \quad (4.1)$$

which represent the starting position of  $M+1$  binding sites on the genome. We also introduce the spacing variables  $d_i = s_i - s_{i-1}$ . Formally, this can be seen as the realization of  $M$  events, starting from time  $s_0$ , drawn from a stochastic point process, in which the spacing distances are random variables. In the absence of evolutionary pressure, it would be reasonable to expect that random insertions of foreign DNA have been independent events. Therefore, we will consider that the spacing variables  $d_i$  are drawn from independently and identically distributed (i.i.d.) random variables that we denote with capital letters,  $D_i$ . Thus we may model the insertion of NAPs binding sites as a stochastic point process with independent increments:

$$\mathcal{P} = (s_0, s_1, s_2, \dots, s_M, \dots) \quad S_i - S_{i-1} = D_i \stackrel{\mathcal{L}}{\equiv} D. \quad (4.2)$$

We may also make the more restrictive assumption on the spacing random variable  $D$ :

$$\Pr(D \geq d) = \Pr(D - d_0 \geq d \mid D \geq d_0), \quad (4.3)$$

which is a non-aging condition in standard survival stochastic point processes. As a consequence, eq. (4.3) ensures that  $D$  is an exponentially distributed random variable, with probability distribution function (p.d.f.)

$$\mu(d) = \frac{1}{\langle d \rangle} e^{-d/\langle d \rangle}, \quad (4.4)$$

which is equivalent to say that  $\mathcal{P}$  is a Poisson stochastic point process.

Therefore, if NAPS have a regulatory role underlying cooperative binding between distant sites along the DNA sequence, this should be visible as a bias in the insertion of binding sites throughout time (fig. 4.4). In particular, the independence between consecutive binding sites insertions is flawed and deviation from the exponential distribution in eq. (4.4) should arise. However, it is reasonable to think that at large genomic distances, binding site insertions become uncorrelated. We may thus define a cross-over distance  $d^*$  such that:

$$\begin{cases} D_{<} = \mathbb{1}_{\{d < d^*\}} D & \text{is exponentially distributed,} \\ D_{>} = (1 - \mathbb{1}_{\{d < d^*\}}) D & \text{is exponentially distributed.} \end{cases} \quad (4.5)$$

In conclusion, we propose to compute the p.d.f. of the spacing distance between consecutive NAPS binding sites (we will shortly present how). If it is exponentially distributed, then no evolutionary pressure has flawed the Poisson-dot-process-like insertion of the binding sites. In that case, one can doubt that any regulatory role is exerted by NAPS. Conversely, if it is non-exponentially distributed, it is the signature for the existence of a non-random layout of NAPS binding sites with a regulatory role. The cross-over between the two regimes will give us the scale that should be considered when modeling the effect of NAPS on the chromosome architecture.

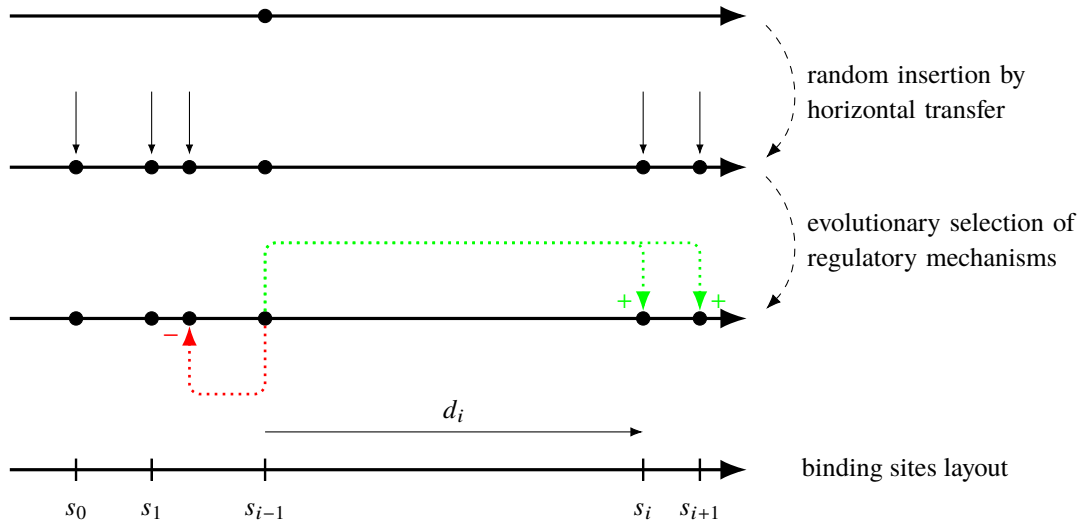


**Figure 4.4** – Random insertion of NAPS binding sites and evolutionary selection of sites playing an essential regulatory role.

### 4.3.3 Binding sites spacing analysis from AT content

In a first approach, we consider that NAPS binding sites correspond to AT-rich sequences. This is valid to some extent because as discussed in the last section, H-NS indeed binds preferentially to AT-rich

sequences [115]. In order to perform this investigation, we use the MG1655 *E. coli* genome, available from [136]. Then we define the density of AT nucleotides at coordinate  $s$  on the genome,  $\rho_{AT}(s)$ , by considering a running window of size  $L$ :

$$\rho_{AT}(s) = \frac{1}{L} \sum_{k=s}^{s+L-1} \mathbb{1}_{\{A,T\}}(b_k) \quad (4.6)$$

where  $b_k \in \{A, T, G, C\}$  is the nucleotide at coordinate  $k$ . The corresponding p.d.f. can be computed and is shown in fig. 4.5 for different sizes of the running window.

In order to identify potential NAPs binding sites, we need to set a threshold  $\bar{\rho}$  such that an occupancy variable can be defined as:

$$\chi_{AT}(s) = \begin{cases} 1 & \text{if } \rho_{AT}(s) > \bar{\rho} \\ 0 & \text{otherwise,} \end{cases} \quad (4.7)$$

and used to identify binding sites to coordinates where  $\chi_{AT}(s) = 1$ . The threshold was set by fitting the AT-density  $\rho_{AT}(s)$  with a sum of Gaussian distributions. For example, for  $L = 20$  the distribution of  $\rho_{AT}(s)$  is well fitted by a single Gaussian p.d.f. whereas for  $L = 200$  two Gaussian p.d.f. were required (fig. 4.5). We then set the threshold as:

$$\bar{\rho} = \mu + 3\sigma \quad (4.8)$$

where  $\mu$  and  $\sigma^2$  are the mean and variance of the dominant Gaussian distributions. In fig. 4.6, we show the binding regions obtained ( $\chi_{AT}(s) = 1$ ) for a chunk of the *E. coli* genome. We have chosen genomic coordinates in the range  $3.8 \times 10^6$ - $3.9 \times 10^6$  bp in agreement with [32], which will be used in the next section.

Eventually, we are able to analyze the presence of long-range interactions in the NAPs binding sites repartition. Following the directions given in section 4.3.2, we have computed the p.d.f. for the distance between consecutive binding regions (fig. 4.7). In other words, we computed the p.d.f. of the size of the empty regions. We observe that this p.d.f. has an exponential tail, suggesting that no evolutionary constraint is exerted at distances  $d > d^* \approx 2$  kbp. On the contrary, deviations from the exponential decay are seen for  $d < d^*$  and characterized by an over-represented fraction of empty regions with small sizes.

For cross-validation, we have also computed the (connected) auto-correlation function of the AT-density:

$$C_{AT} = \langle \rho_{AT}(s + s_0) \rho_{AT}(s_0) \rangle - \langle \rho_{AT}(s) \rangle \langle \rho_{AT}(s_0) \rangle \quad (4.9)$$

where  $s_0$  can be any coordinate on the genome. We observed a non-exponential decay at short genomic distances (fig. 4.8). Moreover, an exponential fit of the tail suggests that the cross-over indeed takes place for genomic distances of a few kbp.

#### 4.3.4 Binding sites spacing analysis from ChIP-seq data

While the previous approach can give insight on existing correlations between NAPs binding sites on the genome, it is clear that limiting NAPs binding sites to AT-rich regions is a crude approximation of the reality. Incidentally, ChIP-seq experiments provide a way to measure directly the *in vivo* genomic positions of NAPs binding sites. Therefore, in this section, we will consider this ChIP-seq experimental data and use the Poisson-point-process analogy described in section 4.3.2.

ChIP-seq experiments measure the density of binding for a protein of interest to the chromosome. Briefly, ChIP-seq experiments involve first a cross-linking step to fix proteins bound to DNA. Then DNA

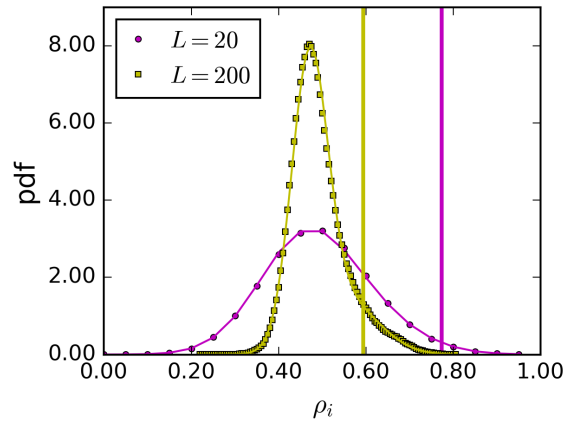


**Figure 4.5** – Probability distribution function of the AT-content  $\rho_{AT}(s)$  (data points), fitted to a sum of Gaussian p.d.f. . We used a window size  $L = 20$  or  $L = 200$ .

is sheared and the proteins, tagged with an anti-body, are immuno-precipitated. After purification, DNA fragments that were bound to such proteins remain and are amplified by PCR. An alignment step follows, in which the read sequences are mapped to genomic coordinates with a typical resolution of 200 bp. Hence, for each bin at coordinate  $s$ , we obtain the number of times the protein of interest was bound to this particular location. Actually, the counts obtained represent the number of binding events up to the PCR amplification ratio. However, we shall consider that this operation only changes the normalization of the counts. In summary, a counting variable  $n_{chip}(s)$  is obtained. Here we use recent high-throughput CHIP-seq data for H-NS and FIS [32].

Let us now define the density of binding:

$$\rho(s) = \frac{1}{N} n(s), \quad N = \sum_s n(s), \quad (4.10)$$

where we have dropped the “*chip*” index for the sake of clarity. As before, we need to define a threshold that allows us to label each coordinate  $s$  as a binding or a non-binding site.

It may seem natural to assume that the density of binding at coordinate  $s$  is a Boltzmann weight [124]:

$$\rho(s) = \frac{1}{Z} e^{-\beta \varepsilon(s)}, \quad (4.11)$$

where  $\varepsilon(s)$  is the binding energy of the protein to the sequence at coordinate  $s$ ,  $\beta = (k_B T)^{-1}$  is the inverse temperature and  $Z$  is a normalization.

Let us also assume that there is a finite number  $M$  of binding energy levels encountered throughout the genome, such that:

$$\varepsilon_M < \varepsilon_{M-1} < \dots < \varepsilon_1 < \varepsilon_0 \quad (4.12)$$

where  $\varepsilon_0$  is the unbound state and  $\varepsilon_i$  with  $i \geq 1$  are bound states. The bound states may represent different binding modes and correspond to the existence of binding sites with different affinities, *e.g.* primary and auxiliary binding sites. Then the probability for a protein to be bound to to the chromosome with energy  $\varepsilon$  is expressed as a sum of delta functions:

$$\Pr(\varepsilon) = \sum_{k=1}^M \alpha_k \delta(\varepsilon - \varepsilon_k), \quad (4.13)$$

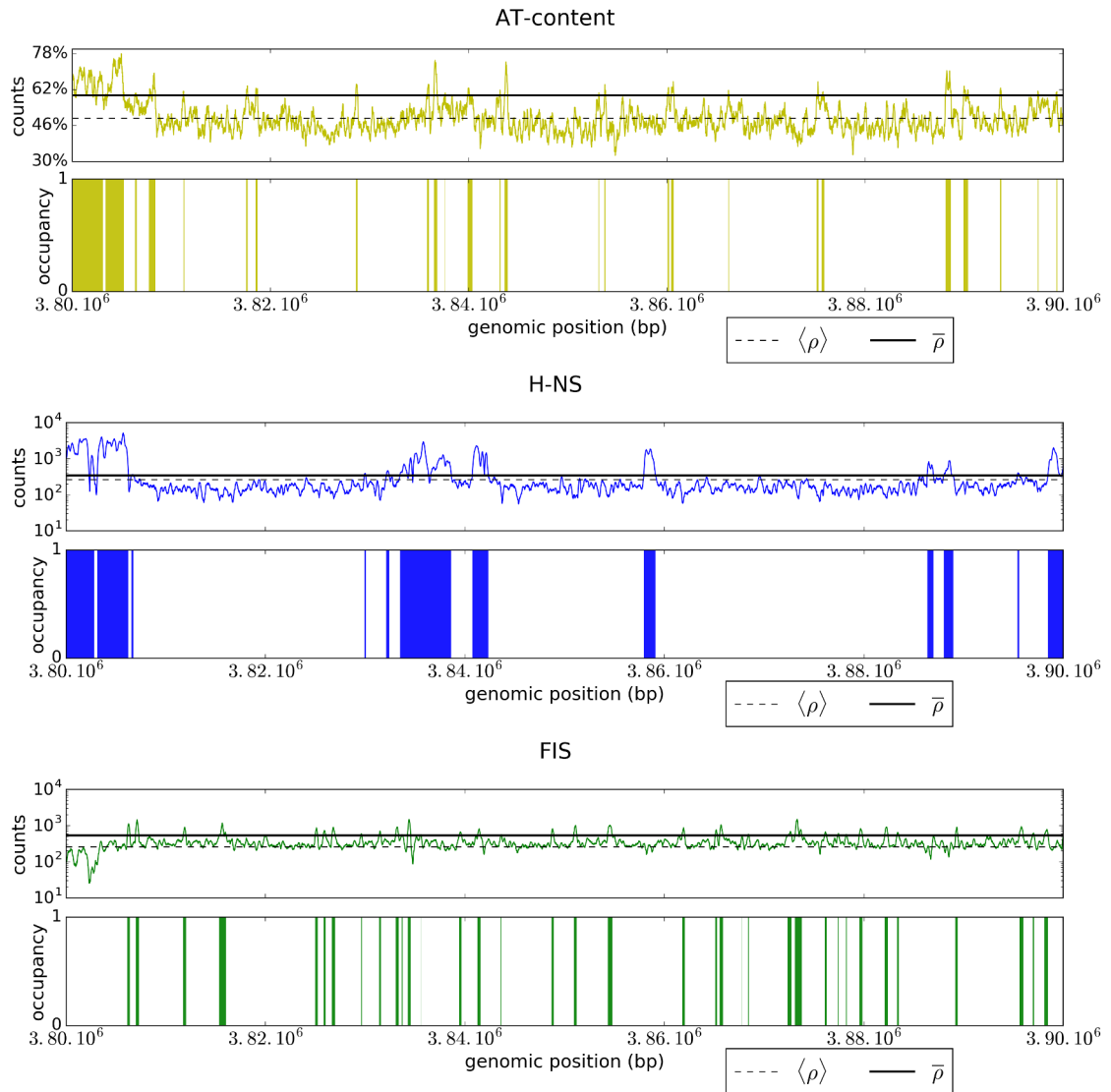


**Figure 4.6** – Binding regions in a chunk of *E. coli* genome computed from AT-content ( $L = 200$ ) or from ChIP-seq counts with H-NS and FIS.

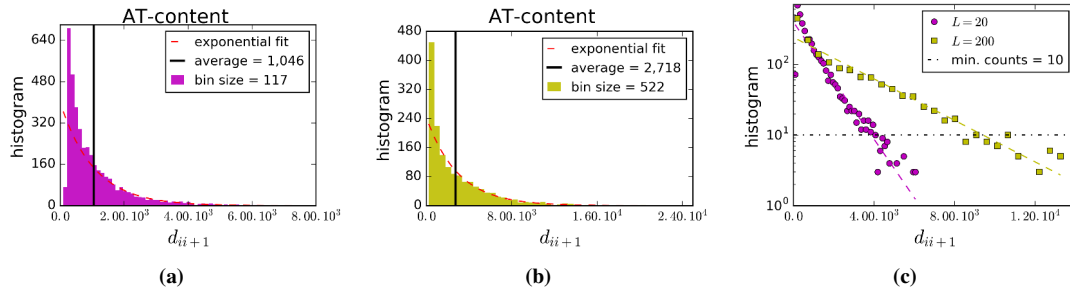


**Figure 4.7** – Probability distribution of the distance between consecutive binding sites for (a)  $L = 20$  and (b)  $L = 200$ . (c) Fit with an exponential (logarithmic scale). We only considered bins of the histograms with a number of data points greater than 10.

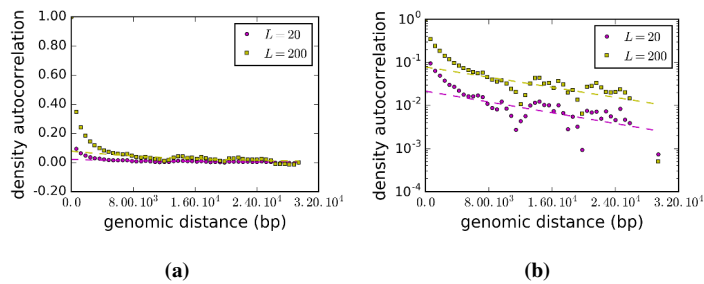


**Figure 4.8** – Auto-correlation of  $\rho_{AT}(s)$ : (a) standard and (b) logarithmic scale.

where  $\alpha_k$  is the proportion of sequences with binding energy  $\varepsilon_k$  in the genome.

In reality, the energy states might not be exactly discrete because the space of binding sequences is very large. Hence a better description might be to replace the delta-functions introduced in eq. (4.13) by Gaussian weights:

$$\Pr(\varepsilon) = \sum_{k=1}^M \alpha_k \frac{1}{\sqrt{2\pi\sigma_k^2}} \exp\left(-\frac{(\varepsilon - \varepsilon_k)^2}{2\sigma_k^2}\right), \quad (4.14)$$

where  $\sigma_k^2$  is the variance of the energy fluctuations of the NAP binding in mode  $k$ , with mean energy  $\varepsilon_k$ . For both H-NS and FIS, fitting  $-\ln n(s)$  to a sum of Gaussian distribution according to eq. (4.14) appeared to be a good approximation. For H-NS (fig. 4.9b), we can clearly distinguish two peaks in the energy levels distribution. In particular, we can assess the difference between the bound state and the unbound state to  $\varepsilon_0 - \varepsilon_1 \approx 2 k_B T$ . Note however that the energy scale in  $k_B T$  depends on the PCR amplification ratio. For FIS (fig. 4.9c), the conclusion is less clear because only one mode remains in the binding energy distribution. It seems highly unlikely however that FIS be present only in the unbound state because it has a strong affinity with DNA. Instead we prefer to consider that the bulk of the proteins is actually bound to the chromosome.

In summary, we can extract the binding energies of the protein (up to a constant) from the logarithm of the ChIP-seq counts, and fitting the energy p.d.f. to a multi-variate Gaussian mixture model gives us the associated energy levels. In particular, we can use this information to define a threshold that retain only the bound states. More accurately, we considered the sum of the  $M^*$  dominant Gaussian distributions such that

$$\sum_{k \leq M^*} \alpha_k > \underline{\alpha}, \quad (4.15)$$

with  $\underline{\alpha} = 50\%$ . This defines a distribution  $f_b(c)$  for the bulk of the binding sequences with mean and standard deviation given by:

$$\varepsilon_b = \frac{\sum_{k=1}^{M^*} \alpha_k \varepsilon_k}{\sum_{k=1}^{M^*} \alpha_k}, \quad \sigma_b^2 = \frac{\sum_{k=1}^{M^*} \alpha_k (\varepsilon_k^2 + \sigma_k^2)}{\sum_{k=1}^{M^*} \alpha_k} - \varepsilon_b^2, \quad (4.16)$$

which appears to be a better description of the dominant mode (unbound for H-NS) than taking the single Gaussian distribution with  $k = 0$ . As announced, this enables the definition the thresholds:

$$\underline{\varepsilon} = \varepsilon_b - 3\sigma_b, \quad \bar{\rho} = \exp(-\underline{\varepsilon}), \quad (4.17)$$

from which we defined an occupancy field, similar to eq. (4.7):

$$\chi(s) = \begin{cases} 1 & \text{if } \rho(s) > \bar{\rho}, \\ 0 & \text{otherwise,} \end{cases} \quad (4.18)$$

such that coordinates where  $\chi(s) = 1$  are considered as binding sites.

We have applied this method to H-NS and FIS (fig. 4.9) and scanned the ChIP-seq counts along the genome to find potential binding sites. In fig. 4.6, we show the result for the same genome window as the one used in [32]. In order to attenuate inaccuracies related to the resolution of ChIP-seq experiments, and following the same authors, we have joined binding regions separated by less than 200 bp. The obtained

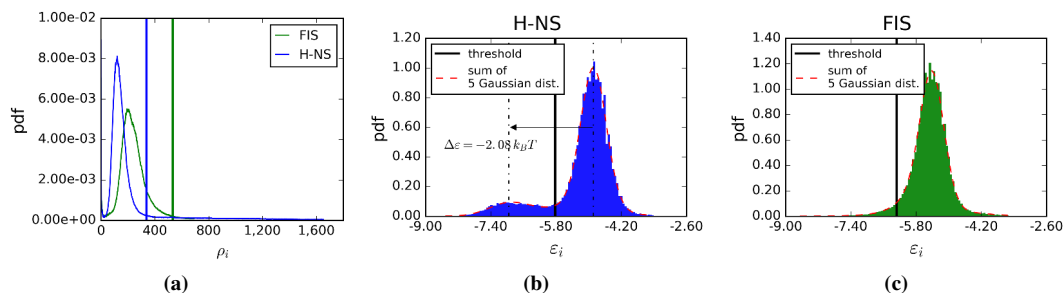


**Figure 4.9** – (a) Distribution of the ChIP-seq counts  $\rho(s)$  and determination of a threshold separating non-binding from binding sites. (b)-(c) Fit of  $\varepsilon(s) = -\ln \rho(s)$  with a Gaussian multi-variate distribution from which the threshold is determined, for H-NS and FIS.

binding regions are in qualitative agreement with [32], so we conclude that our definition for the threshold is consistent, and stick to it because it has a clearer physical interpretation in terms of binding energies.

We are now ready to analyze the presence of long-range interactions in the NAPs binding sites repartition. Similarly to section 4.3.2, we have computed the p.d.f. for the distance between consecutive binding regions on the genome (*i.e.* the p.d.f. for the length of the empty regions). For both H-NS and FIS, we obtain that this p.d.f. is well fitted by an exponential distribution, except at short genomic distances (fig. 4.10). Actually, a large number of distances fall within the first bin of the histogram in our figure and result in a deviation from the exponential decay. Altogether, the distribution for the distance between consecutive binding sites can be considered as exponential for genomic distances  $d > d^*$ , with  $d^* \approx 3$  kbp for H-NS and FIS. Note that the exponential distribution of the distance between binding regions for FIS is consistent with a previous work which found it to be well described by an exponential p.d.f. with average 5 kbp [19].

We cross-validated our results by computing the auto-correlation function for the ChIP-seq counts  $n(s)$ :

$$C(s) = \langle n(s + s_0)n(s_0) \rangle - \langle n(s + s_0) \rangle \langle n(s_0) \rangle, \quad (4.19)$$

where  $s_0$  can be any coordinate on the genome. For both H-NS and FIS, we obtain that  $C(s)$  decays exponentially for genomic distances larger than a few kbp (fig. 4.11). For shorter genomic distances, it is clear that  $C(s)$  does not have exponential variations, as can be seen in logarithmic scale. For genomic distances larger than 5 kbp, the auto-correlation functions seems to collapse on an exponential curve.

### 4.3.5 Conclusion

In this section, we have exploited an analogy between a Poisson stochastic point process and the insertion of NAPs binding sites in the genome throughout evolution. We found that the repartition of NAPs binding sites in *E. coli* genome presents very few correlations at long genomic distances. This suggests that any regulatory mechanism induced by an architectural change of the chromosome following NAPs binding can be investigated for chromosome chunks of length  $d < d^*$ .

Using ChIP-seq data for H-NS and FIS, we found  $d^* \approx 3$  kbp. We conclude that it is sufficient to study H-NS and FIS in regions with a size of a few  $d^*$  (typically  $N \approx 10$  kbp) because it is unlikely that regulatory mechanisms involving architectural changes exist at larger genomic distances. In particular,

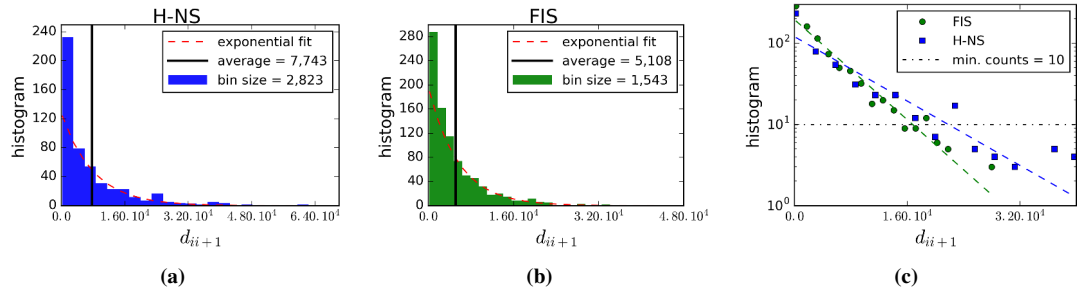


**Figure 4.10** – Probability distribution of the distance between consecutive binding sites for (a) H-NS and (b) FIS. (c) Fit with an exponential (logarithmic scale). We only considered bins of the histograms with a number of data points greater than 10.

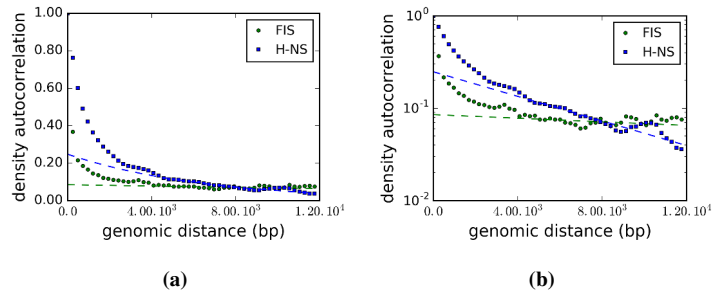


**Figure 4.11** – Auto-correlation of the ChIP-seq counts for FIS and H-NS. (a) Standard scale. (b) Logarithmic scale.

this suggests that BD simulations at a relatively low resolution (*i.e.* with a monomer size  $b \approx 10$  bp) may be used to investigate the effect of NAPs on the chromosome architecture, and infer regulatory effects.

## 4.4 Model for the regulatory effect of H-NS

As seen in the previous section, we may assume that it is sufficient to model the effect of H-NS on the chromosome architecture on relatively short scales. In this section, we investigate a view of genetic regulation in which short H-NS binding regions of the DNA experience transitions between an open state, in which the chromatin is accessible to RNAP, and a closed (or looped) state which prevents RNAP binding and therefore represses transcription.

### 4.4.1 Experimental evidences of H-NS loops

Atomic-force microscopy experiments (AFM) have shown that H-NS induces the formation of DNA filaments (fig. 4.3a on page 73) [110]. These filaments result from the action of H-NS, which can bridge two neighboring DNA sequences together. Other experiments were performed with a *rrnB* promoter (the main promoter of one of the seven ribosomal RNA synthesis genes in *Escherichia coli*) inserted in the middle of a 1200 bp long linear DNA fragment [122]. First, when introduced into the medium, RNAP appeared to bind the promoter, and in most cases induced a local curvature of the DNA fiber. Second, the introduction of H-NS resulted in the formation of DNA filaments in the vicinity of the promoter. More accurately, the structure obtained can be compared to a hairpin loop. Remarkably in many cases, RNAP appeared to be trapped at the apex of such hairpin loops (fig. 4.3b). Such RNAP-trapping mechanism is thought to silence transcription of the gene under the control of this promoter, but also to enable quick transcription restart once the H-NS mediated repression is relieved because RNAP does not need to be recruited from the bulk.

It was also demonstrated with high-throughput ChIP-seq techniques that H-NS binding sites are clustered in regions, or tracks, of varying size  $L$  [32]. Regions of size  $L > 1000$  bp appeared to correspond to genes with very low transcription levels. On the contrary, in short regions of size  $L < 1000$  bp transcription levels were not so low. Actually, many of these short regions appeared to fall within the promoters. Following earlier discussions, we may assume that large regions are transcriptionally silent because of the formation of DNA filaments by H-NS. In short regions however, the overall force to maintain the DNA hairpin loop is weaker, and consequently, DNA filaments may disassemble under the effect of perturbations, leading to the removal of one or several H-NS proteins from the complex. Such perturbations may result from the binding to DNA of a protein with higher affinity, or simply from the entropic fluctuations of the DNA polymer. Altogether, the disruption of DNA hairpin loops in binding regions of short lengths under the effect of thermal fluctuations or by the binding of an external protein, may lead to the derepression of the downstream genes.

In summary, we propose that H-NS regulatory functions have derived from its original sentinel role. Long binding regions are strongly repressed because they are confined in DNA filaments where RNAP cannot bind. In shorter regions, the looped state is more sensitive to perturbations and can undergo transitions to an open state, that can be used to modulate the expression of genes. This suggests that there is a characteristic length for the size of H-NS binding regions which separates the two regimes. In the sequel, we present a simplified model for the underlying physical mechanism in which such a characteristic length naturally emerges.

## 4.4.2 Model for the formation of H-NS loops

### 4.4.2.1 Free energy for hairpin configurations

As usual, we model a chunk of chromosome by a discrete polymer chain of size  $N$ . The chain consists of  $N + 1$  monomers with coordinates  $\mathbf{r}_0, \mathbf{r}_1, \dots, \mathbf{r}_N$ ;  $N$  bonds defined as  $\mathbf{u}_i = \mathbf{r}_i - \mathbf{r}_{i-1}$ ; and  $N - 1$  joints characterized by an angle  $\alpha_i$  such that  $\cos \alpha_i = \mathbf{u}_i \cdot \mathbf{u}_{i+1}$ . Furthermore, we use the WLC model, with internal energy given by:

$$\beta U_b [\{\mathbf{r}_i\}] = l_p \sum_{i=1}^{N-1} (1 - \cos \alpha_i), \quad \|\mathbf{u}_i\| = 1 \quad (4.20)$$

where  $\beta = (k_B T)^{-1}$  is the inverse temperature and  $l_p$  is the persistence length.

In first approximation, we assume that the bridging effect of H-NS can be modeled implicitly by introducing effective interactions between DNA monomers. Hence we consider a chain made of  $2P$  monomers and a "sticky" sequence of  $2(L + 1)$  monomers in its center (fig. 4.12a). This constitutes a chain of size  $N = 2P + 2L + 1$ . We are interested in the equilibrium of this system, and in particular in the probability of the configurations in which the sticky sequence is paired with itself. For simplicity, we assume that the configurations space is reduced to two configurations:

- Open (o): the chain is free; in particular the sticky sequence is not paired.
- Closed (c): the sticky sequence is paired in a hairpin structure of length  $L$ .

Hence the partition function of this system reduces to a two-state model:

$$Z = Z_o + Z_c. \quad (4.21)$$

In the rest of this section, we shall use notations introduced in section 1.3 to describe a discrete worm-like chain. In particular, let us introduce again the entropy per monomer  $z$  (see eq. (1.19) on page 15), and the chain propagator  $q_N(\mathbf{u})$  (see eq. (1.17) on page 15). The first term in the right-hand side (r.h.s.) of eq. (4.21) is simply the partition function of the free chain, *i.e.*

$$Z_o = 4\pi z^{2P+2L}. \quad (4.22)$$

The second term is obtained as follows. We divide the polymer in three pieces (see fig. 4.12a) which are: the paired sequence of size  $2L + 1$  and the two dangling extremities of length  $P$ . The partition function for the closed configuration is then obtained by summing the Boltzmann weights of two free polymer chains of length  $P$ , plus the Boltzmann weight corresponding to a polymer folded in a hairpin configuration with direction  $\mathbf{u}$ . It can be expressed by using the Chapman-Kolmogorov structure of the worm-like chain propagator  $q_n(\mathbf{u})$ :

$$\begin{aligned} Z_c &= 2\pi \int d\mathbf{u}_{P+1} d\mathbf{u}_{P+2L+1} q_P(\mathbf{u}_{P+1}) q_P(\mathbf{u}_{P+2L+1}) \delta(\mathbf{u}_{P+1} + \mathbf{u}_{P+2L+1}) e^{-\beta E_L} \\ &= 2\pi \int d\mathbf{u} q_P(\mathbf{u}) q_P(-\mathbf{u}) e^{-\beta E_L}, \end{aligned} \quad (4.23)$$

where  $E_L$  is the enthalpic contribution of the hairpin configuration. We considered this enthalpic gain to be extensive in the hairpin length and proportional to the pairing energy  $-2\varepsilon$ , and the enthalpic cost comes from the chain bending rigidity. Thus we have  $\beta E_L = 2l_p - 2L\varepsilon$ . Note that without loss of generality, we

have considered that the apex of the hairpin has a double-elbow structure with  $\alpha_{P+L} = \alpha_{P+L+1} = \pi/2$ . There is also a factor  $2\pi$  due to the invariance by rotation around the hairpin axis. Finally, we obtain for the Boltzmann weight for the close state:

$$Z_c = \frac{1}{2} (4\pi)^2 z^{2P} e^{-2l_p + 2L\varepsilon}. \quad (4.24)$$

The closed configuration will be dominant at thermal equilibrium if its free energy is lower than the open configuration free energy:

$$-\ln Z_c < -\ln Z_o \quad \Leftrightarrow \quad L > L^* = \frac{l_p - \ln \sqrt{2\pi}}{\varepsilon - \ln z}. \quad (4.25)$$

Therefore, a characteristic length naturally arises that separates a regime in which the closed configuration prevails at equilibrium, for  $L > L^*$ , from another regime in which the open state prevails, for  $L < L^*$ . The precise value of  $L^*$  results from a competition between the chain bending rigidity, the pairing energy and the conformational entropy per monomer, through  $l_p$ ,  $\varepsilon$  and  $\ln z$  respectively.

The probabilities for the two states at equilibrium are then simply given by

$$\begin{aligned} \Pr(o) &= \frac{Z_o}{Z_o + Z_c} = \frac{1}{1 + \Upsilon^{1-L/L^*}} \\ \Pr(c) &= \frac{Z_c}{Z_o + Z_c} = \frac{\Upsilon^{1-L/L^*}}{1 + \Upsilon^{1-L/L^*}} \end{aligned} \quad \text{with} \quad \Upsilon = 2\pi e^{-2l_p} \quad (4.26)$$

When increasing the length of the sticky sequence, the probability of the closed configuration increases progressively from  $\Pr(c) = 0$  to  $\Pr(c) = 1$ . At  $L = L^*$ , the two states have the same probabilities  $\Pr(o) = \Pr(c) = 1/2$ . Note that this is not a phase transition because the cross-over between the two regimes is continuous. However, this result breaks down in the limit  $l_p \rightarrow \infty$ . In that case, the probability of the closed configuration jumps abruptly from  $\Pr(c) = 0$  to  $\Pr(c) = 1$  at  $L = L^*$  and it is a phase transition.

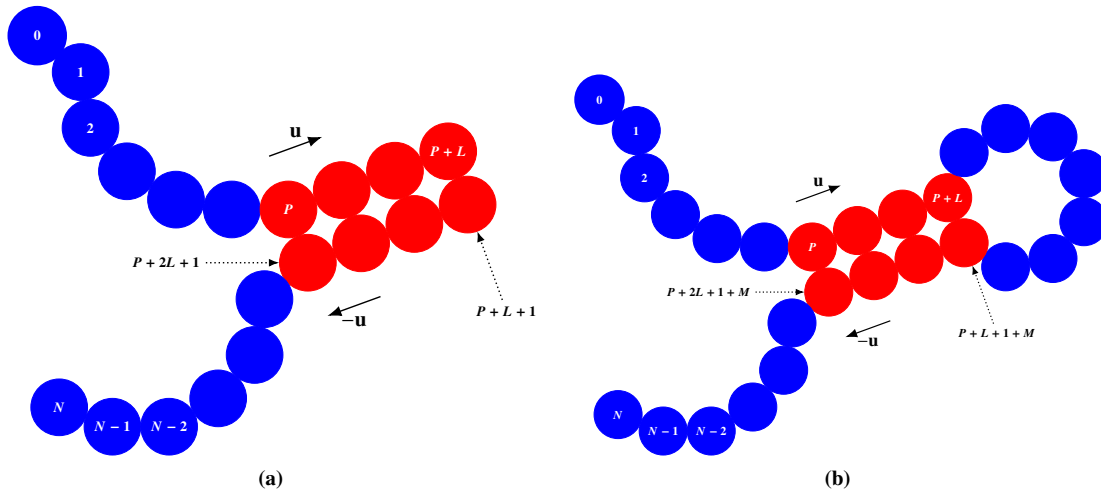


**Figure 4.12** – (a) Bridged configuration with no loop (hairpin). (b) Bridged configuration with a loop.

#### 4.4.2.2 Free energy for hairpin-plus-loop configurations

We have just studied the case of a polymer chain containing a unique “sticky” region of size  $2L + 1$ . We now consider the case in which a chain contains two sticky regions, each of size  $L$ , and separated by a linker of  $M$  non-sticky monomers (fig. 4.12b). As before, the rest of the chain is made of  $2P$  monomers. The partition function of the closed configuration now reads

$$Z_c = \int d^2\mathbf{u} q_P(\mathbf{u}) q_P(-\mathbf{u}) e^{2L\varepsilon} G_M(\mathbf{u}) \quad (4.27)$$

where  $G_M(\mathbf{u})$  is the Boltzmann weight for the linker:

$$G_M(\mathbf{u}) = \int d^2\mathbf{u}_\perp T^{M+2}(-\mathbf{u} | \mathbf{u}) \delta(\mathbf{u}_{P+L+1} + \dots + \mathbf{u}_{P+L+M+1} - \mathbf{u}_\perp) \delta(\mathbf{u} \cdot \mathbf{u}_\perp) \quad (4.28)$$

where  $\mathbf{u}_\perp$  is by construction a unit vector perpendicular to  $\mathbf{u}$ , and  $T$  is the transfer matrix used to describe a worm-like chain (see eq. (1.16) on page 15). With the same arguments as before, we obtain a more general expression for the characteristic length in eq. (4.25):

$$L^* = -\frac{1}{2} \frac{\ln G_M}{\varepsilon - \ln z} \quad (4.29)$$

In particular, for a chain with no linker,  $M = 0$ , we have  $G_0 = 2\pi \exp(-2l_p)$  and eq. (4.29) reduces to the previous expression of eq. (4.25).

### 4.4.3 Investigation with Brownian Dynamics

We have obtained the existence of a characteristic length for H-NS binding regions from a very simple polymer model. In particular we have considered implicit interactions so far. To cross validate our result, we now present a BD model with explicit proteins and compute the probabilities of the open and close states.

#### 4.4.3.1 Model for DNA and H-NS

Following the results of section 4.3, we model the chromosome at a resolution close to the naked DNA fiber. In particular, we take monomers of size  $b \approx 10 \text{ bp} = 3.3 \text{ nm}$ . It is also close to the size of one H-NS binding site. Thus we model a chunk of chromosome of size 4 kbp as a beads-on-string polymer with  $N + 1 = 400$  monomers and persistence length  $l_p = 15b$ . As usual we use a FENE potential to model the bonds elasticity, a Kratky-Porod potential to model the chain bending rigidity and a truncated Lennard-Jones potential to model excluded volume. A summary of the potentials considered for BD simulations is given in table 4.2.

We also introduce the H-NS protein as a sphere with same dimensions as the DNA monomers. But in reality, H-NS is a divalent protein, with two DNA binding sites roughly making a  $180^\circ$  angle with the center of mass of the protein. In order to reproduce this anisotropy in the binding to DNA, we introduce two tiny spheres of diameters  $d$ , tangent to the protein sphere of diameter  $b$  (fig. 4.13a). Note that such spheres are fake atoms that we have introduced only to construct a numerical model for H-NS bivalency. This design was inspired by previous work [46]. In the sequel, we have taken  $d = 0.2b$ .

Similarly, H-NS binding sites can only bind one H-NS protein at a time. Thus, for DNA monomers able to bind H-NS, we also introduce a fake atom of diameter  $d$  (fig. 4.13b). Let us denote  $\mathbf{v}_i$  the unit

vector giving the direction to the H-NS binding site from the DNA monomer center with coordinates  $\mathbf{r}_i$ . Incidentally, the covalent bonds between H-NS and DNA are formed with bases making contacts through the major groove. However, at the scale considered,  $b$  corresponds approximately to one helical turn of the major groove, which is of 11 bp. Due to DNA torsional stiffness, H-NS binding sites on consecutive monomers should point approximately in the same direction. In order to reproduce this property in our simulations we had to introduce additional potentials. First, we introduce a bending rigidity potential to favor configurations in which the H-NS binding site points in a direction orthogonal to the bond direction. More explicitly we introduce the potential:

$$U_{\perp} = k_{\perp} \sum_{i=0}^N (1 - \sin \gamma_i), \quad \sin(\gamma_i) = \mathbf{u}_i \cdot \mathbf{v}_i, \quad (4.30)$$

in which it is seen that the penalty is a minimum when  $\gamma_i = \pi/2$ . This ensures that the H-NS binding site remains on the surface of the tube of diameter  $b$  containing the DNA monomers (*i.e.* the DNA fiber). Second, we need to ensure that consecutive H-NS binding sites tend to point in the same direction. This is achieved by introducing a dihedral potential:

$$U_{\parallel} = k_{\parallel} \sum_{i=1}^{N-1} (1 - \cos \varphi_i), \quad (4.31)$$

where  $\varphi_i$  is the azimuthal angle between H-NS binding sites for the monomers  $i$  and  $i - 1$  in the spherical coordinate system whose zenith direction is  $\mathbf{u}_i$ . It is a dihedral potential because computing the angle  $\varphi_i$  involves two DNA monomers with their respective H-NS binding sites, *i.e.* four atoms. Altogether, the combination of these two potentials mimics the DNA torsional rigidity that tends to maintain consecutive H-NS binding sites aligned. In our simulations, we chose  $k_{\perp} = 50 k_B T$  and  $k_{\parallel} = 1 k_B T$ . A snapshot of BD simulation implementing this model is shown in fig. 4.14.

Finally, the attractive interaction between H-NS and DNA must be a Coulombic screened interaction, which can be well represented by a Yukawa potential:

$$U_{coul}(r) = A \frac{e^{-r/r_d}}{r}, \quad (4.32)$$

where  $A$  is a scale in  $k_B T$  measuring the strength of the interaction and  $r_d$  is the range of the interaction. Since the Debye-Hückel length is of the order of 1 nm in the cytosol [137], the range of the interaction is small and essentially reduces to the dimensions of the objects interacting together. In our simulations, we took a cutoff  $r_d = 0.3b \approx 1$  nm (table 4.2).

We considered a polymer of  $N + 1 = 400$  monomers and  $P = 100$  spheres in a cubic volume of size  $80b$  with periodic boundary conditions. A relaxation run was performed first for  $10^7$  iterations in order to loose the memory of the initial configuration. We then performed a run of  $10^6$  iterations with a soft pair potential to remove overlaps between atoms. Finally, we performed a run of  $2 \times 10^8$  iterations with all interactions in table 4.2, with integration time step  $dt = 7 \times 10^{-4}$ , from which we extracted 200 evenly sampled configurations.

#### 4.4.3.2 Detection of DNA/H-NS bridges

The goal of our BD simulations is to assess the existence of DNA/H-NS bridges characterized in experiments and check whether they are maintained at equilibrium. Therefore, we need a strategy to detect

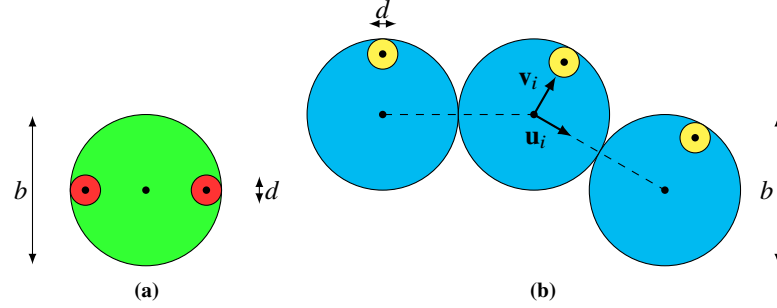


**Figure 4.13** – Numerical model for H-NS binding to DNA. (a) Model for H-NS as a divalent protein. (b) Model for monovalent DNA monomers binding to H-NS.

Property	Model	Values
Bonds elasticity	FENE potential: $U_{fene} = -\frac{k_e r_0^2}{2b^2} \sum_{i=1}^N \ln \left( 1 - \frac{u_i^2}{r_0^2} \right)$ with: $\mathbf{u}_i = \mathbf{r}_i - \mathbf{r}_{i-1}$	$k_e = 30 k_B T$ $r_0 = 1.5 b$
Bending rigidity	Worm-Like chain potential: $U_{wlc} = \beta^{-1} \sum_{i=1}^{N-1} \frac{l_p}{b} (1 - \cos \alpha_i)$	$l_p = 15 b$
Excluded volume interactions	Truncated Lennard-Jones potential: $U_{ev}(r) = V_{LJ}(r) - V_{LJ}(r^{th}), \text{ if } r < r^{th}$ with: $V_{LJ}(r) = 4\epsilon \left[ \left( \frac{\sigma}{r} \right)^{12} - \left( \frac{\sigma}{r} \right)^6 \right]$	$\sigma = b$ $\epsilon = 1 k_B T$ $r^{th} = 2^{1/6} \sigma$
Short-range coulombic interaction	Yukawa potential: $U_{coul}(r) = A \frac{\exp(-r/r_d)}{r}$	$r_d = 0.3 b$

**Table 4.2** – Numerical model to perform Brownian Dynamics simulation of H-NS/DNA bridges

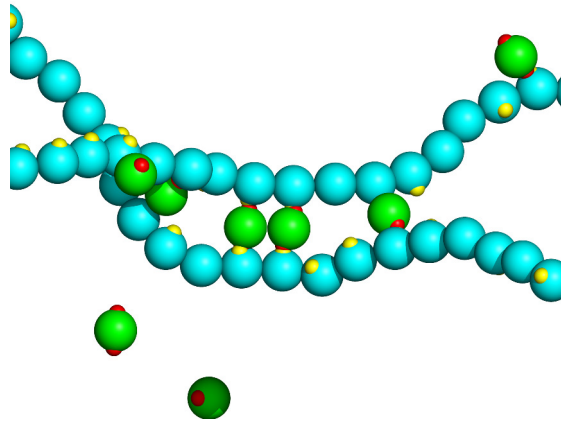


**Figure 4.14** – Snapshot of Brownian dynamics simulation implementing the model of bivalency for H-NS (green with two red binding sites) and monovalency for H-NS binding sites (cyan with one yellow binding site). Fake atoms are represented with an exaggerated diameter in order to be seen.

such structures from BD trajectories. Following conventions from protein folding analysis, we define the contact diagram associated with a configuration of the binding region as a sequence of  $L$  pairs  $(i_e, j_e)$  with  $e = 1, \dots, L$  such that  $j_e$  is the closest of the monomers in contact with  $i_e$ , and reciprocally  $i_e$  is the closest of the monomers in contact with  $j_e$ . A contact is said to occur between monomers  $i_e$  and  $j_e$  when  $|\mathbf{r}_{i_e} - \mathbf{r}_{j_e}| < \xi$ , where  $\xi$  is a threshold to be defined. In practical applications, we have taken  $\xi = 2.25$ , and we have ignored contacts between nearest neighbors (up to third nearest neighbors). Such contact diagrams can be represented by drawing an arc for each pair of monomers in contact (fig. 4.15).

Starting from a contact diagram, we will say that a subset of pairs  $(i_e, j_e)$  with  $e = 1, \dots, H$  form a helix of length  $H$  when there is no crossing between the arcs joining the monomers in contact. There are only two possibilities. First, when

$$i_1 < i_2 < \dots < i_H < j_H < \dots < j_2 < j_1, \quad (4.33)$$

we will say that it is an anti-parallel (or “-”) helix. Alternatively, when  $j_H - i_H$  is sufficiently small, we may call such a helix a hairpin loop. Second, when

$$i_1 < i_2 \dots < i_H < j_1 < j_2 < \dots < j_H, \quad (4.34)$$

we will say that it is a parallel (or “+”) helix. Moreover, we impose that the contour distance between consecutive monomers of a helix is not too large. In other words,  $|i_e - i_{e+1}| \leq l_b$  and  $|j_e - j_{e+1}| \leq l_b$  where  $l_b$  can be seen as the length of the smallest bubble allowed in a helix. In practical applications, we have taken  $l_b = 3$ . Examples of helices detected in configurations obtained from BD simulations are shown in fig. 4.15.

For a given BD trajectory, we can compute  $N_h^-(t)$  (resp.  $N_h^+(t)$ ), which is the number of “-” helices (resp. “+” helices) present in the configuration at time  $t$ . These quantities display dynamical variations, as can be seen in fig. 4.16. We can compute the probability to have a “+” (or “-”) helix at equilibrium as:

$$\Pr(\pm) = \langle \mathbb{1}_{\mathbb{R}_+^*}(N_h^\pm) \rangle, \quad (4.35)$$

where the brackets stand for a thermodynamical average performed over several configurations sampled from a BD trajectory. Finally, the probability for the existence of a helix at equilibrium is simply the sum

of the probabilities of the two types of helices:

$$\Pr(\text{helix}) = \Pr(+)+\Pr(-). \quad (4.36)$$

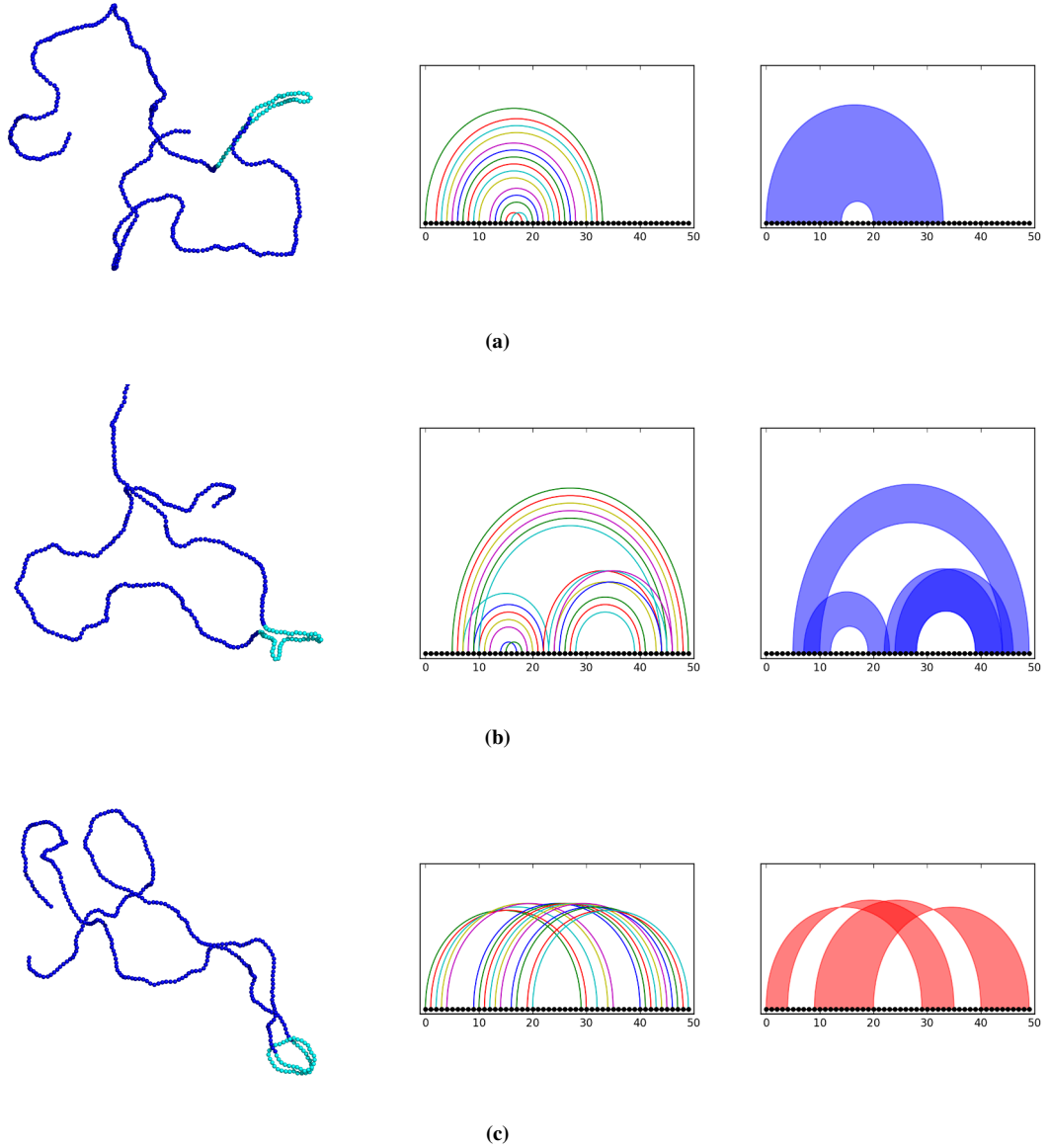


**Figure 4.15** – Examples of helices detected from BD simulations. (a) One anti-parallel helix. (b) Several anti-parallel helices. (c) Parallel helices arising from a toroidal shape. We show in the first column a snapshot of the conformation used. In the second column, we show the contact diagrams for the binding region in which monomers in contact are joined with an arc. In the third column, we represent the helices present in the configuration of length  $H \geq 4$ . All three conformations were taken from a single BD trajectory with  $N = 400$ ,  $L = 50$  and  $A = 8.0 k_B T$ . H-NS spheres are not represented.

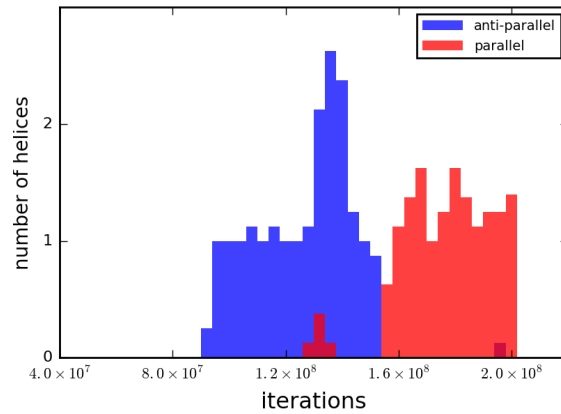


**Figure 4.16** – Time evolution of the number of helices. BD simulation performed with  $N = 400$ ,  $L = 50$  and  $A = 8.0 k_B T$ .

#### 4.4.3.3 Critical size of the binding region

On the basis of these definitions, we can investigate numerically the existence of the characteristic length  $L^*$  for the binding region. For several values of the binding region size  $L$  we performed 50 independent BD simulations as detailed above. Then we computed the helix and hairpin probabilities according to eqs. (4.35) and (4.36). Note that to detect hairpin loops, we actually detected "-" helices with  $j_H - i_H \leq l_h = 15$ .

In fig. 4.17, we represent these probabilities as a function of  $L$  for  $A = 7.0 k_B T$  and  $A = 8.0 k_B T$ . In both case  $L^*$  is clearly visible. For  $L < L^*$  we have  $\text{Pr}(\text{hairpin}) \approx 0$ , hence such structures are not found at equilibrium. On the contrary for  $L > L^*$ , we have  $\text{Pr}(\text{hairpin}) \lesssim 1$ , hence such structures can be found at equilibrium. The fact that  $\text{Pr}(\text{hairpin})$  is close but not equal to one means however that these structures undergo dynamical fluctuations, as has already been seen in fig. 4.16. Finally, for  $A = 7.0 k_B T$  we have  $L^* \approx 60$  whereas for  $A = 8.0 k_B T$  we have  $L^* \approx 20 \sim l_p$ . Therefore, we qualitatively recover that the critical binding region size decreases when the H-NS/DNA binding energy increases, as claimed in eq. (4.29).

#### 4.4.4 Conclusion

In conclusion, we have investigated whether H-NS/DNA filaments characterized in AFM experiments do correspond to equilibrium structures. Our analysis was also grounded on the observation that H-NS binding regions follow a peculiar layout throughout the *E. coli* genome, characterized with ChIP-seq assays. In particular, the fact that H-NS binding sites cluster in tracks means that binding regions can be found in the genome with various size  $L$ . Such a layout suggests that H-NS binding regions can fold in helices or even hairpins.

We have addressed this issue by first considering a simplified physical model in which only one binding region of size  $L$  is present, and in which DNA monomers belonging to the binding region experience attractive interactions between themselves. It is an implicit model for the effect of H-NS proteins. In this framework, we have shown that a critical length for the binding region naturally emerges, separating an open regime in which the binding regions remains unfolded, from a looped regime in which the binding region folds into a hairpin conformation (possibly with a loop at the apex). We have then confirmed this

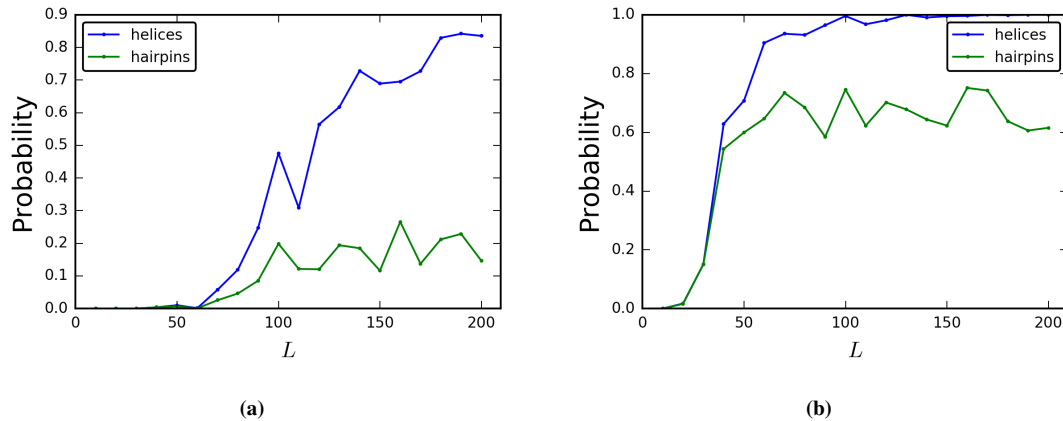


**Figure 4.17** – Characterization of the existence of the critical length  $L^*$  for the H-NS binding region. The probability for each points was obtained by performing an average as in eq. (4.35) over 50 BD trajectories computed independently. BD simulations were performed with  $N = 400$  and: (a)  $A = 7.0 k_B T$  and (b)  $A = 8.0 k_B T$ .

prediction using BD simulations. In the latter, we have considered the H-NS proteins explicitly, and we have also designed a numerical model in order to reproduce the bivalency of the H-NS proteins and the monovalency of the H-NS binding sites.

## 4.5 Discussion

In this chapter, we have sought to relate directly transcription to the chromosome architecture. Naturally, we have started our investigation by reviewing the properties of NAPs, which are abundant proteins in the bacterial cell and well known for their role in structuring the chromosome. The high degree of conservation among bacteria species, combined with their prevalence over other transcription factors suggests that their role is not only architectural, but that instead they are involved in biological processes and for that reason have been selected during Evolution. In our review of the literature, we have seen that their effect on cell physiology includes some elements of transcription regulation. Therefore, NAPs seem to illustrate the connection that exists between chromosome architecture and transcription. We are convinced that this connection is dynamical and may rely on a feedback mechanism between these two components.

Much uncertainty remains however on the precise link between structures entailed by NAPs and the transcriptional response. In particular, the genomic scale of such regulatory mechanisms has remained elusive. On the basis of an analogy between a stochastic point process and the insertion of NAPs binding sites throughout Evolution, we have analyzed the presence of correlations in the NAPs binding sites insertions. Using ChIP-seq data available for FIS and H-NS, we have concluded that it is very unlikely that regulatory mechanisms selected by Evolution exist on genomic scales larger than 10 kbp in *E. coli* bacteria. In particular, the distribution of the distances between NAPs binding sites appeared to have an exponential tail above this genomic scale.

Then we have studied in more details a typical structure induced by H-NS and well characterized in AFM experiments: DNA hairpin loops. The effect of these hairpin loops on the transcription have been thoroughly discussed in the existing literature, and appear to be at stake in the regulation of the important

*rrn* operon in *E. coli* bacteria. In general, H-NS/DNA filaments lead to a repression of transcription by preventing RNAP binding. Yet, the result obtained from ChIP-seq experiments, that short H-NS binding regions are found preferentially near the promoters led us to conjecture that short hairpins may be used as dynamical switches to modulate the transcription level of downstream genes. Using a very simple polymer model of H-NS binding sites, we have found that a characteristic size for the binding region naturally emerges, resulting from the competition between the chain entropy of the DNA polymer, the bending rigidity (*i.e.* the persistence length of the DNA fiber) and the bridging effect of H-NS. Binding regions with larger sizes lead to stable hairpins whereas smaller binding regions cannot form such hairpins at equilibrium. We have confirmed this finding with BD simulation, using a model in better agreement with the biological reality. Namely, we have considered divalent beads to model H-NS and monovalent beads to model H-NS binding sites on the chromosome.

The existence of a characteristic length for H-NS binding regions suggests an ambivalent role. For binding regions of large sizes, H-NS has a repressive role mediated by the formation of long DNA hairpin loops, or helices. These helices are stable and can be maintained over biological time scales. Second for regions with a size close to the characteristic length, the dynamical assembly and disassembly of DNA hairpins may modulate the genetic repression or entail fast transcriptional response, such as the so-called RNAP trapping mechanism. It also suggests that these hairpins, lying at the limit of the stability condition, can be easily disrupted by external perturbations. For instance, it could be the binding of another transcription factor with a larger affinity with DNA, such as FIS. In other words, FIS may introduce local defects to the H-NS filament. Consequently, the two remaining binding regions flanking the FIS binding site will have a size  $\tilde{L} < L^*$ , resulting in the disassembly of the filament. This is a possible model for transcription activation by FIS, that we call a transcriptional “switch”, and possibly at stake at the *rrn* operon. Because it is based on the local structure of the DNA, which namely depends on the presence of H-NS binding sites, it may explain why the effect of FIS on the transcription is so heterogeneous in *E. coli* bacteria.

Of course, these speculations need to be refined and confirmed with further work. In particular, we plan to model a chunk of the *E. coli* genome and include the real distribution of binding sites for H-NS and FIS, based on ChIP-seq assays. We will investigate which among the H-NS binding regions form hairpin structures. Furthermore, upon addition of FIS, we will see which ones are easily disrupted, and which ones are not. It will be interesting to see if the dynamical re-organization observed in BD simulations indeed correspond to known regulatory sites such as promoter regions. Nonetheless, we underscore that a study based solely on BD simulations has many limitations. In particular, the biological values for the binding energies are often unknown, and when experimental measures were performed, it is actually the free energy which is measured and not the enthalpic binding energy alone. Therefore, such approaches require some arbitrary choices. However, they also constitute a first step in relating more accurately architectural changes and transcription regulation.



## Chapter 5

# Reconstruction of chromosome architecture from chromosome conformation capture experiments

In this chapter, we address the problem of finding a model for the chromosome architecture from contact probabilities measured in Chromosome Conformation Capture (CCC) experiments.

We start by introducing the reasons to find a better representation of the chromosome architecture. We then present in more details what are CCC techniques and how contact probability matrices can be generated. In particular we will present the methods used in this work to normalize CCC counts maps. We conclude this introductory section by reviewing methods which have proposed models for the chromosome architecture based on CCC contact matrices.

We then move on to present our model for reconstructing chromosome architecture. It consists of a Gaussian chain polymer representation of the chromosome to which we add effective interactions between DNA monomers under the form of harmonic springs. Such effective interactions do not have any microscopic signification but instead represent a coarse-grained approach. Besides they are to be determined from an input contact probability matrix. The resulting model defines a Gaussian effective model (GEM). More formally, we may say that we address the problem of finding the connected object, as a Gaussian chain, that produces a given contact matrix.

As an important result, we will obtain an analytical closed-form relating these effective couplings to the contact probabilities at the Boltzmann equilibrium for the GEM. This method can be used to propose a physical model of the chromosome under the form of a GEM which reproduces exactly the experimental contacts. Yet it can result in a non-physical model when the correlation matrix of the GEM has negative eigenvalues. Therefore we will present an alternative method, more demanding computationally, that addresses this issue and yields a stable effective model of the chromosome.

Finally, we will apply our method to contact matrices from CCC experiments and comment on the biological significance of the architecture obtained.

## 5.1 Introduction

The primary function of the chromosome is to encode the genetic information of each cell individual. Yet, chromosome folding (that we call architecture) has an impact on several biological processes including replication, chromosomes segregation and transcription. On a local scale, divalent transcription factors (TFs) can bind to DNA and locally alter the structure of the chromosome, namely by forming DNA loops. In the case of the *lac* operon in *Escherichia coli*, the formation of a DNA loop leads to the repression of the *lac* gene. On a global scale, chromosome architecture is constrained and shaped by structuring proteins, which are nucleoid-associated proteins (NAPs) in bacteria and histones in eukaryotes. In chapter 4, we have shown how structures of the chromosome entailed by NAPs can affect transcription regulation. Therefore, a better understanding of chromosome folding seems like a keystone to unveil complex regulatory mechanisms underlying the genetic expression.

A fundamental consequence of chromosome folding on transcription is to bring co-regulated genes close in space. Chromosome folding is also assumed to induce the existence of transcription factories [28, 70, 71, 74], or for instance the global silencing of genes in H-NS clusters [111]. At first, such co-localization effects were called into question because the existence of molecular crowding together with the confinement of the chromosome in the nucleus/cell result in strong topological constraints. However, several Brownian dynamics (BD) and Monte-Carlo (MC) studies have demonstrated that co-localization of a large number of genes can be achieved despite these constraints [45, 46].

From a broader perspective, co-localization can be seen as a way to synchronize biological processes in the nucleus/nucleoid. For the transcription, this would be achieved by sharing higher local concentrations of RNA polymerase (RNAP) in transcription factories. In the context of epigenetics, regions on the chromosome are tagged with marks (like methylations) which affects locally genes expression. In particular, such marks can result in transcriptionally active (euchromatin) and inactive (heterochromatin) regions. Epigenetics marks held by a region of the chromosome can also propagate to neighboring regions, and turn them for instance into actively transcribed euchromatin. Therefore chromosome architecture entails a spatial network in which biological “signals” can propagate to nearest neighbors. We think this constitutes a major determinant of cell physiology. Yet it is not clear whether chromosome architecture induces physiological changes by selecting genes to be transcribed, or to the contrary whether physiological changes lead to biological responses which alter chromosome architecture, or both.

Chromosome architecture can be investigated with physical models introducing binding proteins [49, 50, 138, 139]. However, it is a difficult problem for several reasons. First, the copy number of all TFs without distinction is huge (up to  $10^6$  in *E. coli* [116]). Second, there are many different binding proteins, with different binding energies and binding sites. A common approach to address this problem is to consider a generic type of protein with average properties and representing several protein families at the same time [46, 50]. Third, the values of the binding energies are in general not known, which leaves the investigator with a free parameter to fit (or to guess) [49]. Simulations and theoretical studies have usually dealt with these limitations by considering simplifying assumptions which decrease the underlying complexity. For example, taking a crude model for the protein-DNA interaction, reducing the number of target types on the genome or considering several protein species as one. . . *etc.* Consequently, it is hard to expect more than qualitative agreements between results of such studies and experimental data sets. Therefore, models of chromosome architecture better rooted in biological data sets and which can be used in BD studies are actively sought.

## 5.2 Chromosome Conformation Capture experiments

### 5.2.1 Historical context

Chromosome Conformation Capture (CCC) techniques were developed during the years 2000s. At first, they aimed at counting the number of contacts of a particular location on the chromosome (or locus) with an other locus and were denoted by the acronym 3C. Later improvements have consisted in counting the contacts of a single locus with several other loci on the chromosome (4C), and then of many loci between themselves (5C). Finally, the combination of CCC techniques with high throughput sequencing methods (Hi-C) brought these techniques to a larger scale by enabling the measurement of contacts between thousands of loci on the chromosome. Hence these methods yield an enormous amount of data to deal with.

During the last decade, Hi-C experiments have revolutionized experimental biology. Before them, measures of the spatial distance between different loci or genes on the chromosome were essentially performed with fluorescence techniques. Yet even with state-of-the-art techniques, like localization-based super-resolution imaging (STORM or PALM) which can be used to survey the subcellular distributions of DNA sequences tagged with a fluorophore, the resolution achieved and the amount of data generated is very humble in comparison with Hi-C methods.

For historical reasons, Hi-C techniques were first used in eukaryotic cells, like in human [35] or yeast [140], but they have also been used later in bacteria [141, 142]. They have also lead us to revise our conception of chromosome architecture. In particular, contact matrices generated by these experiments generally exhibit checkerboard patterns. In eukaryotes, such patterns have been conjectured to represent a high level organization of the chromosome into Topologically Associated Domains (TADs) with a size slightly below the megabase pair. Although the biological relevance of TADs is still controversial, it has been shown in eukaryotes that TADs are highly conserved in a population of cells with the same type. Yet significant changes are visible during cell differentiation [143–145] and cell senescence [146]. In bacteria, the existence of TADs is less clear given the smaller size of the bacterial chromosome. Yet changes in the physiological conditions have been shown to induce significant re-organization in the contact matrices measured [34]. In short, Hi-C techniques have provided a novel type of biological data. In particular, it has led to studies fostering the idea that chromosome architecture and gene's expression are intimately connected.

### 5.2.2 Method

From a practical point of view, a restriction enzyme able to cut DNA at specific restriction sites (*i.e.* a nuclease) must be chosen. The DNA segments in between two restriction sites (or cuts) are called restriction fragments. A critical requirement is therefore to find an enzyme whose restriction sites are sufficiently degenerate and common in the genome to yield a subdivision of the genome as regular as possible. Typically, restriction enzymes recognize a specific DNA sequence of 6 base pairs. Hence, it cuts DNA every  $4^6 = 4096$  bp in average. Ideally, all restriction fragments should have the same size, which of course is never reached in experimental settings. The experimental procedure then relies on the following steps [35] (fig. 5.1a). First, a population of cells is cross-linked with formaldehyde and lysed. This results in the formation of covalent links between adjacent chromatin segments. Second, the restriction enzyme is introduced in order to shear the chromosome, resulting in free pairs of cross-linked restriction fragments with dangling ends. Third, a ligation step is performed in order to join the dangling ends in

each restriction fragment pair, which leads to the formation of small DNA rings made of two restriction fragments. This step also removes the restriction sites and adds biotin tags in place for use in the next step. Fourth, the DNA solution is purified and all ligated fragments are obtained by immuno-precipitation of the biotin tags. Finally, the collection of fragments are amplified by PCR and sequenced, yielding a collection of “reads”. A complex bioinformatics treatment is then required to map the reads to the original genome and identify the loci in contact. This last step has many caveats and is known to be prone to error [33, 147]. The genome is then divided into bins of equal size, longer than the restriction fragment length. The collection of mapped sequences can then be assigned to each bin and used to produce a counts map where each matrix element  $n_{ij}$  is the number of contact events between bins  $i$  and  $j$  on the genome (fig. 5.1b). The typical size of the bins ranges from a few kbp to 1 Mbp [34, 35, 148].

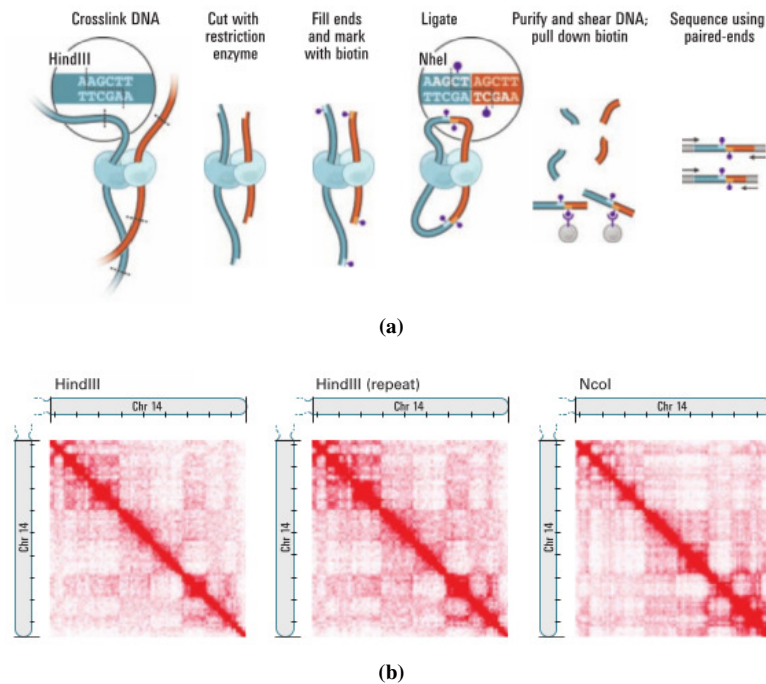


**Figure 5.1** – Hi-C experiments (from [35]). (a) Experimental procedure to generate pairs of sequence “reads” corresponding to DNA segments in contacts. (b) counts maps obtained.

### 5.2.3 Caveats

The reliability and repeatability of Hi-C experiments has been frequently called into question. Besides, processing Hi-C experiments raw measures involves a number of bioinformatics steps which are cumbersome and prone to error. Therefore, the counts maps which are a prerequisite for the computation of contact probability matrices should be considered with caution. Without pretending to exhaustivity, we review some of the experimental and methodological artifacts which should be kept in mind and that can affect the quality of the experimental data.

First, the experimental protocol involves several steps in which inaccuracies can accumulate and lead to inconsistencies. In particular, formaldehyde in aqueous solution is present in the form of methylene

glycol HOCH<sub>2</sub>OH monomers, but it also exists in the form of oligomers HO(CH<sub>2</sub>O)<sub>n</sub>H, where  $n$  is a polymerization index. The equilibrium of the polymerization reaction depends on the formaldehyde concentration. For instance, in an aqueous solution with 40 % mass fraction of formaldehyde at 35 °C, the proportion of monomers in solution is only 26.80 %, the rest being oligomers with  $n > 1$  [149]. This is very close to the conditions used in [35], with 37 % mass fraction of formaldehyde, which clearly suggests that cross-links between restriction fragments have varying size depending on the formaldehyde oligomer that made the cross-link. Furthermore, the size of the cross-link itself between formaldehyde and DNA is of varying length [150]. For these reasons, it may be better to consider that the actual distance between a pair of cross-linked restriction fragments is a Gaussian distribution centered around a most-likely distance  $\xi$ , rather than always below a threshold distance  $\xi$ .

Another origin of inconsistency in the experimental protocol may come from the PCR amplification of the purified reads. Indeed, an important requirement is to perform as few PCR cycles as possible ( $\sim 10$ ). This ensures a linear amplification of the reads and preserves the counts distribution up to a normalization [148]. Finally, several control experiments must be carried out to check the quality of the produced Hi-C library (the collection of read pairs). For instance, the distribution of the size of restriction fragments can be checked by gel electrophoresis. Ideally, they should all have the same size.

Another control carried out consists in re-digesting the obtained Hi-C library with the restriction enzyme to check that a complete digestion of the chromosome occurred. Note also that in the original Hi-C study [35], counts map had been generated with two different restriction enzymes in order to cross-validate the obtained results. This practice has somehow been lost since all subsequent Hi-C publications have only used one restriction enzyme.

Once the Hi-C library has been obtained, it must still be processed with bioinformatics methods in order to transform the raw data of read pairs into a counts map with elements  $n_{ij}$  counting the number of contacts (to a normalization) between genomic locations  $i$  and  $j$  [33, 35, 147]. In particular this implies mapping each read to a location on the genome. At a low level, a primary source of concern is to actually successfully map all reads. For instance, reads from regions with many DNA repeats (coming for instance from transposon elements) or small reads can often not be mapped uniquely to a specific genomic location. These ambiguous reads are therefore discarded. There are also cases in which a read cannot be mapped to the genome. This can originate from DNA recombinations which occur during the experimental protocol, PCR/sequencing errors, reads alignment issues... In this work, we used the results of these procedures as it is available from the literature. In particular, we worked directly with the counts maps computed in previous research works [34, 35].

## 5.2.4 From counts to contact probabilities

### 5.2.4.1 Normalization issue

The counts map can be used to assess the contact probability  $c_{ij}$  between any pair  $(i, j)$  of loci on the genome. However, this step is not straightforward because the normalization to transform counts into contact probabilities is not known.

In [35] the contact probabilities are computed as  $c_{ij} = n_{ij}/\langle n_{ij} \rangle$ , where  $\langle n_{ij} \rangle$  simply means the average over genomic loci pair  $(p, q)$  separated by the same contour distance,  $|p - q| = |i - j|$ . However there is no rigorous justification for this choice of normalization. Other studies have attempted to address the normalization problem by designing a numerical procedure that ensures that the obtained contact probabilities produce a stochastic matrix, *i.e.* the line sums  $\sum_j c_{ij} = 1$  [33, 147, 151]. However, although

this tends to smoothen the variations of the contact probabilities, we do not see clear reasons supporting the idea that the contact probability matrix should be a stochastic matrix. For instance, in the case of a Gaussian polymer, the probability that the distance between any pair  $(i, j)$  of monomers vanish,  $d_{ij} = 0$ , is:

$$c_{ij} = \left( \frac{3}{2\pi b^2} \right)^{3/2} |i - j|^{-3/2}, \quad (5.1)$$

where  $b$  is the size of a monomer. It obviously does not satisfy the stochastic matrix condition. Consequently, we have chosen to consider an alternative approach (although less sophisticated than the methods just mentioned) to normalize counts maps into contact probability matrices.

In principle, the normalization factor between counts and contact probabilities should be the total number of cells in the experimental sample (possibly multiplied by the PCR amplification ratio). Then  $n_{ij}$  is simply the number of cells in which a contact between loci  $i$  and  $j$  is observed. Assuming that the experimental sample contains  $\mathcal{N}$  cells, the contact probability is then simply expressed as  $c_{ij} = n_{ij}/\mathcal{N}$ . In practice however,  $\mathcal{N}$  is unknown. We now propose two simple approximations for this normalization.

#### 5.2.4.2 Trace normalization

It is natural to expect that the closer restriction fragments are on the DNA sequence, the higher their contact probability is. In particular, restriction fragments falling into the same bin should always be in contact, *i.e.*  $c_{ii} = 1$ , and indeed diagonal elements  $n_{ii}$  usually take the largest values. Hence, we may be tempted to assume that each diagonal element is equal to the number of cells in the sample. However, in real data sets, all diagonal elements are not equal. Thus we consider instead that the number of cells in the sample can be approximated by the average value of the diagonal elements. The contact probability is then computed as:

$$c_{ij} = \frac{n_{ij}}{\mathcal{N}}, \quad \mathcal{N} = \frac{1}{N} \sum_{i=1}^N n_{ii}. \quad (5.2)$$

#### 5.2.4.3 Maximum normalization

It is possible however that diagonal counts  $n_{ii}$  are abnormally high. This might be due for instance to self-ligations of isolated restriction fragments or cross-linking with sister DNA during replication. In order to circumvent this issue, we assume that there exists at least one pair of off-diagonal loci  $(i_0, j_0)$  which are always in contact, *i.e.*  $c_{i_0 j_0} = 1$ . Note that this assumption is different from the stochastic matrix condition, which assumes that every monomer is always in contact with at least one other monomer. Therefore, the number of cells in the sample is estimated as the maximum of the off-diagonal counts. Actually, counts are very high not only on the diagonal, but also near the diagonal. Therefore, we may choose to discard counts such that  $|i - j| < l_d$  where  $l_d \geq 1$  is a length to adjust. In the end, the contact probability is computed as:

$$c_{ij} = \frac{n_{ij}}{\mathcal{N}}, \quad \mathcal{N} = \max_{|i-j| \geq l_d} (n_{ij}). \quad (5.3)$$

This method with  $l_d = 3$  gives a contact probability matrix in qualitative agreement with [35] (see figs. 5.1 and 5.2).

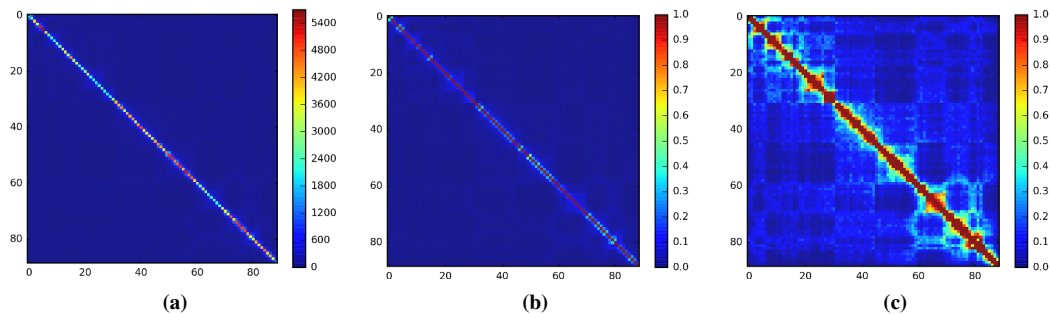


**Figure 5.2** – Normalization of Hi-C counts into contact probabilities. (a) Counts map of human chromosome 14 with bin size 1 Mbp [35]. (b) “Trace” normalization. (c) “Maximum” normalization with  $l_d = 3$ .

## 5.3 Previous approaches to predict chromosome folding from Hi-C data

We now review some of the models which have been investigated in the past to address the reconstruction of chromosome architecture from CCC data.

### 5.3.1 Models based on an estimate of the distance matrix

#### 5.3.1.1 Non-polymer models

**Harmonic model.** A numerical procedure relying on the introduction of harmonic potentials has been proposed to reconstruct the equilibrium configurations of the chromosome from the experimental contact probabilities [142]. Harmonic interactions are introduced between each restriction fragment pair  $(i, j)$ , such that:

$$\beta U(\{\mathbf{r}_i\}) = \sum_{i < j} \frac{k}{2} (r_{ij} - r_{ij}^0)^2, \quad (5.4)$$

in which  $r_{ij} = |\mathbf{r}_j - \mathbf{r}_i|$  is the distance between loci  $i$  and  $j$ ,  $k$  is an arbitrarily chosen elastic constant and  $r_{ij}^0$  is the length of the corresponding spring. A Monte-Carlo simulation is then performed to sample equilibrium configurations of the system defined in eq. (5.4). These configurations are used to represent the chromosome configurations (fig. 5.3a).

In this method, the elastic constant was assigned arbitrarily to  $k = 5 k_B T$ . The fact that this elastic constant is the same for all  $(i, j)$  is a first limitation in this approach. The spring lengths are taken such that  $r_{ij}^0 = d_{ij}$ , where  $d_{ij}$  is the distance desired between beads  $i$  and  $j$ . The authors assumed that the equilibrium distance between two restriction fragments is inversely proportional to the contact probability,  $d_{ij} = 1/c_{ij}$ . We will come back to this assumption at the end of this section. Importantly, in a network of connected springs such as defined in eq. (5.4), the average distance at thermal equilibrium between a locus  $(i, j)$  is in general not equal to the spring length, hence  $\langle r_{ij} \rangle \neq d_{ij}$ . This is an example of frustrated systems, and constitutes a fundamental limitation of this approach.

**Constraint satisfaction.** Another approach is to cast the problem of reconstituting chromosome architecture into a constraint satisfaction problem [140]. The reformulated problem then consists in finding

the coordinates  $\{\mathbf{r}_i\}$  such that the distances between any  $(i, j)$  restriction fragment pair is bounded from below and from above:

$$r_{ij} < r_{ij} < \bar{r}_{ij}. \quad (5.5)$$

In eq. (5.5) the upper bound is taken inversely proportional to the experimental contact probability,  $\bar{r}_{ij} \propto 1/c_{ij}$ , and the proportionality coefficient is a parameter of the method. The lower bound  $r_{ij}$  is introduced to take into account excluded volume between restriction fragments, and to penalize contacts between adjacent fragments due to the chromosome bending rigidity. This is a constraint satisfaction problem, which can be solved with the simplex method. The obtained solution is then used to represent a chromosome configuration (fig. 5.3b).

The main limitation of this approach is clearly that the choice of the lower and upper bounds must be adjusted by the user and adapted to each data set. Beside, this is not a physical model of the chromosome architecture.

**Singular value decomposition of the spatial correlation matrix.** Let us consider the matrix  $R$  of size  $d \times N$ , where  $d$  is the space dimension and  $N$  is the number of bins in the Hi-C contact matrix. The matrix element  $r_{\alpha i}$  is therefore the spatial coordinate of loci  $i$  along the  $\alpha$ -axis ( $\alpha = x, y, z$ ). Next we consider the Singular Value Decomposition (SVD) of  $R$ :

$$r_{\alpha i} = \sum_{\gamma=1}^d \lambda_{\gamma} u_{\alpha\gamma} v_{i\gamma}, \quad (5.6)$$

where  $U$  and  $V$  are two orthogonal matrices, and  $\{\lambda_{\gamma}\}_{\gamma=1, \dots, d}$  are the singular values of  $R$ . Then  $C = R^T R$  and  $\tilde{C} = R R^T$  have the same non-zero eigenvalues, which are  $\lambda_1^2$ ,  $\lambda_2^2$  and  $\lambda_3^2$  (if  $d = 3$ ). Finally we introduce the matrix of distances,  $D$ , with elements:

$$d_{ij} = \sqrt{\sum_{\alpha=1}^d (r_{\alpha i} - r_{\alpha j})^2}. \quad (5.7)$$

It was pointed out that the correlation matrix  $C$  can be obtained from the distance matrix  $D$  [34, 152]. Therefore, from the knowledge of the distances, one can infer the singular values of the coordinates matrix, and obtain an approximation for  $R$ .

**Relation between contact probability and average distance.** The methods that we have presented have the inconvenient to rely on an estimate of the distances between loci on the chromosome, taken to be inversely proportional to the contact probabilities, *i.e.*  $d_{ij} \propto 1/c_{ij}$ . This assumption can be called into question.

### 5.3.1.2 Polymer models

Models presented in section 5.3.1.1 lack a physical model of the chromosome. In clear, the Hi-C bins define a gas of particles with coordinates  $\{\mathbf{r}_i\}$  and minimizing eq. (5.4) (resp. solving eqs. (5.5) and (5.7)) can result in configurations that violate topological constraints of the polymer chain representing the chromosome. Therefore, subsequent improvements have consisted in incorporating a polymer model of the chromosome when attempting to reconstruct chromosome architecture.

**Random walk backbone with tethered loops.** Another way to look at Hi-C data is to consider that when the contact probability between loci  $i$  and  $j$  is high enough, it defines a DNA loop. This is the approach taken in [153]. In short, whenever

$$c_{ij} > \underline{c}, \quad (5.8)$$

with an arbitrary lower bound  $\underline{c}$  on the contact probability, the authors considered that the DNA subchain in the interval  $[i, j]$  constitutes a loop, with  $\mathbf{r}_i = \mathbf{r}_j$ . The chromosome is then represented by a backbone polymer with Gaussian statistics on which are tethered polymer loops with varying sizes (fig. 5.3c). Numerical simulations are then performed on the basis of this polymer model of the chromosome.

Although this backbone-with-loops model takes into account some sort of connectedness of the chromosome as a polymer, it is an *ad hoc* model and therefore can only give rather qualitative insights.

### 5.3.1.3 Discussion on the relation between distances and contact probabilities

The methods introduced in section 5.3.1.1 assume that the distance between any restriction fragment pair  $(i, j)$  can be related to their contact probability in such a way that:

$$d_{ij} \propto 1/c_{ij}. \quad (5.9)$$

While eq. (5.9) may appear to be a reasonable assumption, there is no fundamental reason to support it. For instance, if we model the chromosome as a polymer with scaling exponent  $\nu$ , we have [53]:

$$\Pr(\mathbf{r}_{ij}) \simeq \frac{1}{\langle r_{ij} \rangle^d} f_p\left(\frac{r_{ij}}{\langle r_{ij} \rangle}\right), \quad f_p(x) \underset{x \sim 0}{\sim} x^g \quad (5.10)$$

$$\langle r_{ij} \rangle \simeq b |i - j|^\nu$$

Let us consider that the contact probabilities are given by  $c_{ij} = \Pr(r_{ij} = b)$ , and write  $d_{ij} = \langle r_{ij} \rangle$ . Then, we obtain the relation:

$$d_{ij} \sim 1/c_{ij}^{1/(d+g)}. \quad (5.11)$$

For a Gaussian chain, we have  $g = 0$ , and for a self-avoiding chain,  $g = 1/3$ . Hence we obtain ( $d = 3$ ),  $d_{ij} \sim 1/c_{ij}^{0.33}$  and  $d_{ij} \sim 1/c_{ij}^{0.3}$ , in direct contradiction with eq. (5.9). Besides, we have seen that the contact probabilities are already an approximation obtained from the counts maps. Hence, this assumption on the relation between average distances and contact probabilities may add significant inaccuracies that one may want to avoid.

Following this line of thoughts, we emphasize that all the methods reviewed previously have in common to aim at a characterization of the 3D-folding of the chromosome. That is to say, the solution consists in a collection of coordinates  $\{\mathbf{r}_i^*\}$  that represent an average conformation of the Hi-C restriction fragments. Without rejecting the quality of the research carried out, let us emphasize that reducing chromosome architecture to a mere conformation is probably unrealistic. Indeed, co-localization of loci on the chromosome results from the effect of divalent (or multivalent) proteins. Such proteins have preferred binding sites which are commonly represented with a Position Weight Matrix (PWM) [135]. We may estimate the strength of the binding by considering contributions of about one  $k_B T$  per significant contact [125]. For H-NS, which binds widely on the genome, we have approximately three significant contacts. For CRP, which recognizes more specific sequences, we have approximately eight significant contacts. For more specific transcription factors, we may have of the order of fifteen significant contacts.

Therefore, we may consider that structuring proteins have a binding energy with DNA in the range  $\varepsilon = 3 - 15 k_B T$ . Consequently, as seen above, we may assess the probability to form a DNA loop between loci  $i$  and  $j$  as:

$$\Pr(i \leftrightarrow j) = \frac{1}{|i - j|^{\nu(d+g)}} e^{\beta\varepsilon}, \quad (5.12)$$

where  $\nu(d + g) = 2$  for a self-avoiding polymer chain with scaling exponent  $\nu = 3/5$ . For example, considering a relatively strong transcription factor, with  $\beta\varepsilon = 10 k_B T$ , the contact probability  $c_{ij} \simeq 1$  when  $|i - j| = 150$  monomers and falls quickly to zero for larger contour distances. Here a monomer typically represents the scale at which a beads-on-string polymer representation of the chromosome is valid, *i.e.* when the size of one monomer is of the order of the DNA fiber diameter. In bacteria for instance, the chromosome can be seen as a fiber of diameter  $2.5 \text{ nm} \simeq 7.5 \text{ bp}$ . In eukaryotes, a monomer typically represents  $3000 \text{ bp}$ . Yet, in Hi-C contact matrices a bin typically represent  $10^3 - 10^6 \text{ bp}$  [34, 35]. This suggests that loops interactions between loci identified with Hi-C data are rather weak. In other words, thermodynamic fluctuations may provide the chromosome folding with a non negligible conformational entropy. In particular it seems a bit awkward to reduce the chromosome architecture to an average conformation.

### 5.3.2 A polymer model reproducing experimental contact frequencies

Instead of finding a chromosome folding which satisfies constraints on the monomer pair distance  $d_{ij}$ , an alternative approach is to seek a physical model of the chromosome which reproduces the experimental contact probabilities. This has been proposed and investigated with BD simulations [50, 154]. However, as mentioned earlier, due to the complexity of chromosome interactions with proteins, this kind of studies could only be made under strong simplifying assumptions. In particular, a unique generic type of protein is included and the variety in the binding energies with different loci on the chromosome is replaced by a single binding energy (or just a few). Consequently, comparisons with experimental contact matrices have been rather qualitative.

If such simplifications are performed, we put forward the idea that chromosome architecture might be well described with an effective model in which microscopical details, such as proteins and sequence effects, are coarse-grained. In particular, the effect of structuring proteins can be taken into account implicitly by introducing an effective potential  $V_{ij}(r)$  between each  $(i, j)$  monomer pair. In other words, each location on the genome experiences an effective interaction with the other loci on the genome, which mimics the effect of multivalent proteins. An inspiring approach was carried out recently, in which such potentials are considered to be short-range square potentials [155]:

$$V_{ij}(r) = \begin{cases} +\infty & \text{if } r < \sigma \\ -\varepsilon_{ij} & \text{if } \sigma < r < \xi \\ 0 & \text{otherwise,} \end{cases} \quad (5.13)$$

where  $\sigma$  is the hard-core distance and  $\xi$  is a threshold which defines at the same time the range of the potential and the distance below which monomers  $i$  and  $j$  are said to be in contact. By performing MC simulations on a polymer model with the pair potentials in eq. (5.13), one can obtain equilibrium configurations and use them to compute contact probabilities between monomer pairs.

Let us note  $c_{ij}^{exp}$  the experimental contact probability between restriction fragments  $i$  and  $j$  obtained from Hi-C experiments, and  $c_{ij}$  the contact probability between monomers  $i$  and  $j$  obtained from MC

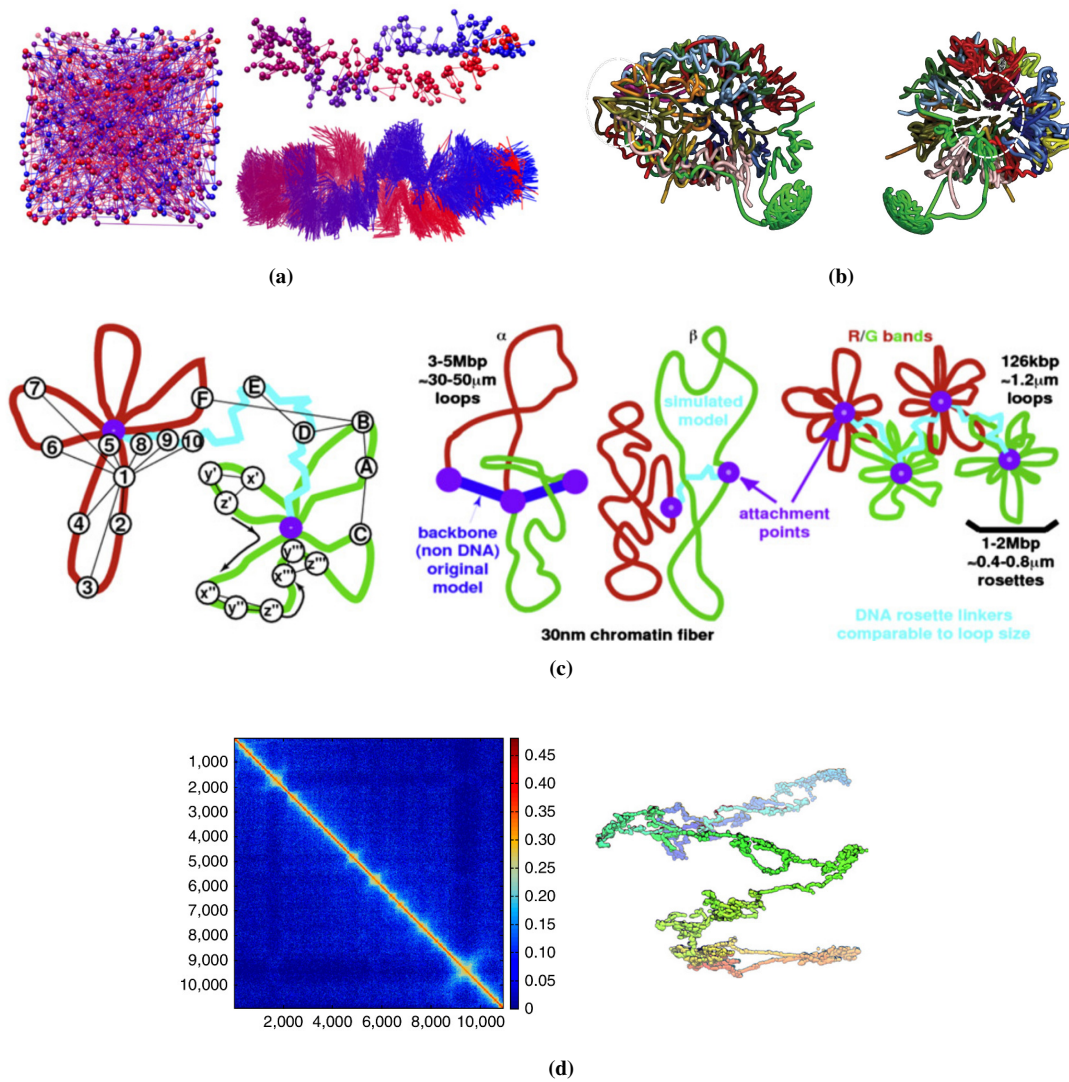


**Figure 5.3** – Models for reconstructing chromosome architecture. (a) Harmonic model [142]. (b) Constraint satisfaction model [140]. (c) Random walk with tethered loops [153]. (d) Singular value decomposition of the correlation matrix [152].

simulations of a polymer model with potentials as in eq. (5.13). We define the least-square distance between the experimental and the predicted contact matrices:

$$d(c_{ij}, c_{ij}^{exp}) = \frac{1}{\mathcal{N}} \sum_{i < j} (c_{ij} - c_{ij}^{exp})^2, \quad (5.14)$$

where  $\mathcal{N}$  is the number of monomer pairs. Finding a good model for chromosome architecture now consists in finding a collection of potentials  $V_{ij}(r)$  that minimize  $d(c_{ij}, c_{ij}^{exp})$ . The solution is achieved at the optimal values for  $\sigma$ ,  $\xi$  and the matrix of binding energy  $\varepsilon_{ij}$ .

In [155], a MC simulation was performed at each step of the minimization procedure, in order to re-sample equilibrium configurations of the chromosome and compute the  $c_{ij}$  values. Therefore the computational burden is high.

Following these tracks, we propose in the sequel a method giving a chromosome architecture under the form of a physical model that predicts contact probabilities which match as closely as possible the experimental ones. Our approach retains some of the features introduced here, namely the representation of the chromosome with a coarse-grained polymer and effective interactions.

## 5.4 Gaussian Effective Model

### 5.4.1 Model

From now on, we model the chromosome as a polymer of length  $N$ , *i.e.* made of  $N + 1$  monomers with coordinates  $\{\mathbf{r}_i\}$ . Each monomer represents a Hi-C bin with size  $b$ . We assume that the chromosome can be well modeled by a Gaussian chain with energy:

$$\beta U_e [\{\mathbf{r}_i\}] = \frac{3}{2b^2} \sum_{i=1}^N (\mathbf{r}_i - \mathbf{r}_{i-1})^2, \quad (5.15)$$

where as usual  $\beta = (k_B T)^{-1}$ . For a more accurate theory, one may include an additional term to eq. (5.15) in order to model the chain bending rigidity:

$$\beta U_b [\{\mathbf{r}_i\}] = \frac{l_p}{2} \sum_{i=1}^{N-1} (\mathbf{r}_{i+1} + \mathbf{r}_{i-1} - 2\mathbf{r}_i)^2, \quad (5.16)$$

where  $l_p$  is the chain persistence length. In that case, the total chain energy is given by

$$\beta U_0 [\{\mathbf{r}_i\}] = \beta U_e [\{\mathbf{r}_i\}] + \beta U_b [\{\mathbf{r}_i\}]. \quad (5.17)$$

However, we have seen earlier that Hi-C experiments have a resolution which typically gives  $b \approx 10^3 - 10^6$  bp. Therefore, as a first approximation, we choose to neglect the bending rigidity of the chromosome and take  $\beta U_0[\{\mathbf{r}_i\}] = \beta U_e[\{\mathbf{r}_i\}]$ . We now introduce effective interactions between the monomers under the form of harmonic potentials with unknown rigidity constants. The interaction energy reads

$$\beta U_I [\{\mathbf{r}_i\}] = \frac{3}{2b^2} \sum_{i < j} k_{ij} (\mathbf{r}_i - \mathbf{r}_j)^2, \quad (5.18)$$

where a coupling matrix  $K$  with elements  $k_{ij}$  has been introduced. Finally, the total energy (or Hamiltonian) is defined by

$$\beta U [\{\mathbf{r}_i\}] = \beta U_0 [\{\mathbf{r}_i\}] + \beta U_I [\{\mathbf{r}_i\}]. \quad (5.19)$$

The physical system with energy as in eq. (5.19) defines the Gaussian Effective Model (GEM). It simply corresponds to a Gaussian chain model of the chromosome to which are added harmonic interactions between monomer pairs  $(i, j)$ , which are effective interactions representing the superimposition of many microscopic interactions (fig. 5.4). Before writing down the partition function, let us point out that this system is ill-defined at this stage. To break the translational invariance, we attach the first monomer to the origin and consider  $\mathbf{r}_0 = 0$ . After this preliminary remark, we can write the GEM partition function. The energy in eq. (5.19) is quadratic, hence the partition function is computed as a Gaussian integral:

$$\begin{aligned} Z &= \int \prod_{i=1}^N d^3 \mathbf{r}_i \exp(-\beta U[\{\mathbf{r}_i\}]) \\ &= \int \prod_{i=1}^N d^3 \mathbf{r}_i \exp\left(-\frac{3}{2b^2} \sum_{i,j} \mathbf{r}_i \cdot \mathbf{r}_j \sigma_{ij}^{-1}\right) \\ &= \left(\frac{2\pi b^2}{3}\right)^{3N/2} \det \Sigma^{3/2}, \end{aligned} \quad (5.20)$$

where we have introduced the inverse correlation matrix with elements  $\sigma_{ij}^{-1}$ :

$$\Sigma^{-1} = T + W, \quad (5.21)$$

with:

$$T = \begin{pmatrix} 2 & -1 & \dots & 0 & 0 \\ -1 & 2 & \dots & 0 & 0 \\ \vdots & \vdots & \ddots & \vdots & \vdots \\ 0 & 0 & \dots & 2 & -1 \\ 0 & 0 & \dots & -1 & 1 \end{pmatrix}, \quad W = \begin{pmatrix} \sum_{\substack{j=0 \\ j \neq 1}} k_{1j} & -k_{12} & \dots & -k_{1N-1} & -k_{1N} \\ -k_{21} & \sum_{\substack{j=0 \\ j \neq 2}} k_{2j} & \dots & -k_{2N-1} & -k_{2N} \\ \vdots & \vdots & \ddots & \vdots & \vdots \\ -k_{N-11} & -k_{N-12} & \dots & \sum_{\substack{j=0 \\ j \neq N-1}} k_{N-1j} & -k_{N-1N} \\ -k_{N1} & -k_{N2} & \dots & -k_{NN-1} & \sum_{\substack{j=0 \\ j \neq N}} k_{Nj} \end{pmatrix}. \quad (5.22)$$

$T$  is the tridiagonal matrix enforcing the chain structure from eq. (5.15) and  $W$  is the matrix of reduced couplings enforcing the interactions from eq. (5.18). Being a Gaussian model, the system is fully determined by its correlation matrix. In particular, we have:

$$\langle \mathbf{r}_i \cdot \mathbf{r}_j \rangle = \sigma_{ij} b^2, \quad (5.23)$$

where the brackets stand for a thermodynamical average with a Boltzmann weight defined from the partition function in eq. (5.20), *i.e.* for any function of the monomer coordinates,  $A(\{\mathbf{r}_i\})$ :

$$\langle A(\{\mathbf{r}_i\}) \rangle = \frac{1}{Z} \int \prod_{i=1}^N d^3 \mathbf{r}_i A(\{\mathbf{r}_i\}) \exp(-\beta U[\{\mathbf{r}_i\}]). \quad (5.24)$$

Note that when  $W = 0$ , we retrieve the standard Gaussian chain with  $\langle \mathbf{r}_i \cdot \mathbf{r}_j \rangle = \min(i, j) b^2$ . Let us emphasize that the GEM is stable only when  $\Sigma$  has all its eigenvalues strictly positive. Therefore not every choice of coupling matrix  $K$  leads to a physical model.

Polymer models with Gaussian interaction Hamiltonian as defined in eq. (5.18) have received some attention in the past. They were introduced in the context of cross-linked polymers, in order to predict the size of a collapsed polymer of size  $N$  with  $M$  cross-links [156–158]. However, an essential difference with the GEM presented here is that in those studies, the effective interactions were uniform, *i.e.*  $k_{ij} = k$ . More recently, such model has been re-introduced to account for the particular scaling of the gyration radius of the chromosome in the interphase nucleus [159]. More accurately, the radius of gyration is reaching a plateau for genomic distances larger than a few Mbp,  $\langle R_g^2 \rangle \sim O(1)$ . This scaling was recovered by considering the above GEM model, in which the  $k_{ij}$  are Bernoulli random variables with probability distribution function (p.d.f.) such that  $\Pr(k_{ij} = k) = p\delta(k_{ij} - k) + (1 - p)\delta(k_{ij})$ . Under this assumption, each non-zero value  $k_{ij}$  defines a loop between monomer  $i$  and  $j$  with harmonic spring constant  $k$ . For this reason, this model was named Random Loop Model. The theoretical results obtained on the radius of gyration scaling were confirmed later with BD simulations [160].

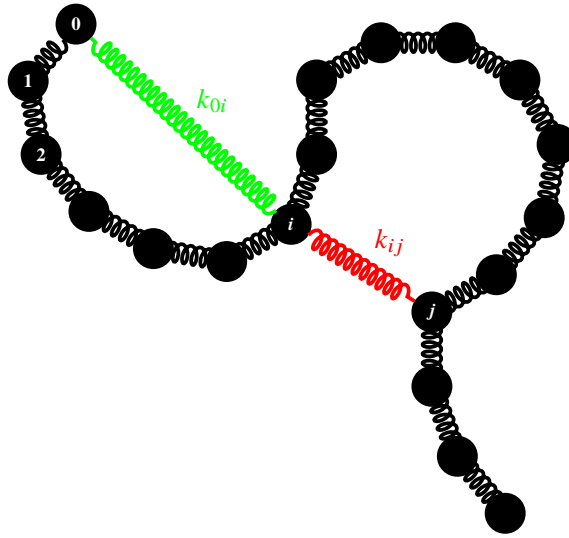


**Figure 5.4** – Gaussian Effective Model. Harmonic interactions with elastic coefficient  $k_{ij}$  are added on top of the Gaussian polymer model.

## 5.4.2 Naive approach

### 5.4.2.1 Rationale

As argued in section 5.3.2, a reasonable strategy seems at first to seek the coupling matrix  $K$  which minimizes  $d(c_{ij}, c_{ij}^{exp})$ , as defined in eq. (5.14), between the experimental contact probabilities and the ones predicted by the GEM. The optimal coupling matrix,  $K^{opt}$  can then be used as a model for chromosome architecture. Intuitively, one may expect the contact probabilities to be proportional to the values of the couplings:

$$k_{ij} = \Lambda c_{ij}, \quad (5.25)$$

where  $\Lambda$  is a scaling coefficient which needs to be adjusted. For each value of  $\Lambda$ , we can run BD simulations in order to sample equilibrium configurations of the corresponding GEM. Then, for any  $(i, j)$

pair of monomers, we can compute the contact probabilities as:

$$c_{ij} = \langle \theta(\xi - r_{ij}) \rangle, \quad (5.26)$$

where the brackets here mean that we perform an average over the system configurations,  $\theta$  is the theta function (*i.e.* the indicator function of  $\mathbb{R}_+$ ), and  $\xi$  is a threshold distance below which a contact is said to occur. Therefore the computed contact probabilities depend on the coupling scale  $\Lambda$  and on the threshold  $\xi$ . However, the threshold is clearly arbitrary and should be chosen in order to best fit the experimental contacts. Therefore, we may define the optimal threshold  $\xi^{opt}$  that minimizes the contacts least-square distance:

$$\xi^{opt}(\Lambda) = \operatorname{argmin}_{\xi} [d(c_{ij}, c_{ij}^{exp})], \quad c_{ij}^{opt}(\Lambda) = c_{ij}(\Lambda, \xi^{opt}). \quad (5.27)$$

and similarly, we may define the optimal scale,  $\Lambda^{opt}$  as:

$$\Lambda^{opt} = \operatorname{argmin}_{\Lambda} [d(c_{ij}^{opt}, c_{ij}^{exp})]. \quad (5.28)$$

Since the method to compute the contact probabilities  $c_{ij}$  relies on BD simulations, we may consider other polymer models than the Gaussian chain defined in eq. (5.15). In particular, we can add excluded volume interactions between monomers.

#### 5.4.2.2 Application

We have applied this method to Hi-C data from the human chromosome 14 [35]. The experimental contact matrices were computed by applying either the ‘‘Trace’’ or ‘‘Maximum’’ method on the available counts map, as described in section 5.2.4. In fig. 5.5a, we show the experimental contact matrix obtained by using the ‘‘Maximum’’ normalization method with  $l_d = 2$ . The p.d.f. of the corresponding contact probabilities,  $c_{ij}^{exp}$ , is shown in fig. 5.5b.

In order to have a reasonable amount of non-zero  $k_{ij}$ , we fitted the  $c_{ij}^{exp}$  distribution with a sum of  $M$  Gaussian distributions, *i.e.*

$$\Pr(c_{ij}^{exp} = c) = \sum_{k=1}^M \alpha_k \frac{1}{\sqrt{2\pi\sigma_k^2}} \exp\left(-\frac{1}{2} \frac{(c - \mu_k)^2}{\sigma_k^2}\right). \quad (5.29)$$

We then considered the sum of the  $M^*$  dominant Gaussian distributions such that

$$\sum_{k \leq M^*} \alpha_k > \underline{\alpha}, \quad (5.30)$$

with  $\underline{\alpha} = 75\%$ . This defines a distribution  $f_b(c)$  for the bulk of the  $k_{ij}$ , with mean and standard deviation given by:

$$\begin{aligned} \mu_b &= \frac{\sum_{k=1}^{M^*} \alpha_k \mu_k}{\sum_{k=1}^{M^*} \alpha_k} \\ \sigma_b^2 &= \frac{\sum_{k=1}^{M^*} \alpha_k (\mu_k^2 + \sigma_k^2)}{\sum_{k=1}^{M^*} \alpha_k} - \mu_b^2, \end{aligned} \quad (5.31)$$

which we used to define the threshold:

$$\underline{c} = \mu_b + 3\sigma_b. \quad (5.32)$$

Therefore, the coupling matrix  $K$  was set using eq. (5.25), but we discarded all values such that  $c_{ij}^{exp} < \underline{c}$ . We applied this procedure for  $0 \leq \Lambda \leq 1$ , using a discretization such that  $d\Lambda = 2 \times 10^{-2}$ .

For the BD simulations, we modeled the chromosome as a flexible polymer with FENE bonds. We also introduced Lennard-Jones interactions to model excluded volume interactions between monomers. In order to sample equilibrium configurations, we first performed a relaxation run of  $10^7$  iterations with integration time step  $dt = 10^{-2}$  and without excluded volume interactions. The value of  $\Lambda$  was progressively increased to reach its final value. This relaxation run is meant to loose the memory of the initial condition and to sample many configurations without topological constraints. We then performed an intermediate run of  $10^6$  iterations with integration time step  $dt = 10^{-3}$  in which overlaps between monomers are removed. Finally, the main run consists of  $10^8$  iterations of Langevin dynamics with integration time step  $dt = 10^{-3}$ , in which the excluded volume interactions are modeled with a Lennard-Jones potential. From this final trajectory, we extracted  $10^3$  evenly sampled configurations that we used to compute the model contact probability matrix.

After sampling a BD trajectory for each value of  $\Lambda$ , we computed the model contact matrix for  $0 \leq \xi \leq 2$  with  $d\xi = 2 \times 10^{-2}$ , and selected the threshold minimizing the distance between experimental and predicted contacts. In fig. 5.5d we showed the distance  $d(c_{ij}^{opt}, c_{ij}^{exp})$  as a function of the couplings scale  $\Lambda$ . This distance reaches a minimum at  $\Lambda = \Lambda^{opt}$ , which corresponds to the optimal GEM given the experimental contacts. The coupling matrix at the optimal scale,  $K = K^{opt}$ , is shown in fig. 5.5e and the corresponding predicted contacts obtained with the optimal threshold applied to the BD trajectory is shown in fig. 5.5c.

### 5.4.2.3 Conclusion

We have presented here a simple method to model chromosome architecture. If we assume that a proportionality relation holds between couplings and contact probabilities, the value obtained for  $\Lambda^{opt}$  determines the closest GEM reproducing the experimental contacts. The proportionality hypothesis from eq. (5.25) requires solely to adjust the scale  $\Lambda$ , and the numerical procedure is therefore computationally less demanding than adjusting all  $k_{ij}$  independently as in [155]. However, it is clear that this proportionality assumption has no rigorous justification. *A fortiori* there is no better reason to choose this one rather than the  $d_{ij} \sim 1/c_{ij}$  assumption made in the literature. Therefore, in the sequel we present another approach rooted in an analytical expression of the contact probabilities  $c_{ij}$  of a GEM.

## 5.4.3 One-to-one correspondence between couplings and contact probabilities

We now investigate a more rigorous choice for the couplings  $k_{ij}$  of the GEM. Let us formally express the contact probability between monomers  $i$  and  $j$  as:

$$\begin{aligned} c_{ij} &= \langle \mu(r_{ij}) \rangle \\ &= \int d^3\mathbf{r} \mu(r) \langle \delta(\mathbf{r}_{ij} - \mathbf{r}) \rangle, \end{aligned} \quad (5.33)$$

where  $\mu(r) = \theta(\xi - r)$ . As before,  $\theta$  stands for the theta function and  $\xi$  is the threshold distance below which a contact is said to occur. In order to make progress, we need to express the p.d.f. of the pair

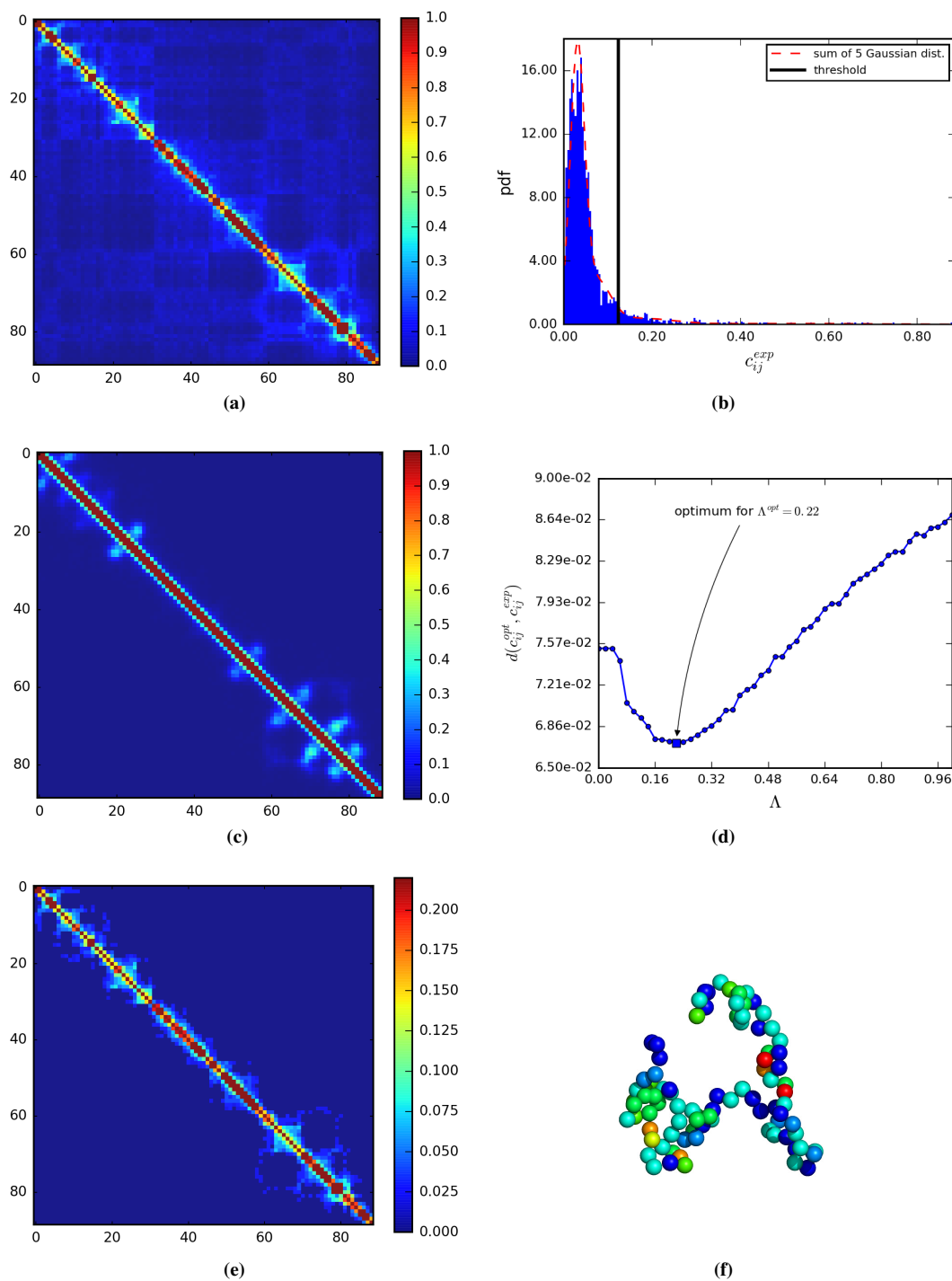


**Figure 5.5** – Application of a naive approach to identify an optimal GEM model matching the Hi-C contact matrix generated from ref. [35] with bin size 1 Mbp. (a) Experimental contact matrix constructed from the counts map using a “Maximum” normalization with  $l_d = 2$  (see section 5.2.4). (b) Probability distribution of the experimental contacts. A threshold is defined from a fit with a sum of Gaussian distributions. (c) Final contact matrix obtained from a Brownian dynamics trajectory with  $\Lambda^{opt} = 0.06$ . The threshold used to compute the contact probabilities is  $\xi^{opt} = 1.82$ . (d) Plot of the least-square distance  $d(c_{ij}^{opt}, c_{ij}^{exp})$ . Each point is obtained by performing a BD simulation and finding the optimal threshold  $\xi^{opt}$  that minimizes  $d(c_{ij}, c_{ij}^{exp})$ . (e) Coupling matrix  $k_{ij}^{opt}$  corresponding to the final GEM obtained by applying eq. (5.25) with  $\Lambda = \Lambda^{opt}$ . (f) Snapshot of a Brownian dynamics configuration for the optimal GEM with  $\Lambda = \Lambda^{opt}$ . The color represents the intensity of the bond rigidity between monomers pairs.

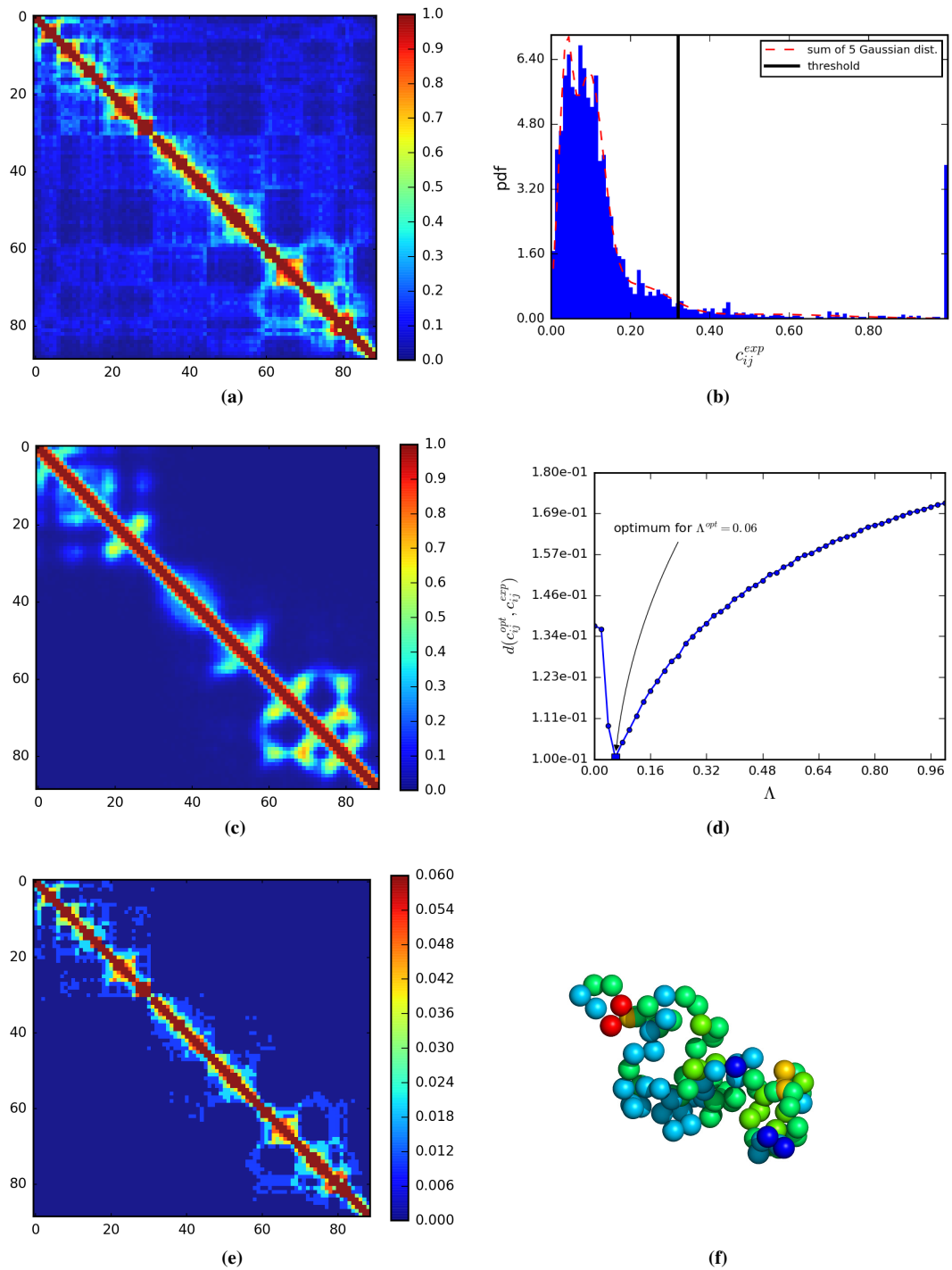


**Figure 5.6** – Same as fig. 5.5 but with a “Maximum” normalization with  $l_d = 3$  for the Hi-C contact probability matrix.

distance,  $\langle \delta(\mathbf{r}_{ij} - \mathbf{r}) \rangle$ . This quantity can be evaluated by standard Gaussian calculus using the weight in eq. (5.24). We obtain:

$$\langle \delta(\mathbf{r}_{ij} - \mathbf{r}) \rangle = \left( \frac{2\pi b^2 \gamma_{ij}}{3} \right)^{-3/2} \exp\left(-\frac{3}{2b^2} \frac{r^2}{\gamma_{ij}}\right), \quad (5.34)$$

where we have introduced the matrix  $\Gamma$  of the average square distances whose matrix elements are:

$$\begin{aligned} \gamma_{ij} &= \sigma_{ii} + \sigma_{jj} - 2\sigma_{ij} = \frac{1}{b^2} \langle r_{ij}^2 \rangle \quad \text{for } 0 < i < j \leq N, \\ \gamma_{0j} &= \sigma_{jj} = \frac{1}{b^2} \langle r_j^2 \rangle \quad \text{for } 0 < j \leq N. \end{aligned} \quad (5.35)$$

The pair distance is a Gaussian distribution, hence the integral in eq. (5.33) can be calculated and yields:

$$\begin{aligned} c_{ij} &= F_T(\gamma_{ij}) \\ &= \text{erf}\left(\frac{X}{\sqrt{2}}\right) - \sqrt{\frac{2}{\pi}} X \exp\left(-\frac{X^2}{2}\right), \quad X = \frac{\xi}{a} \sqrt{\frac{3}{\gamma_{ij}}}, \end{aligned} \quad (5.36)$$

where we have introduced the standard error function:

$$\text{erf}(x) = \frac{2}{\sqrt{\pi}} \int_0^x dt e^{-t^2}. \quad (5.37)$$

The function  $F_T(\gamma_{ij})$  is a bijection. Hence, to any contact probability  $c_{ij}$ , eq. (5.36) associates a unique average square distance  $\gamma_{ij}$ . The correlation matrix  $\Sigma$  of the GEM can then be determined using eq. (5.35), and finally the coupling matrix  $K$  can be obtained by inverting  $\Sigma$  and using eqs. (5.21) and (5.22). Thus, we have found a unique mapping between the couplings and the contact probabilities of a GEM. A strategy to infer chromosome architecture then consists in using this mapping to obtain the GEM that reproduces the experimental contact probabilities. Let us emphasize that this is an exact result.

#### 5.4.4 Form factors

So far, we have considered that the measure in eq. (5.33) was a theta function, *i.e.*  $\mu(r) = \mu_T(r)$  with

$$\mu_T(r) = \theta(\xi - r). \quad (5.38)$$

In the context of Hi-C experiments, this is equivalent to considering that every restriction fragment pair separated by a distance  $r < \xi$  is cross-linked. Or in other words, the probability that restriction fragments separated by a distance  $r$  cross-link is

$$\Pr(\text{cross-link between } i \text{ and } j \mid r_{ij} = r) = \begin{cases} 1 & \text{if } r < \xi \\ 0 & \text{otherwise.} \end{cases} \quad (5.39)$$

However, there are many experimental artefacts that make this assumption quite unrealistic. In particular as already pointed out in section 5.2.3, the chemical compound used to cross-link DNA, which is formaldehyde, is known to polymerize in aqueous solution. Thus formaldehyde oligomers with different polymerization indices are present in solution, resulting in cross-links with varying lengths. For

that reason, the cross-linking probability may be more accurately represented by a measure which ensures that most of the cross-links occur for distances  $r < \xi$ , but also allow for few cross-links to occur when  $r > \xi$ . To serve this purpose, we introduce a Gaussian measure:

$$\mu_G(r) = \exp\left(-\frac{3}{2} \frac{r^2}{\xi^2}\right), \quad (5.40)$$

and an exponential measure:

$$\mu_E(r) = \exp\left(-\frac{r}{\xi}\right). \quad (5.41)$$

Let us emphasize that the form factor  $\mu(r)$  is not a p.d.f. so it does not need to be normalized. It should rather be considered as a probability for a Bernoulli random variable. For a restriction fragment pair separated by a distance  $r$ , the probability to cross-link is  $\mu(r)$  and the probability not to cross-link is  $1 - \mu(r)$ . Note that  $\mu(0) = 1$ .

The contact probability in eq. (5.33) can be re-computed for each form factor to obtain a mapping between contact probabilities and couplings, similarly to eq. (5.36). We obtain for the Gaussian form factor:

$$\begin{aligned} c_{ij} &= F_G(\gamma_{ij}) \\ &= \left(1 + \frac{b^2 \gamma_{ij}}{\xi^2}\right)^{-3/2}, \end{aligned} \quad (5.42)$$

and for the exponential form factor:

$$\begin{aligned} c_{ij} &= F_E(\gamma_{ij}) \\ &= (1 + Y^2) \left(1 - \operatorname{erf}\left(\frac{Y^2}{2}\right)\right) \exp\left(\frac{Y^2}{2}\right) - Y \sqrt{\frac{2}{\pi}}, \quad Y = X^{-1} = \left(\frac{\xi}{a} \sqrt{\frac{3}{\gamma_{ij}}}\right)^{-1}. \end{aligned} \quad (5.43)$$

In addition to representing more faithfully the experimental conditions, the Gaussian and exponential form factors can be seen as regularization parameters for the contact probabilities. Namely, the saturation of  $c_{ij} \rightarrow 1$  as  $\gamma_{ij} \rightarrow 0$  is less pronounced than with the theta form factor (fig. 5.7). In that respect, the Gaussian form factor appears to be the best because  $F_G(\gamma_{ij})$  tends to have a greater slope for  $c_{ij}$  in the range 0.1-1.0. Thus it is less sensitive to inaccuracies in the measured contact probabilities.

### 5.4.5 Conclusion

In conclusion, we have introduced a physical model for chromosome architecture. We called this model a Gaussian Effective Model because all interactions between loci on the chromosome have been replaced by effective Gaussian potentials with rigidity coefficients  $k_{ij}$ . Within this simplified framework, we have been able to compute an analytical expression for the contact probability  $c_{ij}$  between monomers  $i$  and  $j$ . It turns out that the contact probability matrix is uniquely determined by the couplings, and reciprocally. We will sometimes refer to this property as the ‘‘GEM mapping’’ in the sequel. Importantly, this mapping relies on the choice of a threshold  $\xi$  and on a form factor  $\mu$ . We have found that a Gaussian form factor has the advantage of decreasing the mapping sensitivity to the inaccuracies in the  $c_{ij}$  values, and account for formaldehyde polymerization which results in Hi-C contacts to be detected for distances of varying lengths.

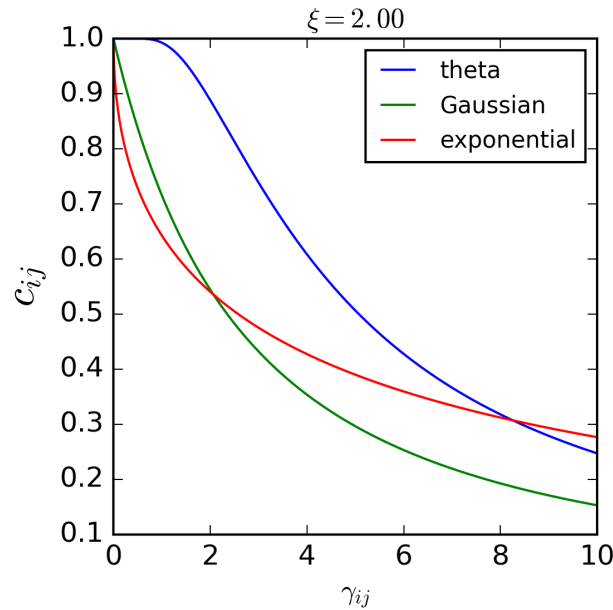


**Figure 5.7** – Comparison of mappings between contact probabilities and average square distances for the theta, Gaussian and exponential form factors. The functions are defined in eqs. (5.36), (5.42) and (5.43). We used  $b = 1$ .

## 5.5 Reconstruction from artificial contact probability matrices

### 5.5.1 Artificial contact probability matrices

We plan to use the GEM mapping as a method to give a prediction of chromosome architecture from Hi-C contact probabilities under the form of a GEM. In order to validate the method, we first apply it to artificial contact matrices generated with BD simulations from GEM whose couplings  $k_{ij}^{th}$  are known. We have carried out this validation for various sizes ranging from  $N + 1 = 20$  to  $N + 1 = 1000$ . However, in this section, we present the results for  $N + 1 = 200$  because it is a reasonable compromise between a not-too-small contact matrix, and not-too-large computational time for BD simulations.

In order to construct arbitrary coupling matrices  $k_{ij}^{th}$ , we randomly choose  $N_c$  elements and assign to them a value such that:

$$k_{ij}^{th} = \Lambda U, \quad (5.44)$$

in which  $U$  is a uniform random variable between 0 and 1, and  $\Lambda$  is a scale parameter. We therefore obtain a coupling matrix with  $N_c$  non-zero elements, which represent the number of constraints of the GEM. An example of such a matrix is shown in fig. 5.8.

Using the one-to-one mapping between the coupling matrix and the contact probability matrix of a GEM, we can compute the theoretical contact probabilities,  $c_{ij}^{th}$ , associated to the theoretical couplings  $k_{ij}^{th}$  of the model. In order to check the validity of this mapping, we run BD simulations of a GEM with the aforementioned couplings. The chain internal energy was Gaussian, as defined in eq. (5.15). Simulations were run for  $10^8$  iterations with integration time step  $dt = 10^{-3}$ , from which 1000 configurations evenly sampled were extracted in order to compute the experimental contact matrix  $c_{ij}^{exp}$ , with threshold  $\xi^{exp}$

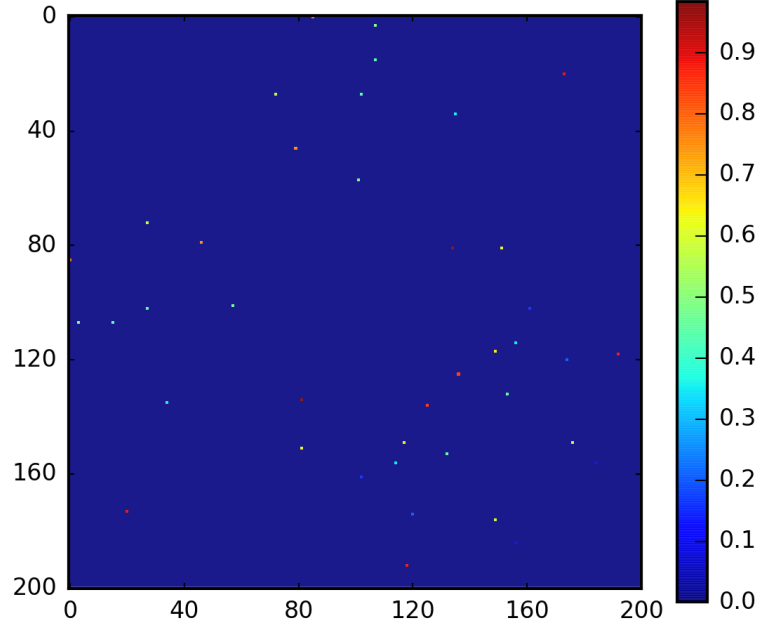


**Figure 5.8** – Theoretical coupling matrix  $k_{ij}^{th}$  for  $N = 200$ . It is made of  $N_c = 20$  uniform random variable with scale  $\Lambda = 1$ .

and form factor  $\mu^{exp}$ . Note the distinction that we have introduced for the form factors. Indeed, we need to use a theoretical form factors  $\mu^{th}$  when computing the theoretical contact probabilities  $c_{ij}^{th}$  from the theoretical couplings; and we also need to specify a form factor  $\mu^{exp}$  which is used to compute the contact probabilities  $c_{ij}^{exp} = \langle \mu^{exp}(r_{ij}) \rangle$  from configurations sampled with BD simulations. In the sequel, unless stated otherwise, we used a Gaussian form factor to compute both the theoretical and experimental contacts, *i.e.*  $\mu^{th} = \mu^{exp} = \mu_G$ . As shown in fig. 5.9, the theoretical and experimental contact probability matrices are in very good agreement. The difference can be attributed to thermal fluctuations and the finite number of configurations used to compute the experimental contacts.

In conclusion, the correspondence found in section 5.4 between couplings and contact probabilities of a GEM has been checked with BD simulations. We now move on to use this relation in order to infer the couplings from a given experimental contact probability matrix. In the rest of this section, we will call experimental contact probabilities the probabilities computed from BD simulations.

## 5.5.2 Direct method for reconstructing a Gaussian effective model

Here we provide a first method to derive chromosome architecture from experimental contacts. We shall use the GEM mapping to express the model average square distances from the experimental contacts:

$$\hat{\gamma}_{ij} = F_G^{-1}(c_{ij}^{exp}) \quad (5.45)$$

where we used hats to emphasize that this is a prediction of GEM matching the experimental contacts. Actually, because the previous relation is exact, the predicted and experimental contacts are the same and  $\hat{c}_{ij} = c_{ij}^{exp}$ . The predicted couplings,  $\hat{k}_{ij}$ , can then be simply computed using eqs. (5.21) and (5.35). Thus this method is quite straightforward.

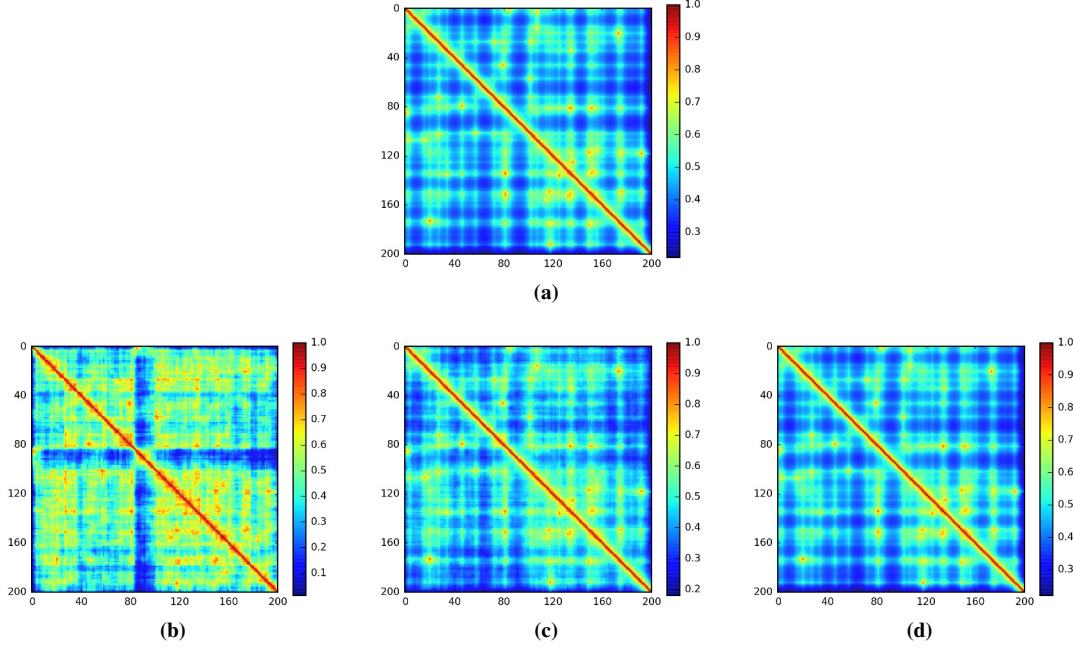


**Figure 5.9** – (a) Theoretical contact probability matrix  $c_{ij}^{th}$  computed from the GEM with couplings  $k_{ij}^{th}$  ( $N_c = 20$  and  $\Lambda = 1$ ). (b), (c) and (d) Experimental contact probability matrix  $c_{ij}^{exp}$  obtained from BD simulations of the GEM using 10, 100 or 1000 sampled configurations. We used  $\xi^{th} = \xi^{exp} = 3.00$  and  $\mu^{th} = \mu^{exp} = \mu_G$ .

However, what should be the threshold  $\xi$  used in eq. (5.45)? In section 5.4.2, free parameters were adjusted in order to minimize the distance between predicted and experimental contacts. But precisely because  $\hat{c}_{ij} = c_{ij}^{exp}$ , we cannot hope to use this method to find the optimal threshold  $\xi^{opt}$ . In the present case, because we know the couplings of the underlying GEM model used to generate the experimental contacts, it is pretty obvious that the optimal threshold should minimize  $d(k_{ij}, k_{ij}^{th})$ . In other words, the predicted couplings should be as close as possible to the theoretical ones. Consequently, we define:

$$\xi^* = \underset{\xi}{\operatorname{argmin}}(d(k_{ij}, k_{ij}^{th})), \quad (5.46)$$

which can be seen as a hidden optimal threshold.

In practical applications however, experimental contact matrices are not generated from an underlying GEM, therefore we have to find another criterion to choose the threshold in the reconstruction procedure. Intuitively, one may expect that a good GEM candidate should not alter the rigidity of the underlying polymer chain. In other words, couplings near the diagonal should be close to zero, so that the sum in eq. (5.21) on page 111 leaves the  $t_{ij}$  elements unchanged. In order to do this, we monitored the norm of the matrix  $\Delta_l$  obtained by taking only  $k_{ij}$  values such that  $|i - j| \leq l$ , and assigning other values to zero. Thus we define:

$$\xi^{opt} = \underset{\xi}{\operatorname{argmin}} \|\Delta_l\|. \quad (5.47)$$

In fig. 5.10, we show that  $d(k_{ij}, k_{ij}^{exp})$  and  $\|\Delta_l\|$  have approximately the same variations, and in most cases, their minimum is achieved for the same threshold, *i.e.*  $\xi^* = \xi^{opt}$ . For the experimental contact matrices computed from the same BD trajectory, we used either a Gaussian form factor ( $\mu^{exp} = \mu_G$ )

or an exponential form factor ( $\mu^{exp} = \mu_E$ ). We then applied eq. (5.45) with a Gaussian form factor in both case to obtain a candidate GEM. Note that we did not show the result for an experimental contact matrix using a theta form factor ( $\mu^{exp} = \mu_T$ ) because the inversion procedure gave an unstable GEM (the correlation matrix is not positive definite). When applying the retrieval method to the Gaussian contact matrix we retrieve that the optimal threshold is  $\xi^{opt} = \xi^{exp}$ . On the contrary, when we apply the retrieval method to the exponential contact matrix, we have  $\xi^{opt} \neq \xi^{exp}$ . This is due to the discrepancy between the exponential form factor used to compute the experimental contacts and the Gaussian form factor of the retrieval method ( $\mu \neq \mu^{exp}$ ). Furthermore, we see that when there is such a discrepancy, the variations of both criteria become jagged as the threshold  $\xi$  used in the retrieval method increases (fig. 5.10b). This leads to the existence of several local minima that makes the definition of the optimal threshold in eq. (5.47) ambiguous. To solve this ambiguity, we took for  $\xi^{opt}$  the first local minimum found from the left, *i.e.* when increasing progressively the threshold from small values.

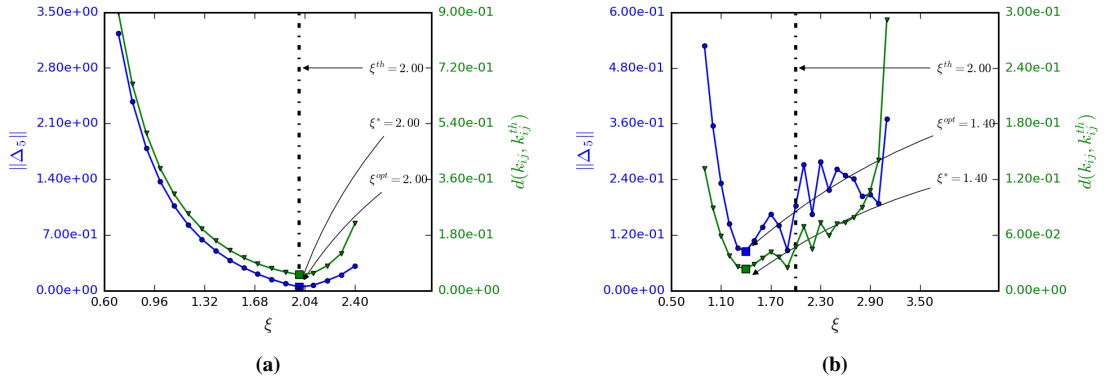


**Figure 5.10** – Comparison of  $d(\hat{k}_{ij}, k_{ij}^{th})$  and  $\|\Delta_5\|$  for different thresholds in the direct reconstruction procedure with  $\mu = \mu_G$ . Experimental contact matrix  $c_{ij}^{exp}$  were computed from a BD trajectory using a threshold  $\xi^{exp} = 2.00$  and: (a) a Gaussian form factor  $\mu^{exp} = \mu_G$ ; (b) an exponential form factor  $\mu^{exp} = \mu_E$ .

Nonetheless, we do not always find  $\xi^{opt} = \xi^*$ . This is expected because the criterion used to define  $\xi^{opt}$ , that is to say  $\|\Delta_l\|$ , is rather phenomenological. Therefore, we investigated to which extent this criterion can be trusted in order to find the best GEM matching the experimental contacts. In order to do this, we computed the least-square distance between  $\xi^{opt}$  and  $\xi^*$  obtained for a large number of experimental contacts:

$$\chi^2(\xi_a^{opt}, \xi_a^*) = \frac{1}{2} \sum_a |\xi_a^{opt} - \xi_a^*|^2, \quad (5.48)$$

where the index  $a$  runs over different experimental contact matrices. More accurately, we sampled BD trajectories for a number of constraints  $N_c = 5, 20, 50, 100$  and scaling coefficient  $\Lambda = 1, 5, 10$ , from which we computed experimental contact matrices using either a Gaussian ( $\mu^{exp} = \mu_G$ ) or an exponential form factor ( $\mu^{exp} = \mu_E$ ). We then applied the retrieval procedure and computed  $\xi^{opt}$  and  $\xi^*$  as explained above. The results obtained suggest that  $\xi^{opt}$  is a good approximation of  $\xi^*$  (fig. 5.11). Actually, we also carried out this analysis for other criteria. Namely we monitored:  $\|K\|$ , the Froebenius norm of the coupling matrix;  $|K| = \sum |k_{ij}|$ ;  $\max(K) = \max(k_{ij})$  and  $\text{entr}(K)$ , the entropy of the p.d.f. of the couplings  $k_{ij}$ . Yet,  $\|\Delta_l\|$  appeared to be the best criterion in the sense of eq. (5.48). We also found that important deviations of  $\xi^{opt}$  from  $\xi^*$  occurred mostly for experimental contact matrices obtained from

GEM with very few constraints or with a large couplings scale  $\Lambda$ . Indeed, the same analysis carried out by discarding GEMs with  $N_c = 5$  and  $\Lambda > 1$  significantly improved the performances of the  $\|\Delta_l\|$  criterion (fig. 5.12). Finally, most deviations of  $\xi^{opt}$  from  $\xi^*$  occurred when  $\mu^{exp} \neq \mu$ . In that case,  $\xi^{opt}$  has a tendency to slightly overestimate  $\xi^*$ . Altogether, the definition taken for  $\xi^{opt}$  gave consistent results.

In conclusion, the bijective relation that exists between the couplings and the contact probabilities of a GEM can be used to propose a chromosome architecture under the form of a GEM with couplings  $\hat{k}_{ij}$ . The GEM obtained has the property to exactly reproduce the experimental contacts. However, the computation of the GEM couplings from the contact probabilities requires to choose a threshold, which is a parameter in the form factor (see eq. (5.40) on page 118). In this section, we have shown that choosing the threshold that minimizes the norm  $\|\Delta_l\|$ , where  $\Delta_l$  is the matrix of couplings in which only the diagonal band of length  $l$  has been retained, appeared to be a good estimate of the optimal threshold. In particular, we used home-made GEMs together with their contact matrices computed from BD simulations to ensure that the distance  $d(\hat{k}_{ij}, k_{ij}^{th})$  between predicted and theoretical couplings is minimum at  $\xi = \xi^{opt}$ . From a computational standpoint, this method is particularly efficient since it only requires to invert the correlation matrix  $\Sigma$  in order to obtain the coupling matrix  $\hat{k}_{ij}$ .

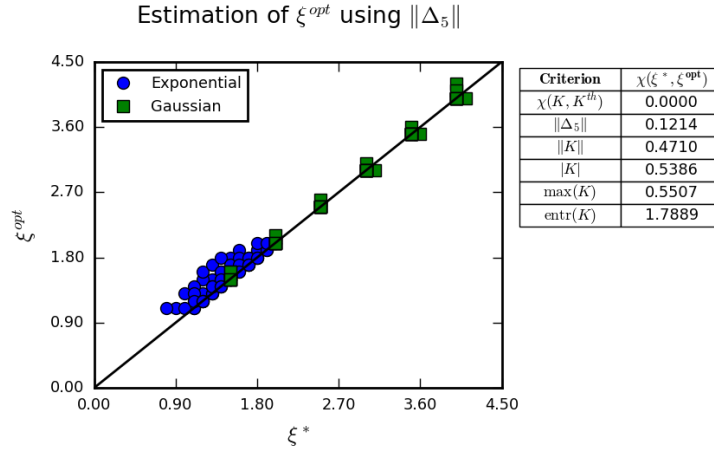


**Figure 5.11** – Least-square difference between  $\xi^{opt}$  and  $\xi^*$ . The points correspond to the optimal threshold obtained using the  $\|\Delta_5\|$  criterion. We used the direct reconstruction procedure applied to experimental contact matrices computed from BD simulations of a GEM with  $N = 200$ ,  $N_c = 5, 20, 50, 100$  and  $\Lambda = 1, 5, 10$ , and using a Gaussian or an exponential form factor  $\mu^{exp}$ . The form factor used in the retrieval procedure was Gaussian,  $\mu = \mu_G$ .

### 5.5.3 Stability analysis

In the last section, we have presented a method to compute the GEM reproducing a given experimental contact probability matrix. However, nothing ensures that the GEM obtained is stable, *i.e.* that the correlation matrix  $\Sigma$  has only positive eigenvalues. Incidentally, we found that applying the direct reconstruction method to contact matrices generated using a theta form factor (which is maybe the simplest definition of a contact matrix) resulted in unstable GEMs. This is a fundamental weakness of the direct reconstruction method, and it is therefore desirable to better understand under which conditions such instabilities occur. In particular, we may expect that Hi-C contact matrices contain some noise due

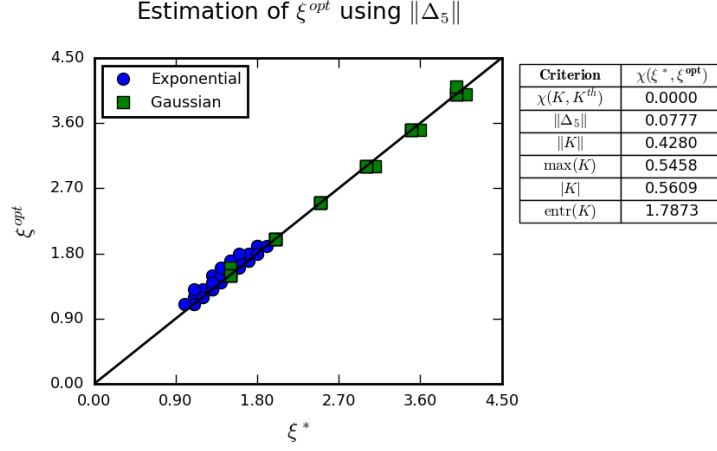


**Figure 5.12** – Same as fig. 5.11 but with  $N_c = 20, 50, 100$  and  $\Lambda = 1$  only.

to inaccuracies in the measures or biases inherent to the experimental procedure. Thus, before presenting an alternative method in the next section, we analyze here the effect of corrupting contact probability matrices with noise on the performance of the direct reconstruction method.

Let us start again from our artificial GEM with couplings  $k_{ij}^{th}$ . We compute the associated contact matrix  $c_{ij}^{th}$ , using a threshold  $\xi^{th}$  and a form factor  $\mu^{th}$ . When we perform BD simulations of this system, we obtain configurations from which we compute the experimental contact matrix  $c_{ij}^{exp}$ , using a threshold  $\xi^{exp}$  and a form factor  $\mu^{exp}$ . We assume  $\mu^{th} = \mu^{exp}$ . Thermal fluctuations, together with the finite number of such configurations results in  $c_{ij}^{exp} \neq c_{ij}^{th}$ . We may therefore write the experimental contact probabilities as:

$$c_{ij}^{exp} = c_{ij}^{th} + \eta_{ij}, \quad (5.49)$$

where  $\eta_{ij}$  can be considered as a noise with unknown distribution, corrupting the “true” contact matrix. For  $N = 200$ ,  $N_c = 20$  and  $\Lambda = 1$ , we computed the p.d.f. of the difference  $c_{ij}^{th} - c_{ij}^{exp}$ . We used a Gaussian form factor for both the experimental and the theoretical contact matrices,  $\mu^{th} = \mu^{exp} = \mu_G$ , and we took  $\xi^{exp} = 2.50$  and different values for  $\xi^{th}$  (fig. 5.13). We obtained that when  $\xi^{th} = \xi^{exp}$  the p.d.f. of  $\eta_{ij}$  fits well a centered Gaussian distribution. Actually, we also obtained this result when computing the noise with  $\mu^{exp} = \mu^{th} = \mu_E$  or  $\mu^{exp} = \mu^{th} = \mu_T$ .

Consequently, instead of running BD simulations in order to compute experimental contact matrices  $c_{ij}^{exp}$ , we may construct pseudo-experimental contact matrices by adding a Gaussian noise with mean and variance given by

$$\langle \eta_{ij} \rangle = 0, \quad \langle \eta_{ij}^2 \rangle = \varepsilon^2, \quad (5.50)$$

to the theoretical contact matrix  $c_{ij}^{th}$ . This trick allows us to investigate the stability of the direct reconstruction method as a function of the noise amplitude  $\varepsilon$ . Furthermore, it also allows us to explore more values for  $N_c$  than if we had to run systematically a BD simulation.

Following this observation, we explored the stability of the direct reconstruction method in the  $(\varepsilon, N_c)$  plane. Note that for this study only, we used a larger size of polymer and considered  $N = 1000$ . For each value of  $N_c$ , we generated a random coupling matrix  $k_{ij}^{th}$  with scale  $\Lambda = 1$ , and the associated theoretical

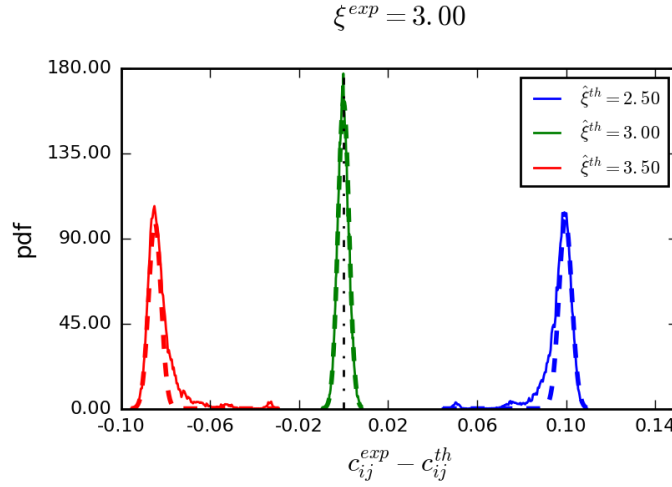


**Figure 5.13** – Distribution of the noise  $\eta_{ij} = c_{ij}^{exp} - c_{ij}^{th}$ , fitted to a Gaussian distribution. We used a Gaussian form factor to compute both contact matrices.  $N = 200$ ,  $N_c = 20$  and  $\Lambda = 1$ .

contact probabilities  $c_{ij}^{th}$ . We used  $\xi^{th} = 3.00$  and  $\mu^{th} = \mu_G$ . Then we computed a pseudo-experimental contact probability matrix  $c_{ij}^{exp}$  by adding to the theoretical contact probabilities a centered Gaussian noise with standard deviation  $\varepsilon$ . Following our previous observation, we assume that the contact probabilities obtained are a good approximation of the experimental contact probabilities that would be obtained by performing a BD simulation of the GEM and computing the contact probabilities with  $\xi^{exp} = \xi^{th}$  and  $\mu^{exp} = \mu^{th}$ . Then we applied the direct reconstruction procedure to  $c_{ij}^{exp}$  using  $\mu = \mu^{exp}$  and  $\xi = \xi^{exp}$ , which is the optimal threshold. We therefore obtained a predicted GEM with couplings  $\hat{k}_{ij}$  that we compared to the theoretical couplings by computing  $d(\hat{k}_{ij}, k_{ij}^{th})$ . The result of this analysis is shown in fig. 5.14, in which we shaded in grey the region where the predicted couplings  $\hat{k}_{ij}$  result in an unstable GEM with a correlation matrix  $\Sigma$  having negative eigenvalues. We obtain that for each value of the number of constraints,  $N_c$ , there is an upper bound  $\bar{\varepsilon}$  on the noise amplitude such that for  $\varepsilon > \bar{\varepsilon}$ , the direct reconstruction method fails, in the sense that the predicted GEM is unstable. It is remarkable that for  $\varepsilon < \bar{\varepsilon}$  the direct reconstruction methods perform very well, with  $d(\hat{k}_{ij}, k_{ij}^{th}) \lesssim 10^{-2}$  in the worse cases. Therefore, the reconstruction appears to be robust to noise until some critical value of the noise amplitude is reached. Then the method suddenly starts to fail. We also note that the value of  $\bar{\varepsilon}$  seems to depend on the number of constraints of the underlying GEM. In particular, it is clear that the performances of the direct reconstruction method get worse when  $N_c \rightarrow 0$ . Specifically, for  $N_c = 0$ , we observe that even blurring the theoretical contacts with a noise of amplitude as small as  $\varepsilon = 10^{-6}$  is sufficient to make the retrieval fail. To the contrary, the value of  $\bar{\varepsilon}$  seems to be maximum in a range of constraints between  $N_c = 10\%N$  and  $N_c = 100\%N$ .

In conclusion, we have shown that the primary reason causing the direct reconstruction method to fail is when the predicted couplings produce an unstable GEM. By definition of the Gaussian effective model, this means that the correlation matrix  $\Sigma$  of the Gaussian model has negative eigenvalues. This occurs suddenly when the experimental contacts are corrupted with a noise whose amplitude is above a critical value. However, when the noise's amplitude (or experimental precision error) is below this threshold, the predicted couplings appeared to be close to the theoretical ones. Hence whenever the direct reconstruction

method gives a stable GEM, we may consider that this is the theoretical GEM from which the experimental contact matrix was generated. Therefore, when applying this method to an experimental matrix from a Hi-C experiment, we may consider similarly that whenever the reconstructed GEM is stable, it constitutes a reliable model for the chromosome architecture.

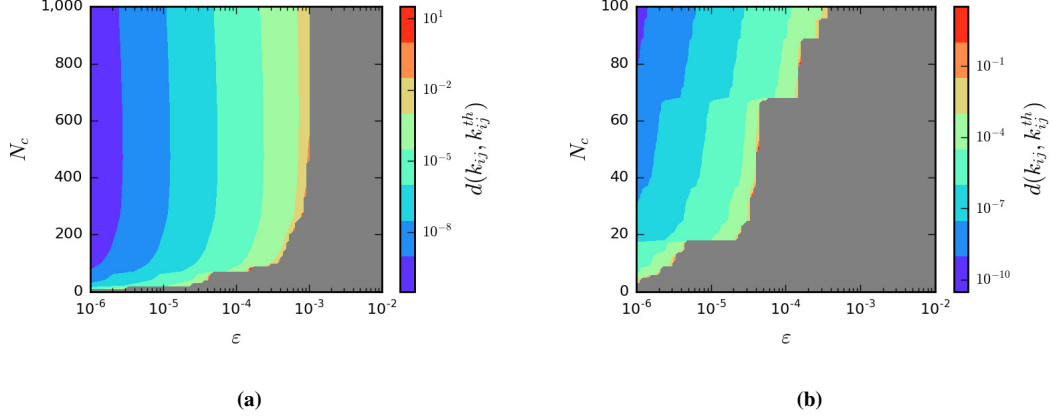


**Figure 5.14** – Performance of the direct reconstruction method when the theoretical contact probabilities  $c_{ij}^{th}$  are blurred with a Gaussian noise such that  $\langle \eta_{ij} \rangle = 0$  and  $\langle \eta_{ij}^2 \rangle = \epsilon^2$ . We used  $N = 1000$ . The region in which the predicted couplings  $\hat{k}_{ij}$  define an unstable GEM was shaded in grey. (a)  $N_c = 0, \dots, 1000$ . (b) Zoom for  $N_c = 0, \dots, 100$ .

## 5.5.4 Reconstruction of a stable Gaussian effective model

### 5.5.4.1 How to ensure the stability of the reconstructed Gaussian effective model?

When the input experimental contacts are very noisy, we have seen that the direct reconstruction procedure fails because the associated GEM is unstable. However, in the space of contact matrices, there may exist a nearby contact matrix which can be mapped to a stable GEM. This remark motivates the design of an alternative method which aims at reconstructing the closest stable GEM. In particular, the predicted contact probabilities may not exactly reproduce the experimental ones. This suggests an approach in which one seeks to minimize the distance  $d(c_{ij}, c_{ij}^{exp})$  between the contact matrix predicted by a GEM and the experimental contact matrix, under the constraint that the GEM is stable.

A rigorous enforcement of this principle would be to ensure that the correlation matrix of the candidate GEM has strictly positive eigenvalues. Yet, this constraint seems difficult to implement in practice. Instead we turn our attention to the more restrictive condition:

$$k_{ij} > 0, \quad (5.51)$$

which ensures the positivity of the couplings. It is clear that eq. (5.51) is a sufficient although not necessary condition for  $\Sigma$  to be a positive definite matrix. Indeed, if it is so, then the sum in eq. (5.18) on page 110 is always positive.

### 5.5.4.2 Minimization procedure

Finding the best stable GEM matching an input experimental contact matrix can therefore be recast in a minimization problem on the  $k_{ij}$  variables, with Lagrangian:

$$\mathcal{L} = \mathcal{A} + \mathcal{B}. \quad (5.52)$$

The two functionals in the right-hand side (r.h.s.) of eq. (5.52) have the expressions:

$$\mathcal{A} = \frac{1}{2} \|\Sigma^{exp} \cdot \Sigma^{-1} - I\|^2, \quad (5.53)$$

where  $I$  is the identity matrix, and:

$$\mathcal{B} = \sum_{i < j} \theta(-k_{ij}) \left( \frac{|k_{ij}|}{\underline{k}} \right)^p. \quad (5.54)$$

For  $\mathcal{A}$ , we have preferred the expression in eq. (5.53) to  $d(c_{ij}, c^{exp})$  because it is quadratic in the  $k_{ij}$ , which is desirable for a function to minimize. In particular, in the absence of  $\mathcal{B}$  the minimization would reduce to the minimization of a quadratic function whose regularity and convexity ensure straight convergence to the global minimum with standard minimization techniques. We can hope that the addition of the  $\mathcal{B}$  functional will not alter too much this property. From a computational standpoint, computing  $\mathcal{A}$  and its derivatives is very straightforward while computing  $d(c_{ij}, c_{ij}^{th})$  requires first to invert  $\Sigma^{-1}$  in order to compute the average square distances  $\gamma_{ij}$  from which can be computed the contact probability matrix  $c_{ij}$ . The latter option involves therefore an additional computational burden that we want to avoid. However, due to the GEM mapping between the inverse correlation matrix with elements  $\sigma_{ij}^{-1}$  and the  $c_{ij}$ , both criteria are equivalent. We give the derivatives of  $\mathcal{A}$ :

$$\frac{\partial \mathcal{A}}{\partial k_{ij}} = \begin{cases} \frac{\partial \mathcal{A}}{\partial w_{jj}} & \text{if } 0 = i < j \\ \frac{\partial \mathcal{A}}{\partial w_{ii}} + \frac{\partial \mathcal{A}}{\partial w_{jj}} - \frac{\partial \mathcal{A}}{\partial w_{ij}} & \text{if } 0 < i < j, \end{cases} \quad (5.55)$$

with:

$$\begin{aligned} \frac{\partial \mathcal{A}}{\partial w_{ii}} &= [S^T (S \cdot \Sigma^{-1} - I)]_{ii} \\ \frac{\partial \mathcal{A}}{\partial w_{ij}} &= [S^T (S \cdot \Sigma^{-1} - I)]_{ij} + [S^T (S \Sigma^{-1} - I)]_{ji}, \end{aligned} \quad (5.56)$$

where we have used  $S = \Sigma^{exp}$  to alleviate notations, and  $w_{ij}$  is a matrix element of the reduced coupling matrix. Note the particular shape for the derivative of the off-diagonal elements in the second line of eq. (5.56) which appears when we enforce that the coupling matrix  $k_{ij}$  is symmetric.

The  $\mathcal{B}$  functional has been chosen arbitrarily to enforce the positivity of the couplings, as required from eq. (5.51). The theta function ensures that the penalty is applied only when some couplings become negative. Besides,  $\underline{k}$  can be seen as the modulus of the smallest negative coupling allowed. Indeed, due to the power law in eq. (5.54), the penalty increases abruptly when  $k_{ij} < -\underline{k}$ . The values of  $p$  and  $\underline{k}$  have been adjusted from our particular experience. Actually, decreasing  $\underline{k}$  results in a more stringent constraint and tends to increase the number of iterations required for the minimization to converge. To a lesser extent

increasing  $p$  also resulted in a more stringent constraint, but the consequences on the convergence speed were less visible. In practice, we typically used  $\underline{k} = 0.1$  and  $p = 8$ .

Last but not least, we enforced  $k_{ii+1} = 0$  and removed these variables from the minimization. We have made this choice to ensure that the bonds rigidity of the Gaussian chain in eq. (5.15) is not modified.

For the practical implementation of the minimization, we used a standard steepest descent method. In other terms,  $k_{ij}$  values were updated according to the equation of motion:

$$\frac{\partial k_{ij}}{\partial t}(t) = -\frac{\partial \mathcal{L}}{\partial k_{ij}}(\{k_{ij}(t)\}), \quad (5.57)$$

or more precisely its discretized version:

$$k_{ij}^{(n+1)} = k_{ij}^{(n)} - h \frac{\partial \mathcal{L}^{(n)}}{\partial k_{ij}}, \quad (5.58)$$

where  $n$  is the time (or iteration) and  $h$  represents the time step. Actually, we have also tried more sophisticated methods such as the conjugate-gradient method. However, although the number of iterations required to converge is significantly decreased, each step then requires to perform a line minimization, with several evaluations of  $\mathcal{A}$  per iteration. Yet, evaluating  $\mathcal{A}$  requires of the order of  $O(N^2)$  operations. Therefore we have found that using a simple steepest descent method resulted in a faster convergence to the minimum. Following ideas developed in section 5.4.2, we chose to initialize the couplings to  $k_{ij}^{(0)} = c_{ij}^{exp}$ .

### 5.5.4.3 Speeding up convergence

While the computation of  $\mathcal{A}$  has a complexity in  $O(N^2)$ , the computation of the gradient of  $\mathcal{A}$  requires of the order of  $O(N^3)$  operations. This scaling seems at first particularly unadapted to deal with contact matrices with size  $N \sim 10^2$  or  $10^3$  like in Hi-C experimental data sets. However this issue can be circumvented.

The key is to reduce the complexity of the gradient evaluation. It turns out that during the minimization, only a few  $k_{ij}$  tend to non-zero values and represent significant constraints. The bulk of the  $k_{ij}$  actually decreases quickly to near zero values, which then fluctuate in the vicinity of zero, with a magnitude well below the relevant couplings scale chosen for the procedure:  $|k_{ij}| \ll \underline{k}$ . Computational time spent to perform the dynamics on these couplings may be regarded as wasted because they do not correspond in the end to significant constraints and it is of little interest to know whether these couplings have a magnitude near zero or exactly equal to zero.

Therefore, every  $n_t$  iterations, we performed a “trim” operation. We set all couplings such that  $|k_{ij}| < \underline{k}$  to  $k_{ij} = 0$  and removed them from the minimization. As a consequence, computing the gradient of  $\mathcal{A}$  becomes of complexity  $O(MN^2)$  where  $M$  is the number of  $k_{ij} \neq 0$ . In general,  $M$  quickly decreases to  $M \sim N_c < N$ . Hence this trick enables us to save a significant amount of time in the minimization. For practical implementations, we typically used  $n_t = 100$ .

### 5.5.4.4 Results

In order to validate the minimization method, we applied it to experimental contact matrices obtained from BD simulations performed on our artificial GEMs. We used a form factor  $\mu^{exp}$  and a threshold  $\xi^{exp}$  but as before, we assumed that this information is hidden in the reconstruction procedure.

Starting from the experimental contact probabilities  $c_{ij}^{exp}$ , we perform a minimization on the  $k_{ij}$  as described above. The couplings  $\hat{k}_{ij}$  where  $\mathcal{L}$  is minimum define the best stable GEM matching the

experimental contacts. Nonetheless, to compute  $\Sigma^{exp}$  we had to choose a form factor  $\mu$  and a threshold  $\xi$ . The goal is to find the GEM whose associated contact probability matrix  $\hat{c}_{ij}$  is as close as possible to the experimental one. Therefore we define the optimal threshold as the one minimizing the distance to the experimental contacts:

$$\xi^{opt} = \underset{\xi}{\operatorname{argmin}}(d(\hat{c}_{ij}, c_{ij}^{exp})). \quad (5.59)$$

We considered BD trajectories of GEMs with  $N = 200$ ,  $\Lambda = 1$  and  $N_c$  constraints. We then applied the minimization procedure to the experimental contact matrices computed using a Gaussian form factor  $\mu^{exp} = \mu_G$  and a threshold  $\xi^{exp} = 3.0$ . In fig. 5.15, we report the results for  $N_c = 20, 50, 100$ . In the first column we represented  $d(\hat{c}_{ij}, c_{ij}^{exp})$  as a function of the threshold  $\xi$ . Since we know the true couplings of the GEM used to produce the experimental contacts, we also represented the distance between the retrieved couplings  $\hat{k}_{ij}$  and the theoretical ones, *i.e.*  $d(\hat{k}_{ij}, k_{ij}^{th})$ . We observe that  $d(\hat{c}_{ij}, c_{ij}^{exp})$  display one narrow local minimum and another “fat” local minimum for smaller values of  $\xi$ , which is rather unexpected. However,  $d(\hat{k}_{ij}, k_{ij}^{th})$  diverges near the “fat” minimum so we conclude that this is an unphysical minimum. We do not have clear explanation for the existence of this secondary minimum, but we suspect that it is due to the positivity constraint on the  $k_{ij}$ . That being said, if we admit that the first minimum encountered from the right (*i.e.* when decreasing progressively  $\xi$  from large values) corresponds to the optimal threshold  $\xi^{opt}$  as defined in eq. (5.59), then the performances of the method are very good. In particular we recover that  $\xi^{opt} = \xi^{exp}$ . In the second and third columns, we show the optimal coupling matrix  $k_{ij}^{opt}$  and contact matrix  $c_{ij}^{opt}$  when  $\xi = \xi^{opt}$ . Note that  $k_{ij}^{opt}$  reproduces  $k_{ij}^{th}$  to a very good precision. We also carried out the same procedure on contact maps such that  $\mu^{exp} = \mu_T \neq \mu$  and  $\xi^{exp} = 1.5$  (fig. 5.16). Due to the discrepancy between the form factors, we now have  $\xi^{opt} \neq \xi^{exp}$ . Although a little bit less accurate than with  $\mu^{exp} = \mu_G$ , we still obtain satisfactory results and the optimal couplings are very close to the theoretical ones. Interestingly, when  $\mu^{exp} \neq \mu$ , the “fat” minimum of  $d(\hat{c}_{ij}, c_{ij}^{exp})$  almost vanishes and we are left with a pronounced and dominant global minimum at  $\xi = \xi^{opt}$ .

Let us emphasize that despite its apparent computational burden, this method is still more efficient than the method proposed in [155]. Indeed, the latter one also uses a minimization scheme such as eq. (5.57), yet at each step  $n$ , evaluating  $\mathcal{L}$  requires to perform a full Monte-Carlo simulation to sample configurations of the system in the canonical ensemble and use them to compute the contact matrix associated to the values of the couplings at time  $n + 1$ . Besides, the free parameters in this same approach ( $\sigma$  and  $\xi$  in eq. (5.13)) are adjusted by hand while here we adjust the free parameter  $\xi$  in order to find the optimal GEM matching the experimental contacts. That being said, when the system size is not too large (say  $N < 100$ ), their approach allows to virtually consider any polymer model, and any type of monomer-monomer interaction, while our approach is valid only when the system’s Hamiltonian is Gaussian.

In conclusion, we have presented here a method to reconstruct the true couplings of an underlying GEM from an input experimental contact matrix. In contrast to the direct reconstruction method, it ensures that the obtained GEM is stable. It is therefore safer to apply to noisy experimental contact matrices, coming for instance from Hi-C experiments. As a drawback, the minimization involves a heavier computational burden that we somehow attenuated by trimming small couplings values during the minimization. The method has  $\xi$  as a free parameter, which is chosen *a posteriori* to minimize the distance between the experimental and the reconstructed contact probabilities. Applying this method to BD trajectories of our artificial GEMs has proven quite successful. Hence we now attempt to apply it to real contact matrices coming from Hi-C experiments.

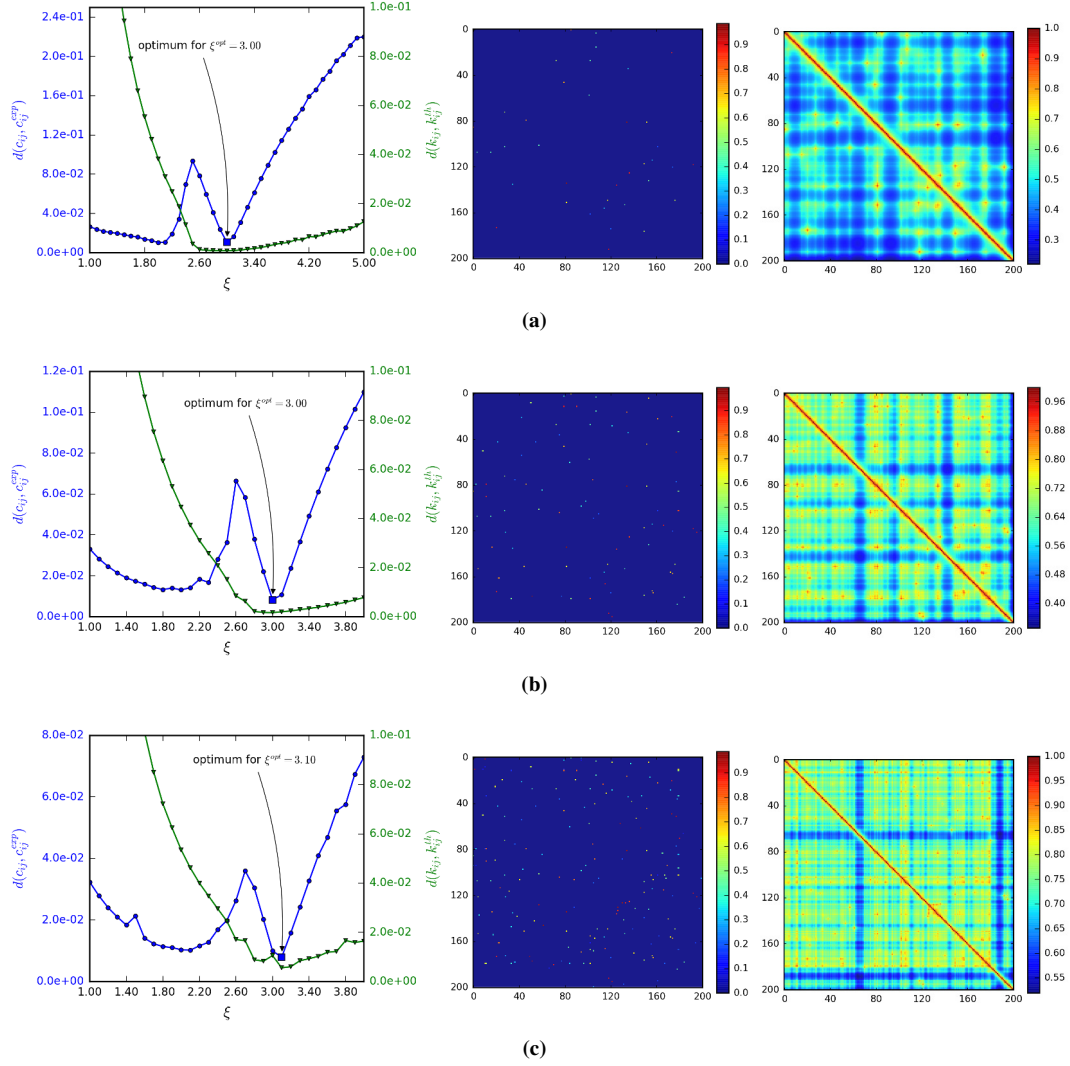


**Figure 5.15** – Application of the minimization method to experimental contact matrices generated from a BD trajectory of a GEM ( $N = 200$  and  $\Lambda = 1$ ). We used  $\xi^{exp} = 3.00$  and  $\mu^{exp} = \mu_G$  (Gaussian form factor). We show in the first column  $d(\hat{c}_{ij}, c_{ij}^{exp})$  and  $d(\hat{k}_{ij}, k_{ij}^{th})$  as a function of the threshold  $\xi$  used in the minimization. The optimal threshold  $\xi^{opt}$  minimizing  $d(\hat{c}_{ij}, c_{ij}^{exp})$  is shown. The optimal coupling matrix  $k_{ij}^{opt}$  and the associated contact matrix  $c_{ij}^{opt}$  are shown in the second and third column. (a)  $N_c = 20$ . (b)  $N_c = 50$ . (c)  $N_c = 100$ .

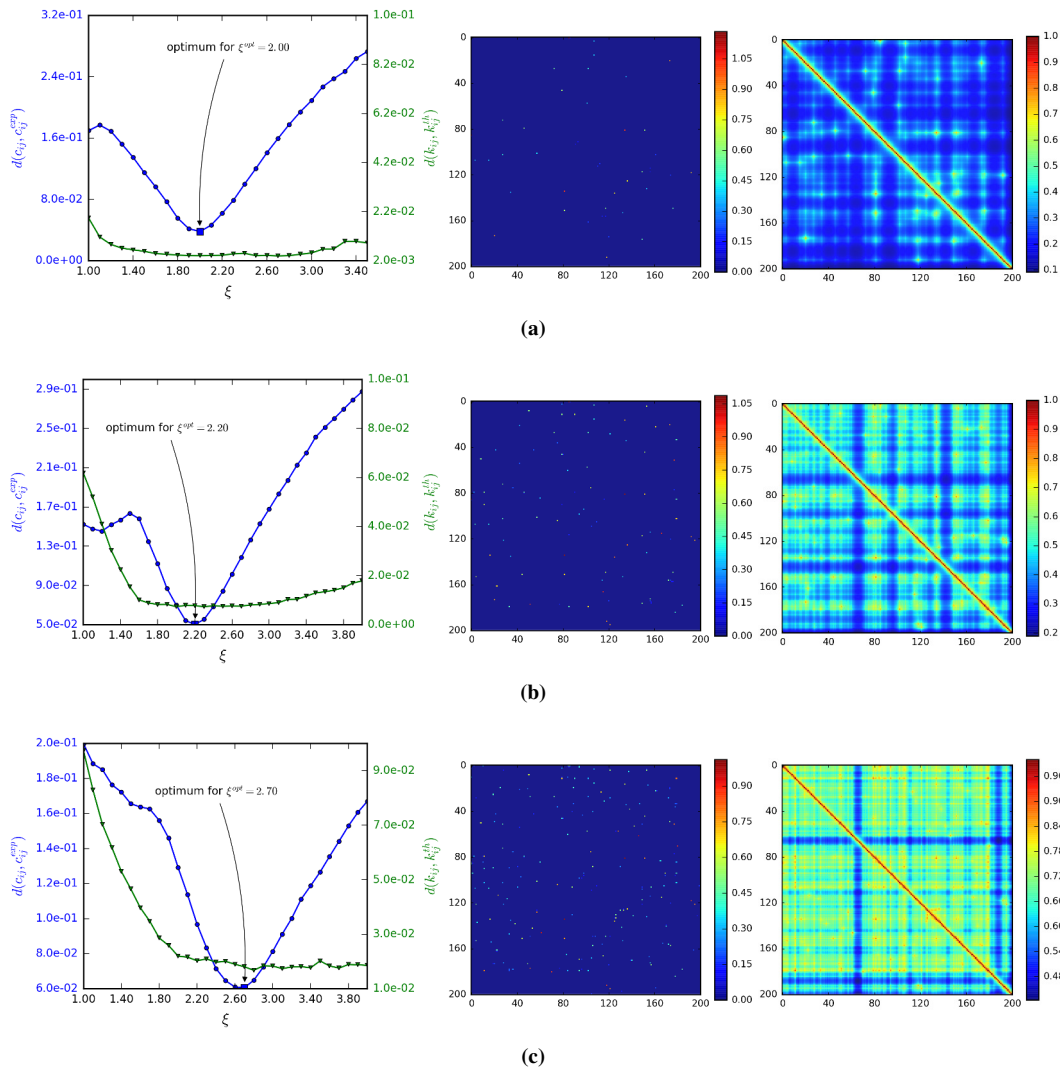


**Figure 5.16** – Same as fig. 5.16 but the experimental contact matrices were generated from the BD trajectories with a theta form factor instead:  $\mu^{exp} = \mu_T$  and  $\xi^{exp} = 1.50$ . (a)  $N_c = 20$ . (b)  $N_c = 50$ . (c)  $N_c = 100$ .

## 5.6 Reconstruction from Hi-C contact probability matrices

In this section, we shall use Hi-C data from the human chromosome 14 [35]. Because we did not have clear arguments to prefer one normalization over the others, we have normalized the counts map in a contact probability matrix according to each of the methods presented in section 5.2.4 and applied the reconstruction procedure to obtain a Gaussian effective model of the chromosome.

First, we have tried to use the direct reconstruction method. However, the method has failed because the GEMs obtained were unstable. Therefore we have implemented the minimization method. We show the results for contact matrices normalized with the “Maximum” method and  $l_d = 2$  or  $l_d = 3$ . For  $l_d = 2$  (fig. 5.17), the optimal GEM has a contact probability matrix very close to the experimental one, with  $d(c_{ij}^{opt}, c_{ij}^{exp}) < 0.1$ . Yet, with this choice of normalization, only short-range interactions emerge from the optimal coupling matrix. For  $l_d = 3$  (fig. 5.18), we obtain a more complex architecture, with the presence of long-range interactions in the optimal coupling matrix. Besides, there are compartments visible in the contact probability matrix associated to the reconstructed GEM, in good global agreement with the experimental contact probability matrix. However, we now have  $d(c_{ij}^{opt}, c_{ij}^{exp}) > 0.1$ . The configurations obtained with BD simulations of this GEM are typical of a collapsed polymer and may model “rosette” structures conjectured for chromosome architecture [22]. Noting that the experimental contact probability matrix generated with  $l_d = 3$  has globally entries with larger values and less smooth variations, we may interpret this increased distance,  $d(c_{ij}^{opt}, c_{ij}^{exp})$ , by saying that it is harder to fit the experimental contacts with a GEM than when  $l_d = 2$ .

## 5.7 Discussion

### Representation of the chromosome architecture with a Gaussian effective model

On the basis of an inspiring study [155], in this chapter we have sought to propose a polymer model of the chromosome that reproduces the contact probabilities measured in Hi-C experiments. In order to address this issue, we have investigated a physical model that we called Gaussian effective model (GEM). Specifically, we started from a Gaussian chain model of the chromosome, and added effective interactions between monomers under the form of harmonic springs with rigidity coefficients  $k_{ij}$ . The problem of reconstructing the chromosome architecture is then equivalent to find the  $k_{ij}$  values such that the GEM reproduces, at Boltzmann equilibrium, the experimental contact probabilities,  $c_{ij}^{exp}$ . As a central result of our investigation, we found that within this theoretical framework, the contact probabilities of the GEM,  $c_{ij}$ , are uniquely related to the matrix of couplings,  $c_{ij} \Leftrightarrow k_{ij}$ . In particular, an analytical closed-form has been obtained. This mapping depends on two parameters which are: a threshold  $\xi$  and a form factor  $\mu$ , which specify the probability that two monomers separated by a distance  $r$  are found in contact. These parameters depend on the particular experimental setup and need to be adjusted *a posteriori*. Besides, in our investigation we have chosen to use a Gaussian form factor,  $\mu_G(r) = (1 + b^2 \gamma_{ij} / \xi^2)^{-3/2}$ , in order to account for the dispersion in the cross-linking distances due to formaldehyde polymerization in Hi-C experiments.

### Validation of the analytical relation between couplings and contact probabilities

In order to validate the analytical closed-form obtained, we have generated Brownian dynamics (BD) trajectories of artificial GEM with known couplings,  $k_{ij}^{th}$ , from which we extracted  $M$  configurations to compute virtual contact matrices. We compared these matrices to the matrix of contacts predicted by

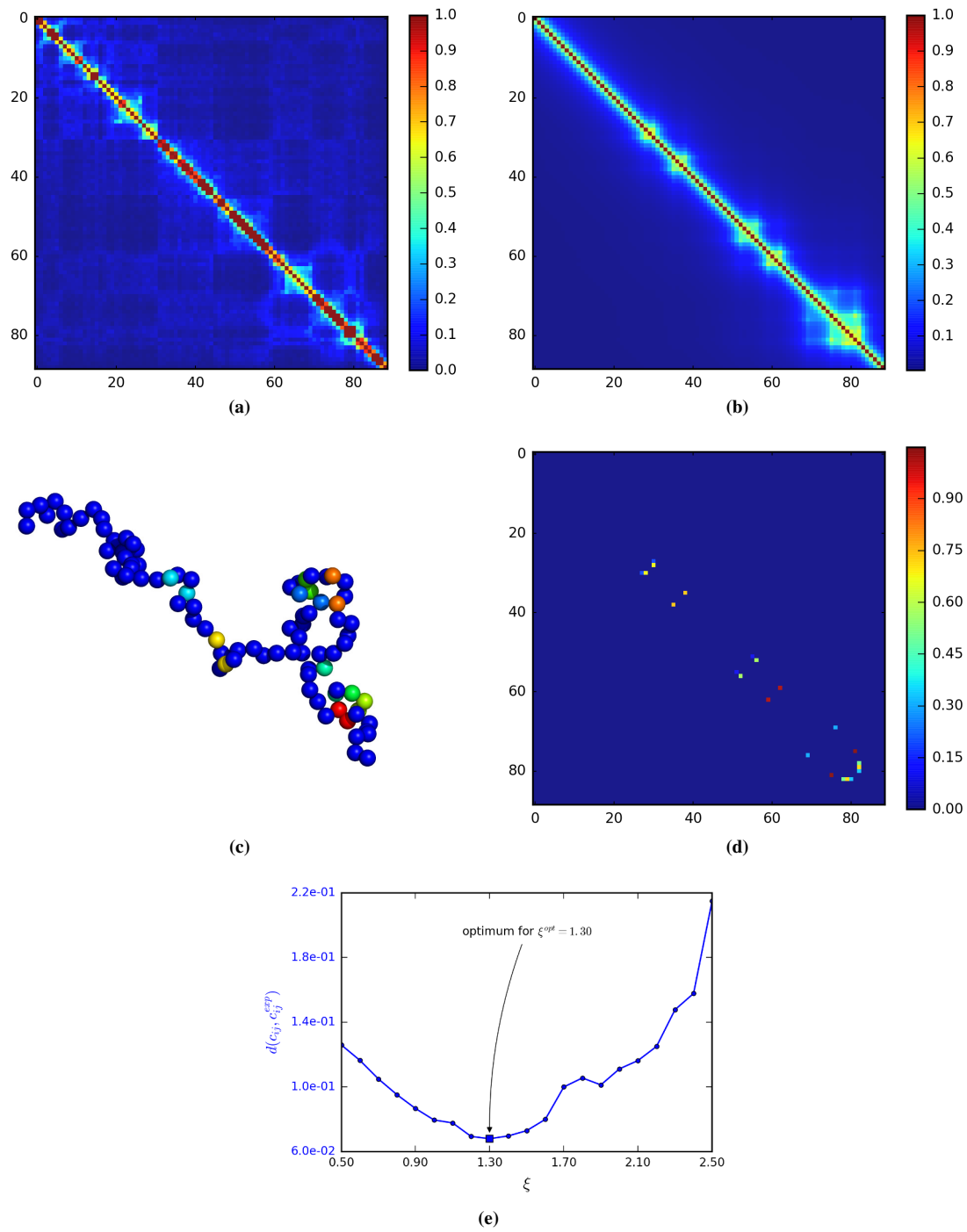


**Figure 5.17** – Application of the minimization procedure to Hi-C data from the human chromosome 14 with bin resolution 1 Mbp [35]. (a) Experimental contact probability matrix obtained from the counts map with the “Maximum” normalization and  $l_d = 2$ . (b) Contact probability matrix of the optimal GEM. (c) Snapshot of a BD simulation of the optimal GEM. (d) coupling matrix of the optimal GEM. (e) Result of the minimization method.

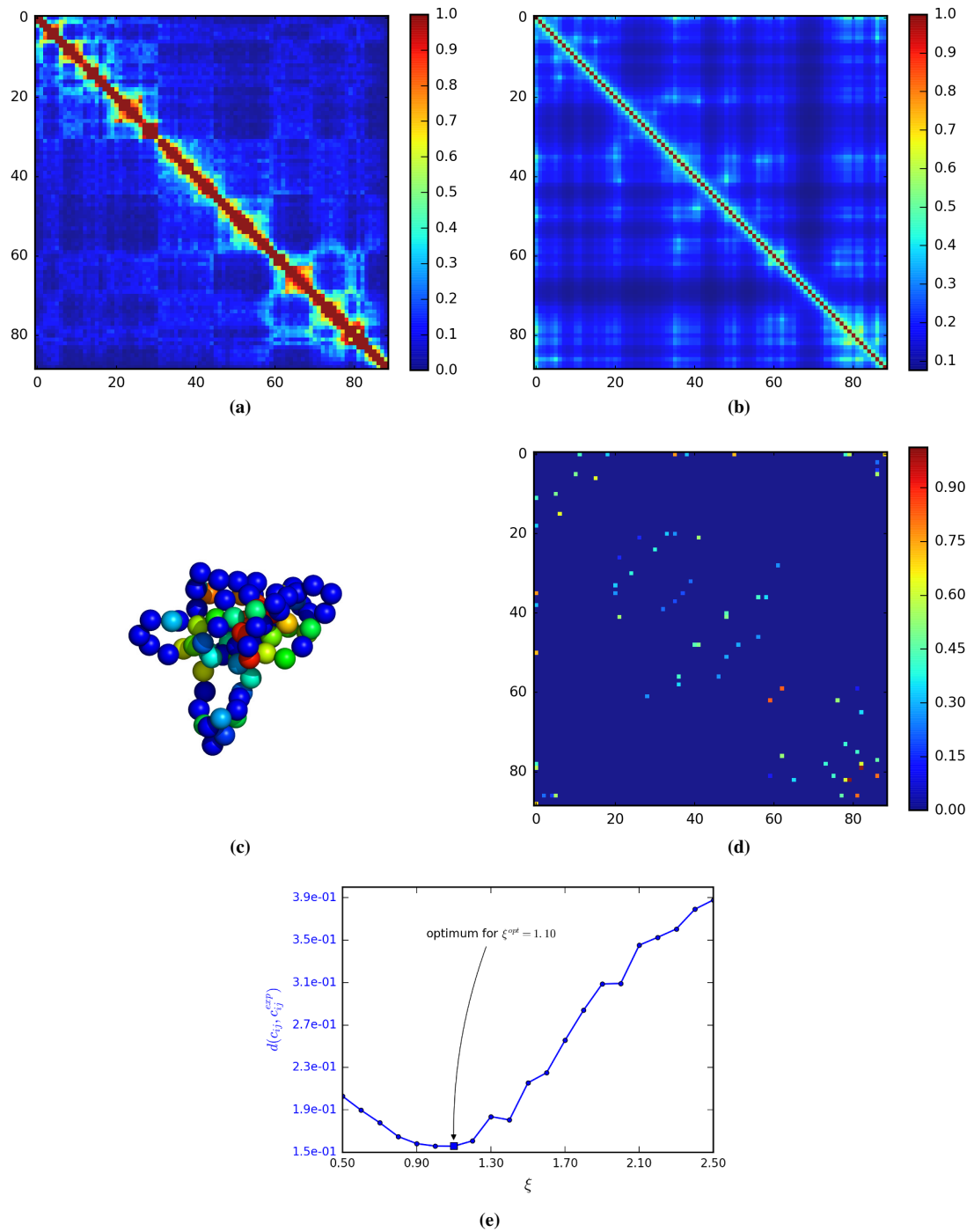


**Figure 5.18** – Same as fig. 5.17 but with  $l_d = 3$  rather than 2.

the GEM mapping,  $c_{ij}^{th}$ . We found that the distance between the two was very small. For example, with  $M = 1000$  configurations, we had  $d(c_{ij}^{th}, c_{ij}^{exp}) \sim 5 \times 10^{-3}$ , where the distance actually represents the average difference between matrix elements. Hence we concluded that the analytical relation obtained was reliable.

### Direct reconstruction method

This led us to propose a first method to reconstruct chromosome architecture. Starting from an experimental contact matrix,  $c_{ij}^{exp}$ , this method uses the aforementioned mapping to give the couplings which define a GEM with the same contact probability matrix,  $\hat{c}_{ij} = c_{ij}^{exp}$ . This method performed very well on virtual contact matrices generated from BD simulations. Namely, the original couplings  $k_{ij}^{th}$  were retrieved within a very good accuracy. Yet, we were faced with an unexpected problem when applying this method to experimental contact matrices from Hi-C experiments. It turns out that the GEM mapping does not ensure that the model obtained is physical. That is to say, the reconstructed couplings may result in a Gaussian correlation matrix with negative eigenvalues, corresponding to an unstable GEM. We characterized this phenomenon by showing that the method is sensitive to the presence of noise in the experimental contact probabilities. More accurately, when the noise amplitude increases above a certain value, which depends on the number of non-zero couplings in the GEM (*i.e.* the number of constraints  $N_c$ ), the reconstruction can fail even though the underlying contact matrix was generated from a stable GEM. The effect can be particularly devastating on the input data. For instance, for contact matrices generated from a free polymer ( $N_c = 0$ ), a noise of amplitude of  $10^{-6}$  was sufficient to result in an unstable GEM.

### Finding a stable Gaussian effective model

To address the stability issue, we had to consider an alternative approach. Instead of considering that an input contact probability matrix should be directly associated to a GEM, we rather decided to find the closest element, in the space of contact matrices, which is associated to a stable GEM. To implement this approach, we considered the minimization of a function of the  $k_{ij}$  variables, and consisting of two terms. The first term was the distance between the experimental contacts and the contact matrix associated to the current  $k_{ij}$  vector through the GEM mapping. The second term corresponded to a constraint on the  $k_{ij}$  to ensure that the GEM is stable. This minimization is carried out for several values of the threshold used in the mapping, and the GEM having the closest contact matrix,  $\hat{c}_{ij}$ , to the experimental one is retained.

We demonstrated that this method gave consistent results by applying it as before to contact probability matrices generated from BD trajectories. We found that the minimum of the distance  $d(\hat{c}_{ij}, c_{ij}^{exp})$  indeed corresponded to a satisfactory retrieval of the hidden couplings. The method however is less accurate than the direct reconstruction discussed above. First, by construction the reconstructed contact matrix is no longer equal to the experimental one,  $\hat{c}_{ij} \neq c_{ij}^{exp}$ . In particular, at the optimum, the distance between the two matrices was of the order  $d(\hat{c}_{ij}, c_{ij}^{exp}) \sim 5 \times 10^{-2} - 10^{-1}$ . Furthermore, the distance as a function of the threshold displayed a secondary and unexpected minimum for small values of the threshold. We suspect that it is due to the stringent constraint imposed on the  $k_{ij}$  to enforce the GEM stability. Indeed, the condition that we impose is  $k_{ij} > 0$ . Although having positive couplings is sufficient to obtain a positive definite Gaussian correlation matrix, it is not a necessary condition. Therefore, this condition may be too strong and prevent proper relaxation of the couplings to a GEM with an associated contact matrix closer to the experimental one.

### Application to matrices from Hi-C experiments

Finally, we applied the reconstruction by minimization method to Hi-C experimental data sets [35]. It is not clear in our view how to properly normalize the experimental counts in contact probabilities. Therefore we used the “Maximum” normalization method presented in section 5.2 with  $l_d = 2$  or  $l_d = 3$ . In the first case, we obtained a predicted GEM where all the non-zero couplings correspond to short contour distances between monomer pairs. The distance between predicted and experimental contacts was quite small, with  $d(\hat{c}_{ij}, c_{ij}^{exp}) \simeq 5 \times 10^{-2}$ . In contrast, with  $l_d = 3$  the predicted GEM presented several long-range interactions. The distance between predicted and experimental contacts was less satisfactory, namely  $d(\hat{c}_{ij}, c_{ij}^{exp}) > 0.1$ . An interpretation is that the GEM obtained is overfitting the variations of the bulk of the  $c_{ij}$ , namely the checkerboard patterns in the Hi-C experimental contact probability matrix. Hence a future improvement may consist in filtering first the experimental contacts  $c_{ij}^{exp}$  in order to smoothen the background variations. Incidentally, methods that normalize the Hi-C counts to produce stochastic contact matrices precisely achieve this effect. Therefore it may be interesting to resort to these methods [33, 147].

Furthermore, we performed BD simulations of the reconstructed GEM. For  $l_d = 2$  the polymer configurations sampled corresponded to an open coil whereas for  $l_d = 3$  they were rather those of a globule. Although at first, open coil configurations may seem a more reasonable model of the chromosome, the globule configurations have the advantage to reproduce the effect of cell wall confinement. Hence, maybe an appropriate normalization of the Hi-C counts should precisely correspond to a transition from an open coil to a globule for the associated GEM. Incidentally, studies on cross-linked polymers have shown that for ideal Gaussian chain as it is the case here, this transition should occur when the number of non-zero  $k_{ij}$  is of the order of the number of monomers,  $N_c \sim N$  [157]. This gives a criterion to assess the relevance of the predicted GEMs.

### Computational efficiency

Our investigation has led us to use three reconstruction methods to obtain a GEM of the chromosome. Let us now briefly review their computational advantages and drawbacks.

Our first attempt has been to try a naive approach relying on BD simulations. In this approach, we did not use the GEM mapping to relate the couplings to the contact probabilities. Instead, we postulated that they are proportionally related with a scaling coefficient  $\Lambda$ , namely  $k_{ij} = \Lambda c_{ij}$ . We then performed BD simulations for several values of  $\Lambda$  and chose the value that minimizes the distance between the Hi-C and the virtual contact probability matrices from BD simulations. This approach is obviously subject to the same criticism that we made for studies using Monte-Carlo (MC) simulations [155]. Yet an important difference is that in our approach the minimization is performed as a function of just one variable,  $\Lambda$ , and it is therefore sufficient to run BD simulations for several values of this scaling coefficient. In contrast, in [155] the minimization runs over all the  $k_{ij}$ , which is much more complex. Hence the naive approach presented in this chapter is more scalable and can be used on contact matrices of larger size.

Our second attempt has been to perform the GEM mapping directly on the experimental contacts. From a computational standpoint, this approach only requires to invert a  $N \times N$  matrix where  $N + 1$  is the size of the probability contact matrix. Hence it is a particularly appealing method, in which we placed much hope at first. However we have seen that it can result in an unstable GEM. Altogether, it may be a good practice to systematically try this method before one of the other two methods.

Our third and last attempt has consisted in the minimization of the distance between an experimental contact matrix and another one corresponding to a stable GEM. Similarly to [155], this method assumes a minimization as a function of all the  $k_{ij}$ . Yet, in our case each iteration only requires to evaluate a cost

function  $\mathcal{L}$  together with its gradient, in comparison with a full BD or MC simulation. At first we thought that this would provide us with a significant advantage. Yet evaluating the gradient of  $\mathcal{L}$  is an  $O(N^3)$  operation, therefore involving a significant computational burden. Presently, with a non-optimized code it takes more than two days on a multi-threaded CPU with twelve cores to minimize  $\mathcal{L}$  for  $N = 1000$  (and a few minutes for  $N = 100$ ). It is not clear at the moment whether this procedure can be significantly improved to yield more reasonable time. Besides, within our current setup, this method must be repeated for each values of the threshold  $\xi$  in the GEM mapping. Unfortunately, most Hi-C contact matrices have a size such that  $N \sim 1000$ .

### Conclusion

Despite some caveats just discussed, we find that the methods presented in this chapter to reconstruct chromosome architecture are rather novel and pave the way for interesting applications. It is clear that a Gaussian effective model cannot help us to better describe the biological processes at the molecular level. However it can be used to propose a mesoscopic model for the chromosome. Namely the GEM obtained can be used as a basis to perform BD simulations. In comparison with BD models where interactions between DNA and proteins are chosen arbitrarily it has the advantage to be by construction better rooted in biological experiments.

Last but not least, from a theoretical standpoint, the correspondence found between the couplings of a GEM and the Boltzmann contact probabilities constitute a (humble) contribution to the problem of finding if a contact matrix can be produced by a connected physical object such as a polymer. As far as we know, advances on this subject in the literature are rather rare.



## Chapter 6

# Concluding remarks

### Achievements

The binding of many divalent proteins to the chromosome entails the formation of DNA loops or compact structures, which result in a chromosome architecture (or folding) that we do not fully understand. Biological assays have demonstrated that this organization is intimately related to the transcription. Namely, the observation that co-regulated genes tend to be close in space and the characterization of transcription factories have been milestones in this new thinking. In this thesis, I have investigated the physical origin of such structures and proposed models that underlie their existence. To serve this purpose, I have combined analytical approaches from statistical physics with Brownian dynamics simulations. A major challenge in this endeavor has been two reconcile the microscopic scale of the molecular biology with the mesoscopic scale of chromosome folding.

In chapters 2 and 4, I have considered first principles models to identify the physical mechanisms responsible for features characterized in experiments. Namely, the approaches undertaken explicitly considered the effect of proteins on the chromosome. In chapter 2, I have proposed a model for the existence of transcription factories. I concluded that such clusters can indeed occur at equilibrium under the effect of a generic type of binding protein. I also proposed that at small scales, binding proteins can induce the collapse of the chromosome in a crystalline phase. Incidentally, such aggregates do form in the bacterial cell, and have often the role to protect DNA from detrimental factors. In chapter 4, I have investigated the formation of DNA hairpin loops by the H-NS protein. In the looped state, RNA polymerase cannot bind, resulting in the silencing of genes whose promoters are sequestered in these DNA loops. My findings suggest that such hairpins are stable only when the length of the H-NS binding region is above a characteristic length. This gives credit to a conjecture proposing that genes silencing mediated by H-NS/DNA loops constitutes a mechanism for transcription regulation. Namely H-NS binding regions of intermediate lengths can lead to fragile DNA hairpins which can be easily perturbed, for instance by the binding of more dedicated transcription factors. In short, the formation of DNA hairpin loops by the H-NS protein may be seen as a mechanical switch for regulating the transcription.

In chapter 5, I have investigated the inverse problem which is to reconstruct the chromosome folding from chromosomal contacts measured in Chromosome Conformation Capture (CCC) experiments. Using analytical results and Brownian dynamics simulations, I have proposed reconstruction methods relying on a representation of the chromosome with an effective polymer model. The main achievement of these methods was to reproduce the experimental contacts. Although perfectible, these methods represent in my view an original departure from what have been proposed in the literature during the last decade. Namely,

the effective model obtained may be used to perform Brownian dynamics simulations of the chromosome better rooted in biological data.

### **Value of the predictions**

A common denominator of our approaches has been to base our investigation on experimental evidences. However, accurate *in vivo* measurements are not always available. For example, measuring the transcription level of a pair of genes as a function of their spatial distance is an experimental challenge, and most often biologists must resort to indirect measures. Besides, even though high-throughput techniques relying on DNA sequencing and Polymerase Chain Reaction have produced a mine of experimental data, the relevant biological information can be hard to extract or it can be corrupted by noise. For these reasons, we are not yet in an era where established models can be confirmed by experiments to a quantifiable accuracy. This may explain partly at least why in this thesis I have remained at a rather qualitative level of comparison with experimental data. Maybe a fundamental limitation is the lack of a minimal biological system on which can be tested competing models. Indeed, bacteria are often considered as the simplest living system that can be investigated experimentally. Yet many biological processes in bacteria, like transcription regulation, replication or the cell-cycle control are very complex and not fully understood.

### **Link between architecture and transcription**

The work presented in this thesis is a humble contribution to the broader scientific effort that has been undertaken to unveil the relation between chromosome architecture and genetic expression. Specifically, it has become clear that the interplay between chromosome folding and transcription regulation is highly dynamical and should be more generally considered as two related components of the cell physiology. Understanding the link between these two components is critical to decipher complex regulatory mechanisms of the genetic expression. For instance, chromosome folding seems to play an important role in still unresolved biological processes such as cell differentiation and cell senescence. More generally, it is widely assumed that a better understanding of chromosome architecture is a prerequisite for addressing modern challenges in biology such as conditional gene expression and epigenetics.

During my investigation, I have acquired the conviction that the chromosome should be envisioned as a cellular organ rather than as a mere carrier of the genetic information. In particular, the chromosome might provide a physical medium, or scaffold, for propagating genetic signals. Such signals can be for instance the transcriptional state (a gene is transcribed or not), or the existence of methylations in the context of epigenetics. Assuming that a genetic signal can propagate to nearest neighbors in space, the outcome of chromosome folding should determine the distribution of genetic signals on the chromosome. This schematic view illustrates the problem of context sensitivity. Transcription levels display uneven variations when considered as a function of the genomic coordinate. Yet this can be seen as the result of an unlucky projection from a three-dimensional to a one-dimensional space. Indeed, one can expect that the three-dimensional folding of the chromosome results in the genomic coordinates with the same transcription levels to be close in space. In short, I put forward the idea that the chromosome should be compared to a “brain” in which every locus is a “neuron” carrying a genetic signal. The particular folding of the chromosome results in contacts between loci that can be seen as synapses enabling the propagation of the genetic signal between neurons. If one associates a particular layout of synapses to a given physiological state, then adjusting chromosome folding can lead to the dynamical re-allocation of these synapses and may be interpreted as the transition to another physiological state.

**Toward the design of synthetic gene networks?**

In the classical view of the operon system, it is the affinity of a protein to a promoter that determines the efficiency of a transcription factor to repress or activate the transcription of a gene. Thus, chemical engineering might be used to produce a protein with a strong binding affinity to a promoter. An important message that I have tried to convey all along this manuscript is that the regulation of transcription can also be achieved by means of structural changes applied to the chromosome. For instance, DNA loops can be envisioned as mechanical switches, and similarly to protein folding, chromosome folding can result in active or inactive domains with a dedicated function. Therefore, designing a regulatory mechanism to obtain a folding of the chromosome with mechanical switches and/or functional domains involves rather a structural and mechanical engineering approach. In short, there has been a shift in our conception of what constitutes a handle for regulating the transcription.

In terms of real applications, the design of a synthetic gene network would require for instance knowing how to position genes on the DNA sequence in order to achieve their co-expression. In particular this would require to have a deterministic knowledge of the functional structures formed. Despite the increasing number of physical models available, we are not able to achieve such a design yet.

**Future research**

My motivation for future research will be to obtain a better understanding of the connection between chromosome architecture and gene expression. Fundamentally, I would like to understand whether changes in the chromosome folding can be the driver of cell differentiation or cell senescence. In the short term, I would like to construct an empirical map that associates chromosome architecture to the physiological state of a cell. To serve that purpose, results obtained in the prediction of chromosome architecture from CCC data may be of precious help. Interesting outcomes of this mapping may be to provide novel diagnosis tools to detect cell deficiencies based on CCC assays.



# Publication

## Article

## Phase Behavior of DNA in the Presence of DNA-Binding Proteins

Guillaume Le Treut,<sup>1,2,\*</sup> François Képès,<sup>2</sup> and Henri Orland<sup>1</sup><sup>1</sup>Institut de Physique Théorique, Université Paris Saclay, CEA, CNRS, Gif-sur-Yvette, France; and <sup>2</sup>Institute of Systems and Synthetic Biology, University of Evry-Val-d'Essonne, CNRS, Genopole Campus 1, Evry, France

**ABSTRACT** To characterize the thermodynamical equilibrium of DNA chains interacting with a solution of nonspecific binding proteins, we implemented a Flory-Huggins free energy model. We explored the dependence on DNA and protein concentrations of the DNA collapse. For physiologically relevant values of the DNA-protein affinity, this collapse gives rise to a biphasic regime with a dense and a dilute phase; the corresponding phase diagram was computed. Using an approach based on Hamiltonian paths, we show that the dense phase has either a molten globule or a crystalline structure, depending on the DNA bending rigidity, which is influenced by the ionic strength. These results are valid at the thermodynamical equilibrium and therefore should be consistent with many biological processes, whose characteristic timescales range typically from 1 ms to 10 s. Our model may thus be applied to biological phenomena that involve DNA-binding proteins, such as DNA condensation with crystalline order, which occurs in some bacteria to protect their chromosome from detrimental factors; or transcription initiation, which occurs in clusters called transcription factories that are reminiscent of the dense phase characterized in this study.

## INTRODUCTION

Predicting the three-dimensional (3D) structure of chromosomes from the primary DNA sequence has become an important goal, as genomic and transcriptomic data are being generated at an elevated pace. In eukaryotes and prokaryotes, transcription of highly active genes has been shown through morphological evidence to occur within discrete foci containing RNA polymerases (RNAPs). It has later been demonstrated that one given focal point was enriched in one type of dedicated transcription factor (TF) (1,2) and one type of gene promoter (3), as well as nascent transcripts (4), thus justifying the naming of such foci as transcription factories. A thermodynamic model has shown that the stiff DNA polymer and properly located attractive sites mimicking TF bridges were necessary and sufficient ingredients to produce a transcription factory through DNA looping (5). Indeed, there is now convincing evidence that chromosomes are organized into loops (Hi-C, 3C, etc.) (2), and that looping brings distant genes together so that they can bind to elevated local concentrations of RNAPs (FISH, 3C, etc.) (6). DNA-binding proteins such as TFs are generally positively charged, thus providing a nonspecific interaction with the negatively charged DNA polymer. DNA sequence-dependent binding offers specific interactions. Together, nonspecific and specific associations allow proteins to search their target DNA sequences more efficiently via facilitated diffusion (7,8), which combines 3D diffusion in the bulk volume and monodimensional diffusion along the DNA. These considerations motivated studies

to characterize the timescale of the dynamics or anomalous diffusion. Molecular dynamics simulations are used to model proteins that diffuse to DNA, bind, and dissociate. The timescales reached in numerical simulations are usually several orders of magnitude smaller than the biological ones, and thus the phenomena observed during such simulations might be transient and irrelevant biologically.

In this article, we present a study of the properties and phase diagram of a DNA-protein solution, at thermodynamic equilibrium, which entails DNA condensation into compact structures induced by nonspecific DNA-binding proteins. The calculated phase diagram is thus expected to be relevant at biological timescales. To do so, we consider a simplified model in which the nucleus (or bacterial nucleoid) is represented by a closed volume  $V$  (Fig. 1). The double-stranded DNA chains are modeled as  $M$  semiflexible polymer chains (polymerization index  $N$ ) that interact with  $P$  spheres, which represent either transcription factors or structural proteins. We consider the nucleus (or bacterial nucleoid) to be a good solvent for DNA chains, so that monomers experience a repulsive interaction between themselves. Conversely, we assume that there is an attractive interaction between proteins and DNA that allows the proteins to bind to DNA. As for the protein-protein interaction, we consider a repulsive (hard-core) interaction, but the case of an attractive (e.g., complexation, dimerization, etc.) interaction could be treated in the same way. Finally, we assume that all interactions are nonspecific. In the sequel, subscripts  $D$  and  $P$  stand for DNA and protein, respectively. We first describe the phase diagram of such a system in the mean-field approximation and show that there is a phase transition from a dilute phase

Submitted July 17, 2015, and accepted for publication October 15, 2015.

\*Correspondence: [guillaume.le-treut@cea.fr](mailto:guillaume.le-treut@cea.fr)

Editor: Rohit Pappu

© 2016 by the Biophysical Society  
0006-3495/16/01/0051/12



<http://dx.doi.org/10.1016/j.bpj.2015.10.027>

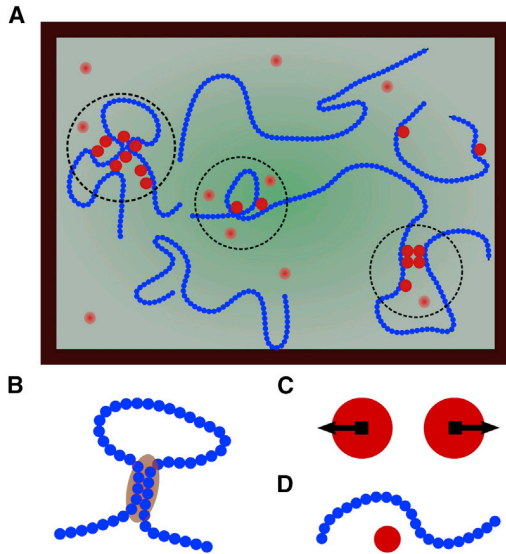


FIGURE 1 (A) Model of DNA represented as beads-on-string polymers (blue) interacting with proteins (red). Dotted circles stand for clusters with high concentrations of DNA monomers and proteins. (B) Monomer-monomer interaction is repulsive. (C) Protein-protein interaction is repulsive. (D) DNA-protein interaction is attractive. To see this figure in color, go online.

at high temperature to a concentrated phase of the DNA and proteins at lower temperature, which can be identified as the transcription factory phase. In a second step, we characterize the structure of the dense phase and show that it can adopt a crystalline order, suggesting an interesting parallel with the existence of some DNA biocrystals in vivo. This general method can be applied to many genome architecture problems.

## Flory-Huggins theory

### Free energy and thermodynamic functions

In the following, we study the phase diagram of the bulk of the bacterial cell (or nucleus) in the mean-field approximation. In the context of polymer theory, this approximation is also called the Flory-Huggins theory (9). A similar kind of approach has been used to study the demixion of a mixture of polymers and colloids, in which the interaction is repulsive (10). By contrast, in our study, the polymer-colloid interaction is taken as attractive. We denote the concentrations of DNA monomers and proteins as  $c_D$  and  $c_P$ , respectively, and the molecular volume of a DNA monomer and of a protein as  $\sigma_D$  and  $\sigma_P$ , respectively. The (Flory-Huggins) free energy per unit volume is as follows:

$$\beta f(c_D, c_P) = \frac{1}{2}\alpha_D c_D^2 + \frac{1}{2}\alpha_P c_P^2 + \nu c_D c_P + \frac{1}{6}w(c_D + c_P)^3 + c_P \log \frac{c_P \sigma_P}{e} + \frac{c_D}{N} \log \frac{c_D \sigma_D}{eN}, \quad (1)$$

where  $\alpha_D$ ,  $\alpha_P$ , and  $\nu$  are second-order virial coefficients denoting the DNA-DNA, protein-protein, and DNA-protein interactions, respectively; and  $w$  is the third virial coefficient, necessary to avoid the collapse of the system. Note that this last term comes mostly from the entropy of the solvent. Indeed, if solvent molecules were present with concentration  $c_S$  and molecular volume  $\sigma_S$ , the solvent translational entropy would be  $c_S \log c_S \sigma_S / e$ . If we assume incompressibility of the DNA-protein-solvent mixture (i.e.,  $c_D + c_P + c_S = c_0$ ), the solvent entropy can be written as a mean-field solution as  $(c_0 - c_D - c_P) \log(c_0 - c_D - c_P) \sigma_0 / e$ , which, when expanded to the third order in  $(c_D + c_P)$ , yields the cubic term in Eq. 1.

The Gibb's free energy per unit volume is the following Legendre transform of Eq. 1:

$$\beta g(c_D, c_P) = \beta f(c_D, c_P) - \mu_D c_D - \mu_P c_P = -\beta \Pi, \quad (2)$$

where  $\Pi$  is the osmotic pressure and  $\mu_D$  and  $\mu_P$  are the chemical potentials of DNA monomers and proteins, respectively. The total number of particles of the system is fixed, but as we show below, these chemical potentials play a useful role when the system separates into two phases at equilibrium. At thermal equilibrium, the Gibb's energy is an extremum:  $\partial \beta g / \partial c_D = 0$  and  $\partial \beta g / \partial c_P = 0$ , from which we deduce the following chemical potentials:

$$\begin{aligned} \mu_D(c_D, c_P) &= \frac{\partial \beta f}{\partial c_D} = \alpha_D c_D + \nu c_P + \frac{1}{2}w(c_D + c_P)^2 \\ &\quad + \frac{1}{N} \ln \left( \frac{c_D \sigma_D}{N} \right) \\ \mu_P(c_D, c_P) &= \frac{\partial \beta f}{\partial c_P} = \alpha_P c_P + \nu c_D + \frac{1}{2}w(c_D + c_P)^2 \\ &\quad + \ln(c_P \sigma_P). \end{aligned} \quad (3)$$

By inserting the last expressions in Eq. 2, we see that  $\alpha_D$ ,  $\alpha_P$ , and  $\nu$  are indeed identified to the coefficients of a virial expansion.

The free energy in Eq. 1 is quite general and holds for arbitrary interactions between the constituents. It is possible to relate  $\alpha_D$ ,  $\alpha_P$ , and  $\nu$  to any pair potential, say  $u(r)$ , used to model the corresponding interaction. Indeed, these virial coefficients can be computed to lowest order (in the density) using the following well-known Mayer relation:

$$\alpha = - \int d^3 \mathbf{r} (e^{-\beta u(\mathbf{r})} - 1), \quad (4)$$

and the same for  $\nu$ .

In physiological conditions, salt (e.g., NaCl and KCl) and ions (e.g.,  $\text{Ca}^{2+}$  and  $\text{Mg}^{2+}$ ) are present in solution, giving rise to screened electrostatic interactions. The interactions are therefore short-ranged with a range given by the Debye-Hückel length. Yet, at the mean-field level, the specific shapes of the interaction potentials is irrelevant, and the

effect of ions in solution only arises through an adjustment of the Mayer coefficients  $\alpha_D$ ,  $\alpha_P$ , and  $v$ . The DNA excluded volume coefficient  $\alpha_D$ , which accounts also for the electrostatic repulsion between negatively charged monomers, is positive. The protein-protein coefficient  $\alpha_P$  in general is positive (repulsive), because of electrostatic repulsion between identically charged proteins; but it can be attractive (negative) for specific molecules, which may undergo dimerization or hybridization. For hard spheres, for instance,  $\alpha = 2^3\sigma$ ,  $\sigma$  is the volume of one sphere. We hereafter restrict our focus to the case where DNA-DNA and protein-protein interactions are purely repulsive (steric).

Conversely, we assume  $v < 0$ , i.e., the DNA-protein interaction has an attractive tail, which is temperature-independent (in first approximation). As we show below, the Flory-Huggins theory predicts the existence of a critical temperature  $T^c$ . We assume that  $v(T)$  is analytic in  $|T - T^c|$  and can be written to the leading order as in the following:

$$v(T) = v(T^c) \frac{\theta - T}{\theta - T^c}, \quad (5)$$

where  $\theta$  is the Flory-Huggins temperature for which  $v(\theta) = 0$ , i.e., the interaction vanishes.

#### The regime of phase separation

As mentioned previously, there is a phase transition when the homogeneous solutions  $c_D = MN/V$  and  $c_P = P/V$  become unstable. It is well known that generically, when the temperature decreases, the system separates into two phases. At the phase separation point, the homogeneous high-temperature phase may stay metastable down to a point, called the spinodal point, where the homogeneous phase becomes totally unstable. The so-called spinodal condition is given by the following equation:

$$\left| \frac{\partial^2(\beta f)}{\partial(c_D, c_P)} \right| = \begin{vmatrix} \partial^2 \beta f / \partial c_D^2 & \partial^2 \beta f / \partial c_D \partial c_P \\ \partial^2 \beta f / \partial c_D \partial c_P & \partial^2 \beta f / \partial c_P^2 \end{vmatrix} \leq 0, \quad (6)$$

where the array denotes the determinant of the matrix.

In general for  $v(T)$  fixed, Eq. 6 with the equality determines a line of spinodal points, delimiting the region where the homogeneous mean-field solution is stable from the region where it is not. In the unstable regions, the system undergoes a phase separation. If  $T$  is increased,  $v(T)$  becomes less negative. At some point, the spinodal lines merge into a point when  $T$  reaches a critical value  $T^c$  (Fig. 2). This is a tricritical point. For  $T > T^c$ , the homogeneous solution is stable for any value of  $c_D^*$  and  $c_P^*$ , where we use the \* superscript to emphasize that these concentrations are the mean-field solutions in the absence of phase separation. There are critical lines emerging from the tricritical point when the temperature is decreased, as we show below.

In a biphasic regime, the concentrations are different but uniform in each of the two phases, separated by an interface whose energy is not extensive (the interfacial free energy is proportional to the surface of the interface). **We label the dilute phase by *I*, and the dense phase by *II*.** The total system free energy then reads as follows:

$$\frac{\beta F^{tot}}{V} = \phi^I \beta f(I) + \phi^{II} \beta f(II), \quad (7)$$

where  $f(I)$  is a shorthand for  $f(c_D^I, c_P^I)$  and  $\phi^I$  and  $\phi^{II}$  denote the volume fraction of the dilute and dense phase.

A straightforward minimization of Eq. 7, with the constraints of conservation of volume and particles number of  $D$  and  $P$ , yields the following usual equations of coexistence between phase  $I$  and phase  $II$ :

$$\begin{cases} \mu_D(I) & = & \mu_D(II) \\ \mu_P(I) & = & \mu_P(II) \\ \Pi(I) & = & \Pi(II) \end{cases}, \quad (8)$$

where  $\Pi$  denote the osmotic pressures of each phase. The above equations are simply the equalities of the chemical potentials and the osmotic pressures. It trivially implies  $\phi^{II} = 1 - \phi$  with  $\phi = \phi^I$ . Note that Eq. 8 is a system of three equations with five variables ( $c_P^I, c_D^I, c_P^{II}, c_D^{II}, T$ ); thus it determines a surface of coexistence.

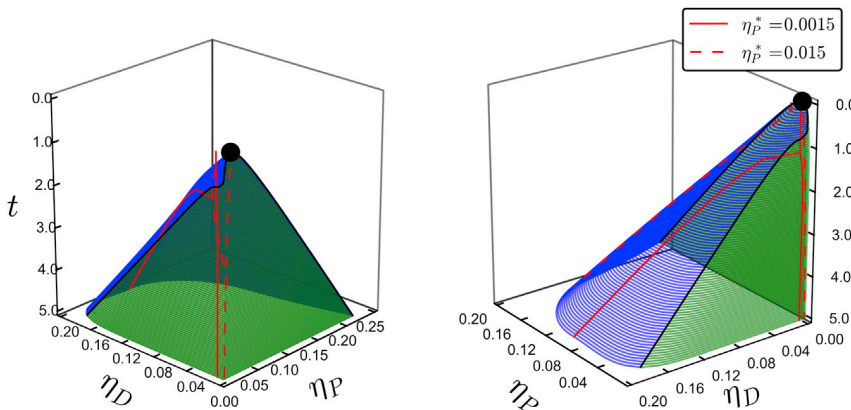


FIGURE 2 Three-dimensional representation of the coexistence surface in a  $(\eta_D, \eta_P, t)$  coordinate system. Coexistence lines are shown for  $\eta_P^* = 0.0015$  and  $0.015$ , with  $\eta_D^* = 0.01$  (red lines). Critical lines (black lines) emerge from the tricritical point (black dot). To see this figure in color, go online.

## MATERIALS AND METHODS

### Molecular dynamics simulations

To sample configurations of our system we used the LAMMPS (large-scale atomic/molecular massively parallel simulator) software package. The system is coarse-grained so that DNA is modeled as a beads-on-string polymer and proteins as spheres. The simulations are run in the Brownian dynamics (BD) mode. The resulting dynamics consists in the integration of the following Langevin equation:

$$m_i \frac{d^2 \mathbf{r}_i}{dt^2} = \mathbf{F}_i - \gamma_i \frac{d\mathbf{r}_i}{dt} + \sqrt{2k_B T \gamma_i} \boldsymbol{\eta}_i(t), \quad (9)$$

where  $i$  is the index of one bead,  $\mathbf{r}_i$  is the position of the bead,  $\gamma_i$  is the friction coefficient,  $\mathbf{F}_i$  is the resulting force exerted on the bead from the rest of the system,  $k_B$  is the Boltzmann constant, and  $T$  is the temperature. The last term is a stochastic force in which  $\boldsymbol{\eta}_i(t)$  is a Gaussian white noise such that  $\langle \boldsymbol{\eta}_i(t) \boldsymbol{\eta}_j(t') \rangle = \delta_{ij} \delta(t - t')$ . Simulations were run with  $m_i = 1$ ,  $\gamma_i = 1$ , and  $k_B T = 1$ , in a cubic volume of size  $L = 100$  with periodic boundary conditions, and we took a polymer with  $N = 400$  beads. The diameter  $a$  of the beads was taken as the unit length.

As for the polymer chain model, beads  $i$  and  $i + 1$  are connected with a finitely extensible nonlinear potential (FENE) that results in the following:

$$U_{el}(\mathbf{u}_i) = -\frac{K_{el}}{2} r_0^2 \ln \left( 1 - \frac{u_i^2}{r_0^2} \right), \quad (10)$$

where  $\mathbf{u}_i = \mathbf{r}_i - \mathbf{r}_{i-1}$ . Simulations were run with  $K_{el} = 30 k_B T / a^2$  and  $r_0 = 1.5 a$ .

The bending rigidity of the polymer chain is introduced through the following Kratky-Porod potential:

$$U_b(\theta_i) = K_b (1 - \cos \theta_i), \quad (11)$$

where  $\theta_i$  is the angle between vectors  $\mathbf{u}_i$  and  $\mathbf{u}_{i+1}$ . The bending coefficient is related to the persistence length by  $K_b = l_p \times k_B T$ .

We restricted our analysis to the case of DNA monomers and protein spheres of same dimension (with diameter  $a$ ). This assumption does not alter the main qualitative features of the physics but makes the discussion simpler. Steric as well as attractive interactions between beads are introduced using a truncated Lennard-Jones potential such as the following:

$$U_{LJ}(\mathbf{r}_{ij}) = \begin{cases} 4\epsilon \left[ \left( \frac{a}{r_{ij}} \right)^{12} - \left( \frac{a}{r_{ij}} \right)^6 - \left( \frac{a}{d^r} \right)^{12} + \left( \frac{a}{d^r} \right)^6 \right] & \text{if } r_{ij} < d^r \\ 0 & \text{otherwise} \end{cases}. \quad (12)$$

Unless stated otherwise, we took the values indicated in Table 1. The DNA-DNA interaction being purely repulsive, we retrieve  $\alpha_D \approx 2^3 \sigma_D$ , where  $\sigma_D$  is the volume of one monomer. The same argument holds for the proteins. Conversely, the monomer-sphere coefficient  $v(T)$  is largely negative (Table 1 and Fig. 3).

We systematically performed equilibration runs of  $10^5$  time units to reach thermal equilibrium. We then performed sampling runs of  $10^6$  time units that we used to measure physical quantities. Our simulation time units can be understood as follows. The diffusion coefficient can be expressed as  $D = a^2 / \tau_B$ , where  $\tau_B$  is the Brownian time corresponding to one simulation time unit. Therefore, we can do a mapping to physical units. Assuming a diffusion coefficient of  $D \approx 10 \mu\text{m}^2 \text{s}^{-1}$  for a protein in the bacterial nucleoid (11), we find  $\tau_B = 600 \text{ ns}$  for  $a = 6 \text{ nm}$ , and  $\tau_B = 2.0 \mu\text{s}$  for  $a = 20 \text{ nm}$ .

**TABLE 1** Parameters for the truncated Lennard-Jones potential modeling the DNA-DNA, protein-protein, and DNA-protein interactions

1	2	$\epsilon$	$a$	$d^r$	Mayer Coefficient $\alpha$
DNA	DNA	1.00	1.00	1.12	4.40
Protein	Protein	1.00	1.00	1.12	4.40
DNA	Protein	3.00	1.00	2.00	-62.6

The mean-field pair coefficients are computed using Mayer formula.

### Mean-field concentrations

To assess physiological concentrations, we assimilate an *Escherichia coli* (*E. coli*) bacteria to a cylinder of radius  $0.5 \mu\text{m}$  and length  $1 \mu\text{m}$ . We took a genome length of  $4.6 \cdot 10^6$  base pairs (*bp*). We consider that the diameter of one monomer is  $1 a = 6 \text{ nm} \equiv 17 \text{ bp}$ , so that one such chromosome is modeled as a polymer of  $N = 2.6 \cdot 10^5$  monomers with diameter  $1 a$ . This leads to a density of DNA  $\eta_D \sim 10^{-2}$ . As for the proteins, there are several DNA-binding proteins, called nucleoid-associated proteins, which act on the structure of the DNA. In *E. coli*, for instance, HU, H-NS, Fis, RecA, Dps, and other proteins have this structuring function. We choose to use Fis as a reference because it is a well-known structural protein with a large number of target sites (12) and binds to DNA sequences of 17 nucleotides (13). In *E. coli*, there are  $\sim 75,000$  Fis proteins per genome copy (14) in the early exponential growth phase, yielding a ratio  $\eta_P / \eta_D \approx 0.3$ . This is also consistent with previous numerical studies for which  $0.1 < \eta_P / \eta_D < 0.5$  (15). Eventually we suggest that this ratio might be quite general and can also be mapped to eukaryotes. Indeed, we could either consider a human cell (genome length of  $\sim 3.3 \cdot 10^9 \text{ bp}$  and nucleus diameter of  $10 \mu\text{m}$ ) and take  $1 a = 20 \text{ nm}$  as a unit length (size of protein complex). Considering that the DNA would be packed as euchromatin with a linear packing fraction  $\nu = 100 \text{ bp/nm}$  (16), the unit length is  $1 a \equiv 1.71 \cdot 10^6 \text{ bp}$  and we get  $\eta_D \sim 10^{-2}$ . In the former case, the proteins are assumed to be  $\sim 6 \text{ nm}$  in diameter, whereas the latter case better describes the interaction of DNA with large protein complexes.

### Computation of the phase diagram

The coexistence surface is computed by solving Eq. 8. Because of numerical accuracy limitations, we computed the phase diagrams for chains with a

polymerization index of  $N = 5000$ . Because the critical values scale like  $1/\sqrt{N}$  (Fig. 4), this arbitrary choice captures the essential features of the  $N \rightarrow \infty$  limit. Finally, the model relies on a free parameter  $w$ , which can be used to fit the model. In Flory-Huggins theory,  $w$  is extracted from the development of the entropy of mixing and would be  $w_F = 1/c_0^2$ , where  $c_0$  is the close packing concentration. However, cells are crowded environments, containing other species, metabolites, or organelles. Furthermore, biological compartments can also restrict the accessible volume. Eventually, this value is underestimated and we arbitrarily choose  $w = 10 \times w_F$ . Although it could be much larger, the variations of  $c_p^c$  above this value are quite slow and do not alter dramatically the previous phase diagrams (Fig. 4). With all these parameters, we find for the tricritical point coordinates:  $c_p^c = 2.2 \cdot 10^{-2} a^{-3}$ ,  $c_D^c = 7.7 \cdot 10^{-4} a^{-3}$ , and  $\beta^c v(T^c) = -25.67 a^3$ .

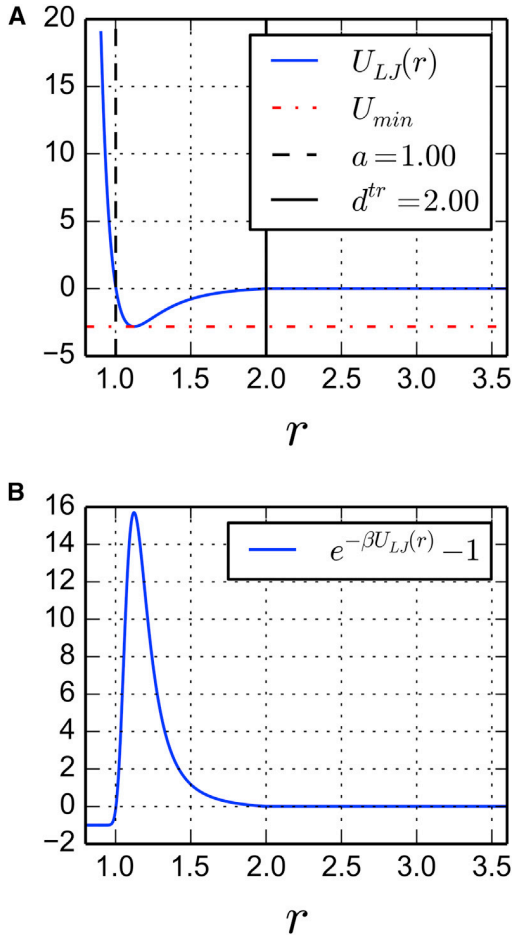


FIGURE 3 Truncated Lennard-Jones potential modeling an attractive interaction between DNA and proteins with parameters indicated in Table 1: (A) potential shape and (B) Mayer function. To see this figure in color, go online.

## RESULTS

We present in this section the results of the mean-field theory and defer the discussion of the actual values of the parameters (see Materials and Methods). We assume that DNA and protein spheres have the same size (diameter  $a$ ) that we use as the new unit length. The temperature  $T$  and the coefficient  $v(T)$  are related through Eq. 5, and we therefore introduce the order parameter  $t$  in the following:

$$v(T) = v(T^c)(1 + t). \quad (13)$$

We choose to discuss the phase separation in terms of  $t$  and of the densities  $\eta_D = c_D \sigma_D$  and  $\eta_P = c_P \sigma_P$ . The coexistence surface is then computed numerically by solving Eq. 8 and is shown in Fig. 2. At the critical point, Eq. 8 has a unique solution, namely the triplet  $(\eta_D^c, \eta_P^c, T^c)$ . As previously reported for such systems (10), we find the following:

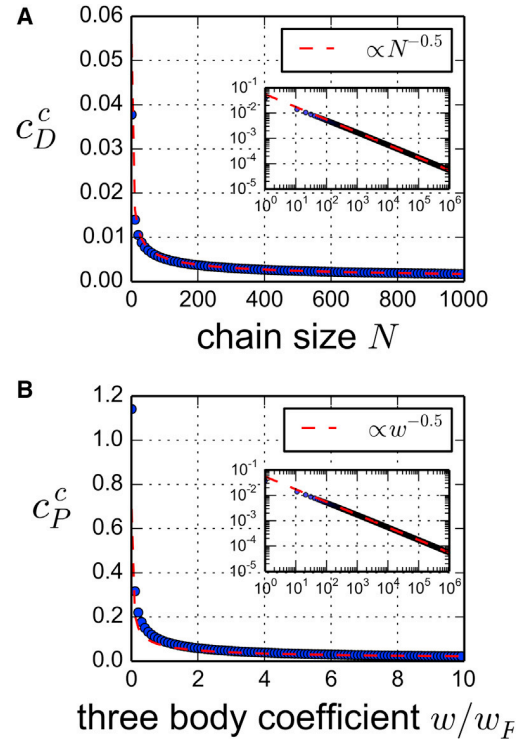


FIGURE 4 (A) The DNA critical concentration  $c_D^c \sim 1/\sqrt{N}$ . (B) For  $w > 10w_F$  the variations of  $c_P^c$  and of the other critical parameters are very slow. To see this figure in color, go online.

$$\eta_D^c \sim \frac{1}{\sqrt{N}}. \quad (14)$$

This is the same scaling as the overlap density for polymer chains of size  $N$ , which is the density at which polymer coils begin to interpenetrate (see, for instance, (9)). Given that DNA is present in the nucleoid at concentrations close to the overlap density, this suggests that biological systems may function at the vicinity of this tricritical point.

For  $T < T^c$  we have  $v(T) < v(T^c) < 0$ , which corresponds to a DNA-protein interaction more attractive than at the critical point and the solutions of Eq. 8 are distributed on a closed curve. This closed curve is in fact the collection of all pairs of coexisting dilute  $(c_D^l, c_P^l)$  and dense  $(c_D^h, c_P^h)$  phases. They are represented in Fig. 5, where the pairs of coexisting phases are connected by tie lines. Although there is an infinite set of possible states of coexistence, the total number of DNA and protein spheres selects a unique solution pair. The resulting coexistence state is uniquely determined by the following relation, whose graphical interpretation is shown in Fig. 5:

$$\phi \begin{pmatrix} c_D^l \\ c_P^l \end{pmatrix} + (1 - \phi) \begin{pmatrix} c_D^h \\ c_P^h \end{pmatrix} = \begin{pmatrix} c_D^* = MN/V \\ c_P^* = P/V \end{pmatrix}. \quad (15)$$

An important point to note is that in general, the concentration of DNA in the dilute phase is very small. Indeed, the

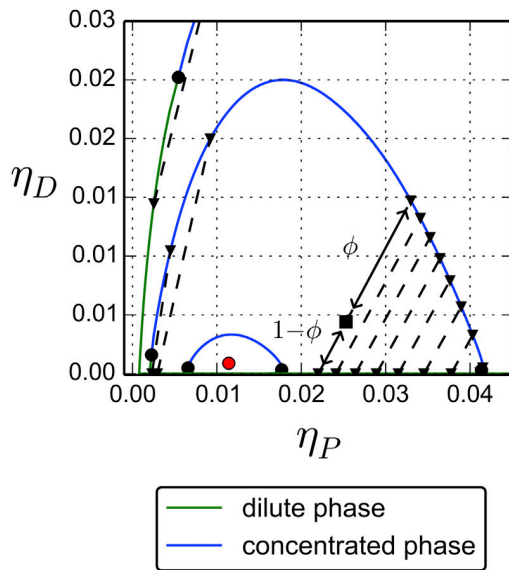


FIGURE 5 Coexistence lines for  $t = 0.05, 0.5, 1.0$ . The coexistence line shrinks toward the tricritical point (red dot) when  $t \rightarrow 0$ . For each curve, the dilute phase is shown in green and the concentrated phase is shown in blue. Coexisting states are connected by tie lines (dotted segments). The volume fraction of each phase is determined (black arrows) according to Eq. 15. To see this figure in color, go online.

translational entropy of DNA is small, because of the factor  $1/N$ , and thus there is no entropic gain for the DNA to be in the dilute phase, whereas it has an important enthalpic advantage to be in the concentrated phase. To illustrate how one can determine the composition of the system, we now explain how phase separation takes place when cooling the system from high to low temperature. We consider the following case of DNA and protein densities:

$$\eta_D^* = 0.01, \quad (16)$$

$$\eta_P^* = 0.0015. \quad (17)$$

Again, we defer the justification for this choice of the parameters. The system splits into two phases at a temperature  $T^*$ . For  $T > T^*$ , the system is homogeneous with values of the concentration given by Eq. 16, whereas for  $T < T^*$ , the system splits into two phases whose composition is determined by Eqs. 8 and 15. The line of coexistence obtained is shown on Fig. 2. Note that at  $T = T^*$ , the phase transition is first order, except when  $T^*$  is on a critical line, in which case it is second order. Let us now assume that the concentration of proteins is increased by a factor of 10 to  $\eta_P^* = 1.5 \cdot 10^{-2}$ . When the system is cooled from high temperatures, it splits into two phases, and as before, the coexisting states are distributed on the surface of coexistence. However, the mass conservation requirement (Eq. 15) yields a different line of coexistence. The new line of coexistence is shown with dashed lines in Figs. 2 and 6. As might have been expected, an augmentation of the protein concentration results in an increased protein concentration in both the dilute and concentrated phases (Fig. 6 A). The DNA concentration, however, shows a two-step pattern. When additional proteins are added to the solution, the free DNA monomers of the dilute phase are transferred to the concentrated one, and consequently, the DNA concentration in the dense phase first increases. But at some point, the DNA concentration in the dense phase reaches a maximum and starts to decrease (Fig. 6, B and C). Indeed, a fraction of the newly added proteins populate the concentrated phase and make it swell, while the amount of DNA remains the same. Therefore, varying the total quantity of proteins can induce

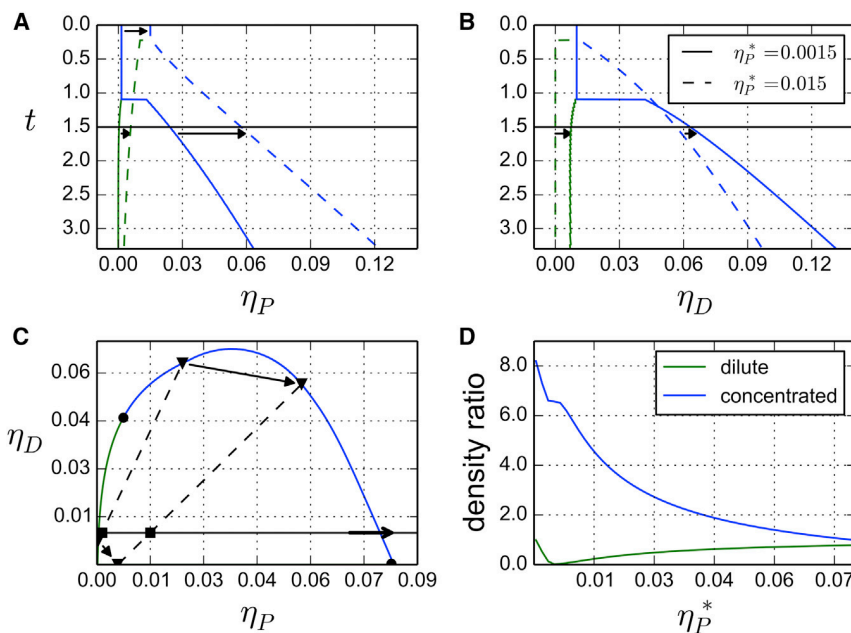


FIGURE 6 Coexistence lines for  $\eta_P^* = 0.0015$  and  $0.015$ , with  $\eta_D^* = 0.01$ . These are the projections of the coexistence lines of Fig. 2 as a function of the density of (A) proteins or (B) DNA. (C) Section of the phase diagram at  $t = 1.5$  (corresponding to the parameters given in Table 1). A path corresponding to a fixed DNA density of  $\eta_D^* = 0.01$  is drawn (black line). (D) Density ratio  $(\eta_D + \eta_P)/(\eta_D^* + \eta_P^*)$  for the dilute phase and dense phase, for a density of DNA fixed to  $\eta_D^* = 0.01$ . To see this figure in color, go online.

nonmonotonous variations of the DNA concentration in the phases of the system.

### Structure of the dense phase

#### Example of structures

We showed above how the Flory-Huggins theory predicts the existence of a phase separation between two homogeneous phases. It is well known that within the Flory-Huggins approximation, the chain structure is not taken into account, except through the suppression of the translational entropy of the chains. In particular, the fact that chains may have a strong bending rigidity (long persistence length) does not play any role at this level. Therefore, the predicted structure of the dense phase is that of a melt of collapsed polymer with spheres. However, several studies have highlighted that the bending rigidity of the polymer has an influence on the microstructure of the dense phase (15-17). This is well characterized (Fig. 7). A standard way to characterize the effect of the chain structure is to use the random phase approximation (RPA) (see (9)). We have performed such RPA calculations, but we do not report them in this article, because they did not show any interesting instability in the dense phase. The reason for the failure of RPA is that the phase

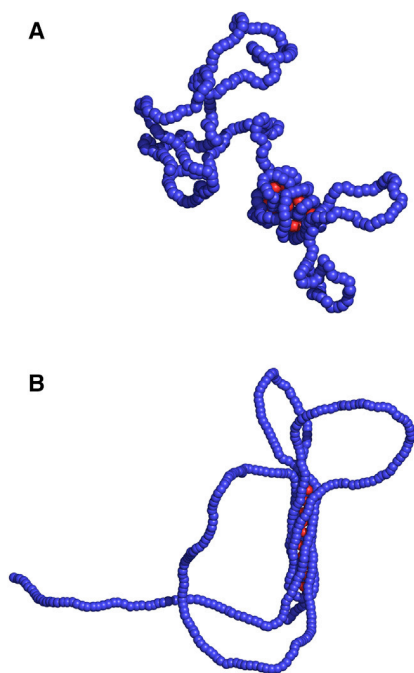


FIGURE 7 Two equilibrium configurations of a single polymer chain (blue) displaying the coexistence of a dense and a dilute phase, with persistence length  $l_p = 1$  (A) and  $l_p = 20$  (B) interacting with proteins (red). For small bending rigidity, the structure of the dense phase is globular whereas it is cylindrical in the other case. We performed simulations with  $P = 10$  spheres (see Materials and Methods). To see this figure in color, go online.

transition from the homogeneous to the separated phases is first order and thus is not driven by critical fluctuations. This is a typical case when RPA fails to give insights about the dense phase structure.

#### Theory of Hamiltonian paths

Because RPA is not appropriate to describe the system in the dense phase, we adopt another approach. Because of their attractive interactions with the DNA, the spheres in which the polymer is immersed play the role of colloid particles that bridge various parts of the polymers. Consequently, these spheres induce an effective attraction between the monomers. We thus turn to a model of a semiflexible polymer chain on a lattice that has been proposed initially to explain the folding of a protein in compact structures (17-19) (see Fig. 8). An attraction energy  $\epsilon_v$  between nonbonded nearest neighbors is included, which favors compact configurations. A bending energy of the chain is introduced as a corner penalty. It penalizes corners by an energy  $\epsilon_h$  and thus plays the role of a bending rigidity. As we show below, this term induces an ordering transition between a random (molten) globule where corners are mobile in the bulk, and a crystalline phase, where corners are expelled to the surface of the globule. Using mean-field theory, it was shown that depending on the temperature and chain stiffness, three phases can exist, namely a dilute phase where the polymer is swollen; a condensed phase, which we call a molten globule, where the polymer is collapsed and disordered; and finally a second condensed phase where the polymer is collapsed but with a local crystalline ordering. The phase diagram is described simply by the two parameters  $\epsilon_v$  and  $\epsilon_h$ . For fixed small  $\epsilon_h$ , there is a second-order phase transition at a temperature  $T = T_\theta$  between a dilute and a disordered condensed phase, followed by a first-order freezing transition at  $T_F$  between the disordered condensed phase and a locally ordered condensed phase of the

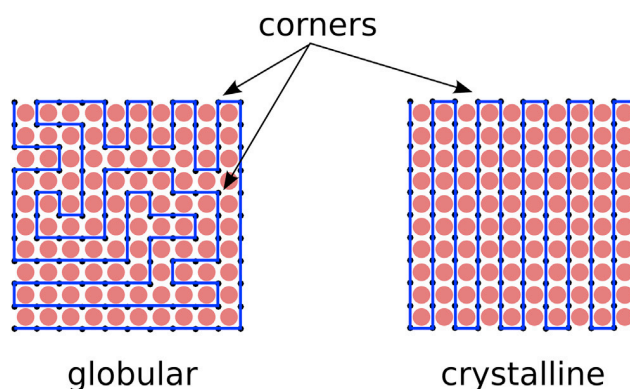


FIGURE 8 Two realization of Hamiltonian paths on a cubic lattice. The globular state contains an extensive number of corners whereas the crystalline state contains a nonextensive number of corners (proportional to the surface). To see this figure in color, go online.

polymer. Upon increasing the chain stiffness  $\epsilon_h$ , the molten globule region shrinks until it eventually vanishes. For larger stiffness, the polymer goes abruptly from a swollen to a frozen configuration ( $T_F > T_\theta$ ) through a direct first-order transition (Fig. 9). These theoretical results were readily confirmed and improved by Monte-Carlo simulations (17,20,21).

In its simplest form, this model considers a completely collapsed polymer on a lattice. It is represented as a Hamiltonian path (HP) on a lattice, that is a path that visits each site once and only once. Thus the density of monomer is  $\eta = 1$ . A good approximation to the total number  $\mathcal{N}$  of HP on a lattice was shown to be (22) the following:

$$\mathcal{N} = \left(\frac{q}{e}\right)^N, \quad (18)$$

where  $N$  is the total number of points of the lattice and  $q$  is the coordination number of the lattice, e.g.,  $q = 2d$  on a  $d$ -dimensional cubic lattice.

In the case of semiflexible polymers (HP with corner penalty), the partition function is the following (17):

$$\mathcal{Z} = \sum_{\{HP\}} e^{-\beta \epsilon_h N_C(HP)}, \quad (19)$$

where  $N_C(HP)$  counts the number of corners of a HP realization.

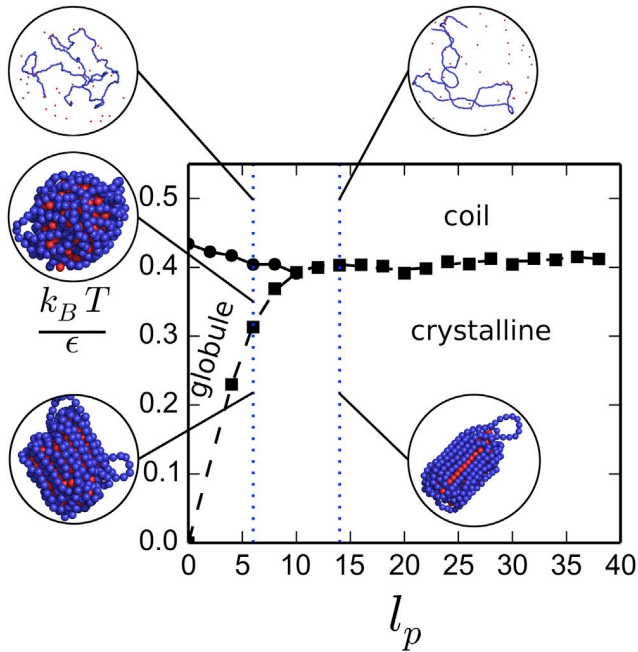


FIGURE 9 Phase diagram obtained for a polymer chain interacting with spheres. The phase diagram is plotted as a function of  $k_B T / \epsilon$  and  $l_p$ , where  $\epsilon$  is the strength of the Lennard-Jones DNA-protein interaction and  $l_p$  is the persistence length. We performed simulations with  $P = 100$  spheres (see Materials and Methods). To see this figure in color, go online.

A saddle-point approximation gives the following corresponding free energy per monomer:

$$\beta f = -\ln \frac{q(\beta)}{e}, \quad (20)$$

where

$$q(\beta) = 2 + 2(d-1)e^{-\beta \epsilon_h}, \quad (21)$$

is an effective coordination number,  $e = 2.71828\dots$ , and  $d$  is the dimensionality of the lattice. Note that if the corner penalty vanishes, we recover the result of Eq. 18.

As the temperature decreases, the effective coordination number  $q(\beta)$  decreases, and the free energy increases. There is a temperature  $T_F$  for which  $q(\beta) = e$ , giving a free energy per monomer  $f(T_F) = 0$ . For  $T < T_F$ ,  $f(T)$  would become positive in Eq. 20 if the saddle-point approximation were still valid. However,  $f(T)$  is a negative quantity (18) and, therefore, remains zero the freezing temperature  $T_F$ . Consequently for temperatures  $T > T_F$ , the corners are mobile in the bulk, leading to a liquid-like structure for the corners; whereas for  $T < T_F$ , the polymer is frozen in stretched configurations with  $f(T) = 0$ , in which corners are expelled to the surface and polymer segments tend to be aligned inside (Fig. 8). These configurations have been studied previously: they are elongated neck structures or toroids (23), whose typical size is given by the following:

$$\frac{\epsilon_h}{U(\beta)} \sim l_p, \quad (22)$$

where  $U(\beta) = \partial(\beta f) / \partial \beta$  is the internal energy.

This simple model can be extended to the case where the volume fraction  $\eta < 1$ . It requires the introduction of the parameter  $\epsilon_v = -\chi$ , where  $\chi$  is the Flory-Huggins parameter of a polymer chain in a solvent and denotes the effective attraction between monomers induced by the proteins. This leads to the computation of the above mentioned phase diagram in terms of the two parameters  $\epsilon_v$  and  $\epsilon_h$ .

### Results

To make the HP approach more quantitative, it is interesting to relate its parameters to our simplified picture of DNA interacting with proteins. Namely, we would like to relate  $\epsilon_v$  and  $\epsilon_h$  to the parameters of the Flory-Huggins free energy in Eq. 1. But in the last one, the monomer-monomer attraction is mediated by spheres. In the dense phase, the total concentration of monomers and spheres:  $c = c_D + c_P$  is essentially fixed to the close packing concentration  $c_0$ . By inserting this in Eq. 1, we obtain the following:

$$\beta f = \left(\frac{\alpha_D + \alpha_P}{2} + v(T)\right) c_D^2 + \frac{1}{6} c^3 + (c - c_D) \ln \frac{c - c_D}{e}, \quad (23)$$

where we neglect the translational entropy of the polymer in the dense phase and drop the linear terms in  $c_D$  as this results

in an adjustment of the chemical potentials. We then have the following correspondence:

$$\varepsilon_v \equiv -v(T) - \frac{\alpha_D + \alpha_P}{2}. \quad (24)$$

For low temperature,  $v(T)$  can reach large negative values. This is mapped to a large  $\varepsilon_v$  in the HP model. Depending on the rigidity of the chain, the dense phase might be globular (low  $l_p$ ) or crystalline (large  $l_p$ ). The effective monomer density in the dense phase is given by the following:

$$\eta \equiv \frac{c_D}{c_D + c_P}. \quad (25)$$

One important result obtained using a HP model is the phase diagram of a polymer on a lattice (implicit solvent) with bending rigidity, obtained in an earlier mean-field study (17) and then supplemented by Monte Carlo studies (20). We show in our study that the phase diagram of a semiflexible polymer interacting explicitly with spheres in an off-lattice volume is very similar. We performed BD simulations with a polymer chain of  $N = 400$  beads and  $P = 100$  protein spheres in a cubic volume of size  $L = 100$  with periodic boundary conditions (see [Materials and Methods](#)). Polymer beads and protein spheres interact through a Lennard-Jones potential with a well depth given by the energy scale  $\varepsilon$  (in  $k_B T$ ). We used a Kratky-Porod model of polymer, with bending rigidity characterized by the persistence length  $l_p$ . By varying  $l_p$  and  $\varepsilon$  independently, we were able to explore the phase behavior of this system. We monitored the coil-globule transition by looking at the quantity in the following:

$$q = \frac{\log R_g}{\log N}, \quad (26)$$

where  $R_g$  is the radius of gyration of the polymer. For a self-avoiding polymer with scaling law  $R_g \sim bN^\nu$ ,  $q = \nu + cst/\log N$ . In a good solvent, the polymer is swollen with  $\nu = 0.588$ , whereas in a bad solvent it collapses with  $\nu = 1/3$ . It is clear that  $q$  varies like  $\nu$ .

Following the same authors (20), we define the quantity  $n_\alpha = \sum |\mathbf{u}_i \cdot \mathbf{e}_\alpha|$  for  $\alpha = x, y, z$ , in which  $i$  runs over all the bonds of the polymer,  $\mathbf{u}_i$  is the unit vector having the same direction as the bond  $i$  and  $\mathbf{e}_\alpha$  is the unit vector of the corresponding  $\alpha$ -axis. We then define  $n_{min} = \min_\alpha(n_\alpha)$ ,  $n_{max} = \max_\alpha(n_\alpha)$ , and the following:

$$p = 1 - \frac{n_{min}}{n_{max}}. \quad (27)$$

For an isotropic configuration,  $n_x = n_y = n_z$  resulting in  $p = 0$ . Conversely, for a configuration stretched in one direction, for example, along the  $x$  axis,  $n_x = 1$  and  $n_y = n_z = 0$ , resulting in  $p = 1$ . Thus  $p$  measures the directional order of the polymer.

We plotted the phase diagram obtained as a function of  $k_B T/\varepsilon$  and  $l_p$  (Fig. 9). There is a clear similarity with the case of a polymer on a lattice without explicit proteins. However, we observe that the coil-globule and globule-crystal transitions occur at a higher interaction energy  $\varepsilon$ . This might be a consequence of going from a lattice model to a continuous model. It might also be because of the fact that in the high-temperature regime, the concentration of spheres in solution is smaller than the close packing, therefore making it hardly comparable with an actual solvent. There is a specific persistence length  $l_p^c \approx 10$  such that

- for  $l_p < l_p^c$ , the polymer collapses through a second-order coil-globule transition, followed by a first-order globule-crystal transition when  $\varepsilon$  increases; and
- for  $l_p > l_p^c$ , the coil-globule transition no longer exists and the polymer collapses directly from a coil to a crystalline phase through a first-order phase transition.

## DISCUSSION

### DNA condensation in vitro

The condensation of DNA induced by DNA-binding proteins or ions has been thoroughly studied. It is well known that DNA collapses from disperse structures corresponding to swollen coil configurations into ordered, highly condensed states. This has been the focus of several in vitro experimental studies (24–28). One important conclusion from these studies is that during its collapse, DNA undergoes phase transitions through the following three phases: isotropic fluid, cholesteric, and crystalline (hexagonal), in agreement with our results. As stated above, within the Flory-Huggins theory, the phase transition induced by ions or DNA-binding proteins appears to be first order, except at the tricritical point and on the critical lines. Therefore, the transition from the swollen to the condensed state should be discontinuous and present hysteresis effects, which was indeed observed (27,29). Interestingly, the Flory-Huggins theory predicts another effect. At fixed temperature, there is a line of possible coexisting states. Given a certain amount of DNA, we are able to discuss the consequences of adding proteins to the system. The protein concentration would increase from zero until it reaches a value for which the system splits into two phases. If we keep adding proteins, the system will at some point exit the biphasic regime (Fig. 6, C and D). This phenomenon called reentrance has been observed in some experimental work (26).

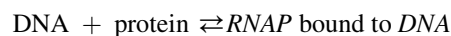
### DNA condensation in vivo

Although it is premature to draw any clear biological conclusion, it is tempting to discuss at least qualitatively the effect of DNA condensation on biological functions. In eukaryotes, nucleosomal organization provides an

effective protection against detrimental factors. This organization is absent in prokaryotes, which have a significantly lower ratio of DNA-binding proteins (30). However, in harsh environmental conditions (radiations, temperature, oxidating agents, and radicals), several bacteria resort to DNA condensation mechanisms to protect their genome. Maybe the most spectacular case is the appearance of macroscopic DNA aggregates with crystal-like order in starved *E. coli* cells. In stressful conditions, the alternative  $\sigma^S$  factor is expressed, in response to low temperature, cell surface stress, or oxidative shock. This in turn induces the expression of the DNA-binding protein Dps (31,32). In starved cells, Dps is the most abundant DNA-binding protein, with ~20,000 Dps protein per cell. Consequently, DNA is condensed into crystal-like aggregates, which make it less accessible to damaging factors. This process is reversible and wild-type *E. coli* cells starved for three days remain unaffected by a high dose of oxidating agents whereas mutants lacking Dps lose viability (31). Interestingly, Dps binds nonspecifically to DNA. In regard to what has been discussed in this article, we may infer that when Dps concentration increases, a dense phase appears. But at a scale of Dps size ( $\sim 10$  nm), the apparent rigidity of DNA is large ( $\sim 50$  nm). Therefore, as Fig. 9 shows, this might be a case where the coil-globule transition is precluded by the freezing transition. Other examples of DNA compaction by nonspecific proteins seem to exist (33,34).

### Local concentration effects and transcription

Increasing evidence suggests that transcription proceeds from nucleation points called transcription factories, which are formed from the interaction of DNA with general and dedicated transcription factors. Although the nonspecific hypothesis is not guaranteed, it is true that RNAP can bind widely onto DNA thanks to its  $\sigma$ -unit. The Flory-Huggins results from this article suggest that a biphasic regime can exist, with a dense phase spanning a volume of size  $(1 - \phi)V$  and with local concentrations of DNA and RNAP increased by a factor of 4-to-8 with respect to the mean-field ones (Fig. 6 D). This would result in shifting the equilibrium of complexation reactions such as the following:



toward the formation of complexes and may favor transcription initiation. This is consistent with some experimental work showing that RNAP clusters are formed during preinitiation and initiation of transcription (35). The same authors also proposed that crowding of enzymes, i.e., higher local concentrations, may aid in rate-limiting steps of gene regulation. From a dynamical standpoint, the confinement of unbound RNAP in a restricted volume of size  $(1 - \phi)V$  can reduce the search time for a promoter. To this extent, it is

worthwhile to point out a recent study claiming that the promoter search mechanism is indeed dominated by 3D diffusion of RNAP over the one-dimensional diffusion along DNA (36).

### Structure of the dense phase

Earlier studies have demonstrated that the frozen phase can present various metastable states (21). In the  $N \rightarrow \infty$  limit ( $N$  is the length of one chain), the transition timescale from one to another could be very large, and the system might well never equilibrate within biological timescales. Finally, the parallel drawn between the HP theory and the Flory-Huggins theory does not pretend to mathematical rigor. One essential difference is that in our case the attractive interaction between monomers is mediated by spheres. A way to compute more precisely the structure of the dense phase would be to go beyond the homogeneous saddle-point approximation, for instance, by using the so-called self-consistent field theory method (37,38), which is a very complex method in the case of semiflexible polymers.

### CONCLUSIONS

We presented in this study two complementary frameworks to describe the phase diagram of polymeric fluids induced by colloids, and we applied it to a DNA chain interacting with DNA-binding proteins. Starting from a Flory-Huggins free energy, we first computed the mean-field phase diagram and found that at low temperature (i.e., high DNA-protein affinity) a biphasic regime exists, consisting of the coexistence of a dilute phase and a concentrated phase. The dilute phase may correspond to swollen configurations of the DNA whereas the concentrated phase is a model for condensed states of DNA. This theory may also apply to DNA condensation by multivalent ions or proteins in general. Second, we addressed the characterization of the dense phase structure and showed that the chain bending rigidity can have dramatic effects. Without bending rigidity, the dense phase has no directional order and is a molten globule. However, when the chain bending rigidity is large enough, there is a freezing transition from the globular to crystalline phase. Eventually for very rigid chains, the coil-globule transition is precluded by the freezing transition and the phase transition predicted in the Flory-Huggins framework does not occur.

In the cell, the existence of a dense phase could be a good approximation for the transcription factories observed experimentally. It is conjectured that this may increase the rate of success in transcription initiation by means of protein crowding and by enhancing the promoter search mechanism. Note that at a scale that is coarse-grained to several thousand base-pairs (gene scale), the chromosome is flexible and the dense phase has the structure of a molten globule. Conversely, at a scale of a few base-pairs, the

apparent rigidity of DNA is much higher. Thus, the Dps protein, which binds nonspecifically to DNA, can induce the collapse of the *E. coli* chromosome into crystal-like aggregates; the dense phase is then frozen. This is not an efficient state for a searching mechanism. But on the contrary, it is very adequate to protect DNA.

The two frameworks are quite general and can be used to describe biological phenomena where DNA compaction occurs under the cooperative effect of binding proteins. In the future, we plan to apply it to other biological cases when more quantitative experiments become available.

## AUTHOR CONTRIBUTIONS

F.K. and H.O. designed the research. G.L.T. and H.O. performed the research; and G.L.T. wrote the software and analyzed the data. All authors contributed to the writing of the article.

## ACKNOWLEDGMENTS

The authors thank the MEGA team members at iSSB for excellent discussions. This work was supported by the IDEX Paris-Saclay grant, CNRS Genopole, and the ANR project Synpathic.

## REFERENCES

1. Montero Llopis, P., A. F. Jackson, ..., C. Jacobs-Wagner. 2010. Spatial organization of the flow of genetic information in bacteria. *Nature*. 466:77–81.
2. Schoenfelder, S., T. Sexton, ..., P. Fraser. 2010. Preferential associations between co-regulated genes reveal a transcriptional interactome in erythroid cells. *Nat. Genet.* 42:53–61.
3. Xu, M., and P. R. Cook. 2008. Similar active genes cluster in specialized transcription factories. *J. Cell Biol.* 181:615–623.
4. Caudron-Herger, M., P. R. Cook, ..., A. Papanonis. 2015. Dissecting the nascent human transcriptome by analysing the RNA content of transcription factories. *Nucleic Acids Res.* 43:e95.
5. Junier, I., O. Martin, and F. Képès. 2010. Spatial and topological organization of DNA chains induced by gene co-localization. *PLOS Comput. Biol.* 6:e1000678.
6. Spilianakis, C. G., M. D. Lalioti, ..., R. A. Flavell. 2005. Interchromosomal associations between alternatively expressed loci. *Nature*. 435:637–645.
7. Sheinman, M., O. Bénichou, ..., R. Voituriez. 2012. Classes of fast and specific search mechanisms for proteins on DNA. *Rep. Prog. Phys.* 75:026601.
8. Berg, O. G., and P. H. von Hippel. 1981. Diffusion-driven mechanisms of protein translocation on nucleic acids 2. *American Chemical Society*. 20:6948–6960.
9. de Gennes, P. 1979. *Scaling Concepts in Polymer Physics*. Cornell University Press, Cornell, NY.
10. Sear, R. P. 2002. Flory-Huggins theory for athermal mixtures of hard spheres and larger flexible polymers. *Phys. Rev. E Stat. Nonlin. Soft Matter Phys.* 66:051401.
11. Elowitz, M. B., M. G. Surette, ..., S. Leibler. 1999. Protein mobility in the cytoplasm of *Escherichia coli*. *J. Bacteriol.* 181:197–203.
12. Kahramanoglou, C., A. S. N. Seshasayee, ..., N. M. Luscombe. 2011. Direct and indirect effects of H-NS and Fis on global gene expression control in *Escherichia coli*. *Nucleic Acids Res.* 39:2073–2091.
13. Nowak-Lovato, K., L. B. Alexandrov, ..., B. S. Alexandrov. 2013. Binding of nucleoid-associated protein fis to DNA is regulated by DNA breathing dynamics. *PLOS Comput. Biol.* 9:e1002881.
14. Ishihama, A., A. Kori, ..., N. Fujita. 2014. Intracellular concentrations of 65 species of transcription factors with known regulatory functions in *Escherichia coli*. *J. Bacteriol.* 196:2718–2727.
15. Johnson, J., C. A. Brackley, ..., D. Marenduzzo. 2015. A simple model for DNA bridging proteins and bacterial or human genomes: bridging-induced attraction and genome compaction. *J. Phys. Condens. Matter*. 27:064119.
16. Brackley, C. A., S. Taylor, ..., D. Marenduzzo. 2013. Nonspecific bridging-induced attraction drives clustering of DNA-binding proteins and genome organization. *Proc. Natl. Acad. Sci. USA*. 110:E3605–E3611.
17. Doniach, S., T. Garel, and H. Orland. 1996. Phase diagram of a semiflexible polymer chain in a theta solvent: application to protein folding. *J. Chem. Phys.* 105:1601–1608.
18. Bascle, J., T. Garel, and H. Orland. 1992. Mean-field theory of polymer melting. *J. Phys. Math. Gen.* 25:1323.
19. Bascle, J., T. Garel, and H. Orland. 1993. Formation and stability of secondary structures in globular proteins. *J. Phys. II France*. 3:245–253.
20. Bastolla, U., and P. Grassberger. 1997. Phase transitions of single semiflexible polymer chains. *J. Stat. Phys.* 89:1061–1078.
21. Doye, J. P. K., R. P. Sear, and D. Frenkel. 1998. The effect of chain stiffness on the phase behaviour of isolated homopolymers. *J. Chem. Phys.* 108:2134–2142.
22. Orland, H., C. Itzykson, and C. de Dominicis. 1985. An evaluation of the number of Hamiltonian paths. *J. Physique Lett.* 46:353–357.
23. Montesi, A., M. Pasquali, and F. C. MacKintosh. 2004. Collapse of a semiflexible polymer in poor solvent. *Phys. Rev. E Stat. Nonlin. Soft Matter Phys.* 69:021916.
24. Bloomfield, V. A. 1996. DNA condensation. *Curr. Opin. Struct. Biol.* 6:334–341.
25. Livolant, F., and A. Leforestier. 1996. Condensed phases of DNA: structures and phase transitions. *Prog. Polym. Sci.* 21:1115–1164.
26. Vasilevskaya, V. V., A. R. Khokhlov, ..., K. Yoshikawa. 1995. Collapse of single DNA molecule in poly(ethylene glycol) solutions. *J. Chem. Phys.* 102:6595–6602.
27. Yoshikawa, K., and Y. Matsuzawa. 1995. Discrete phase transition of giant DNA dynamics of globule formation from a single molecular chain. *Physica D*. 84:220–227.
28. Durand, D., J. Doucet, and F. Livolant. 1992. A study of the structure of highly concentrated phases of DNA by X-ray diffraction. *J. Phys. II France*. 2:1769–1783.
29. Widom, J., and R. L. Baldwin. 1980. Cation-induced toroidal condensation of DNA studied with  $\text{Co}^{3+}(\text{NH}_3)_6$ . *J. Mol. Biol.* 144:431–453.
30. Kellenberger, E., and B. Arnold-Schulz-Gahmen. 1992. Chromatins of low-protein content: special features of their compaction and condensation. *FEMS Microbiol. Lett.* 100:361–370.
31. Almiron, M., A. J. Link, ..., R. Kolter. 1992. A novel DNA-binding protein with regulatory and protective roles in starved *Escherichia coli*. *Genes Dev.* 6 (12B):2646–2654.
32. Altuvia, S., M. Almiron, ..., G. Storz. 1994. The dps promoter is activated by OxyR during growth and by IHF and sigma S in stationary phase. *Mol. Microbiol.* 13:265–272.
33. Frenkiel-Krispin, D., and A. Minsky. 2006. Nucleoid organization and the maintenance of DNA integrity in *E. coli*, *B. subtilis* and *D. radiodurans*. *J. Struct. Biol.* 156:311–319.
34. Newton, G. L., J. A. Aguilera, ..., R. C. Fahey. 1996. Polyamine-induced compaction and aggregation of DNA—a major factor in radio-protection of chromatin under physiological conditions. *Radiat. Res.* 145:776–780.

35. Cisse, I. I., I. Izeddin, ..., X. Darzacq. 2013. Real-time dynamics of RNA polymerase II clustering in live human cells. *Science*. 341:664–667.
36. Wang, F., S. Redding, ..., E. C. Greene. 2013. The promoter-search mechanism of Escherichia coli RNA polymerase is dominated by three-dimensional diffusion. *Nat. Struct. Mol. Biol.* 20:174–181.
37. Edwards, S. F., and M. Doi. 1988. *The Theory of Polymer Dynamics. International Series of Monographs on Physics*. Oxford University Press, Oxford, UK.
38. Fredrickson, G. 2005. *The Equilibrium Theory of Inhomogeneous Polymers. International Series of Monographs on Physics*. Oxford University Press, Oxford, UK.



# Glossary

**base pair** Two nucleotides in a DNA (or RNA) molecule that are paired by hydrogen bonds.

**binding energy** Energy determining the strength of the chemical linkage (or affinity) between two constituents. For instance the binding energy of a protein with DNA.

**central dogma** The fundamental principle that genetic information flows from DNA to RNA to protein.

**ChIP-sequencing** ChIP-seq assays combine chromatin immunoprecipitation (ChIP) with massively parallel DNA sequencing to identify the binding sites of DNA-associated proteins. After post-processing experimental data, it gives access to the density of binding of a protein as a function of the genomic coordinate.

**chromosome (or chromatin)** Term regrouping the DNA molecule with the structuring proteins that are bound to it.

**chromosome conformation capture experiment** Set of experimental techniques that have been developed in order to identify interactions between genomic location (loci) *in vivo*. Namely, these techniques count the number of contacts between different loci on the genome, resulting from the particular folding of the chromosome.

**chromosome folding** The chromosome is a long object, and as such can adopt many three-dimensional configurations. One such configuration defines its folding, or architecture.

**co-regulated genes** Genes whose expressions are regulated by the same regulators.

**cytosol** Intra-cellular space, excluding the organelles.

**divalent protein** Protein with two functional domains enabling the binding to two DNA sites.

**epigenetics** Ensemble of biological processes resulting in genetic effects which are not encoded in the DNA sequence. Such effects may result from external factors that affect how cells express genes. For example, DNA methylation can alter how a gene is expressed, yet it does not involve a change in the nucleotide sequence.

**Fluorescence *in situ* hybridization** Technique that uses fluorescent probes that bind specific DNA (or RNA) sequences by base pair complementarity. Fluorescence microscopy can then be used to detect and localize these specific sequences. In particular, regions of the chromosome can be localized in the cellular compartment, which helps in defining the spatial-temporal patterns of gene expression.

**genome** It is the unique sequence of nucleotides which embeds the genetic information of one individual.

**Hi-C** Experimental technique combining chromosome conformation capture and high-throughput DNA sequencing in order to obtain a high-resolution map of the contacts between chromosomal locations.

**horizontal gene transfer** Process through which DNA is passed from one organism to another. This contrasts with vertical gene transfer which refers to the inheritance of genes from parent to progeny.

**hydrogen bond** A weak chemical bond between an electronegative atom such as nitrogen or oxygen and a hydrogen atom bound to another electronegative atom.

**monomer** Fundamental unit of a polymer.

**nucleoid** In prokaryotes which do not have a nucleus, the chromosome is confined to an area near the center of the cell called the nucleoid.

**nucleus** In eukaryotes, the nucleus contains the chromosomes, and is separated of the rest of the cell by a membrane.

**polymer** Large molecule made of the repetitive assembly of monomers held by chemical bonds. The number of monomers in the polymer is called the polymerization index.

**polymerase** General term for a protein that can assemble monomers together to form a polymer. It catalyzes the process of polymerisation. For instance RNA polymerase is the enzyme responsible for transcribing coding sequences of genes into RNA.

**polymerase chain reaction** Technique used to amplify a target DNA sequence. It relies on denaturation-hybridization-elongation cycles and the usage of a polymerase resistant to high temperatures. This technique enables the production of millions of copies of an initial DNA sequence in just a few hours.

**promoter** DNA region where RNA polymerase binds in order to initiate transcription.

**random phase approximation** In the context of polymer field theories, it is a stability analysis of the saddle-point solution for the polymer density. Namely, the Hamiltonian is expanded to second order around the saddle-point solution in order to obtain the quadratic fluctuations. A Fourier mode analysis can reveal if modulations in the polymer density can trigger instabilities, which are associated to a microphase separation. It is also called the Gaussian fluctuations analysis.

**restriction enzyme** Enzyme that can cleave the DNA molecule at specific sites (restriction sites) corresponding to a specific short sequence of nucleotides.

**super-resolution microscopy** Fluorescence microscopy imaging methods that allow to obtain a resolution beyond the diffraction limit. They rely on the stochastic activation of each fluorophore in the sample from a non-emissive state (or off-state) to an emissive state (or on-state). This ensures that for each image, only a small fraction of the fluorophores (those in the on-state) is emitting photons. This results in very few overlaps between the fluorophore sources and leads to an increased resolution. Transitions from the on-state to the off-state occur through reversible switching in STORM whereas in PALM the phenomenon of photobleaching is exploited.

**transcription factor** Term loosely applied to any protein that can bind to DNA in order to alter (or regulate) the expression of a gene.

**transcription level** The transcription level of one gene can be measured in at least two ways. A direct measure of the transcription level consists in measuring the number of RNA transcripts of a given gene in the cell. This is usually achieved by extracting all messenger RNA from a cell and sequencing them in order to count the transcripts of the gene of interest. An indirect measure of the transcription level is to insert downstream of the gene of interest a reporter gene which encodes a fluorescent protein (such as GFP). The intensity of the fluorescence can be related to the transcription level of the gene of interest.

**transcription factor binding site** DNA sequence to which a transcription factor binds to in order to regulate the transcription of a gene.

**worm-like chain** Model used to describe a polymer with bending rigidity. A key parameter of the model is the persistence length, that characterizes the contour distance above which the polymer loses the memory of its orientation. Also known as the Kratky-Porod model.

**xeno-silencing** Repression of the transcription of genes in foreign DNA sequences acquired by horizontal transfer.



# Acronyms

**3C** chromosome conformation capture experiment.

**AFM** Atomic-force microscopy.

**BD** Brownian dynamics.

**bp** base pair.

**CCC** chromosome conformation capture experiment.

**chIP-seq** ChIP-sequencing experiment.

**EM** electron microscopy.

**FENE** finitely-extensible non-linear elastic potential.

**FISH** Fluorescence *in situ* hybridization.

**GEM** Gaussian effective model.

**Hi-C** CCC with high-throughput DNA sequencing.

**i.i.d.** independently and identically distributed (random variables).

**LAMMPS** Large-scale Atomic/Molecular Massively Parallel Simulator.

**MD** molecular dynamics.

**NAP** nucleoid-associated protein.

**p.d.f.** probability distribution function.

**PALM** photo-activated localization microscopy.

**PCR** polymerase chain reaction.

**PWM** position weight matrix.

**RNAP** RNA polymerase.

**RPA** random-phase approximation.

**SAW** self-avoiding walk.

**STORM** stochastic optical reconstruction microscopy.

**TF** transcription factor.

**TFBS** transcription factor binding site.

**WLC** worm-like chain polymer.

# Bibliography

- [1] G. Le Treut, F. Képès, and H. Orland. 2016. Phase behavior of DNA in the presence of DNA-binding proteins. *Biophysical Journal*, 110(1):51–62.
- [2] J. D. Watson, F. H. Crick, et al. 1953. Molecular structure of nucleic acids. *Nature*, 171(4356):737–738.
- [3] F. Jacob and J. Monod. 1961. Genetic regulatory mechanisms in the synthesis of proteins. *Journal of molecular biology*, 3(3):318–356.
- [4] B. Alberts, D. Bray, K. Hopkin, A. Johnson, J. Lewis, M. Raff, K. Roberts, and P. Walter. 2013. *Essential cell biology*. Garland Science.
- [5] B. Muller-Hill. 1998. Some repressors of bacterial transcription. *Open Opinion in Microbiology*, 1:145–151.
- [6] B. Muller-Hill. 1998. The function of auxiliary operators. *Molecular Microbiology*, 29:13–18.
- [7] B. Revet, B. von Wilcken-Bergmann, H. Bessert, A. Barker, and B. Muller-Hill. 1999. Four dimers of  $\lambda$  repressor bound to two suitably spaced pairs of  $\lambda$  operators form octamers and DNA loops over large distances. *Current Biology*, 9(3):151 – 154.
- [8] M. B. Elowitz, M. G. Surette, P.-E. Wolf, J. B. Stock, and S. Leibler. 1999. Protein mobility in the cytoplasm of *Escherichia coli*. *Journal of Bacteriology*, 181(1):197–203.
- [9] J. M. Vilar and L. Saiz. 2005. DNA looping in gene regulation: from the assembly of macromolecular complexes to the control of transcriptional noise. *Current opinion in genetics & development*, 15(2):136–144.
- [10] V. F. Holmes and N. R. Cozzarelli. 2000. Closing the ring: links between SMC proteins and chromosome partitioning, condensation, and supercoiling. *Proceedings of the National Academy of Sciences*, 97(4):1322–1324.
- [11] B. Alberts, D. Bray, J. Lewis, M. Raff, K. Roberts, J. D. Watson, and A. Grimstone. 1995. Molecular biology of the cell. *Trends in Biochemical Sciences*, 20(5).
- [12] Wikipedia. Chromatin. <https://en.wikipedia.org/wiki/Chromatin>.
- [13] J. Langowski. 2006. Polymer chain models of DNA and chromatin. *The European Physical Journal E*, 19(3):241–249.
- [14] B. Eslami-Mossallam, H. Schiessel, and J. van Noort. 2016. Nucleosome dynamics: Sequence matters. *Advances in Colloid and Interface Science*, 232:101 – 113. Proceedings from the International Workshop on Polyelectrolytes in Chemistry, Biology and Technology.
- [15] B. Mergell, R. Everaers, and H. Schiessel. 2004. Nucleosome interactions in chromatin: Fiber stiffening and hairpin formation. *Phys. Rev. E*, 70:011915.
- [16] D. E. Olins and A. L. Olins. 2003. Chromatin history: our view from the bridge. *Nature reviews Molecular cell biology*, 4(10):809–814.
- [17] E. B. De La Tour and U. Laemmli. 1988. The metaphase scaffold is helically folded: sister chromatids have predominantly opposite helical handedness. *Cell*, 55(6):937–944.

- [18] J. Rattner and C. Lin. 1985. Radial loops and helical coils coexist in metaphase chromosomes. *Cell*, 42(1):291–296.
- [19] B.-K. Cho, E. M. Knight, C. L. Barrett, and B. Ø. Palsson. 2008. Genome-wide analysis of FIS binding in *Escherichia coli* indicates a causative role for A-AT-tracts. *Genome Research*, 18(6):900–910.
- [20] R. Brunetti, G. Prosseda, E. Beghetto, B. Colonna, and G. Micheli. 2001. The looped domain organization of the nucleoid in histone-like protein defective *Escherichia coli* strains. *Biochimie*, 83(9):873 – 882.
- [21] X. Wang, P. M. Llopis, and D. Z. Rudner. 2013. Organization and segregation of bacterial chromosomes. *Nature Genetics*, 14:191.
- [22] P. R. Cook. 2010. A model for all genomes: the role of transcription factories. *J Mol Biol*, 395(1):1–10.
- [23] P. R. Cook. 2002. Predicting three-dimensional genome structure from transcriptional activity. *Nature Genetics*, 32:347–352.
- [24] F. Képès and C. Vaillant. 2004. Transcription-based solenoidal model of chromosomes. *Complexus*, 1(4):171–180.
- [25] I. Junier, O. Martin, and F. Képès. 2010. Spatial and topological organization of DNA chains induced by gene co-localization. *PLoS Comput Biol*, 6(2):1000678.
- [26] D. Frenkiel-Krispin and A. Minsky. 2006. Nucleoid organization and the maintenance of DNA integrity in *E. coli*, *B. subtilis* and *D. radiodurans*. *Journal of Structural Biology*, 156(2):311–319.
- [27] F. Livolant. 1991. Ordered phases of DNA *in vivo* and *in vitro*. *Physica A: Statistical Mechanics and its Applications*, 176(1):117 – 137.
- [28] S. Schoenfelder, T. Sexton, L. Chakalova, N. F. Cope, A. Horton, S. Andrews, S. Kurukuti, J. A. Mitchell, D. Umlauf, and D. S. Dimitrova. 2010. Preferential associations between co-regulated genes reveal a transcriptional interactome in erythroid cells. *Nature Genetics*, 42(1):53–61.
- [29] B. Youngren, H. J. Nielsen, S. Jun, and S. Austin. 2014. The multifork *Escherichia coli* chromosome is a self-duplicating and self-segregating thermodynamic ring polymer. *Genes & development*, 28(1):71–84.
- [30] T. Bailey, P. Krajewski, I. Ladunga, C. Lefebvre, Q. Li, T. Liu, P. Madrigal, C. Taslim, and J. Zhang. 2013. Practical guidelines for the comprehensive analysis of ChIP-seq data. *PLoS Comput Biol*, 9(11):1–8.
- [31] K. S. Myers, H. Yan, I. M. Ong, D. Chung, K. Liang, F. Tran, S. Keles, R. Landick, and P. J. Kiley. 2013. Genome-scale analysis of *Escherichia coli* FNR reveals complex features of transcription factor binding. *PLoS Genet*, 9(6):1–24.
- [32] C. Kahramanoglou, A. S. N. Seshasayee, A. I. Prieto, D. Ibberson, S. Schmidt, J. Zimmermann, V. Benes, G. M. Fraser, and N. M. Luscombe. 2011. Direct and indirect effects of H-NS and FIS on global gene expression control in *Escherichia coli*. *Nucleic Acids Research*, 39(6):2073–2091.
- [33] M. Imakaev, G. Fudenberg, R. P. McCord, N. Naumova, A. Goloborodko, B. R. Lajoie, J. Dekker, and L. A. Mirny. 2012. Iterative correction of Hi-C data reveals hallmarks of chromosome organization. *Nat Meth*, 9:999–1003.
- [34] M. Marbouty, A. L. Gall, D. I. Cattoni, A. Cournac, A. Koh, J.-B. Fiche, J. Mozziconacci, H. Murray, R. Koszul, and M. Nollmann. 2015. Condensin- and replication-mediated bacterial chromosome folding and origin condensation revealed by Hi-C and super-resolution imaging. *Molecular Cell*, 59(4):588 – 602.
- [35] E. Lieberman-Aiden. 2009. Comprehensive mapping of long-range interactions reveals folding principles of the human genome. *Science*, 326(289).
- [36] M. Barbieri, M. Chotalia, J. Fraser, L.-M. Lavitas, J. Dostie, A. Pombo, and M. Nicodemi. 2012. Complexity of chromatin folding is captured by the strings and binders switch model. *Proceedings of the National Academy of Sciences*, 109(40):16173–16178.

- [37] J. M. G. Vilar and S. Leibler. 2003. DNA looping and physical constraints on transcription regulation. *Journal Of Molecular Biology (JMB)*, 331:981–989.
- [38] K. J. Meaburn and T. Misteli. 2007. Chromosome territories. *Nature*, 445(25).
- [39] T. Cremer and C. Cremer. 2001. Chromosome territories, nuclear architecture and gene regulation in mammalian cells. *Nature reviews genetics*, 2(4):292–301.
- [40] A. Grosberg, Y. Rabin, S. Havlin, and A. Neer. 1993. Crumpled globule model of the three-dimensional structure of DNA. *EPL (Europhysics Letters)*, 23(5):373.
- [41] L. A. Mirny. The fractal globule as a model of chromatin architecture in the cell. In *Chromosome research : an international journal on the molecular, supramolecular and evolutionary aspects of chromosome biology*, 2011.
- [42] I. Bronstein, Y. Israel, E. Kepten, S. Mai, Y. Shav-Tal, E. Barkai, and Y. Garini. 2009. Transient anomalous diffusion of telomeres in the nucleus of mammalian cells. *Phys. Rev. Lett.*, 103:018102.
- [43] I. M. Tolić-Nørrelykke, E.-L. Munteanu, G. Thon, L. Oddershede, and K. Berg-Sørensen. 2004. Anomalous diffusion in living yeast cells. *Phys. Rev. Lett.*, 93:078102.
- [44] A. Rosa and R. Everaers. 2008. Structure and dynamics of interphase chromosomes. *PLoS Comput Biol*, 4(8):e1000153.
- [45] M. D. Stefano, A. Rosa, V. Belcastro, D. di Bernardo, and C. Micheletti. 2013. Colocalization of co-regulated genes: a steered molecular study of human chromosome 19. *PLOS*, 9(3).
- [46] C. A. Brackley, S. Taylor, A. Papantonis, P. R. Cook, and D. Marenduzzo. 2013. Non-specific bridging-induced attraction drives clustering of DNA-binding proteins and genome organization. *PNAS*, 110(38):3605–11.
- [47] N. B. Becker and R. Everaers. 2007. From rigid base pairs to semiflexible polymers: Coarse-graining DNA. *Phys. Rev. E*, 76:021923.
- [48] D. Jost, A. Zubair, and R. Everaers. 2011. Bubble statistics and positioning in superhelically stressed DNA. *Phys. Rev. E*, 84:031912.
- [49] T. Pichugina, T. Sugawara, A. Kaykov, W. Schierding, K. Masuda, J. Uewaki, R. Grand, J. Allison, R. Martienssen, P. Nurse, et al. 2016. A diffusion model for the coordination of DNA replication in *Schizosaccharomyces pombe*. *Scientific reports*, 6.
- [50] C. A. Brackley, J. M. Brown, D. Waithe, C. Babbs, J. Davies, J. Hughes, V. J. Buckle, and D. Marenduzzo. 2016. Predicting the three-dimensional folding of CIS-regulatory regions in mammalian genomes using bioinformatic data and polymer models. *ArXiv e-prints*.
- [51] C. Bouchiat and M. Mézard. 2000. Elastic rod model of a super-coiled DNA molecule. *The European Physical Journal E*, 2:377–402.
- [52] M. Peyrard and A. R. Bishop. 1989. Statistical mechanics of a nonlinear model for DNA denaturation. *Phys. Rev. Lett.*, 62:2755–2758.
- [53] P. de Gennes. 1979. *Scaling Concepts in Polymer Physics*. Cornell University Press.
- [54] S. F. Edwards and M. Doi. 1988. *The Theory of Polymer Dynamics*. International Series of Monographs on Physics. Oxford University Press.
- [55] G. Fredrickson. 2005. *The Equilibrium Theory of Inhomogeneous Polymers*. International Series of Monographs on Physics. Oxford University Press.
- [56] K. Kremer and G. S. Grest. 1990. Dynamics of entangled linear polymer melts: A molecular dynamics simulation. *The Journal of Chemical Physics*, 92(8):5057–5086.
- [57] A. A. Zinchenko, K. Yoshikawa, and D. Baigl. 2005. Compaction of single-chain DNA by histone-inspired nanoparticles. *Phys. Rev. Lett.*, 95:228101.

- [58] K.-K. Kunze and R. R. Netz. 2000. Salt-induced DNA-histone complexation. *Phys. Rev. Lett.*, 85:4389–4392.
- [59] O. Kratky and G. Porod. 1949. Röntgenuntersuchung gelöster fadenmoleküle. *Recueil des Travaux Chimiques des Pays-Bas*, 68(12):1106–1122.
- [60] B.-Y. Ha and D. Thirumalai. 1995. A mean-field model for semiflexible chains. *The Journal of chemical physics*, 103(21):9408–9412.
- [61] H. Diamant and D. Andelman. 2000. Binding of molecules to DNA and other semiflexible polymers. *Phys. Rev. E*, 61:6740–6749.
- [62] J. K. Bhattacharjee, D. Thirumalai, and J. D. Bryngelson. 1997. Distribution function of the end-to-end distance of semiflexible polymers. *eprint arXiv:cond-mat/9709345*.
- [63] S. Plimpton. 1995. Fast parallel algorithms for short-range molecular dynamics. *Journal of computational physics*, 117(1):1–19.
- [64] W. H. Press. 2007. *Numerical recipes 3rd edition: The art of scientific computing*. Cambridge university press.
- [65] Wikipedia. DNA. [https://en.wikibooks.org/wiki/Structural\\_Biochemistry/Nucleic\\_Acid/DNA](https://en.wikibooks.org/wiki/Structural_Biochemistry/Nucleic_Acid/DNA).
- [66] D. G. Priest, L. Cui, S. Kumar, D. D. Dunlap, I. B. Dodd, and K. E. Shearwin. 2014. Quantitation of the DNA tethering effect in long-range DNA looping in vivo and in vitro using the *lac* and  $\lambda$  repressors. *Proceedings of the National Academy of Sciences*, 111(1):349–354.
- [67] B. Tolhuis, R.-J. Palstra, E. Splinter, F. Grosveld, and W. de Laat. 2002. Looping and interaction between hypersensitive sites in the active  $\beta$ -globin locus. *Molecular cell*, 10(6):1453–1465.
- [68] R. Schleif. 1992. Dna looping. *Annual review of biochemistry*, 61(1):199–223.
- [69] K. Matthews. 1992. Dna looping. *Microbiological reviews*, 56(1):123–136.
- [70] M. Xu and P. R. Cook. 2008. Similar active genes cluster in specialized transcription factories. *The Journal of Cell Biology*, 181(4):615–623.
- [71] P. M. Llopis, O. Jackson, J. Surovtsev, T. Emonet, and C. Jacobs-Wagner. 2010. Spatial organization of the flow of genetic information in bacteria. *Nature*, 466(7302):77–81.
- [72] C. G. Spilianakis, M. D. Lalioti, T. Town, G. R. Lee, and R. A. Flavell. 2005. Interchromosomal associations between alternatively expressed loci. *Nature*, 435(7042):637–645.
- [73] M. Caudron-Herger, P. R. Cook, K. Rippe, and A. Papantonis. 2015. Dissecting the nascent human transcriptome by analysing the RNA content of transcription factories. *Nucleic Acids Research*.
- [74] I. I. Cisse, I. Izeddin, S. Z. Causse, L. Boudarene, A. Senecal, L. Muresan, C. Dugast-Darzacq, B. Hajj, M. Dahan, and X. Darzacq. 2013. Real-time dynamics of RNA polymerase II clustering in live human cells. *Science*, 341(6146):664–667.
- [75] D. J. Jin, C. Cagliero, and Y. N. Zhou. 2014. Spatial organization of transcription machinery and its segregation from the replisome in fast-growing bacterial cells. *Nucleic Acids Research*.
- [76] D. J. Jin and J. E. Cabrera. 2006. Coupling the distribution of RNA polymerase to global gene regulation and the dynamic structure of the bacterial nucleoid in *Escherichia coli*. *Journal of Structural Biology*, 156(2):284–291.
- [77] J. Des Cloizeaux and G. Jannink. 1990. *Polymers in solution: Their modelling and structure*, volume 25. Oxford University Press.
- [78] Sumedha and M. Weigt. 2008. A thermodynamic model for the agglomeration of DNA-looping proteins. *Journal of Statistical Mechanics: Theory and Experiment*, 2008(11):P11005.
- [79] F. Wang, S. Redding, I. J. Finkelstein, J. Gorman, D. R. Reichman, and E. C. Greene. 2013. The promoter-search mechanism of *Escherichia coli* RNA polymerase is dominated by three-dimensional diffusion. *Nature Structural and Molecular Biology*, 20(2):174.

- [80] K. Yoshikawa and Y. Matsuzawa. 1995. Discrete phase transition of giant DNA dynamics of globule formation from a single molecular chain. *Physica D: Nonlinear Phenomena*, 84:220–227.
- [81] J. Widom and R. L. Baldwin. 1980. Cation-induced toroidal condensation of DNA: studies with  $\text{Co}^{3+}$   $(\text{NH}_3)_6$ . *Journal of Molecular Biology*, 144(4):431–453.
- [82] V. V. Vasilevskaya, A. R. Khokhlov, Y. Matsuzawa, and K. Yoshikawa. 1995. Collapse of single DNA molecule in polyethylene glycol solutions. *The Journal of Chemical Physics*, 102(16):6595–6602.
- [83] L. M. Rapkin, D. R. Anchel, R. Li, and D. P. Bazett-Jones. 2012. A view of the chromatin landscape. *Micron*, 43:150 – 158.
- [84] D. Marenduzzo, J. Johnson, and B. Brackley. 2015. A simple model for DNA bridging proteins and bacterial or human genomes: bridging-induced attraction and genome compaction. *Journal of Physics: Condensed Matter*, 27(6):064119.
- [85] S. Doniach, T. Garel, and H. Orland. 1996. Phase diagram of a semiflexible polymer chain in a  $\theta$  solvent: application to protein folding. *The Journal of Chemical Physics*, 105(4):1601–1608.
- [86] J. des Cloizeaux. 1973. Form factor of an infinite Kratky-Porod chain. *Macromolecules*, 6(3):403–407.
- [87] A. L. Kholodenko. 1993. Analytical calculation of the scattering function for polymers of arbitrary flexibility using the dirac propagator. *Macromolecules*, 26(16):4179–4183.
- [88] J. S. Pedersen and P. Schurtenberger. 1996. Scattering functions of semiflexible polymers with and without excluded volume effects. *Macromolecules*, 29(23):7602–7612.
- [89] A. J. Spakowitz and Z.-G. Wang. 2004. Exact results for a semiflexible polymer chain in an aligning field. *Macromolecules*, 37(15):5814–5823.
- [90] X. Zhang, Y. Jiang, B. Miao, Y. Chen, D. Yan, and J. Z. Y. Chen. 2014. The structure factor of a wormlike chain and the random-phase-approximation solution for the spinodal line of a diblock copolymer melt. *Soft Matter*, 10:5405–5416.
- [91] J. Bascle, T. Garel, and H. Orland. 1992. Mean-field theory of polymer melting. *Journal of Physics A: Mathematical and General*, 25(23):1323.
- [92] J. Bascle, T. Garel, and H. Orland. 1993. Formation and stability of secondary structures in globular proteins. *J. Phys. II France*, 3(2):245–253.
- [93] U. Bastolla and P. Grassberger. 1997. Phase transitions of single semi-stiff polymer chains. *Journal of Statistical Physics*, 89:1061–1078.
- [94] J. P. K. Doye, R. P. Sear, and D. Frenkel. 1998. The effect of chain stiffness on the phase behaviour of isolated homopolymers. *The Journal of Chemical Physics*, 108(5):2134–2142.
- [95] A. Montesi, M. Pasquali, and F. C. MacKintosh. 2004. Collapse of a semiflexible polymer in poor solvent. *Phys. Rev. E*, 69:021916.
- [96] V. Bloomfield. 1996. DNA condensation. *Current Opinion in Structural Biology*, 6(3):334–341.
- [97] F. Livolant and A. Leforestier. 1996. Condensed phases of DNA: structures and phase transitions. *Progress in Polymer Science*, 21(6):1115–1164.
- [98] D. Durand, J. Doucet, and F. Livolant. 1992. A study of the structure of highly concentrated phases of DNA by X-ray diffraction. *J. Phys. II France*, 2:1769–1783.
- [99] S. M. Mel'nikov, V. G. Sergeev, and K. Yoshikawa. 1995. Discrete coil-globule transition of large DNA induced by cationic surfactant. *Journal of the American Chemical Society*, 117(9):2401–2408.
- [100] B. Sung, A. Leforestier, and F. Livolant. 2016. Coexistence of coil and globule domains within a single confined DNA chain. *Nucleic Acids Research*, 44(3):1421–1427.

- [101] Y. Lansac, J. Degrouard, M. Renouard, A. C. Toma, F. Livolant, and E. Raspaud. 2016. A route to self-assemble suspended DNA nano-complexes. *Scientific Reports*, 6:21995.
- [102] B. Bohrmann, M. Haider, and E. Kellenberger. 1993. Concentration evaluation of chromatin in unstained resin-embedded sections by means of low-dose ratio-contrast imaging in STEM. *Ultramicroscopy*, 49:235–51.
- [103] M. Almiron, A. J. Link, D. Furlong, and R. Kolter. 1992. A novel DNA-binding protein with regulatory and protective roles in starved *Escherichia coli*. *Genes & Development*, 6:2646–2654.
- [104] S. Altuvia, M. Almiron, G. Huisman, R. Kolter, and G. Storz. 1994. The DPS promoter is activated by OxyR during growth and by IHF and  $\sigma^S$  in stationary phase. *Molecular Microbiology*, 13(2):265–272.
- [105] G. L. Newton, J. A. Aguilera, J. F. Ward, and R. C. Fahey. 1996. Polyamine-induced compaction and aggregation of DNA – a major factor in radioprotection of chromatin under physiological conditions. *Radiation research*, 145:776–80.
- [106] T. Yoshizaki and H. Yamakawa. 1980. Scattering functions of worm-like and helical worm-like chains. *Macromolecules*, 13(6):1518–1525.
- [107] J. F. Marko and E. D. Siggia. 1995. Stretching DNA. *Macromolecules*, 28(26):8759–8770.
- [108] D. Bensimon, D. Dohmi, and M. Mézard. 1998. Stretching a heteropolymer. *EPL (Europhysics Letters)*, 42:97–102.
- [109] C. J. Dorman. 2007. H-NS, the genome sentinel. *Nat Rev Micro*, 5:157–161.
- [110] R. T. Dame and N. Goosen. 2002. HU: promoting or counteracting DNA compaction? *FEBS Letters*, 529(2–3):151 – 156.
- [111] W. Wang, G.-W. Li, C. Chen, X. S. Xie, and X. Zhuang. 2011. Chromosome organization by a nucleoid-associated protein in live bacteria. *Science*, 333(6048):1445–1449.
- [112] V. McGovern, N. Higgins, R. Chiz, and A. Jaworski. 1994. H-NS over-expression induces an artificial stationary phase by silencing global transcription. *Biochimie*, 76(10–11):1019 – 1029.
- [113] A. Ryter and A. Chang. 1975. Localization of transcribing genes in the bacterial cell by means of high resolution autoradiography. *J Mol Biol*, 98:797–810.
- [114] A. J. Bokal, W. Ross, T. Gaal, R. C. Johnson, and R. L. Gourse. 1997. Molecular anatomy of a transcription activation patch: FIS–RNA polymerase interactions at the *Escherichia coli* *rrnB* P1 promoter. *The EMBO Journal*, 16(1):154–162.
- [115] D. C. Grainger, D. Hurd, M. D. Goldberg, and S. J. W. Busby. 2006. Association of nucleoid proteins with coding and non-coding segments of the *Escherichia coli* genome. *Nucleic Acids Research*, 34(16):4642–4652.
- [116] A. Ishihama, A. Kori, E. Koshio, K. Yamada, H. Maeda, T. Shimada, H. Makinoshima, A. Iwata, and N. Fujita. 2014. Intracellular concentrations of 65 species of transcription factors with known regulatory functions in *Escherichia coli*. *Journal of bacteriology*, 196(15):2718–27.
- [117] C. J. Dorman and P. Deighan. 2003. Regulation of gene expression by histone-like proteins in bacteria. *Current Opinion in Genetics & Development*, 13(2):179 – 184.
- [118] W. W. Navarre, M. McClelland, S. J. Libby, and F. C. Fang. 2007. Silencing of xenogeneic DNA by H-NS facilitation of lateral gene transfer in bacteria by a defense system that recognizes foreign DNA. *Genes & Development*, 21(12):1456–1471.
- [119] R. Schneider, R. Lurz, G. Lüder, C. Tolksdorf, A. Travers, and G. Muskhelishvili. 2001. An architectural role of the *Escherichia coli* chromatin protein FIS in organising DNA. *Nucleic Acids Research*, 29(24):5107–5114.
- [120] T. A. Azam, A. Iwata, A. Nishimura, S. Ueda, and A. Ishihama. 1999. Growth phase-dependent variation in protein composition of the *Escherichia coli* nucleoid. *Journal of bacteriology*, 181(20):6361–6370.

- [121] S. C. Dillon and C. J. Dorman. 2010. Bacterial nucleoid-associated proteins, nucleoid structure and gene expression. *Nature Reviews Microbiology*, 8(3):185–195.
- [122] R. T. Dame, C. Wyman, R. Wurm, R. Wagner, and N. Goosen. 2002. Structural basis for H-NS-mediated trapping of RNA polymerase in the open initiation complex at the *rrnB* P1. *Journal of Biological Chemistry*, 277(3):2146–2150.
- [123] R. T. Dame, C. Wyman, and N. Goosen. 2000. H-NS mediated compaction of DNA visualised by atomic force microscopy. *Nucleic Acids Res.*, 28:3504–3510.
- [124] G. Stormo. 2013. Modeling the specificity of protein-DNA interactions. *Quantitative Biology*, 1(2):115–130.
- [125] M. Sheinman, O. Bénichou, Y. Kafri, and R. Voituriez. 2012. Classes of fast and specific search mechanisms for proteins on DNA. *Reports on Progress in Physics*, 75(2):026601.
- [126] R. T. Dame, M. C. Noom, and G. J. L. Wuite. 2006. Bacterial chromatin organization by H-NS protein unravelled using dual DNA manipulation. *Nature*, 444:387–390.
- [127] R. Spurio, M. Dürrenberger, M. Falconi, A. La Teana, C. Pon, and C. Gualerzi. 1992. Lethal overproduction of the *Escherichia coli* nucleoid protein H-NS: ultramicroscopic and molecular autopsy. *Molecular and General Genetics MGG*, 231(2):201–211.
- [128] P. N. Hengen, S. L. Bartram, L. E. Stewart, and T. D. Schneider. 1997. Information analysis of FIS binding sites. *Nucleic Acids Research*, 25(24):4994–5002.
- [129] D. Skoko, J. Yan, R. C. Johnson, and J. F. Marko. 2005. Low-force DNA condensation and discontinuous high-force decondensation reveal a loop-stabilizing function of the protein FIS. *Phys. Rev. Lett.*, 95:208101.
- [130] D. Skoko, D. Yoo, H. Bai, B. Schnurr, J. Yan, S. M. McLeod, J. F. Marko, and R. C. Johnson. 2006. Mechanism of chromosome compaction and looping by the *Escherichia coli* nucleoid protein FIS. *Journal of Molecular Biology*, 364(4):777 – 798.
- [131] M. D. Bradley, M. B. Beach, A. P. J. de Koning, T. S. Pratt, and R. Osuna. 2007. Effects of FIS on *Escherichia coli* gene expression during different growth stages. *Microbiology*, 153(9):2922–2940.
- [132] K. K. Swinger and P. A. Rice. 2004. IHF and HU: flexible architects of bent DNA. *Current Opinion in Structural Biology*, 14(1):28 – 35.
- [133] K. Wojtuszewski, , and I. Mukerji. 2003. HU binding to bent DNA: a fluorescence resonance energy transfer and anisotropy study. *Biochemistry*, 42(10):3096–3104. PMID: 12627977.
- [134] V. T. Ryan, J. E. Grimwade, C. J. Nievera, and A. C. Leonard. 2002. IHF and HU stimulate assembly of pre-replication complexes at *Escherichia coli* *oriC* by two different mechanisms. *Molecular Microbiology*, 46(1):1365–2958.
- [135] Regulon DB. Position scoring matrices for TFs in *E. coli*. <http://regulondb.ccg.unam.mx>.
- [136] J. Zhou and K. E. Rudd. 2013. EcoGene.org. *Nucleic Acid Research*, 41:D613–D624.
- [137] K.-K. Kunze and R. R. Netz. 2000. Salt-induced DNA-histone complexation. *Phys. Rev. Lett.*, 85:4389–4392.
- [138] L. Czaplá, D. Swigon, and W. K. Olson. 2008. Effects of the nucleoid protein HU on the structure, flexibility, and ring-closure properties of DNA deduced from monte carlo simulations. *Journal of Molecular Biology*, 382(2):353 – 370.
- [139] M. Joyeux and J. Vreede. 2013. A model of H-NS mediated compaction of bacterial DNA. *Biophysical Journal*, 104(7):1615 – 1622.
- [140] Z. Duan, M. Andronescu, K. Schutz, S. McIlwain, Y. Jung Kim, C. Lee, J. Shendure, S. Fields, C. A. Blau, and W. S. Noble. 2010. A three-dimensional model of the yeast genome. *Nature Letters*, 465.
- [141] F. Jin and B. Ren. 2013. A high-resolution map of the three-dimensional chromatin interactome in human cells. *Nature Letters*, 503(290).

- [142] G. M. Church, M. A. Umbarger, E. Toro, M. A. Wright, G. J. Porreca, D. Baù, S.-H. Hong, M. J. Fero, M. A. Marti-Renom, H. H. McAdams, L. Shapiro, and J. Dekker. 2011. The three-dimensional architecture of a bacterial genome. *Mol Cell*, 44:1097–2765.
- [143] T. Sexton and G. Cavalli. 2013. The 3D genome shapes up for pluripotency. *Cell Stem Cell*, 13:3–4.
- [144] T. Sexton, E. Yaffe, E. Kenigsberg, F. Bantignies, B. Leblanc, M. Hoichman, H. Parrinello, A. Tanay, and G. Cavalli. 2012. Three-dimensional folding and functional organization principles of the *Drosophila* genome. *Cell*, 148:458–472.
- [145] J. Fraser, C. Ferrai, A. M. Chiariello, M. Schueler, T. Rito, G. Laudanno, M. Barbieri, B. L. Moore, D. C. Kraemer, S. Aitken, et al. 2015. Hierarchical folding and reorganization of chromosomes are linked to transcriptional changes in cellular differentiation. *Molecular systems biology*, 11(12):852.
- [146] T. Chandra, P. A. Ewels, S. Schoenfelder, M. Furlan-Magaril, S. W. Wingett, K. Kirschner, J.-Y. Thuret, S. Andrews, P. Fraser, and W. Reik. 2015. Global reorganization of the nuclear landscape in senescent cells. *Cell reports*, 10(4):471–483.
- [147] E. Yaffe and A. Tanay. 2011. Probabilistic modeling of Hi-C contact maps eliminates systematic biases to characterize global chromosomal architecture. *Nat Genet*, 43:1059–1065.
- [148] J.-M. Belton, R. P. McCord, J. H. Gibcus, N. Naumova, Y. Zhan, and J. Dekker. 2012. Hi-C: A comprehensive technique to capture the conformation of genomes. *Methods*, 58(3):268–276.
- [149] G. Reuss, W. Disteldorf, A. O. Gamer, and A. Hilt. 2000. *Formaldehyde*. Wiley-VCH Verlag GmbH & Co. KGaA.
- [150] V. Jackson. 1999. Formaldehyde cross-linking for studying nucleosomal dynamics. *Methods*, 17(2):125–139.
- [151] A. Cournac, H. Marie-Nelly, M. Marbouty, R. Koszul, and J. Mozziconacci. 2012. Normalization of a chromosomal contact map. *BMC Genomics*, 13(1):1–13.
- [152] J. Mozziconacci, A. Lesne, J. Riposo, P. Roger, and A. Cournac. 2014. 3D genome reconstruction from chromosomal contacts. *Nature Methods*, pages 1141–1143.
- [153] S. Jhunjhunwala, M. C. van Zelm, M. M. Peak, S. Cutchin, R. Riblet, J. J. van Dongen, F. G. Grosveld, T. A. Knoch, and C. Murre. 2008. The 3D structure of the immunoglobulin heavy-chain locus: Implications for long-range genomic interactions. *Cell*, 133(2):265 – 279.
- [154] D. Jost, P. Carrivain, G. Cavalli, and C. Vaillant. 2014. Modeling epigenome folding: formation and dynamics of topologically associated chromatin domains. *Nucleic Acids Research*, pages 9541–9549.
- [155] L. Giorgetti, R. Galupa, E. P. Nora, T. Pilot, F. Lam, J. Dekker, G. Tian, and E. Heard. 2014. Predictive polymer modeling reveals coupled fluctuations in chromosome conformation and transcription. *Cell*, 157:950–963.
- [156] M. P. Solf and T. A. Vilgis. 1995. Statistical mechanics of macromolecular networks without replicas. *Journal of Physics A: Mathematical and General*, 28(23):6655.
- [157] Y. Kantor and M. Kardar. 1996. Conformations of randomly linked polymers. *Phys. Rev. E*, 54:5263–5267.
- [158] J. D. Bryngelson and D. Thirumalai. 1996. Internal constraints induce localization in an isolated polymer molecule. *Phys. Rev. Lett.*, 76:542–545.
- [159] M. Bohn, D. W. Heermann, and R. van Driel. 2007. Random loop model for long polymers. *Phys. Rev. E*, 76:051805.
- [160] J. Mateos-Langerak, M. Bohn, W. de Leeuw, O. Giromus, E. M. M. Manders, P. J. Verschure, M. H. G. Indemans, H. J. Gierman, D. W. Heermann, R. van Driel, and S. Goetze. 2009. Spatially confined folding of chromatin in the interphase nucleus. *Proceedings of the National Academy of Sciences*, 106(10):3812–3817.